Quantum Networks using Spins in Diamond

Hermans, S.L.N.

DOI
10.4233/uuid:b6ab630d-f054-42de-b5f9-113a08ef4362

Publication date
2022

Document Version
Final published version

Citation (APA)
Hermans, S. L. N. (2022). *Quantum Networks using Spins in Diamond*. [Dissertation (TU Delft), Delft University of Technology]. https://doi.org/10.4233/uuid:b6ab630d-f054-42de-b5f9-113a08ef4362

Quantum Networks using Spins in Diamond

Sophie Hermans

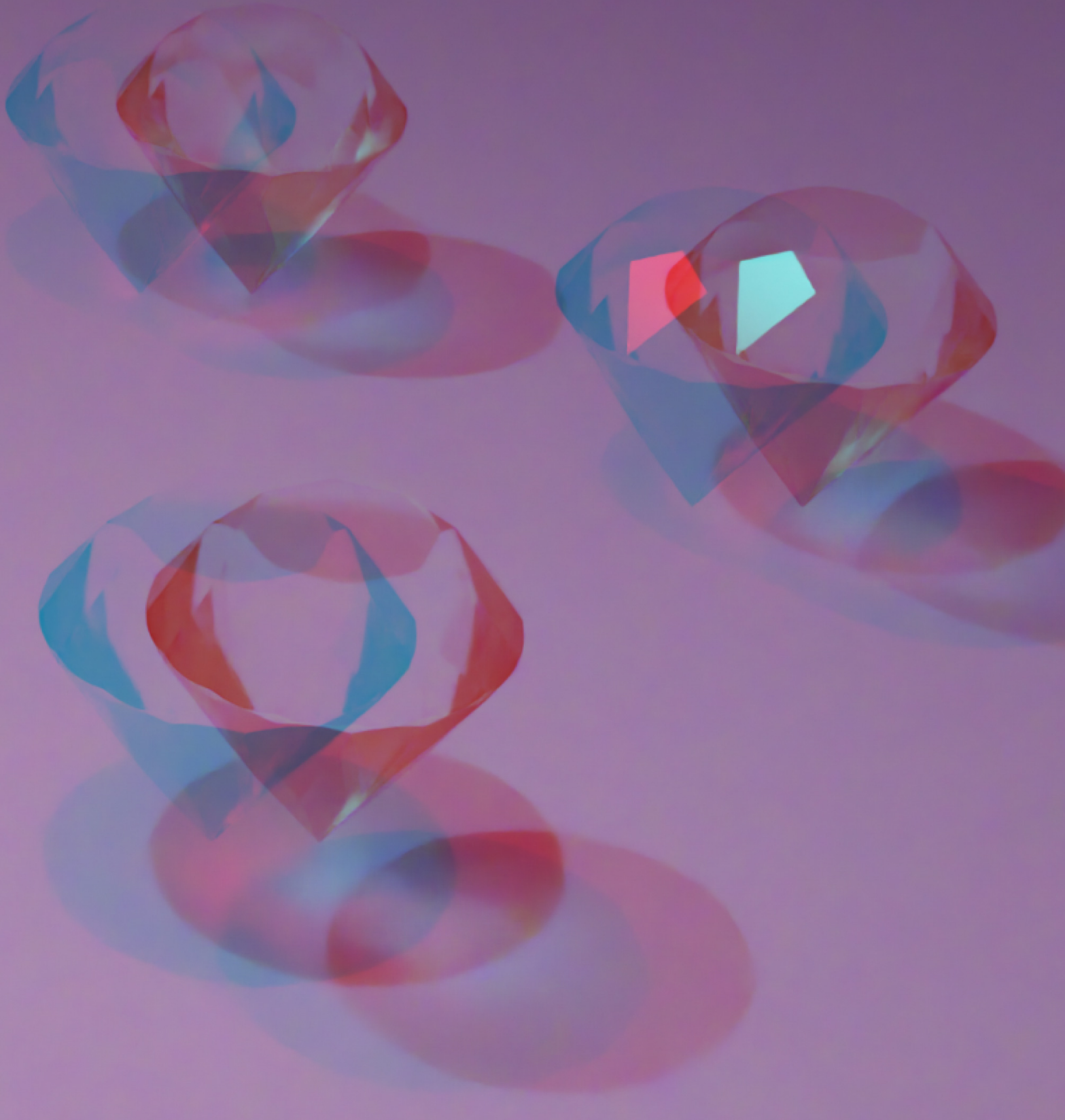

QUANTUM NETWORKS USING SPINS IN DIAMOND

QUANTUM NETWORKS USING SPINS IN DIAMOND

Proefschrift

ter verkrijging van de graad van doctor
aan de Technische Universiteit Delft,
op gezag van de Rector Magnificus prof. dr. ir. T.H.J.J. van der Hagen,
voorzitter van het College voor Promoties,
in het openbaar te verdedigen op donderdag 14 april 2022 om 15:00 uur.

door

Sophie Lucia Nathalie HERMANS

Master of Science in Applied Physics,
Technische Universiteit Delft, Nederland
geboren te Utrecht, Nederland.

Dit proefschrift is goedgekeurd door de promotoren.

Samenstelling promotiecommissie:

Rector Magnificus,	voorzitter
Prof. dr. ir. R. Hanson	Technische Universiteit Delft, promotor
Prof. dr. S.D.C. Wehner	Technische Universiteit Delft, promotor
Onafhankelijke leden:	
Prof. dr. D. Englund	Massachusetts Institute of Technology
Prof. dr. H. de Riedmatten	ICFO
Prof. dr. B.M. Terhal	Technische Universiteit Delft
Dr. M. Blaauboer	Technische Universiteit Delft
Prof. dr. S. Gröblacher	Technische Universiteit Delft, reservelid

Casimir PhD Series, Delft-Leiden 2022-09

ISBN 978-90-8593-520-9

An electronic version of this dissertation is available at
`http://repository.tudelft.nl/`.

CONTENTS

SUMMARY

A future quantum internet will bring revolutionary opportunities. In a quantum internet, information will be represented using qubits. These qubits obey the rules of quantum mechanics. The possibilities to create superposition and entangled states, and to perform projective measurements give the quantum internet its unique strengths. A quantum internet will enable fundamentally secure communication, quantum computations in the cloud with complete privacy and quantum enhanced sensing. But it is likely that many of its applications are still unknown.

A full-scale quantum internet puts demanding requirements on the individual components. In the last decades single nodes and remote entanglement have been explored, but a small-scale prototype quantum network does not yet exist. In this thesis we go beyond single- or two-node experiments and realize the first multi-node quantum network using nitrogen-vacancy centers in diamond. The electron spin of this defect serves as the communication qubit and nearby ^{13}C nuclear spins as memory qubits. We investigate the performance of the network and demonstrate multiple key network-primitive protocols. In addition, we further explore and improve the individual building blocks.

Firstly, we implement a quantum frequency conversion process, crucial in mitigating photon losses between distant nodes. By converting photons emitted by the nitrogen-vacancy center from 637 nm to 1588 nm, we generate an entangled state between the electron spin qubit and a telecom-wavelength photon with time-bin encoding. To verify the entangled state, we use an imbalanced fiber interferometer to access the measurement bases other than the computational basis of the photonic qubit.

Secondly, we realize a multi-node quantum network. We demonstrate three experiments on the quantum network; we establish a genuine multi-partite entangled state across all nodes, perform entanglement swapping and teleport a qubit between the non-neighboring nodes in the network. To enable these experiments, we develop a scalable architecture for stabilizing the optical phase, we implement a tailored heralding scheme for high-fidelity entanglement generation, we enhance the average readout fidelity of the memory qubit and improve the memory qubit coherence during network activity.

Thirdly, we study the entanglement generation process in more detail. We develop a general theoretical model, tailor the result to our experimental implementation and experimentally verify the effect of several parameters, such as the initial superposition states, a frequency difference between the emitters and the power of the optical excitation pulses. Furthermore, we show that the implementation of a Charge-Resonance check can yield transform-limited optical linewidths of the emitter.

SAMENVATTING

Een toekomstig quantuminternet zal revolutionaire kansen met zich meebrengen. In een quantuminternet wordt informatie weergegeven met behulp van qubits. Deze qubits volgen de regels van de quantummechanica. De mogelijkheid om superposities en verstrengelde toestanden te creëren en projectieve metingen uit te voeren, geeft het quantuminternet zijn unieke kracht. Een quantuminternet zal fundamenteel veilige communicatie, quantumberekeningen in de cloud met volledige privacy en een netwerk van quantumsensoren mogelijk maken. Maar het is waarschijnlijk dat veel van zijn toepassingen nog onbekend zijn.

Een wereldwijd quantuminternet stelt hoge eisen aan de afzonderlijke componenten. In de afgelopen decennia zijn enkele knooppunten en verstrengeling op afstand onderzocht, maar een kleinschalig quantumnetwerk prototype bestaat nog niet. In dit proefschrift gaan we verder dan experimenten met één of twee knooppunten en realiseren we het eerste quantumnetwerk met meerdere knooppunten met behulp van stikstofholtecentra in diamant. De elektronische spin van dit defect dient als communicatiequbit en nabijgelegen ^{13}C kernspins als geheugenqubits. We onderzoeken de prestaties van het netwerk en demonstreren meerdere belangrijke netwerk protocollen. Daarnaast verkennen en verbeteren we de afzonderlijke bouwstenen.

Ten eerste implementeren we een frequentieconversieproces, cruciaal bij het verminderen van fotonverliezen tussen verre knooppunten. Door fotonen die door het stikstofholtecentrum worden uitgezonden om te zetten van 637 nm naar 1588 nm, genereren we een verstrengelde toestand tussen de elektronische spinqubit en een foton met telecom golflengte met een tijd-bin-codering. Om de verstrengelde toestand te verifiëren, gebruiken we een interferometer met verschillende armlengtes om toegang te krijgen tot andere meetbases dan de klassieke basis van de fotonische qubit.

Ten tweede realiseren we een quantumnetwerk met meerdere knooppunten. We demonstreren drie experimenten op het quantumnetwerk; we brengen een verstrengelde toestand tot stand over alle knooppunten, geven verstrengeling door met behulp van het middelste knooppunt en teleporteren een qubit tussen de niet-naburige knooppunten in het netwerk. Om deze experimenten mogelijk te maken, ontwikkelen we een schaalbare architectuur voor het stabiliseren van de optische fase, implementeren we een methode om verstrengelde toestanden van hoge kwaliteit te maken, verbeteren we de uitleestechniek van de geheugenqubit en verlengen we de geheugenqubit-coherentie tijdens netwerkactiviteit.

Ten derde bestuderen we het proces van het verstrengelen in meer detail. We ontwikkelen een generiek theoretisch model, specificeren het voor onze experimentele implementatie en verifiëren experimenteel het effect van verschillende parameters, zoals de initiële superpositietoestanden, een frequentieverschil tussen de uitgezonden fotonen en het vermogen van de optische excitatiepulsen. Verder laten we zien dat de implementatie van een lading-resonantiecheck Fouriertransformatie gelimiteerde optische lijnbreedten van de uitgezonden fotonen kan opleveren.

1

INTRODUCTION

1.1. THE QUANTUM INTERNET: A PROMISING TECHNOLOGY

The internet has become indispensable in our daily lives. In just fifty years since the realization of the first internet primitive in 1969 [1], a world without the world-wide-web has become unimaginable. We communicate via email and social media. We read the news online. We plan our traffic routes using online navigation tools. We order groceries or clothing via online stores. And we can even arrange all our financial matters online. Who would have thought that in 1969?

Just as the classical internet has brought many unforeseen applications, a future quantum internet will bring revolutionary opportunities too. In a quantum internet, information will be represented using quantum bits, or in short qubits. These qubits obey the rules of quantum mechanics and therefore behave differently than their classical counterparts. In particular, the possibilities to create superposition states and entangled states, and to perform projective measurements gives the quantum internet its unique strengths.

Several promising applications of a future quantum internet are already known. A quantum internet will enable fundamentally secure communication, quantum computations in the cloud with complete privacy and quantum enhanced sensing [2–7]. Moreover, the quantum internet can even serve as a platform where quantum mechanics itself can be tested [8]. But similarly to the early days of the classical internet, many of its uses are probably not yet discovered and the development of applications is an active research area in itself [9].

1.2. REQUIREMENTS FOR QUANTUM NETWORKS

The quantum internet does not yet exist, but several visions have been proposed [9–12]. These visions outline possible architectures for the network and the requirements for its constituents. In a common view, future quantum networks will be composed of multiple connected nodes between which both quantum and classical information can be communicated. And it is typically considered that each of these nodes consists of multiple qubits, which can be used to store and process quantum information.

Based on the proposed visions [9–12], we can compile a set of requirements for the qubits within a single node of the network:

(i) One must be able to initialize each qubit into a known state.

(ii) One must be able to perform a universal set of quantum gates on each qubit.

(iii) One must be able to measure the state each qubit.

(iv) One must be able to perform real-time logic. Many protocols require quantum operations to be executed dependent on a measurement outcome obtained elsewhere in the network.

(v) One must be able to preserve quantum states on the qubit for relevant time scales. The relevant time scales are set by the specific applications running on the net-

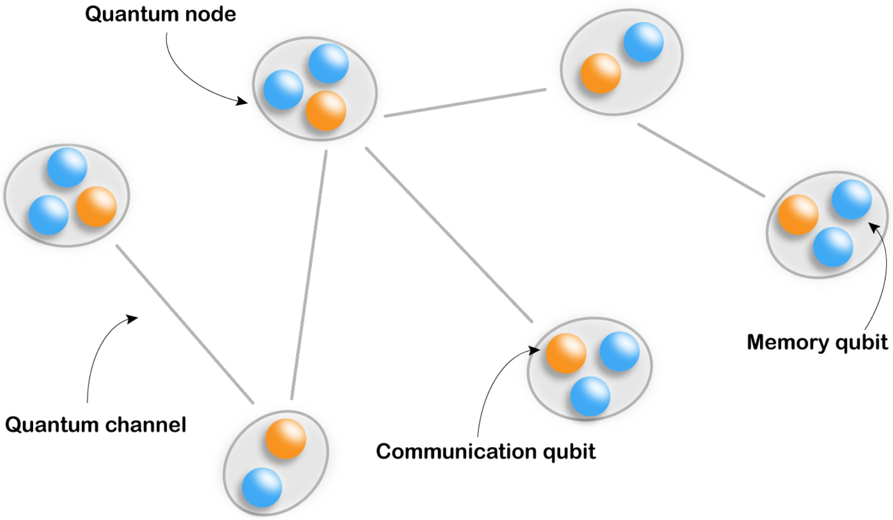

Figure 1.1: The quantum internet will consist of multiple connected nodes [9, 11]. The nodes are connected via a quantum channel to transfer quantum information between them. Each node contains several qubits. At least one of these qubits will be dedicated to generate remote entanglement with neighboring nodes, these are the communication qubits. Memory qubits will be used for storage of quantum states and small computations.

work. For example an entangle-and-measure-type of application requires shorter coherence times than a protocol with a larger circuit depth, such as blind quantum computation [4].

Additional to the requirements for the individual qubits, we can identify two requirements related to connecting, or entangling, qubits in distant nodes:

(vi) At least one of the qubits in each node must have a coherent optical interface to mediate entanglement with neighboring nodes.

(vii) Remote entanglement must be generated deterministically or in a heralded fashion. In either case, one must know when an entangled state with a sufficient fidelity with respect to the maximally entangled state is generated.

Within each node we can assign dedicated qubits to different tasks based on their performance and characteristics. In this thesis, we denote the qubit hosting the optical interface as the communication qubit. Qubits exhibiting long coherence times will be used to store quantum states and we refer to those qubits as memory qubits.

1.3. DEVELOPING A QUANTUM NETWORK: THE CHALLENGES

Due to this demanding set of requirements, a full-scale quantum internet or even a small prototype quantum network does not yet exist. In the last decades many of the building blocks, like single nodes and remote entanglement between two distant nodes, have been explored. Many different types of qubits with an optical interface have been investigated, for example trapped ions, neutral atoms, color defects in diamond and quantum dots [12–15]. Remote entanglement between separate nodes has been demonstrated using various platforms [8, 16–24]. However, generating complex entangled states across a truly large scale network involves more challenges.

One of these challenges is generating remote entanglement over large distances (>10km). In fiber-based networks, photon loss between the nodes reduces the entanglement rate (and in the presence of noise even prohibits the generation of quantum entangled states) at these distances. Photons generated at telecom wavelengths (λ =1500 -1600 nm) would be ideal due to their low absorption losses in optical glass fibers [25]. For this reason, qubit platforms that naturally emit or store photons at these frequencies have attracted a lot of attention [26, 27]. Another solution is to convert single photons from their original frequency to the telecom band using quantum frequency conversion techniques [28–34].

A second challenge is to simultaneously host (parts of) multiple remote entangled states in a single node, which is a requirement for many protocols [6, 35–37]. This requires the storage of an entangled state on a memory qubit while generating a second entangled state with the communication qubit. This storage turned out to be a major hurdle, because of additional decoherence induced by the entanglement generation process [38–40]. However, different experimental implementations have been able to store dephasing-insensitive eigenstates and superposition states, albeit for a limited amount of time during entanglement generation [40, 41].

As mentioned above, research efforts have so far focused on one or two nodes. On single nodes multi-qubit registers have been used for long-time storage of quantum states and to perform error correction codes [42–45]. Two-node entangled links have been used to show several network primitives such as qubit teleportation, non-local quantum gates and entanglement distillation [41, 46–51].

1.4. THESIS OVERVIEW

Going beyond single- or two-node experiments, and combining all building blocks in a scalable way, has not yet been achieved [1]. In this thesis we will take this next step and we will realize the first multi-node quantum network using nitrogen-vacancy centers in diamond. We will investigate its performance and demonstrate multiple key network-primitive protocols.

This thesis consists of the following chapters

- In chapter 2 we will present the main building blocks of the quantum network and explain the experimental methods and concepts. We begin by describing our qubit platform, the nitrogen-vacancy (NV) center in diamond. The electronic spin of this defect serves as the communication qubit and nearby carbon-13 nuclear

---

[1] Earlier work has involved more than two nodes [52, 53], but these experiments did not fulfill requirement (vii), a key requirement for scalable networks.

isotopes act as memory qubits. Next, we discuss the protocols to generate remote entanglement and to teleport qubits. Then, we describe the process of quantum frequency conversion, an essential element to generate remote entanglement over large distances. Lastly, we present the experimental layout.

- In chapter 3 we perform quantum frequency conversion to convert the wavelength of the photons emitted by the NV center to a wavelength in the telecom band. We show that the qubit-photon entanglement is preserved, a fundamental prerequisite for its use in quantum networks.

- In chapter 4 we present the first demonstration of a multi-node quantum network. We start by explaining the different elements of the network and their performance. Then, we show two canonical experiments; we generate a genuine multi-partite entangled state shared by all nodes, a so-called GHZ state and we perform the entanglement swapping protocol to realize an entangled state between two nodes that share no direct physical connection.

- Future applications of a quantum internet will rely on the transfer of quantum information. The teleportation protocol offers a lossless method to transfer qubits from one node to another. In chapter 5 we demonstrate teleportation of an arbitrary qubit state between non-neighboring nodes in the quantum network.

- Having a detailed understanding of the entanglement protocol is vital for generating remote entangled states with high fidelity and high rate. In chapter 6 we will discuss the single-photon entanglement scheme in more detail and investigate how different experimental parameters affect the heralded entangled state.

- In chapter 7 we provide a summary and conclusions based on the key results. We give an outlook for interesting future research lines, both near-term improvements and long-term directions.

REFERENCES

[1] H. Bidgoli, *The Internet Encyclopedia, Volume 2* (John Wiley & Sons, Inc., 2004) pp. 39–40.

[2] A. Ekert and R. Renner, *The ultimate physical limits of privacy,* Nature **507**, 443 (2014).

[3] L. Jiang, J. M. Taylor, A. S. Sørensen, and M. D. Lukin, *Distributed quantum computation based on small quantum registers,* Physical Review A **76**, 1 (2007).

[4] A. Broadbent, J. Fitzsimons, and E. Kashefi, *Universal Blind Quantum Computation,* (2009) pp. 517–526.

[5] D. Gottesman, T. Jennewein, and S. Croke, *Longer-baseline telescopes using quantum repeaters,* Physical Review Letters **109**, 1 (2012).

[6] N. H. Nickerson, J. F. Fitzsimons, and S. C. Benjamin, *Freely scalable quantum technologies using cells of 5-to-50 qubits with very lossy and noisy photonic links,* Physical Review X **4**, 1 (2014).

[7] P. Kómár, E. M. Kessler, M. Bishof, L. Jiang, A. S. Sørensen, J. Ye, and M. D. Lukin, *A quantum network of clocks,* Nature Physics **10**, 582 (2014).

[8] B. Hensen, H. Bernien, A. E. Dreaú, A. Reiserer, N. Kalb, M. S. Blok, J. Ruitenberg, R. F. Vermeulen, R. N. Schouten, C. Abellán, W. Amaya, V. Pruneri, M. W. Mitchell, M. Markham, D. J. Twitchen, D. Elkouss, S. Wehner, T. H. Taminiau, and R. Hanson, *Loophole-free Bell inequality violation using electron spins separated by 1.3 kilometres,* Nature **526**, 682 (2015).

[9] S. Wehner, D. Elkouss, and R. Hanson, *Quantum internet: A vision for the road ahead,* Science **362** (2018).

[10] D. P. DiVincenzo, *The physical implementation of quantum computation,* Fortschritte der Physik **48**, 771 (2000).

[11] H. J. Kimble, *The quantum internet,* Nature **453**, 1023 (2008).

[12] M. Ruf, N. H. Wan, H. Choi, D. Englund, and R. Hanson, *Quantum networks based on color centers in diamond,* Journal of Applied Physics **130**, 070901 (2021).

[13] L. M. Duan and C. Monroe, *Colloquium: Quantum networks with trapped ions,* Reviews of Modern Physics **82**, 1209 (2010).

[14] M. Saffman, T. G. Walker, and K. Mølmer, *Quantum information with Rydberg atoms,* Reviews of Modern Physics **82**, 2313 (2010).

[15] R. Uppu, L. Midolo, X. Zhou, J. Carolan, and P. Lodahl, *Quantum-dot-based deterministic photon–emitter interfaces for scalable photonic quantum technology,* Nature Nanotechnology (2021).

[16] D. L. Moehring, P. Maunz, S. Olmschenk, K. C. Younge, D. N. Matsukevich, L. M. Duan, and C. Monroe, *Entanglement of single-atom quantum bits at a distance,* Nature **449**, 68 (2007).

[17] I. Usmani, C. Clausen, F. Bussières, N. Sangouard, M. Afzelius, and N. Gisin, *Heralded quantum entanglement between two crystals,* Nature Photonics **6**, 234 (2012).

[18] J. Hofmann, M. Krug, N. Ortegel, L. Gérard, and M. Weber, *Heralded Entanglement Between Widely Separated Atoms,* Science **337**, 72 (2012).

[19] S. Ritter, C. Nölleke, C. Hahn, A. Reiserer, A. Neuzner, M. Uphoff, M. Mücke, E. Figueroa, J. Bochmann, and G. Rempe, *An elementary quantum network of single atoms in optical cavities,* Nature **484**, 195 (2012).

[20] A. Delteil, Z. Sun, W. B. Gao, E. Togan, S. Faelt, and A. Imamoglu, *Generation of heralded entanglement between distant hole spins,* Nature Physics **12**, 218 (2016).

[21] H. Bernien, B. Hensen, W. Pfaff, G. Koolstra, M. S. Blok, L. Robledo, T. H. Taminiau, M. Markham, D. J. Twitchen, L. Childress, and R. Hanson, *Heralded entanglement between solid-state qubits separated by three metres,* Nature **497**, 86 (2013).

[22] R. Stockill, M. J. Stanley, L. Huthmacher, E. Clarke, M. Hugues, A. J. Miller, C. Matthiesen, C. Le Gall, and M. Atatüre, *Phase-Tuned Entangled State Generation between Distant Spin Qubits,* Physical Review Letters **119**, 1 (2017).

[23] P. C. Humphreys, N. Kalb, J. P. Morits, R. N. Schouten, R. F. Vermeulen, D. J. Twitchen, M. Markham, and R. Hanson, *Deterministic delivery of remote entanglement on a quantum network,* Nature **558**, 268 (2018).

[24] D. Lago-rivera, S. Grandi, J. V. Rakonjac, A. Seri, and H. D. Riedmatten, *Telecom-heralded entanglement between multimode solid-state quantum memories,* Nature **594** (2021).

[25] K. Nagayama, M. Kakul, M. Matsul, T. Saitoh, and Y. Chigusa, *Ultra-low-loss (0.1484dB/km) pure silica core fibre and extension of transmission distance,* Electronics letters **38**, 1 (2002).

[26] A. I. Lvovsky, B. C. Sanders, and W. Tittel, *Optical quantum memory,* Nature Photonics **3**, 706 (2009).

[27] I. Craiciu, M. Lei, J. Rochman, J. G. Bartholomew, and A. Faraon, *Multifunctional on-chip storage at telecommunication wavelength for quantum networks,* Optica **8**, 114 (2021).

[28] S. Tanzilli, W. Tittel, M. Halder, O. Alibart, P. Baldi, N. Gisin, and H. Zbinden, *A photonic quantum information interface,* Nature **437** (2005).

[29] Y. O. Dudin, A. G. Radnaev, R. Zhao, J. Z. Blumoff, T. A. Kennedy, and A. Kuzmich, *Entanglement of light-shift compensated atomic spin waves with telecom light,* Physical Review Letters **105**, 1 (2010).

[30] K. De Greve, L. Yu, P. L. McMahon, J. S. Pelc, C. M. Natarajan, N. Y. Kim, E. Abe, S. Maier, C. Schneider, M. Kamp, S. Höfling, R. H. Hadfield, A. Forchel, M. M. Fejer, and Y. Yamamoto, *Quantum-dot spin-photon entanglement via frequency downconversion to telecom wavelength,* Nature **491**, 421 (2012).

[31] M. Bock, P. Eich, S. Kucera, M. Kreis, A. Lenhard, C. Becher, and J. Eschner, *High-fidelity entanglement between a trapped ion and a telecom photon via quantum frequency conversion,* Nature Communications **9**, 1 (2018).

[32] P. Farrera, G. Heinze, and H. De Riedmatten, *Entanglement between a Photonic Time-Bin Qubit and a Collective Atomic Spin Excitation,* Physical Review Letters **120**, 100501 (2018).

[33] T. Walker, K. Miyanishi, R. Ikuta, H. Takahashi, S. Vartabi Kashanian, Y. Tsujimoto, K. Hayasaka, T. Yamamoto, N. Imoto, and M. Keller, *Long-Distance Single Photon Transmission from a Trapped Ion via Quantum Frequency Conversion,* Physical Review Letters **120**, 203601 (2018).

[34] V. Krutyanskiy, M. Meraner, J. Schupp, V. Krcmarsky, H. Hainzer, and B. P. Lanyon, *Light-matter entanglement over 50 km of optical fibre,* npj Quantum Information **5** (2019).

[35] H. Briegel, W. Dür, J. I. Cirac, and P. Zoller, *Quantum Repeaters The Role of Imperfect Local Operations in Quantum Communication,* Physical Review Letters **81**, 5932 (1998).

[36] C. Monroe, R. Raussendorf, A. Ruthven, K. R. Brown, P. Maunz, L. M. Duan, and J. Kim, *Large-scale modular quantum-computer architecture with atomic memory and photonic interconnects,* Physical Review A - Atomic, Molecular, and Optical Physics **89**, 1 (2014).

[37] S. W. de Bone, R. Ouyang, K. Goodenough, and D. Elkouss, *Protocols for Creating and Distilling Multipartite GHZ States With Bell Pairs,* in *IEEE Quantum Engineering* (2020).

[38] D. Hucul, I. V. Inlek, G. Vittorini, C. Crocker, S. Debnath, S. M. Clark, and C. Monroe, *Modular entanglement of atomic qubits using photons and phonons,* Nature Physics **11**, 37 (2015).

[39] A. Reiserer, N. Kalb, M. S. Blok, K. J. van Bemmelen, T. H. Taminiau, R. Hanson, D. J. Twitchen, and M. Markham, *Robust quantum-network memory using decoherence-protected subspaces of nuclear spins,* Physical Review X **6**, 1 (2016).

[40] N. Kalb, P. C. Humphreys, J. J. Slim, and R. Hanson, *Dephasing mechanisms of diamond-based nuclear-spin memories for quantum networks,* Physical Review A **97**, 1 (2018).

[41] N. Kalb, A. A. Reiserer, P. C. Humphreys, J. J. Bakermans, S. J. Kamerling, N. H. Nickerson, S. C. Benjamin, D. J. Twitchen, M. Markham, and R. Hanson, *Entanglement distillation between solid-state quantum network nodes,* Science **356**, 928 (2017).

[42] M. H. Abobeih, J. Cramer, M. A. Bakker, N. Kalb, M. Markham, D. J. Twitchen, and T. H. Taminiau, *One-second coherence for a single electron spin coupled to a multi-qubit nuclear-spin environment,* Nature Communications **9**, 1 (2018).

[43] C. E. Bradley, J. Randall, M. H. Abobeih, R. C. Berrevoets, M. J. Degen, M. A. Bakker, M. Markham, D. J. Twitchen, and T. H. Taminiau, *A Ten-Qubit Solid-State Spin Register with Quantum Memory up to One Minute,* Physical Review X **9**, 31045 (2019).

[44] J. Cramer, N. Kalb, M. S. Blok, M. A. Rol, T. H. Taminiau, M. Markham, B. Hensen, R. Hanson, and D. J. Twitchen, *Repeated quantum error correction on a continuously encoded qubit by real-time feedback,* Nature Communications **7**, 1 (2016).

[45] L. Egan, D. M. Debroy, C. Noel, A. Risinger, D. Zhu, D. Biswas, M. Newman, M. Li, K. R. Brown, M. Cetina, and C. Monroe, *Fault-tolerant control of an error-corrected qubit,* Nature **598** (2021), 10.1038/s41586-021-03928-y.

[46] S. Olmschenk, D. N. Matsukevich, P. Maunz, D. Hayes, and C. Monroe, *Quantum Teleportation between Distant Matter Qubits,* Science **323**, 486 (2009).

[47] X. H. Bao, X. F. Xu, C. M. Li, Z. S. Yuan, C. Y. Lu, and J. W. Pan, *Quantum teleportation between remote atomic-ensemble quantum memories,* Proceedings of the National Academy of Sciences of the United States of America **109**, 20347 (2012).

[48] C. Nölleke, A. Neuzner, A. Reiserer, C. Hahn, G. Rempe, and S. Ritter, *Efficient teleportation between remote single-atom quantum memories,* Physical Review Letters **110**, 1 (2013).

[49] W. Pfaff, B. J. Hensen, H. Bernien, S. B. Van Dam, M. S. Blok, T. H. Taminiau, M. J. Tiggelman, R. N. Schouten, M. Markham, D. J. Twitchen, and R. Hanson, *Unconditional quantum teleportation between distant solid-state quantum bits,* Science **345**, 532 (2014).

[50] S. Langenfeld, S. Welte, L. Hartung, S. Daiss, P. Thomas, O. Morin, E. Distante, and G. Rempe, *Quantum Teleportation between Remote Qubit Memories with only a Single Photon as a Resource,* Physical Review Letters **126**, 130502 (2021).

[51] S. Daiß, S. Langenfeld, S. Welte, E. Distante, P. Thomas, L. Hartung, O. Morin, and G. Rempe, *A quantum-logic gate between distant quantum-network modules,* Science **371**, 614 (2021).

[52] D. Bouwmeester, J.-w. Pan, M. Daniell, H. Weinfurter, and A. Zeilinger, *Observation of Three-Photon Greenberger-Horne-Zeilinger Entanglement,* Physical Review Letters **82**, 1 (1999).

[53] B. Jing, X. J. Wang, Y. Yu, P. F. Sun, Y. Jiang, S. J. Yang, W. H. Jiang, X. Y. Luo, J. Zhang, X. Jiang, X. H. Bao, and J. W. Pan, *Entanglement of three quantum memories via interference of three single photons,* Nature Photonics **13**, 210 (2019).

2

EXPERIMENTAL METHODS AND CONCEPTS

As discussed in Chapter 1, we build up to the realization of a quantum network. To do so, we perform various experiments in the following chapters. These experiments involve many different methods, ranging from measurement techniques and calibration steps to setup components and theoretical models to explain the measurement outcomes. The majority of these methods is based on previous work. Since these methods are only briefly covered in Chapters 3 to 6 we explain the experimental methods in more detail in this chapter.

We start by describing the physical system, the nitrogen-vacancy center in diamond, in Section 2.1. This defect provides us with a communication qubit and memory qubits. Next, we explain the control techniques associated with the communication qubit and subsequently the memory qubits (Sections 2.2 and 2.3). We explain the process of quantum frequency conversion in Section 2.4. In Sections 2.5 and 2.6 we turn to protocols to generate entangled states and discuss quantum teleportation. We finish the chapter with a description of the experimental layout in Section 2.7.

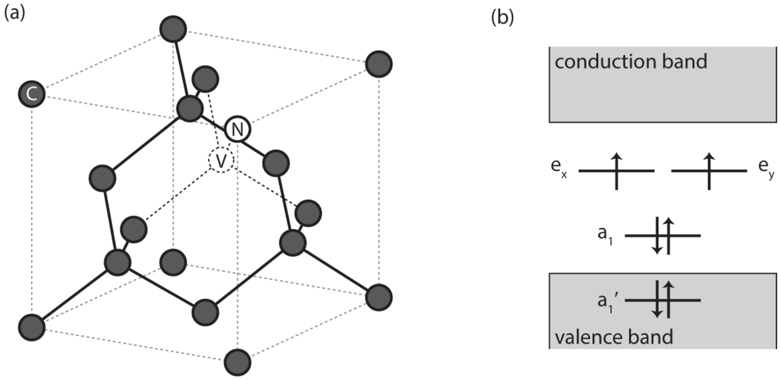

Figure 2.1: **The nitrogen-vacancy (NV) center in diamond (a)** The crystalline structure of the NV center. This point defect consists of a substitutional nitrogen atom and a vacant lattice site. **(b)** Molecular orbitals are formed by a linear combination of the atomic orbitals of the nitrogen atom and the carbon atoms surrounding the vacant site. The energy level of the lowest energy orbital ($a_1^{'}$) lies within the valence band of diamond, while the energy levels of the a_1, e_x and e_y orbitals lie in the bandgap. Figure adapted from Pfaff, Bernien [3, 4].

2.1. THE NITROGEN-VACANCY CENTER IN DIAMOND

In this thesis we use the negatively-charged nitrogen-vacancy center in diamond as our qubit platform. The nitrogen-vacancy (NV) center is a point defect in diamond. Two neighboring carbon atoms are missing from the crystalline lattice, one is replaced by a nitrogen (N) atom and the adjacent lattice site is left vacant (V), see Figure 2.1a. This defect hosts five electrons in the neutral charge state, NV^0, three of these electrons are provided by the dangling bonds of the carbon atoms surrounding the vacant site and two electrons of the dangling bond of the nitrogen atom. Additionally, an extra electron from the environment can be trapped in the defect, resulting in NV$^-$. The NV$^-$has several properties that make it interesting to use as qubit platform [1, 2].

First of all, the NV$^-$is well isolated from its environment. The nitrogen and carbon atomic orbitals are linearly combined to form molecular orbitals [5], $a_1^{'}, a_1, e_x, e_y$, see Figure 2.1b. In the ground state the two lowest energy orbitals are filled with two electrons each, and in the triplet configuration the degenerate e_x and e_y orbitals both host a single electron. In the excited state one of the electrons from the a_1 orbital is promoted to either e_x or e_y (or a superposition of the two). Both in the ground and excited state the energy levels of the not-completely-filled orbitals lie in the diamond bandgap [5]. As a result, the NV$^-$is well isolated from its solid-state environment and exhibits single ion-like properties. In Section 2.2 the level structure is discussed in more detail.

Secondly, the NV$^-$provides an optical interface. Due to its orbital configuration the NV$^-$is a spin-1 system and at cryogenic temperatures the spin-triplet states of the orbital ground state can be excited resonantly. We can excite the different spin states selectively

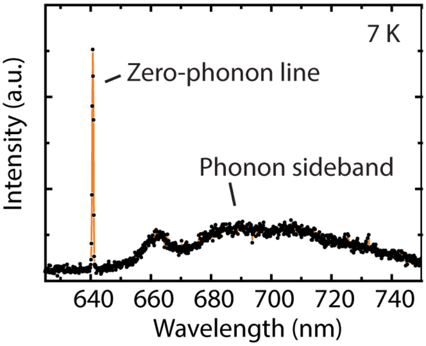

Figure 2.2: **NV$^-$ emission spectrum at cryogenic temperatures** Decay from the excited states can occur resonantly under the emission of a zero-phonon line (ZPL) photon, or off-resonantly via a vibrational state under the emission of a phonon-sideband (PSB) photon and a phonon. Figure adapted from Van der Sar [9].

and because of the (mostly) cyclic nature of these transitions we can create spin-photon entangled states [6]. These spin-photon entangled states can be used to readout the spin state or generate remote spin-spin entangled states, see Sections 2.2.3 and 2.5.

For remote entanglement generation only resonantly emitted photons, so-called zero-phonon line (ZPL) photons, can be used. However, off-resonant decay can occur via vibrational states [5]. In this case, the emitted photon is and accompanied by the emission of a phonon. These off-resonantly emitted photons are referred to as phonon-sideband (PSB) photons. Since the emitted phonon also carries information about the spin state, loss of the phonon will project the qubit state and therefore PSB photons cannot be used for entanglement generation. The ratio between resonantly (ZPL) and off-resonantly emitted photons is set by the Debye-Waller factor and is for the NV$^-$around $\approx 2.55\%$ [7, 8].

Thirdly, the electron spin of the NV$^-$can serve as a central qubit allowing control of additional qubits [10, 11]. Whereas diamond consists predominantly of spinless ^{12}C atoms, the ^{13}C isotope occurs with a natural abundance of 1.1% in non-purified diamond (nuclear spin of $I = 1/2$). On one hand, the resulting spin-bath poses a challenge since it is largely responsible for the intrinsic dephasing of the electronic spin of the NV$^-$. On the other hand, the nuclear spins offer qubit register. Nearby ^{13}C atoms can be sensed individually and controlled due to the hyperfine interaction between the electronic spin of the NV$^-$and the nuclear spin of the ^{13}C atom [12].

In this thesis we use both the electronic spin of the NV$^-$and the ^{13}C nuclear spins as qubits. We refer to the electronic spin of the NV$^-$as the communication qubit because of its optical interface. The ^{13}C nuclear spins are used as memory qubits; they can be used for quantum computations and storage of quantum states [10, 13].

2.2. COMMUNICATION QUBIT CONTROL

Most of the control techniques used for the communication qubit are related to the specific electronic energy level structure of the negatively-charged nitrogen-vacancy center. For this reason we start this section with a more in depth explanation of the level structure, see Figure 2.3. The ground and excited spin-triplet states ${}^3A_2$ and ${}^3E$ are connected via optical transitions and show cyclic behavior. State-dependent decay from the ${}^3E$ states to the singlet excited state ${}^1A_1$ leads to an intersystem crossing and results in a spin-flipping decay channel [6, 14–16], instrumental to the spin-initialization procedure discussed later.

The ${}^3A_2$ ground state is split into two levels due to spin-orbit interactions and exhibits a zero-field splitting $D \approx 2.88$ GHz [5, 18]. In the presence of a magnetic field $\vec{\mathbf{B}}$ the $|m_s = \pm 1\rangle$ ground states are split due to the Zeeman effect. Thus the ground state Hamiltonian H_{gs} (neglecting effects from strain, external electric fields and couplings to nearby nuclear spins) is given by

$$H_{gs} = DS_z^2 + \gamma_e \vec{\mathbf{B}} \cdot \vec{\mathbf{S}} \tag{2.1}$$

with S_i the spin-1 Pauli operators and the z-axis defined to be along the NV crystal axis. In Eq. (2.1) γ_e is the gyromagnetic ration and has a value of $2\pi \times 2.802$ MHz/G. In this thesis we choose the qubit subspace of the communication qubit to be $|0\rangle \equiv |m_s = 0\rangle$ and $|1\rangle \equiv |m_s = +1\rangle$ or $|m_s = -1\rangle$. The choice for $|m_s = -1\rangle$ or $|m_s = +1\rangle$ as the $|1\rangle$ state depends on several factors. For instance, the ability to drive the $|0\rangle \leftrightarrow |1\rangle$ transition using microwave pulses (see Section 2.2.4) and a small probability to off-resonantly excite close-by transitions.

The ${}^3E$ excited state is split into four levels due to spin-spin and spin-orbit interactions [19, 20]. The levels are shifted and split further by strain and electric fields. For the experiments in this thesis we use the $|m_s = 0\rangle \leftrightarrow |E_x\rangle$ or $|E_y\rangle$ as the transition to readout the qubit state and to create remote entangled states (Sections 2.2.3 and 2.5), again the choice for $|E_x\rangle$ or $|E_y\rangle$ is dependent on factors such as limited off-resonant excitation as well as the ability to tune the transition (see below) and the collection efficiency of the photons with horizontal or vertical polarization. Additionally, we use the $|m_s = \pm 1\rangle \leftrightarrow |E_{1,2}\rangle$ transitions for initialization (Section 2.2.2).

We use photons associated with the $|E_x\rangle \rightarrow |0\rangle$ (or $|E_y\rangle \rightarrow |0\rangle$) to generate entanglement between communication qubits of distant nodes. To ensure perfect indistinguishable of the photons, we require the emitted photons to be of the same frequency. However, sample-specific strain causes in frequency differences of the optical transitions between different diamond samples. A solution is to induce a DC Stark shift by gate tuning [21]; via gate electrodes on the diamond sample we can apply an electric field to shift the frequencies to a common frequency set point, see Figure 4.1.

2.2.1. CHARGE-RESONANCE CHECK

Prior to - and directly - after any experimental repetition, we perform a so-called Charge-Resonance (CR) check to ensure that the defect is in the right charge state (NV$^-$) and on

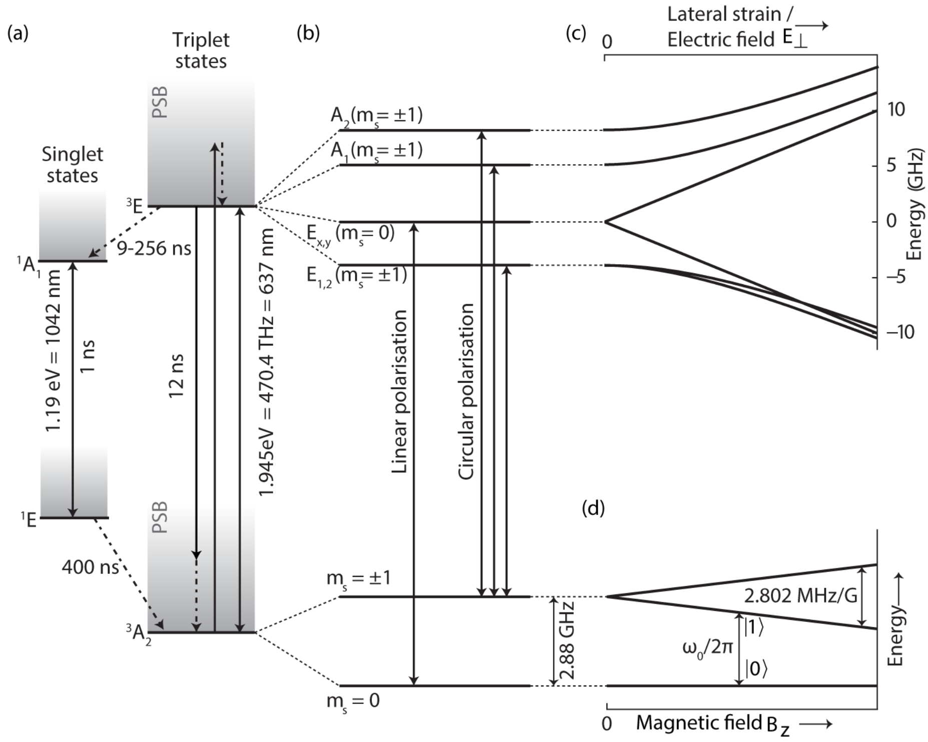

Figure 2.3: **Electronic energy level structure of NV$^-$** Adapted from Bernien, Pfaff, Kalb [3, 4, 17] **(a)** The spin-triplet ground states $^3A_2$ and excited states ^3E are optically connected, as well as the spin-singlet ground state ^1E and excited state $^1A_1$. Excitation and emission can happen resonantly or off-resonantly via vibronic states, the phonon side band (PSB, shaded blocks). A spin-flipping channel is opened via an intersystem crossing, the ^3E states can decay to $^1A_1$, with a rate dependent on the exact state (9 – 256ns [16]). The decay from the ^1E state to the $^3A_2$ states is temperature dependent and at cryogenic temperatures ≈ 400ns [16]. **(b)** Due to spin-orbit interactions the $^3A_2$ ground state is split into two levels. The ^3E excited states are split because of spin-spin and spin-orbit couplings. These couplings result in two doubly degenerate states $E_{x,y}$ and $E_{1,2}$. At cryogenic temperatures, the optical transitions can be addressed state selectively. **(c)** Strain or electric fields can distort the crystalline symmetry of the defect and shift the energy levels of the excited state. **(d)** An external magnetic field along the NV crystal axis, B_z, splits the energy levels of the $|m_s = \pm 1\rangle$ spin states due to the Zeeman effect.

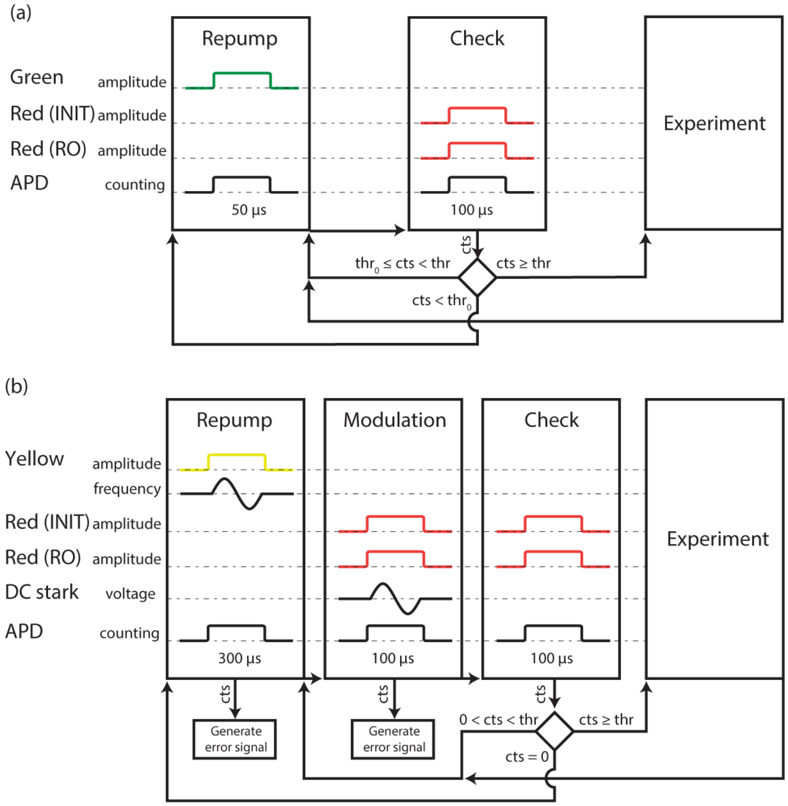

Figure 2.4: **Charge-Resonance check** Adapted from Hensen [18]. **(a)** Charge-Resonance (CR) check using green laser pulses (λ = 515nm) to perform the charge repump. This implementation of the CR check consists of a repump phase and a check phase. We start with the check phase. During this phase we turn on both red lasers, one tuned to the transition used for initialization (INIT in the diagram) and one tuned to the readout transition (RO), and measure photon counts using an avalanche photodiode (APD). When we measure a number of photon counts (*cts* in the diagram) larger than a set threshold *thr*, we conclude the NV to be in the correct charge state and on resonance with the control lasers and begin the experimental repetition. When we measure *cts*< *thr*, we use a second threshold thr$_0$. When $cts \geq thr_0$ we perform the check phase again, else we go the repump phase. In the repump phase we turn on green laser light to prepare the NV in the correct charge state, NV$^-$, and afterwards we perform another check. **(b)** CR check using yellow laser pulses (λ = 575nm) to perform the charge repump. This implementation is similar to the one using green laser pulses but it has one additional phase, a modulation phase. We use the modulation phase to bring the NV$^-$on resonance with the control lasers. During this modulation phase we modulate the voltage applied via the gate electrodes, use the measured *cts* to generate an error signal and adjust the gate voltage accordingly to be at the point where the NV center emits most photons, i.e. is on resonance with the control lasers. Since the yellow laser pulses address the transitions of NV^{0}resonantly, see main text, we also modulate the yellow laser frequency to keep it on resonance.

resonance with the control lasers [22]. For example, during experimental sequences the NV^-center could lose its extra electron via a two-photon absorption process [23, 24], causing the communication qubit to be outside of the qubit subspace and this may result in an error. Next to this, changes in the charge environment of the defect shift the optical frequencies, making the operations of the control lasers ineffective. In the case of remote entanglement generation these shifts are especially unfavorable because of the above-mentioned photon-indistinguishability requirement.

To prepare the correct charge state we use two techniques to convert $NV^0 \rightarrow NV^-$. We use either green laser pulses (515 nm) or yellow laser pulses (575 nm). Green pulses drive the transitions associated with NV^0off-resonantly and convert the defect to $NV^-$with $\approx 75\%$ probability [25]. This method requires relatively high powers ($\approx 20\mu$W in front of the microscope objective) and the high-energy pulses can shuffle the charge environment causing the resonance frequency of $NV^-$to shift. Yellow laser pulses on the other hand, drive the transitions of NV^0resonantly, require low optical powers ($\approx$10 nW) and induce no spectral shifts, but convert $NV^0 \rightarrow NV^-$with a smaller probability and solely when the laser frequency is on resonance with the transition [22, 26].

To prepare the defect in the right charge state, as well as on resonance with the control lasers, and to verify successful preparation, we can implement the CR check in two different ways dependent on the charge conversion method [18, 22], see Figures 2.4a-b. The *check* phase is the same for both implementations; we apply laser pulses resonant with the transitions used for initialization and readout while detecting emitted photons. When we detect a number of photons above the threshold *thr* we consider the communication qubit prepared and start the experiment. Detecting counts below *thr* can be due to three scenarios: (i) The communication qubit is on resonance but because of photon statistics we detected a smaller number of photons, (ii) the communication qubit is in NV^-but not on resonance, (iii) the communication qubit is in the wrong charge state.

The two implementations differ in the way failing the threshold is handled. In the case of using green laser pulses, we introduce a second threshold thr_0. If we detect a number of photons larger than thr_0 but smaller than *thr* we conclude that the communication qubit is in the right charge state and we perform the check again to try to distinguish scenario 1 from scenario 2. If we detect a number of photons lower than thr_0 we go the *repump* phase. By applying the green laser pulse we convert to the right charge state and we specifically make use of the induced spectral shifts to change the resonance condition. Afterwards we again perform the *check* and repeat the entire CR check until we have passed the threshold *thr* to start the experiment.

In the case of using yellow laser pulses we follow a similar reasoning; effectively we set $thr_0 = 1$. If we detect one or more photons during the *check*, we conclude that the communication qubit is in the correct charge state but not on resonance and we perform a *modulation* step. In this step we implement a PID feedback loop to shift the optical transitions using a voltage applied on the gate electrodes to be on resonance with the control lasers. Afterwards we perform a *check* again. In the case we detect zero photons

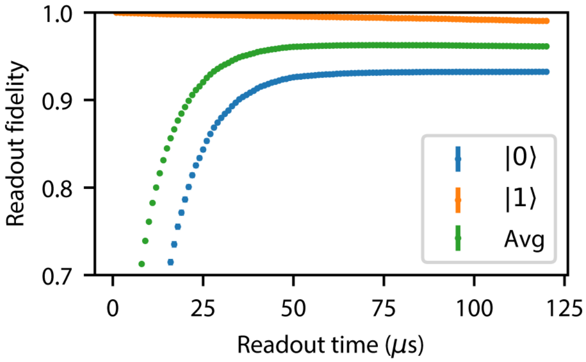

Figure 2.5: **Calibration of the readout duration** To calibrate the optimal readout duration, we measure the readout fidelity while varying the time in which we apply laser light. We define the readout fidelity as the probability to assign the correct outcome. During the calibration we measure the fidelities of reading out both eigenstates ($|0\rangle$ and $|1\rangle$) and determine at which duration the average readout fidelity (Avg) is maximal.

during the check phase, we apply the yellow pulse. As the yellow resonance transition of $NV^0$is also subject to changes, we use another PID feedback loop to keep the yellow laser frequency on resonance. Since the detection of zero photons could also indicate the communication to be off resonant with the control lasers we perform the modulation step subsequently before going to the *check* phase.

2.2.2. INITIALIZATION

In any quantum information experiment, the qubits must at some point be initialized in a well-defined state [27]. To initialize the communication qubit we apply a laser pulse resonant with the $|m_s = \pm 1\rangle \leftrightarrow |E_{1,2}\rangle$ transition to transfer population from the ground to the excited state. With a small probability this population can decay via the singlet state to the $|0\rangle$. Since we are using spin-selective optical driving, this population will be trapped and remain in the $|0\rangle$ state. If we apply the laser pulse for long enough, this process repeats and ultimately the communication qubit will be initialized in $|0\rangle$ with high probability, >99.8 % [14].

The initialization procedure requires additional complexity when we operate the communication qubit at a relatively high magnetic field, $B_z \approx 1900$G, see Section 4.6.6. Whereas $|m_s = -1\rangle$ and $|m_s = +1\rangle$ can be excited to $|E_{1,2}\rangle$ with the same optical frequency at $B_z \approx 400$G, these transitions get split due to their more spin-like eigenstates at higher magnetic fields [28]. Hence the initialization procedure requires simultaneous driving at two frequencies, which can be accomplished using an additional laser or creating frequency side bands using an electro-optical modulator.

2.2.3. READOUT

To readout the communication qubit we apply a laser pulse resonant with the $|m_s = 0\rangle \leftrightarrow |E_x\rangle$ ($|E_y\rangle$)) transition. Emission of a single photon and subsequent detection (by us or the environment) projects the qubit state into $|0\rangle$. However, for us to assign the correct outcome it is crucial that we detect a photon before the qubit state is altered. In fact, the combination of a low detection efficiency (10-14%, due emission of photons in all directions) and the spin-flipping decay is limiting the average readout fidelity and leads to asymmetric readout fidelities, see Figure 2.5. Namely, given the qubit is in $|0\rangle$ we have a probability to assign correct outcome 0 with 92% to 94% probability depending on the experimental setup. On the contrary, given the qubit is in $|1\rangle$ we have a probability to assign outcome 1 with 99 to 99.5% probability. Or phrased differently, if we detect a photon we have assigned the outcome 0 with high certainty. The readout fidelities can be well calibrated prior to an experiment and therefore we can correct the experimental results for these known readout errors to obtain a better estimate of the underlying statistics [29].

Another aspect related to the spin-flipping is the non-destructiveness of the readout, i.e. is the qubit in the assigned state subsequent to the measurement. Experiments using memory qubits require the communication qubit to be in a well-known state at each point in time (see Section 2.3) and therefore the readout procedure to be non-destructive. For this reason we use a so-called dynamic stop readout with low optical power. In the dynamic stop readout we stop the excitation laser pulse as soon as we have detected a single photon [30]. Using low optical power minimizes the probability for the qubit state to be altered during the response time of the hardware to turn off the laser pulse.

2.2.4. QUANTUM GATES

To drive coherent transitions between the ground states of the communication qubit, or in other words to perform quantum gates, we use microwave (MW) pulses at the resonance frequency. The MW pulses are delivered via a gold strip line on the diamond sample (see Section 2.7) and coherently transfer population from one ground state to another, $|m_s = 0\rangle \leftrightarrow |m_s = -1\rangle$ or $|m_s = 0\rangle \leftrightarrow |m_s = +1\rangle$.

The pulses are calibrated in several steps. First, we determine the resonance frequency using an electron spin resonance (ESR) measurement, see Figure 2.6. Figure 2.6 shows three resonances as a result of the coupling of the electronic spin to the nuclear spin of the nitrogen host of the NV center. The resonance can be further split by a strongly coupled nuclear spin of a nearby ^{13}C (Figure 2.6a). To efficiently perform the quantum gates regardless of the state of the nitrogen nuclear spin, we use a frequency broadened pulse shape, a Hermite pulse [18, 31]. Second, we calibrate specific pulse amplitudes to perform quantum gates such as $\pi, \pi/2$ or arbitrary α rotations, where the phase of the rotation is determined by the phase of the MW pulse.

2.2.5. LONGITUDINAL RELAXATION AND COHERENCE TIME

Ideally qubits maintain their targeted states during the entire experiment, however noise can affect the state and reduce the fidelity. Since depolarizing and dephasing noise have a different effect, it is relevant to discuss the preservation of eigenstates and superposition states separately.

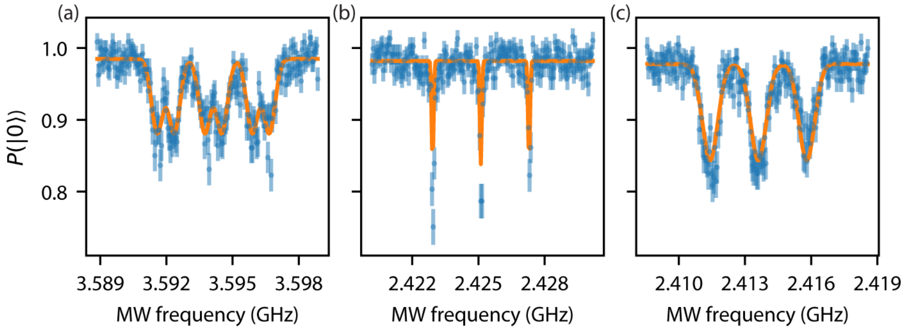

Figure 2.6: **Electron spin resonance** Measured the electron spin resonances (ESR) of the three NV centers, Alice **(a)**, Bob **(b)**, Charlie **(c)**, used in Chapters 4, 5 and 6. We prepare the communication qubit in $|0\rangle$, vary the frequency of microwave (MW) pulses and subsequently readout the qubit. When the microwaves are on resonance with the qubit transition $|0\rangle \rightarrow |1\rangle$, population is transferred and we observe a dip. The resonance condition is split due to interactions with nuclear spins in the environment, see main text. We fit the measured data to extract the center frequency (solid orange lines). The width of the dips is explained by the applied magnetic field. On Bob, we apply a relatively high magnetic field, $B_z \approx 1890$G, and therefore we observe very narrow dips.

For how long eigenstates can be preserved in case of idling, i.e. when no quantum gates are performed, is defined as the longitudinal relaxation time T_1. Operating the communication qubit at cryogenic temperatures and using diamond samples with a low nitrogen concentration, should allow for a very long T_1 time, >1 hour [33]. In our experimental setting, the longitudinal relaxation time could be reduced due to finite extinction of the control lasers and noise from the MW control equipment, but we measure these contributions are negligible on the times scales of our experiments.

The coherence time of superposition states in the case of idling is referred to as the free induction decay time, T_2^*. The T_2^* time of the communication qubit is ≈ 1 - 10 μs, due

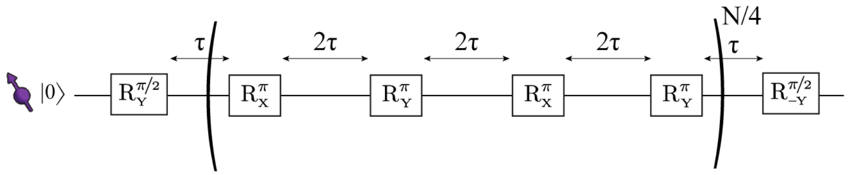

Figure 2.7: **Communication qubit decoupling sequence** Any superposition state encoded on the communication starts to dephase as soon as it is created (by the $R_Y^{\pi/2}$-rotation the diagram), because of undesired interactions with the surrounding spin bath. To preserve superposition or entangled states, we decouple the communication qubit from the bath using sequence of N gates. In these decoupling sequences π-pulses are equally spaced in time, 2τ apart, to cancel dephasing errors caused by the bath. In the diagram an XY4 sequence is shown as an example. Throughout the thesis we make use of XY4 as well as XY8 sequences, as these sequences mitigate the effect of pulse errors [32].

to interactions with the surrounding nuclear spin bath. Even though the intrinsic T_2^* cannot be increased in our current diamond samples, we can extend the coherence time T_{coh} of superposition states by decoupling it from the nuclear spin bath and likewise mitigating the effect of slow changes of the external magnetic field [33]. This decoupling can be achieved by using regularly-spaced π rotations, also known as dynamical decoupling, see Figure 2.7. Using tailored pulse sequences, the coherence time of the communication qubit has been extended up to one second [33]. For experiments carried out in this thesis, T_{coh} is $\approx$ 400ms. Although 400 ms seems long compared to individual gates, finite T_{coh} results in an error for specific experiments in this thesis, albeit small, see Chapters 4 and 5.

2.3. MEMORY QUBIT CONTROL

As previously mentioned we use ^{13}C nuclear spins as our memory qubits. These nuclear spins are randomly distributed in the diamond crystalline lattice, so we must first locate them in the lattice and characterize the coupling to the communication qubit before we can control them and use individual spins as qubits [12, 34].

The communication qubit and the ^{13}C nuclear spins interact via a hyperfine interaction. In the presence of an external magnetic field B_z, the ^{13}C nuclear spins undergo Larmor precession with an angular frequency $\omega_L = \gamma_C B_z$, with the gyromagnetic ratio of of ^{13}C being $\gamma_C = 2\pi \times 1.071$ kHz/G . When a nuclear spin is sufficiently close to the communication qubit, its local magnetic field gets altered depending on the spin state of the communication qubit, see Figure 2.8. The resulting Hamiltonian H of the joint system, the communication and a single nuclear spin, is given by (in the rotating frame of the communication qubit)

$$H = \omega_L I_z + A_\parallel S_z I_z + A_\perp S_z I_x. \tag{2.2}$$

In Eq. (2.2) $A_\parallel$ and $A_\perp$ are the parallel and perpendicular hyperfine couplings and S_i and I_j are the spin-1 and spin-1/2 Pauli matrices for the nuclear spin and communication qubit respectively. In particular, the Hamiltonian of Eq. (2.2) can be rewritten as

$$H = H_0 \left|0\right\rangle \left\langle 0\right| + H_1 \left|1\right\rangle \left\langle 1\right| \tag{2.3}$$

$$H_0 = \omega_L I_z \tag{2.4}$$

$$H_1 = (\omega_L \pm A_\parallel) I_z \pm A_\perp I_x \tag{2.5}$$

indicating the different evolution of the nuclear spin depending on the state of the communication qubit. The ± sign depends on the choice of the communication qubit subsystem; employing $|m_s = +1\rangle$ ($|m_s = +1\rangle$) as $|1\rangle$ results in a $+(-)$ sign.

Making use of this hyperfine interaction accordingly allows us to sense and control weakly-coupled ^{13}C nuclear spins [10]. We can detect the weakly-coupled nuclear spins by decoupling the communication qubit from the nuclear the spin bath with specific interpulse delays τ. We adopt a dynamical decoupling sequence as displayed between the brackets in Figure 2.7 and the corresponding nuclear spin evolution during this sequence

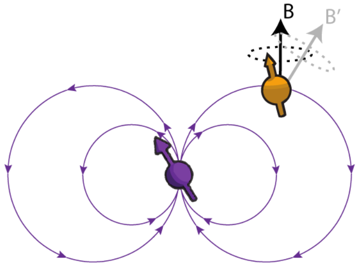

Figure 2.8: **Interaction between the communication qubit and a nearby ^{13}C nuclear spin.** Adapted from Cramer [34]. When the communication qubit (purple spin) is in $|m_s = 0\rangle$, the precession of the nuclear spin (orange spin) is given by the external magnetic field B. When the communication qubit is in $|m_s = \pm 1\rangle$, the local magnetic field of the nuclear spin is altered, as a consequence the nuclear spin will precess with a different frequency around a tilted axis.

is

$$V_0 = \left(e^{-iH_0\tau} \cdot e^{-2iH_1\tau} \cdot e^{-iH_0\tau}\right)^{N/2} \tag{2.6}$$

$$V_1 = \left(e^{-iH_1\tau} \cdot e^{-2iH_0\tau} \cdot e^{-iH_1\tau}\right)^{N/2} \tag{2.7}$$

depending on the initial state of the communication qubit (0/1). When we prepare the communication in a superposition state prior to the decoupling sequence and sweep the inter-pulse delay τ, we observe dips in the coherence of the communication qubit at certain values of τ indicating coupling (or entanglement) with nuclear spins. For a single nuclear spin these dips occur at the resonance condition

$$\tau_k \approx \frac{k\pi}{2\omega_L \pm A_\parallel}, \tag{2.8}$$

for odd integers of k [34]. We can control a single ^{13}C nuclear spin by selecting a well-isolated resonance associated with a weakly-coupled spin and perform rotations conditioned on the state of the communication qubit. To perform a perfect entangling operation, we calibrate the number of pulses N required to do a $R^{\pi/2}_{\pm X}$. Furthermore, to keep track of the phase of nuclear spin and ultimately use it as a memory qubit we measure its precession frequency for both communication qubit states.

By using these entangling operations we can initialize, perform quantum gates and readout the memory qubit [12, 34]. The memory qubit can be initialized using two different methods; measurement-based initialization (MBI) to initialize a superposition state or a *SWAP* initialization method to initialize an eigenstate [10]. Throughout this thesis we use the *SWAP* initialization method and the sequence is displayed in Figure 2.9a. Figure 2.9 also displays the sequences to store a qubit state using the memory qubit and sequences to readout the memory qubit in different bases. In these readout sequences, we map two orthogonal states to the communication qubit and optically readout the communication qubit.

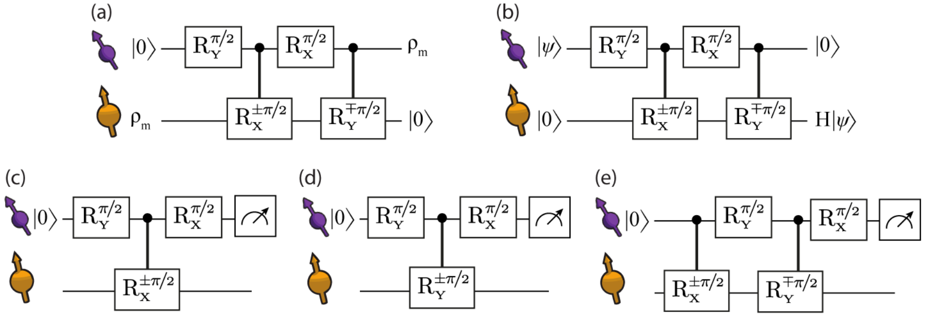

Figure 2.9: **Memory qubit operations (a)** Gate sequence to initialize the memory qubit using a *SWAP* method. ρ_m indicates the fully mixed state [10]. **(b)** Sequence to store the state of the communication qubit on the memory qubit, up to a Hadamard gate [13]. Note that this sequence is not a full swap, as it required the memory qubit to be in $|0\rangle$ at the start of the sequence. **(c - e)** Readout sequences for X, Y and Z respectively [10]. For example in (c) we map $|+X\rangle$ ($|-X\rangle$) on the memory qubit to $|0\rangle$ ($|1\rangle$) on the communication qubit and optically readout the communication qubit to learn the state of the memory qubit.

Besides entangling operations we can perform unconditional rotations. We can apply gates not controlled by the state of the communication qubit by using resonances with even integers k in Eq. (2.8). To find the exact resonance we initialize the memory qubit using the conditional gates, subsequently execute the decoupling primitive while sweeping τ_k and finally readout the memory qubit. The number of pulses N needed for a π or $\pi/2$ rotation is calibrated in a similar manner.

In addition to the control, the coherence time of the memory qubit is an important aspect in the experiments discussed in Chapters 4 and 5, in particular the coherence time during network activity. By network activity we mean the probabilistic process of generating remote entanglement using entanglement attempts. In absence of network activity and with the communication qubit initialized in an eigenstate, the intrinsic free-induction decay T_2^* of the memory qubit is ≈ 10 ms (for the communication qubit in $|m_s = 0\rangle$). However, in presence of network activity, the memory qubit decoheres at a higher rate due to its coupling with the communication qubit [14]. During the entanglement attempts we perform operations on the communication qubits such as initialization, quantum gates and spin-photon entangling pulses. All these operations introduce errors, albeit small, on the communication qubit. As a consequence, the communication qubit spends time in an unknown state, which leads to an unknown precession frequency of the memory qubit and results in a dephasing error [14]. To mitigate the effect of communication qubit errors on the memory qubit, we realize a high magnetic field (B_z = 1890G) in Chapters 4 and 5. Additionally, to combat the intrinsic T_2^* of the memory qubit we implement a decoupling pulse on the memory qubit in Chapter 5.

2.4. QUANTUM FREQUENCY CONVERSION

Now that we have discussed the control of the different qubits and before turning to the entanglement protocols, we discuss the process of quantum frequency conversion

(QFC). In future large-scale fiber-based quantum networks minimal photon loss is required. To mitigate photon loss we can convert the initially visible-wavelength photons emitted by the NV to the telecom band using QFC. In this paragraph we explain the theory behind this process and discuss the implications for entangled states. For a more detailed theoretical background on the conversion process, we would like to refer to References [35–40].

When an electric field is applied to an insulator, i.e. a dielectric material, a polarization $\vec{\mathbf{P}}$ is induced, where we can describe the i^{th} element by

$$P_i = \epsilon_0 \chi^{(1)}_{ij} E_j + \epsilon_0 \chi^{(2)}_{ijk} E_j E_k + \epsilon_0 \chi^{(3)}_{ijkl} E_j E_k E_l + ... \tag{2.9}$$

In Eq. (2.9) $E_j, E_k, E_l, ...$ are the components of the electric field, ϵ_0 is the permittivity of vacuum and $\chi^{(n)}$ are the electric susceptibility tensors of the dielectric material. In most materials we can assume the higher order terms $\chi^{(n>1)} \approx 0$ for weak electrical fields and the system is described by linear optics. However, for strong electric fields and for certain materials the higher-order nonlinear terms cannot be neglected.

As a consequence, the mode equations of electrical field modes with different frequencies are coupled. The term proportional to $\chi^{(2)}_{ijk}$ gives rise to frequency mixing. A specific case of (three wave) frequency mixing is difference frequency generation (DFG). We can use DFG to convert photons emitted by the NV center (with frequency ω_{NV}) to the infrared telecom band (with frequency ω_{DF}) using an additional pump laser (with frequency ω_{pump}). Because of conservation of energy the three frequencies are related in the following manner:

$$\omega_{DF} = \omega_{NV} - \omega_{pump}. \tag{2.10}$$

Conservation of momentum enforces

$$\hbar \Delta \vec{k} = \hbar \left(\vec{k}_{NV} - \vec{k}_{pump} - \vec{k}_{DF} \right). \tag{2.11}$$

In the case of co-aligned NV photons and pump lasers beam, Eq. (2.11) becomes

$$\Delta k = k_{NV} - k_{pump} - k_{DF} \tag{2.12}$$

in the direction of propagation. Maximum efficiency of the conversion process will be achieved when the wave vector mismatch $\Delta k = 0$ and the generated optical waves constructively interfere. However, generally the phase matching condition is not satisfied, due to dispersion in the dielectric material. The wavelength dependent refractive index causes the different beams to travel with different velocities and the DF generated light will destructively interfere with itself. Figure 2.10 shows an example for the second-harmonic generation (SHG) process, but the same arguments hold for the DFG process [40]. The intensity of the generated light will periodically increase and decrease, leading to a small overall conversion efficiency.

Perfect phase matching can be accomplished using several methods [35]. One example is birefringence phase matching. This technique relies on the birefringence of the

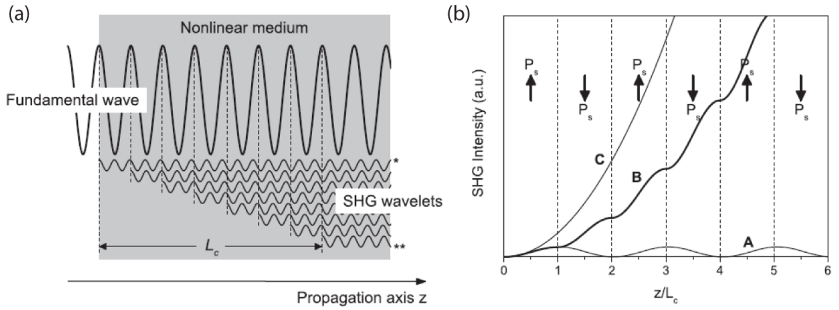

Figure 2.10: **Quasi-phase matching** Adapted from Zaske [40]. **(a)** Illustration of the second-harmonic generation (SHG) process. Over the whole length of the non-linear medium the conversion process converts the fundamental wave to a second-harmonic (SH) wave. Due to dispersion in the medium, the fundamental and the SH wavelets travel with different velocities. After the coherence length L_C, newly generated SH wavelets destructively interfere with SH wavelets created at $L = 0$. **(b)** As a consequence, the conversion efficiency will alternate with a period of L_C and in general be small (A in the diagram). In the case of quasi-phase matching the sign of the induced polarization is changed every L_C by electrical poling and the conversion efficiency will increase of the entire length of the crystal (B in the diagram). For comparison, if we would be able to achieve perfect phase matching, the conversion efficiency would increase as curve C in the diagram.

crystal to compensate the different refractive indices by tuning the propagation angle. Birefringence phase matching has its downsides though. To achieve high conversion efficiencies we would like to use channel waveguides, since those strongly confine the electrical fields and realize spatial overlap of the modes. However, when a wide range of frequencies are desired (as in Chapter 3), the angle tuning of the birefringence phase matching is incompatible with channel waveguides.

Another solution is quasi-phase matching (QPM). In QPM the destructive interference of the generated light is avoided by periodically changing the sign of the induced polarization in the dielectric material. In this way we break the periodicity of the intensity of the generated light and we achieve constructive interference over the entire length of the crystal. Another advantage of this solution is that QPM is a noncritical phase matching technique, i.e. the conversion efficiency is mostly insensitive to slight misalignments of the optical fields.

The periodic change of the sign of the induced polarization for QPM can be realized using electrical poling, by placing periodically structured electrodes on the dielectric material [38]. The resulting quasi-phase matching condition becomes

$$\Delta k = k_{NV} - k_{pump} - k_{DF} - \frac{2\pi}{\Lambda} = 0. \tag{2.13}$$

where Λ is the poling period.

Nonetheless achieving high overall conversion efficiencies is challenging. High intensity of the pump field is required, for this reason we use channel waveguides to strongly confine the electrical fields, as mentioned before. Moreover, as the signal photons with frequency ω_{NV} nm get depleted, back conversion can occur via sum-frequency generation (SFG); photons with frequency ω_{DF} get converted back to ω_{NV}. Additionally, any remaining imperfect phase matching lowers the conversion efficiency. As a result, the conversion efficiency is generally limited to tens of percents [40, 41].

DFG can be used for coherent conversion of entangled photons under a few conditions. In order to leave any entangled state unaffected the conversion process must act with the same efficiency on the two qubit states. Furthermore, the conversion must imprint the same phase on the states, such that this phase can be treated as a global phase [39]. For the experiments performed in Chapter 3 the photonic qubit is encoded using time bins, $|E\rangle$ and $|L\rangle$ for an early and late emitted photon respectively. The time difference between the early and late photons is ≈ 190 ns and on this time scale we can assume that the conversion efficiency and the imprinted phase are constant.

Nevertheless, we add noise by including the conversion process. Apart from DFG other non-linear conversion processes can occur in the dielectric material, for example spontaneous parametric down conversion (SPDC). In this process photons from the pump laser are converted in two photons over a range of frequencies. To obtain a tolerable signal to noise ration (SNR), we can frequency filter the subsequent optical path using prisms and fiber Bragg gratings [41].

All in all, QFC is a promising method to overcome photon losses in long optical fibers. In Chapter 3 we implement a DFG conversion process to convert photons emitted at $\lambda = 637$ nm to $\lambda = 1588$ nm.

2.5. REMOTE ENTANGLEMENT GENERATION

The optical interface discussed in Section 2.2 can be used to generate remote entanglement. Throughout this thesis we address two entanglement generation schemes. In Chapter 3 we generate an entangled state between the communication qubit (or the spin qubit) and a time-bin encoded photon. In Chapters 4 to 6, we use spin-photon entangled state (where the photon is encoded as a number state) to generate spin-spin entanglement between the communication qubits of distant nodes.

Regarding the verification of a state, we compute the fidelity F of the created state to a target state $|\psi\rangle$

$$F = \langle\psi|\rho|\psi\rangle, \tag{2.14}$$

where ρ is the density matrix of the experimentally generated state. Reconstruction of the entire density would allow us to extract the fidelity of the state. However, this requires full state tomography, which can be a difficult and time consuming task. Therefore we measure only the expected non-zero elements of the density matrix. For instance, if we want to measure the fidelity with respect to the $|\Psi^+\rangle$ Bell state we can measure $\langle XX\rangle, \langle YY\rangle$ and $\langle ZZ\rangle$ and compute the fidelity using

$$F = \frac{1}{4}\left(1 + \langle XX\rangle + \langle YY\rangle - \langle ZZ\rangle\right). \tag{2.15}$$

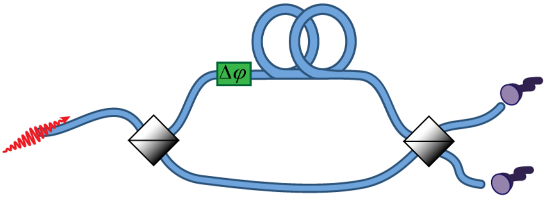

Figure 2.11: **Imbalanced interferometer** We use a fiber-based interferometers with two different arm lengths to interfere photon states from different time bins. Using a piëzo-fiber stretcher we can set a phase difference $\Delta\varphi$ between the two arms.

$\langle ZZ\rangle$ is expectation value of the product of the individual measurement outcomes in the computational basis ($\langle XX\rangle$ and $\langle YY\rangle$ for the X and Y bases respectively), i.e. the correlation between the measurement outcomes.

2.5.1. SPIN-PHOTON ENTANGLEMENT SCHEME

The spin-photon entanglement scheme is a primitive of the two-photon scheme originally proposed by Barrett and Kok [42]. In Chapter 3 we use this scheme to demonstrate the preservation of entangled states upon quantum frequency conversion of the photon. In this scheme we use the spin states $|m_s = 0\rangle$ and $|m_s = -1\rangle$ as the qubit encoding of the communication qubit and early($|E\rangle$) or late ($|L\rangle$) emission as the qubit states of the photon.

To generate the entangled state we start by initializing the communication qubit in the balanced superposition state

$$\frac{1}{\sqrt{2}}\left(|0\rangle + |1\rangle\right). \tag{2.16}$$

We selectively excite the $|0\rangle$ state which results in the emission of an early photon. Then we apply a MW π pulse to invert the population of the communication qubit. Subsequently we selectively excite the $|0\rangle$ for a second time which results in the emission of a late photon. This produces the following entangled state

$$\frac{1}{\sqrt{2}}\left(|1\rangle_c |E\rangle_{ph} + |0\rangle_c |L\rangle_{ph}\right), \tag{2.17}$$

where the subscripts denote the state of the communication qubit (c) and the photon (ph).

To verify the entangled state, we can measure the classical correlations straightforwardly by correlating the measured spin state with the arrival time of the photon. To access the orthogonal quantum bases of the photon we use an imbalanced interferometer, see Figure 2.11. The path length difference between the short and the long arm of the interferometer is chosen to match the time difference between the early and late emission of the photon. As a result, a photon state traveling through the long arm of the interferometer undergoes the following transformation

$$|E\rangle_{ph} \to e^{i\Delta\varphi}|L\rangle_{ph} \tag{2.18}$$

$$|L\rangle_{ph} \to e^{i\Delta\varphi}|T\rangle_{ph} \tag{2.19}$$

with an optical phase difference between the two arms $\Delta\varphi$ and we introduce an extra, third (T), time bin $|T\rangle$. When we apply this transformation to the entangled state in Eq. (2.17) together with the beam splitter transformations we obtain

$$\frac{1}{2\sqrt{2}}\Big(|1\rangle_c \otimes \Big((|E\rangle_{ph,1} - |E\rangle_{ph,2}) + e^{i\Delta\varphi}(|L\rangle_{ph,1} + |L\rangle_{ph,2})\Big) \\ + |0\rangle_c \otimes \Big((|L\rangle_{ph,1} - |L\rangle_{ph,2}) + e^{i\Delta\varphi}(|T\rangle_{ph,1} + |T\rangle_{ph,2})\Big)\Big). \tag{2.20}$$

In Eq. (2.20) the subscripts 1,2 indicate the output ports of the second beam splitter. When we only consider photons arriving in the late time bin, we can trace over the early and the third time bin, normalize the state and get

$$\frac{1}{2}\Big(|0\rangle_c + e^{i\Delta\varphi}|1\rangle_c\Big) \otimes |L\rangle_{ph,1} - \frac{1}{2}\Big(|0\rangle_c - e^{i\Delta\varphi}|1\rangle_c\Big) \otimes |L\rangle_{ph,2}. \tag{2.21}$$

Detecting a photon in one of the two output ports in the late time bin projects the communication qubit in

$$\frac{1}{\sqrt{2}}\Big(|0\rangle_c \pm e^{i\Delta\varphi}|1\rangle_c\Big) \tag{2.22}$$

where the ± is determined by which detector clicked.

The imbalanced interferometer thus allows us to measure correlations between the spin state of the communication qubit and the photonic state. Using the imbalanced interferometer with two orthogonal settings for $\Delta\varphi$, we can measure the fidelity of the spin-photon entangled state to a maximally entangled Bell-state.

2.5.2. SPIN-SPIN ENTANGLEMENT

The spin-spin entanglement scheme is based on the original proposal of Cabrillo *et. al.* [43] and Bose *et. al.* [44] and we use this scheme in Chapters 4 to 6 to create entanglement between communication qubits of distant nodes. It relies on the interference of a single photon and therefore enables high entanglement rates compared to two-photon schemes [42], at the cost of experimental complexity and an inherent protocol error.

The first step of this scheme is to initialize both communication qubits in a superposition state

$$\sqrt{\alpha}|0\rangle_c + \sqrt{1-\alpha}|1\rangle_c. \tag{2.23}$$

After the initialization we selectively drive the $|0\rangle$ state to an optically excited state using a short optical pulse. Since $|0\rangle$ is the qubit state that is associated with the emission of a photon, we refer to it as the bright state and in this manner α in Eq. (2.23) represents the population in the bright state[1]. Moreover, the short optical pulse is treated as an optical π-pulse since the excitation of the ground state to the excited state is a coherent process and can be viewed as $R_X(\pi)$ rotation from $|0\rangle$ to $|E_x\rangle$ (or $|E_y\rangle$, depending on the experimental setup). The selective optical excitation creates an entangled state

$$\sqrt{\alpha}\,|0\rangle_c\,|1\rangle_{ph} + \sqrt{1-\alpha}\,|1\rangle_c\,|0\rangle_{ph} \tag{2.24}$$

between the communication qubit (c) and the number state of the photon (ph) on each node. The indistinguishable photon states are interfered on a beam splitter, removing the which path information. Detection of a single photon on one of the output ports of the beam splitter projects the communication qubits in an entangled state and serves as an heralding signal. In the high-photon-loss regime the two-qubit density matrix ρ is given by

$$\rho = (1-\alpha)\left|\Psi^{\pm}\right\rangle\left\langle\Psi^{\pm}\right| + \alpha\,|00\rangle\,\langle 00|\,. \tag{2.25}$$

with $\left|\Psi^{\pm}\right\rangle = \frac{1}{\sqrt{2}}\left(|01\rangle \pm e^{i\Delta\phi}\,|10\rangle\right)$, a maximally entangled state. The entangled state phase is determined by which detector has observed the photon and additionally depends on $\Delta\phi$, the optical phase difference of the photon states arriving at the beam splitter. Consequently, this optical phase difference must be known each time an entangled state is heralded. For this reason we control $\Delta\phi$ using phase stabilization methods, see Section 4.6.3 more details.

As mentioned above, the single-photon entanglement scheme has an inherent protocol error. Due to photon loss and non-number resolving detectors we have no means to discriminate between the case where both communication qubits were in the bright state $|0\rangle$ or only one of them, causing the $|00\rangle\,\langle 00|$ term in Eq. (2.25). The resulting fidelity to a maximally entangled state is

$$F = 1-\alpha, \tag{2.26}$$

in case of no other noise sources. The probability to herald an entangled state is $p_{click} = 2p_{\mathrm{det}}\alpha$, with p_{det} the detection probability given a photon is emitted. Thus by varying the bright state population α one can obtain higher fidelity states, at the expense of a lower success probability.

In Chapter 6 we discuss the entanglement protocol in more detail and we address the different noise sources that can affect the heralded entangled state.

2.6. QUANTUM TELEPORTATION

While quantum entanglement provides a high-level of coordination or correlation between the nodes, quantum teleportation offers a method to transfer information between different nodes with (in principle) unit efficiency. Therefore it is likely to be one of the central protocols in future large-scale quantum networks [45–47]. The quantum teleportation protocol was first proposed by Bennett *et. al.* [48] in the early ’90s and in

---

[1] The bright state populations α and the single photon detection probabilities p_{det} are generally different for the two nodes. For simplicity we assume $\alpha_A = \alpha_B$ and $p_{\mathrm{det},A} = p_{\mathrm{det},B}$ in the protocol explanation here. Chapter 6 considers a more general case where these experimental parameters of each node can be different.

the description below we follow this original proposal.

The protocol involves two parties, Alice and Bob, and in total three qubits, subscripted by $_{1,2,3}$. Alice holds qubits 1 and 2, and Bob has access to qubit 3. Alice would like to teleport the state of her first qubit, $\left|\psi\right\rangle_1 = \alpha\left|0\right\rangle + \beta\left|1\right\rangle$. Furthermore Alice and Bob share an entangled state, for instance the Bell-state $\left|\Phi^+\right\rangle_{23} = \frac{1}{\sqrt{2}}(\left|00\right\rangle + \left|11\right\rangle)$. We can write this combined system as

$$\begin{aligned}\left|\psi\right\rangle_1 \otimes \left|\Phi^+\right\rangle_{23} &= (\alpha\left|0\right\rangle_1 + \beta\left|1\right\rangle_1) \otimes \frac{1}{\sqrt{2}}(\left|00\right\rangle_{23} + \left|11\right\rangle_{23}) \\ &= \frac{1}{\sqrt{2}}(\alpha\left|000\right\rangle + \alpha\left|011\right\rangle + \beta\left|100\right\rangle + \beta\left|111\right\rangle).\end{aligned} \tag{2.27}$$

At this point we note that every two-qubit eigenstate can be rewritten as a linear combination of Bell-states:

$$\left|00\right\rangle = \frac{1}{\sqrt{2}}(\left|\Phi^+\right\rangle + \left|\Phi^-\right\rangle) \tag{2.28}$$

$$\left|11\right\rangle = \frac{1}{\sqrt{2}}(\left|\Phi^+\right\rangle - \left|\Phi^-\right\rangle) \tag{2.29}$$

$$\left|01\right\rangle = \frac{1}{\sqrt{2}}(\left|\Psi^+\right\rangle + \left|\Psi^-\right\rangle) \tag{2.30}$$

$$\left|10\right\rangle = \frac{1}{\sqrt{2}}(\left|\Psi^+\right\rangle - \left|\Psi^-\right\rangle). \tag{2.31}$$

Using this notion, we can rewrite Eq. (2.27) in the Bell-basis, regroup the terms and obtain

$$\begin{aligned}\left|\psi\right\rangle_1 \otimes \left|\Phi^+\right\rangle_{23} =& \frac{1}{2}\big(\left|\Phi^+\right\rangle_{12} \otimes (\alpha\left|0\right\rangle_3 + \beta\left|1\right\rangle_3) \\ &+ \left|\Phi^-\right\rangle_{12} \otimes (\alpha\left|0\right\rangle_3 - \beta\left|1\right\rangle_3) \\ &+ \left|\Psi^+\right\rangle_{12} \otimes (\alpha\left|1\right\rangle_3 + \beta\left|0\right\rangle_3) \\ &+ \left|\Psi^-\right\rangle_{12} \otimes (\alpha\left|1\right\rangle_3 - \beta\left|0\right\rangle_3)\big).\end{aligned} \tag{2.32}$$

Remarkably, we start to recognize the state Alice would like to teleport in the expression of Bob's qubit. More explicitly, we can write Bob's qubit in Eq. (2.32) as $\left|\psi\right\rangle$ up to a single qubit rotations

$$\begin{aligned}\left|\psi\right\rangle_1 \otimes \left|\Phi^+\right\rangle_{23} =& \frac{1}{2}\big(\left|\Phi^+\right\rangle_{12} \otimes I\left|\psi\right\rangle_3 \\ &+ \left|\Phi^-\right\rangle_{12} \otimes Z\left|\psi\right\rangle_3 \\ &+ \left|\Psi^+\right\rangle_{12} \otimes X\left|\psi\right\rangle_3 \\ &+ \left|\Psi^-\right\rangle_{12} \otimes XZ\left|\psi\right\rangle_3\big),\end{aligned} \tag{2.33}$$

where I is the identity operator, and X and Z the Pauli-X and Pauli-Z gates respectively. So to teleport her qubit state, Alice must measure her two qubits in the Bell-basis and communicate the (classical) outcomes to Bob. Depending on these classical outcomes, Bob can perform the appropriate operation to obtain $\left|\psi\right\rangle$.

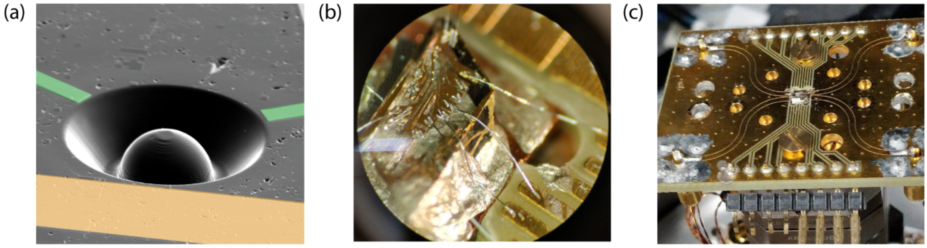

Figure 2.12: **Diamond sample (a)** Adapted from Bernien [4]. False colored scanning electron microscopy (SEM) image of the diamond sample. A solid-immersion lens (SIL) is milled into the diamond surface. Gold structures are deposited on the surface to create a MW strip line (orange) and gate electrodes (green). **(b)** Optical micrscopy image of the diamond sample glued on a printed circuit board (PCB). The strip line and gate electrodes are connected via bond wires to the PCB. **(c)** Photograph of the PCB mounted in the cryostat. Photo taken by Matteo Pompili.

The above described derivation shows that we can teleport qubit states using quantum mechanics' projective measurements. Initially the teleported state ends up in a completely mixed state, only with the knowledge of the outcomes of the Bell-state measurement one can obtain the correct state, prohibiting the transfer of information faster than light.

2.7. EXPERIMENTAL LAYOUT

In this last section of the chapter we discuss the experimental layout. In this thesis we make use of multiple experimental setups, or quantum nodes. Since each node has a very similar design, we give a general description of the experimental layout. We start by discussing the diamond sample. Next, we consider a single quantum node and lastly we treat the central beam splitter and the related equipment to herald entanglement between two nodes. In this section we omit the description of the optics and electronics related to the optical phase stabilization since an extended overview is given in Section 4.6.3.

The diamond samples used throughout this thesis are high-purity type IIa diamonds, grown using chemical-vapor-deposition. The diamond samples are grown along the $\langle 100\rangle$ crystalline orientation and subsequently cut along the $\langle 111\rangle$ direction. During a pre-characterization step, NV centers are selected based on their depth with respect to the diamond surface, orientation and absence of a strongly coupled nuclear spin. For $\langle 111\rangle$-cut diamonds NV centers with their symmetry axis oriented along the $\langle 111\rangle$ axis are preferential because of two reasons: (i) these NV centers will have the dipole moments associated with the $\mathrm{m}_s = 0 \rightarrow E_x$ and E_y transitions parallel to the surface of the diamond, allowing for efficient excitation of the optical transition and ensuring that the collected ZPL photons remain linearly polarized [49]. (ii) A magnetic field in the z-direction (parallel to the NV axis) can be easily applied by placing a magnet at the back of the diamond sample [50]. After this pre-characterization, solid immersion lenses (SILs) are milled around the selected NV centers, to enhance the single photon collection efficiency. Next, gold structures such as a MW strip line and gate electrodes are fabricated on the diamond surface, see Figure 2.12a. Lastly, an Al_2O_3 anti-reflection coating is deposited to additionally enhance the collection efficiency. For more details on the fabrication process, we would like to refer to References [4, 17, 18, 50].

The diamond samples are bonded onto a printed circuit board (PCB). The MW strip line and gate electrodes are connected to the PCB using bond wires, see Figure 2.12b. The PCB is installed inside a cryostat (*Montana Instruments s50* or *Attocube attoDRY 800*). Inside the cryostat, a magnet is placed close to the diamond sample. We use control loops to stabilize the temperature of the magnet. We bring a microscope objective (*Olympus MPLFLN 100x*) close to the diamond sample via a hole in the heat shield. Dependent on the type of cryostat, either the microscope objective or the PCB is mounted on a position stage to align the microscope objective with respect to the selected NV center.

Apart from the cryostat containing the diamond sample, each node has a set of control lasers, electronics and other equipment (Figure 2.13). The control over this equipment can be roughly divided in three time scales with corresponding control units: (i) The host PC is responsible for the control on the time scale of milliseconds. For example, the host PC controls the frequency stabilization of the lasers, it connects with other equipment such as temperature sensors and it provides a user interface. (ii) A microcontroller (MCU, *ADwin Pro-II*) is responsible for the microsecond time scale. Among other tasks, the MCU manages the communication with other quantum nodes, it controls the optical modulators for relatively slow processes such as the CR check and readout of the communication qubit. Furthermore, one of the MCUs will trigger the arbitrary waveform generators (AWGs) on all nodes. (iii) The AWG (*Tektronix 5014* or *Zürich Instruments HDAWG 8*) handles the nanosecond time scale. It allows for precise timing of MW pulses by sending signals to the I- and Q-channel of the MW source (*R&S SGS100A*) and it provides fast control of laser pulses during the entanglement attempts.

Lasers with distinct wavelengths are used for different tasks. The green and yellow laser are used for charge repumping, see Section 2.2.1. One of the red lasers is used for qubit initialization, i.e. spin pumping (Section 2.2.1), while the other is tuned to the readout transition $|m_s = 0\rangle \rightarrow |E_x\rangle$ (Section 2.2.3) and is used for qubit readout, the fast optical pulses for entanglement and phase stabilization. Modulation of the lasers is done using acoustic-optic modulators (AOMs, *Gooch&Housego*). Two of the three setups have an additional electro-optic modulator (EOM, *Jenoptik AM635*) to generate short optical pulses for the entanglement process.

Single photons emitted by the NV center are filtered using a dichroic mirror (DM, *Semrock*), separating the off-resonant PSB photons from the resonant ZPL photons. We use a PSB detection path to readout the communication qubit. To do so, the PSB photons are sent to an avalanche photodiode (APD, *Laser Components*). The photons are counted by the MCU and their detection times are recorded using a time tagging device (*PicoQuant Timeharp*). On the contrary, ZPL photons are used to generate remote entanglement. The ZPL photons are filtered from the excitation light using polarization optics and cou-

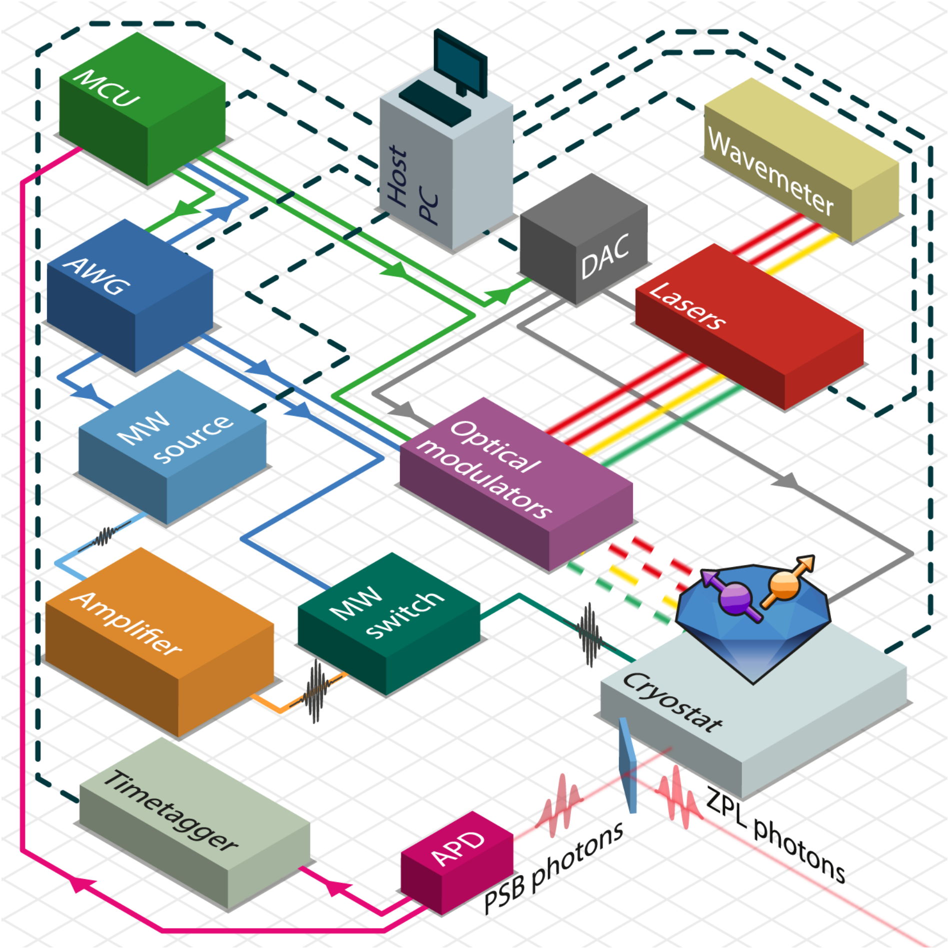

Figure 2.13: **Schematic diagram of the equipment used in a single quantum node** Adapted from Pompili [29] The core of the experimental setup in the diamond sample mounted in the cryostat. To perform experiments using the qubits in the diamond sample each quantum node has a number of instruments. The control of this equipment is done by three control units: the host PC, a microcontroller (MCU) and an arbitrary waveform generator (AWG). We have two sorts of equipment, equipment for optical control and for microwave control. For the optical control we have a set of lasers of which the frequency is stabilized using DACs to set the laser piëzo-voltage and the wavemeter to measure the frequencies. We shape pulses using optical modulators. For the microwave control we use two analog output ports of the AWG as the I and Q input channels on the MW source. The MW source outputs MW signals at a frequency set by the host PC. These signals are amplified and sent to the cryostat. A MW switch ensures proper attenuation when we do not apply pulses. Additionally we use a DAC module connected to a high-voltage source to apply a the voltage on the gate electrodes on the diamond sample. Single photons emitted by the communication qubit are filtered in frequency. The phonon-side band (PSB) photons are sent to an avalanche photodiode (APD) and the timetagger records the detection times of the photons. The zero-phononline (ZPL) are sent to the central beam splitter for remote entanglement generation.

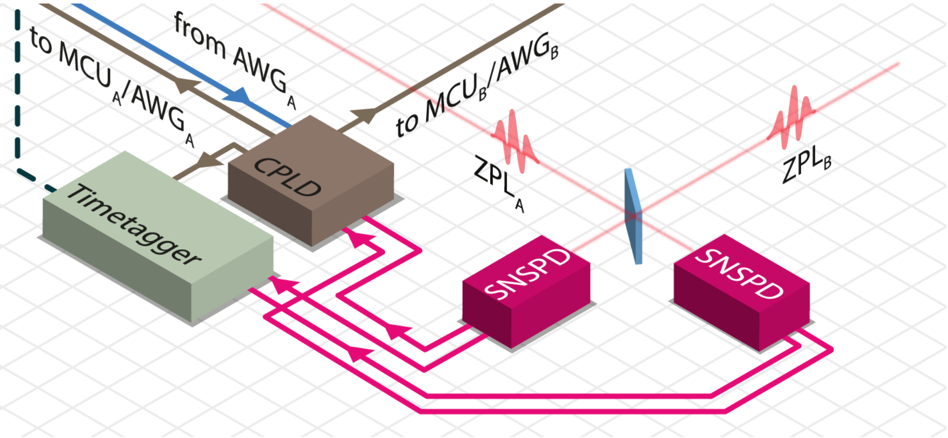

Figure 2.14: **Schematic diagram of the equipment used to herald remote entanglement** Zero-phononline photons from two setups are interfered on the central beam splitter. The output ports of the beam splitter are connected to two superconducting nanowire single photon detectors (SNSPD). The detection times of the photons are recorded using a timetagger. A complex programmable logic device (CPLD) is programmed to determine whether a photon detection is an heralding event based on input signals from the arbitrary waveform generator (AWG) of node A. When entanglement is heralded the CPLD informs the microcontrollers (MCU) and the AWGs of both nodes.

pled to a polarizing maintaining fiber.

In Chapter 3, the fiber-coupled ZPL photons are sent to the conversion setup, see Figure 3.1. In Chapters 4, 5 and 6, the ZPL photons are guided to the input ports of the central beam splitter (*Evanescent Optics*), see Figure 2.14. We have connected the output ports of this beam splitter to two superconducting nanowire single photon detectors (SNSPD, *PhotonSpot*). To decide whether a detected photon is a heralding signal for remote entanglement we send the detection signals of the SNSPDs to a complex programmable logic device (CPLD, *Altera MAX V*) together with a signal from the AWG indicating a detection window in which we expect heralding photons. When a photon is labeled as a heralding signal, the CPLD sends a flag to the quantum nodes, notifying them that the entangled state is established and informs them on which detector has clicked, i.e. whether $\left|\Psi^{+}\right\rangle$ or $|\Psi^{-}\rangle$ is generated. Similar as to the PSB photons, the arrival times of the ZPL photons are recorded using a time tagging device (*PicoQuant Hydraharp*).

REFERENCES

[1] J. R. Weber, W. F. Koehl, J. B. Varley, A. Janotti, B. B. Buckley, C. G. Van De Walle, and D. D. Awschalom, *Quantum computing with defects,* Proceedings of the National Academy of Sciences of the United States of America **107**, 8513 (2010).

[2] M. Ruf, N. H. Wan, H. Choi, D. Englund, and R. Hanson, *Quantum networks based on color centers in diamond,* Journal of Applied Physics **130**, 070901 (2021).

[3] W. Pfaff, *Quantum measurement and entanglement of spin quantum bits in diamond*, Ph.D. thesis, Delft University of Technology (2013).

[4] H. Bernien, *Control, measurement and entanglement of remote quantum spin registers in diamond*, Ph.D. thesis, Delft University of Technology (2014).

[5] M. W. Doherty, N. B. Manson, P. Delaney, F. Jelezko, J. Wrachtrup, and L. C. Hollenberg, *The nitrogen-vacancy colour centre in diamond,* Physics Reports **528**, 1 (2013).

[6] L. Robledo, L. Childress, H. Bernien, B. Hensen, P. F. A. Alkemade, and R. Hanson, *High-fidelity projective read-out of a solid-state spin quantum register,* Nature , 5 (2011).

[7] A. Faraon, C. Santori, Z. Huang, V. M. Acosta, and R. G. Beausoleil, *Coupling of nitrogen-vacancy centers to photonic crystal cavities in monocrystalline diamond,* Physical Review Letters **109**, 2 (2012).

[8] D. Riedel, I. Söllner, B. J. Shields, S. Starosielec, P. Appel, E. Neu, P. Maletinsky, and R. J. Warburton, *Deterministic enhancement of coherent photon generation from a nitrogen-vacancy center in ultrapure diamond,* Physical Review X **7**, 1 (2017).

[9] T. Van Der Sar, *Quantum control of single spins and single photons in diamond*, Ph.D. thesis, Delft University of Technology (2012).

[10] T. H. Taminiau, J. Cramer, T. Van Der Sar, V. V. Dobrovitski, and R. Hanson, *Universal control and error correction in multi-qubit spin registers in diamond,* Nature Nanotechnology **9**, 171 (2014).

[11] C. E. Bradley, J. Randall, M. H. Abobeih, R. C. Berrevoets, M. J. Degen, M. A. Bakker, M. Markham, D. J. Twitchen, and T. H. Taminiau, *A Ten-Qubit Solid-State Spin Register with Quantum Memory up to One Minute,* Physical Review X **9**, 31045 (2019).

[12] T. H. Taminiau, J. J. T. Wagenaar, T. van der Sar, F. Jelezko, V. V. Dobrovitski, and R. Hanson, *Detection and control of individual nuclear spins using a weakly coupled electron spin,* Physical Review Letters **137602**, 1 (2012).

[13] N. Kalb, A. A. Reiserer, P. C. Humphreys, J. J. Bakermans, S. J. Kamerling, N. H. Nickerson, S. C. Benjamin, D. J. Twitchen, M. Markham, and R. Hanson, *Entanglement distillation between solid-state quantum network nodes,* Science **356**, 928 (2017).

[14] N. Kalb, P. C. Humphreys, J. J. Slim, and R. Hanson, *Dephasing mechanisms of diamond-based nuclear-spin memories for quantum networks,* Physical Review A **97**, 1 (2018).

[15] M. L. Goldman, M. W. Doherty, A. Sipahigil, N. Y. Yao, S. D. Bennett, N. B. Manson, A. Kubanek, and M. D. Lukin, *State-selective intersystem crossing in nitrogen-vacancy centers,* Physical Review B **91**, 1 (2015).

[16] M. L. Goldman, A. Sipahigil, M. W. Doherty, N. Y. Yao, S. D. Bennett, M. Markham, D. J. Twitchen, N. B. Manson, A. Kubanek, and M. D. Lukin, *Phonon-induced population dynamics and intersystem crossing in nitrogen-vacancy centers,* Physical Review Letters **114**, 1 (2015).

[17] N. Kalb, *Diamond-based quantum networks with multi-qubit nodes*, Ph.D. thesis, Delft University of Technology (2018).

[18] B. J. Hensen, *Quantum Nonlocality with Spins in Diamond*, Ph.D. thesis, Delft University of Technology (2016).

[19] J. R. Maze, A. Gali, E. Togan, Y. Chu, A. Trifonov, E. Kaxiras, and M. D. Lukin, *Properties of nitrogen-vacancy centers in diamond: The group theoretic approach,* New Journal of Physics **13** (2011).

[20] M. W. Doherty, F. Dolde, H. Fedder, F. Jelezko, J. Wrachtrup, N. B. Manson, and L. C. Hollenberg, *Theory of the ground-state spin of the NV - center in diamond,* Physical Review B - Condensed Matter and Materials Physics **85**, 1 (2012).

[21] P. Tamarat, T. Gaebel, J. R. Rabeau, M. Khan, A. D. Greentree, H. Wilson, L. C. Hollenberg, S. Prawer, P. Hemmer, F. Jelezko, and J. Wrachtrup, *Stark shift control of single optical centers in diamond,* Physical Review Letters **97**, 1 (2006).

[22] H. Bernien, B. Hensen, W. Pfaff, G. Koolstra, M. S. Blok, L. Robledo, T. H. Taminiau, M. Markham, D. J. Twitchen, L. Childress, and R. Hanson, *Heralded entanglement between solid-state qubits separated by three metres,* Nature **497**, 86 (2013).

[23] P. Kehayias, M. W. Doherty, D. English, R. Fischer, A. Jarmola, K. Jensen, N. Leefer, P. Hemmer, N. B. Manson, and D. Budker, *Infrared absorption band and vibronic structure of the nitrogen-vacancy center in diamond,* Physical Review B **88**, 1 (2013).

[24] P. Siyushev, H. Pinto, M. Vörös, A. Gali, F. Jelezko, and J. Wrachtrup, *Optically controlled switching of the charge state of a single nitrogen-vacancy center in diamond at cryogenic temperatures,* Physical Review Letters **110**, 1 (2013).

[25] N. Aslam, G. Waldherr, P. Neumann, F. Jelezko, and J. Wrachtrup, *Photo-induced ionization dynamics of the nitrogen vacancy defect in diamond investigated by single-shot charge state detection,* New Journal of Physics **15** (2013).

[26] D. A. Hopper, J. D. Lauigan, T. Y. Huang, and L. C. Bassett, *Real-Time Charge Initialization of Diamond Nitrogen-Vacancy Centers for Enhanced Spin Readout,* Physical Review Applied **13**, 1 (2020).

[27] D. P. DiVincenzo, *The physical implementation of quantum computation,* Fortschritte der Physik **48**, 771 (2000).

[28] H. Beukers, *Improving coherence of quantum memory during entanglement creation between nitrogen vacancy centres in diamond,* Msc thesis, University of Groningen (2019).

[29] M. Pompili, *Multi-Node Quantum Networks With Diamond Qubits,* Ph.D. thesis, Delft University of Technology (2021).

[30] J. Cramer, N. Kalb, M. S. Blok, M. A. Rol, T. H. Taminiau, M. Markham, B. Hensen, R. Hanson, and D. J. Twitchen, *Repeated quantum error correction on a continuously encoded qubit by real-time feedback,* Nature Communications **7**, 1 (2016).

[31] L. M. Vandersypen and I. L. Chuang, *NMR techniques for quantum control and computation,* Reviews of Modern Physics **76**, 1037 (2004).

[32] G. de Lange, Z. H. Wang, D. Ristè, V. V. Dobrovitski, and R. Hanson, *Universal Dynamical Decoupling of a Single Solid-State Spin from a Spin Bath,* Science **330**, 60 (2010).

[33] M. H. Abobeih, J. Cramer, M. A. Bakker, N. Kalb, M. Markham, D. J. Twitchen, and T. H. Taminiau, *One-second coherence for a single electron spin coupled to a multi-qubit nuclear-spin environment,* Nature Communications **9**, 1 (2018).

[34] J. Cramer, *Quantum error correction with spins in diamond,* Ph.D. thesis, Delft University of Technology (2016).

[35] T. Suhara and M. Fujimura, *Waveguide Nonlinear-Optic Devices* (Springer, 2003) pp. 9–32.

[36] K. Sharma, *Optics* (Academic Press, 2006) pp. 571–623.

[37] D. J. Griffiths, *Introduction to Electrodynamics,* 3rd ed. (Pearson, 2008) pp. 160–193.

[38] S. Tanzilli, W. Tittel, H. D. Riedmatten, H. Zbinden, P. Baldi, and M. D. Micheli, *PPLN waveguide for quantum communication,* The European Physical Journal D **160**, 155 (2002).

[39] S. Tanzilli, W. Tittel, M. Halder, O. Alibart, P. Baldi, N. Gisin, and H. Zbinden, *A photonic quantum information interface,* Nature **437** (2005).

[40] S. Zaske, *Quantum Frequency Down-Conversion of Single Photons in Nonlinear Optical Waveguides,* Ph.D. thesis, Universitat des Saarlandes (2013).

[41] A. Dréau, A. Tcheborateva, A. E. Mahdaoui, C. Bonato, and R. Hanson, *Quantum Frequency Conversion of Single Photons from a Nitrogen-Vacancy Center in Diamond to Telecommunication Wavelengths,* Physical Review Applied **9**, 2 (2018).

[42] S. D. Barrett and P. Kok, *Efficient high-fidelity quantum computation using matter qubits and linear optics,* Physical Review A **71**, 2 (2005).

[43] C. Cabrillo, J. I. Cirac, P. Garcia-Fernandez, and P. Zoller, *Creation of entangled states of distant atoms by interference,* Physical Review A **59**, 1025 (1999).

[44] S. Bose, P. L. Knight, M. B. Plenio, and V. Vedral, *Proposal for teleportation of an atomic state via cavity decay,* Physical Review Letters **83**, 5158 (1999).

[45] M. Ben-Or, C. Crépeau, D. Gottesman, A. Hassidim, and A. Smith, *Secure multiparty quantum computation with (only) a strict honest majority,* Proceedings - Annual IEEE Symposium on Foundations of Computer Science, FOCS , 249 (2006).

[46] S. Wehner, D. Elkouss, and R. Hanson, *Quantum internet: A vision for the road ahead,* Science **362** (2018).

[47] A. S. Arora, J. Roland, and S. Weis, *Quantum weak coin flipping,* Proceedings of the Annual ACM Symposium on Theory of Computing , 205 (2019).

[48] C. H. Bennett, G. Brassard, C. Crépeau, R. Jozsa, A. Peres, and W. K. Wootters, *Teleporting an unknown quantum state via dual classical and Einstein-Podolsky-Rosen channels,* Physical Review Letters **70**, 1895 (1993).

[49] H. Bernien, L. Childress, L. Robledo, M. Markham, D. Twitchen, and R. Hanson, *Two-photon quantum interference from separate nitrogen vacancy centers in diamond,* Physical Review Letters **108**, 1 (2012).

[50] C. E. Bradley, *Order from Disorder: Control of Multi-Qubit Spin Registers in Diamond,* Ph.D. thesis, Delft University of Technology (2021).

3

ENTANGLEMENT BETWEEN A DIAMOND SPIN QUBIT AND A PHOTONIC TIME-BIN QUBIT AT TELECOM WAVELENGTH

A. Tchebotareva *, S. L. N. Hermans *, P. C. Humphreys, D. Voigt, P. J. Harmsma, L. K. Cheng, A. L. Verlaan, N. Dijkhuizen, W. de Jong, A. Dréau & R. Hanson

We report on the realization and verification of quantum entanglement between an NV electron spin qubit and a telecom-band photonic qubit. First we generate entanglement between the spin qubit and a 637 nm photonic time-bin qubit, followed by photonic quantum frequency conversion that transfers the entanglement to a 1588 nm photon. We characterize the resulting state by correlation measurements in different bases and find a lower bound to the Bell state fidelity of $\geq 0.77 \pm 0.03$. *This result presents an important step towards extending quantum networks via optical fiber infrastructure.*

The results of this chapter have been published in Phys. Rev. Lett.**123**, 063601 (2019).

* These two authors contributed equally to this work.

3.1. INTRODUCTION

Quantum networks connecting and entangling long-lived qubits via photonic channels [1] may enable new experiments in quantum science as well as a range of applications such as secure information exchange between multiple nodes, distributed quantum computing, clock synchronization, and quantum sensor networks [2–10]. A key building block for long-distance entanglement distribution via optical fibers is the generation of entanglement between a long-lived qubit and a photonic telecom-wavelength qubit (see Figure 3.1a). Such building blocks are now actively explored for various qubit platforms [11–16].

The NV center in diamond is a promising candidate to act as a node in such quantum networks thanks to a combination of long spin coherence and spin-selective optical transitions that allow for high fidelity initialization and single-shot read out [17]. Moreover, memory qubits are provided in the form of surrounding carbon-13 nuclear spins. These have been employed for demonstrations of quantum error correction [18–20] and entanglement distillation [21]. Heralded entanglement between separate NV center spin qubits has been achieved by generating spin-photon entangled states followed by a joint measurement on the photons [22].

Extending such entanglement distribution over long distances is severely hindered by photon loss in the fibers. The wavelength at which the NV center emits resonant photons, the so-called zero-phonon-line (ZPL) at 637 nm, exhibits high attenuation in optical glass fibers. Quantum-coherent frequency conversion to the telecom band can mitigate these losses by roughly 7 orders of magnitude for a distance of 10 km [23, 24] and would enable the quantum network to optimally benefit from the existing telecom fiber infrastructure. While entanglement between matter systems and photon polarization after frequency conversion has recently been demonstrated[11–13, 16, 25, 26], no experiments using NV centers and no experiments using time-bin photonic qubits have so far been reported. Recently, we have realized the conversion of 637 nm NV photons to 1588 nm (in the telecom L-band) using a difference frequency generation (DFG) process and shown that the intrinsic single-photon character is maintained during this process [27]. However, for entanglement distribution an additional critical requirement is that the quantum information encoded by the photon is preserved during the frequency conversion.

Here we demonstrate entanglement between an NV center spin qubit and a time-bin encoded frequency-converted photonic qubit at telecom wavelength. The concept of our experiment is depicted in Figure 3.1b. We first generate spin-photon entanglement, then convert the photonic qubit to the telecom band, and finally characterize the resulting state through spin-photon correlation measurements in different bases.

3.2. GENERATING A SPIN-PHOTON ENTANGLED STATE

We use two of the NV center electron spin-1 sub levels as our qubit subspace. We denote the $m_s = 0$ and $m_s = -1$ ground states as $|0\rangle$ and $|1\rangle$, respectively. To generate the

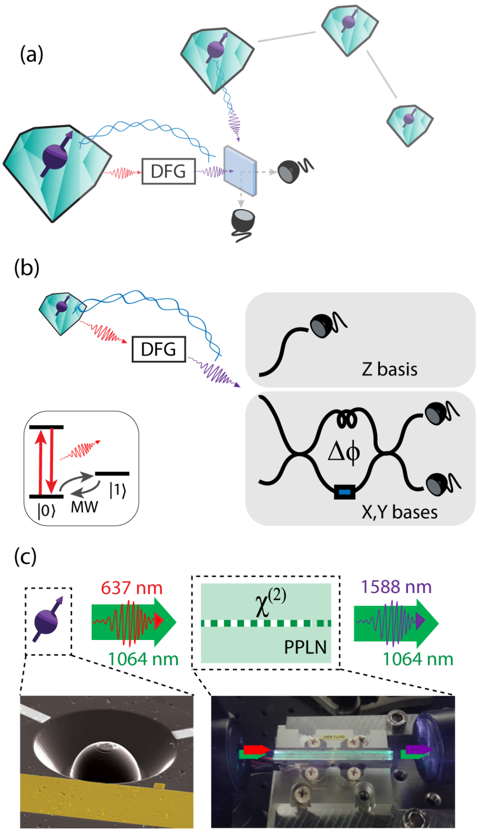

Figure 3.1: (a) In a long-distance quantum network, heralded entanglement between the nodes is generated by interference on a beam splitter and subsequent measurement of telecom photonic qubits. (b) Concept of the experiment. An NV spin qubit - photon qubit entangled state is generated. The photonic qubit is converted to a telecom wavelength by the difference frequency generation (DFG) process [27]. For measuring the photonic qubit in the X and Y basis, an imbalanced interferometer is used. Inset: simplified level scheme of the NV center. (c) DFG process: a 637 nm photon is converted to a wavelength of 1588 nm using a nonlinear PPLN crystal. Left inset: electron microscope image of the diamond device. Right inset: image of the PPLN crystal with ridge waveguides(NTT/NEL).

desired spin-photon entangled state, we first initialize the spin in $|0\rangle$ and prepare the balanced superposition $\left|\psi\right\rangle = \frac{1}{\sqrt{2}}(|0\rangle + |1\rangle)$ using a microwave $\pi/2$-pulse. Then we apply a spin-selective optical π-pulse, such that the $|0\rangle$ state will be excited, followed by photon emission (lifetime of 12 ns). Next, we flip the spin state using a microwave π-pulse and apply the optical excitation for a second time. This generates the following spin-photon entangled state:

$$\left|\text{NV spin, photon}\right\rangle = \frac{1}{\sqrt{2}}|1,E\rangle + \frac{1}{\sqrt{2}}|0,L\rangle, \tag{3.1}$$

where the basis states for the photonic qubit are given by the early ($|E\rangle$) and late ($|L\rangle$) time bins, which are separated in the experiment by 190 ns, limited by the state preparation time.

Next, the photon is converted to the telecom wavelength of 1588 nm using a difference frequency generation (DFG) process, by combining it with a strong pump laser inside a periodically poled lithium niobate (PPLN) crystal waveguide (Figure 3.1c) [27]. The resulting spin-telecom photon state is characterized via correlation measurements. We read out the photonic qubit in the Z basis using time-resolved detection that discriminates between the early and late time bins. To access other photonic qubit bases we use an imbalanced interferometer [28] with a tunable phase difference $\Delta\phi$ between the two arms. For each photonic qubit basis, we read out the spin state in the basis where maximum correlation is expected. From the measured correlations in three orthogonal bases we find the fidelity to the desired maximally entangled state.

The diamond sample containing the NV center is cooled to ≈ 4 K. The optical setup is schematically depicted in Figure 3.2a. Laser light at 637 nm is used to apply the optical π-pulses. In the photon detection path, the emitted 637 nm photons are separated from reflected excitation light using a cross-polarization configuration and time filtering. The off-resonant phonon side band emission is separated by dichroic filtering and sent to a detector (D1) for spin readout. The 637 nm photons are combined with a strong pump laser (emission wavelength of 1064 nm) and directed into the PPLN crystal for the DFG process. Afterwards, the remaining pump laser light is filtered out by a prism, a long-pass dielectric filter and a narrow-band fiber Bragg grating. The total conversion efficiency of the DFG setup is $\eta_c \approx 17\%$ [27]. To ensure the frequency and phase stability of the converted photons, both the NV excitation laser and the pump laser are locked to an external reference cavity (Stable Laser Systems).

Figure 3.2b shows the experimental sequence used in the experiments. Our protocol starts with checking whether the NV center is in the desired charge state and on resonance with the control lasers [29]. Once this test is passed, the spin-photon entangled state is generated. If a photon is detected, we read out the spin state in the appropriate basis and re-start the protocol. In case no photon is detected, we reinitialize the spin and again generate an entangled state. After 250 failed attempts to detect a photon, we re-start the protocol.

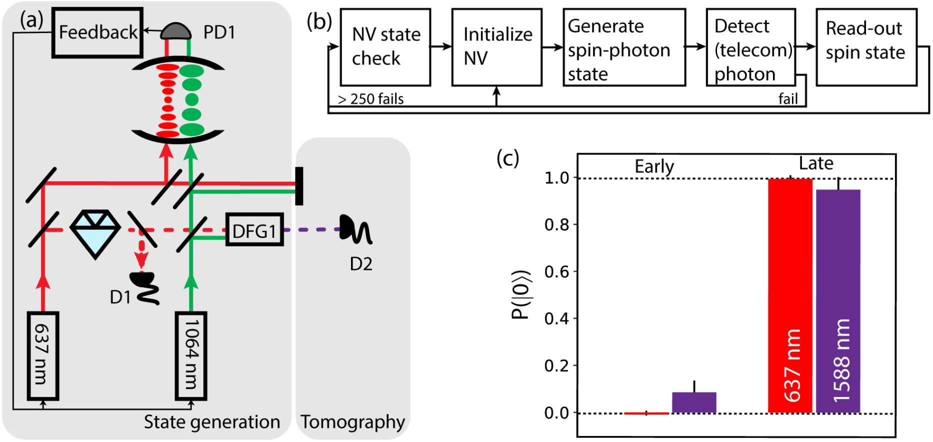

Figure 3.2: (a) Experimental setup for the spin-telecom photon entangled state generation. Emitted 637 nm photons are combined with the pump laser (1064 nm) in the difference frequency generation setup (DFG1). The two lasers are frequency-locked to an external reference cavity. Tomography in the Z-basis: the frequency converted photons are detected using a superconducting nanowire detector (D2) discriminating the early and late time bins. (b) Experimental protocol for generating and detecting spin-telecom photon entangled states (see main text). (c) Results for correlations measured in the Z basis both for the red and for the frequency-converted photons at telecom wavelength.

3.3. EXPERIMENTAL VERIFICATION: CLASSICAL CORRELATIONS

We first measure spin-photon correlations in the ZZ basis. To measure the photon in the Z basis, we send the frequency-converted photons directly to a superconducting nanowire detector (D2) that projects the photonic qubit in the time-bin basis, and, upon photon detection, we read out the spin qubit in the corresponding Z basis. Figure 3.2c shows the observed correlation data. The probability to measure the spin in $|0\rangle$ is plotted for photon detection events in the early and late time-bins. We have performed this measurement for both the 637 nm photons (red) and for the frequency-converted photons at 1588 nm (purple). For the unconverted photons we measure correlations that are perfect within measurement uncertainty (contrast of $E_Z = |P_E(|0\rangle) - P_L(|0\rangle)| = 0.997 \pm 0.018$). For the frequency converted photons we measure $P_E(|0\rangle) = 0.09 \pm 0.05$ for the early time bin and $P_L(|0\rangle) = 0.95 \pm 0.05$ for the late time bin, yielding a contrast of $E_Z = 0.86 \pm 0.07$. All data in this work are corrected for spin readout infidelity and dark counts of the detectors, both of which are determined independently.

The contrast for the telecom photons is lowered by noise coming from spontaneous parametric down converted (SPDC) photons and Raman scattering induced by the strong pump laser [27, 30]. We characterize this noise contribution separately by blocking the incoming 637 nm path and find an expected signal to noise ratio (SNR) between 4.8 and 7.3. This SNR bounds the maximum observable contrast for the ZZ correlations to SNR/(SNR+1) = 0.85 ± 0.03, and thus fully explains our data. We use this SNR later to determine the different noise contributions for the correlation data in the other bases. Additionally, we conclude from the relative number of detection events in the early and late time bin (659 vs 642 events) that the amplitudes of the two parts of the spin-photon entangled state are well balanced.

3.4. EXPERIMENTAL VERIFICATION: QUANTUM CORRELATIONS

To verify the spin-photon entanglement, we measure spin-photon correlations in two other spin-photon bases by sending the frequency-converted photons into the imbalanced fiber interferometer (see Figure 3.3a). The fiber arm length difference is ≈ 40 m, which corresponds to a photon travel time difference of 190 ns between the two arms. In this way the early time bin taking the long arm overlaps at the second beam splitter with the late time bin taking the short arm, thus allowing us to access the phase relation between the two. To access a specific photon qubit basis, we introduce a tunable phase difference $\Delta\phi$ between the long and short arms of the interferometer. In particular, detection of a photon by the detector D3 projects the spin into the state

$$|\mathrm{NV}\rangle_{D3} = \frac{1}{\sqrt{2}}\left(|0\rangle + e^{i\left(\Delta\phi - \frac{\pi}{4}\right)}\,|1\rangle\right). \tag{3.2}$$

We use two orthogonal set points, labeled X and Y, with $\Delta\phi = \pi/4$ and $\Delta\phi = 3\pi/4$, respectively, as indicated in Figure 3.3b.

A key requirement for this experiment is that the interferometer is stable with respect to the frequency of the down-converted photons; any instabilities in the interferometer will reduce the interference contrast and prevent us from accessing the true spin-photon correlations. For this reason the interferometer is thermally and vibrationally isolated. Furthermore, we split the experiment into cycles of 1 second (see Figure 3.4a), of which the first 100 ms is used to actively stabilize the phase set point of the interferometer. Within this 100 ms, we feed metrology light into the interferometer in the reverse direction via shutter S and a circulator. This metrology light is generated by a second DFG setup, using input from the excitation and pump lasers, thus ensuring a fixed frequency relation between the metrology light and the frequency-converted photons. By comparing the light intensities on detectors PD2 and PD3 with the values corresponding to the desired $\Delta\phi$ set point as determined from a visibility fringe (calibrated every 100 s), an error signal is computed and feedback is applied to the fiber piezo stretcher (FPS). After this adjustment the light intensities are measured again. A histogram of the measured phases during the experiments relative to the set points is plotted in Figure 3.4b. We note that one could also measure the spin-photon correlations at the second output of the interferometer, which for symmetric states as Eq. (3.1)1 would yield the same correlations but with opposite sign; however, in the current experiment the slow (≈ 1 s) recovery of the detector after being blinded due to metrology light leakage through this output port prevented us from using the second output.

In the remaining 900 ms of each cycle spin-photon correlations are measured using the same protocol as for the ZZ basis (see Figure 3.4b). To read out the NV spin state in the appropriate rotated basis, the eigenstates $|X\rangle$ ($|Y\rangle$) and the $|\text{-}X\rangle$ ($|\text{-}Y\rangle$) are mapped onto the $|0\rangle$ and $|1\rangle$ states, respectively, by applying an appropriate MW pulse before optical

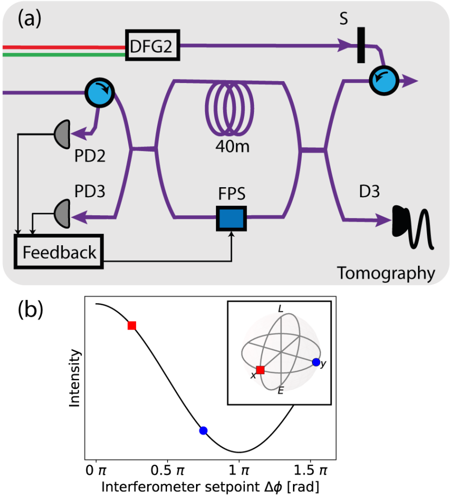

Figure 3.3: (a) Polarization-maintaining fiber-based imbalanced interferometer used for the photon state readout in X and Y bases. The frequency-converted single photons are directed into the interferometer. One output port of the interferometer is connected to a superconducting nanowire detector (detector D3). Every second the phase of the interferometer is stabilized. Classical frequency-converted light created by a second DFG setup (DFG2) is sent into the interferometer via a shutter S and a circulator. Light intensities measured by photodiodes PD2 and PD3 are used to generate a feedback signal to the fiber piezo stretcher (FPS) to maintain the target phase $\Delta\phi$. (b) Bloch sphere with the selected photon qubit readout bases indicated on it, and the corresponding phase set points of the imbalanced interferometer.

readout.

Figure 3.4c shows the measured spin-photon correlations in the X and Y basis (bottom), along with expected correlations for the ideal state (top). The letters indicate the spin and photon bases respectively, for example -XX indicates that the NV spin is measured along the -X axis on the Bloch sphere, while the photon is projected on +X. The measured contrast between the correlations and anti-correlations in the X basis is $E_X = 0.52 \pm 0.07$ and $E_Y = 0.69 \pm 0.07$ in the Y basis.

3.5. CONCLUSION

All data show clear (anti-)correlation between the NV spin qubit and the telecom photonic qubit. With the contrast data from all three orthogonal photon readout bases, we calculate the fidelity F of our produced state (conditioned on photon detection) to the maximally entangled state of Eq. (3.1) as

$$F = \frac{1}{4}\left(1 + E_X + E_Y + E_Z\right), \tag{3.3}$$

yielding a fidelity of $F = 0.77 \pm 0.03$. This value exceeds the classical boundary of 0.5 by more than eight standard deviations, proving the generation of entanglement between the NV spin qubit and the frequency-converted photonic qubit. For comparison, reported fidelities for unconverted NV spin-photon entangled states range from ≈ 0.7 [31, 32] to more than 0.9 (estimated from an observed spin-spin entangled state fidelity of ≈ 0.9 [33]).

The observed fidelity is reduced compared to the ideal value of 1 due to several factors. First, the initial spin-photon entangled state has imperfections, for instance due to photon emission and re-excitation of the NV center during the optical π-pulse [34] and small frequency shifts due to spectral diffusion. In addition, the remaining frequency variations of the two locked lasers (~200 kHz) leads to phase uncertainty between the two terms in Eq. (3.1). All these effects reduce the contrast of the XX and YY correlations, but not that of the ZZ correlations. Second, spontaneous parametric downconversion (SPDC) and Raman scattered photons, produced during the frequency conversion process, add noise to the state as described above and reduce correlations in all bases. Based on these factors, we expect a state fidelity in the range $0.82 - 0.87$.

The slight difference between the expected and measured state fidelity could be due to the inaccuracies and fluctuations in setting the interferometer phase set point. Imperfect interferometer settings result in measurement bases that slightly deviate from the expected X and Y bases, reducing the maximally observable correlations. Therefore, the obtained $F \geq 0.77 \pm 0.03$ sets a lower bound on the true entangled state fidelity.

In conclusion, we demonstrated entanglement between an NV center spin qubit and a time-bin encoded photonic qubit at telecom wavelength, which is an essential step towards long-distance quantum networks based on remote entanglement between NV center nodes. The current frequency conversion combined with recently demonstrated

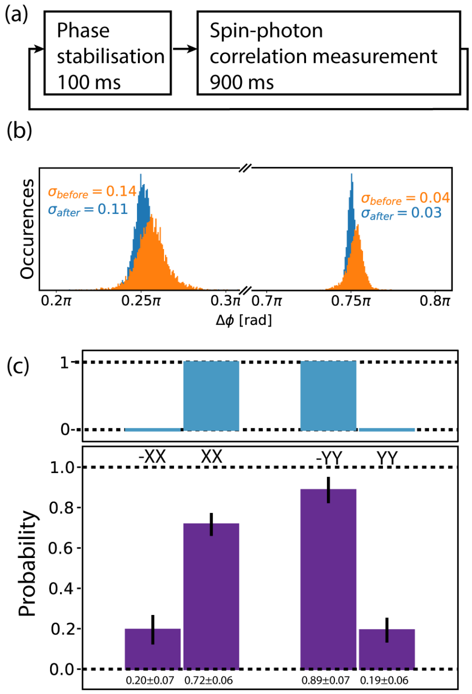

Figure 3.4: (a) Experimental protocol for measurements in the photon X and Y basis. (b) Measured phase difference $\Delta\phi$ just before stabilization (orange, with 900 ms free evolution time) and directly after stabilization (blue) for the two set points $\Delta\phi_X = \pi/4$ and $\Delta\phi_Y = 3\pi/4$. From the standard deviations in these data, we estimate a residual phase drift of 0.05 and 0.01 rad/s for the X and Y photon qubit readout bases, respectively. (c) Results for the correlations in the X and Y basis in purple. The top-panel shows ideal correlations. In total we have measured 1595 photon detection events.

entangling protocols [34] would lead to a spin-spin entangling rate of a few Hz over 30 km of fiber (ignoring heralding signals). In future experiments the observed state fidelity can be further increased in several ways. A more narrow band frequency filtering after the DFG1 setup would reduce the added noise in the frequency conversion, as the current narrow-band filter has a line width ~ 10 times larger than the NV-emitted resonant ZPL photons. The signal could be increased by improving the conversion efficiency. Finally, the emission rate of resonant photons and the collection efficiency can be increased by placing the NV center in an optical cavity [35–40], which could also increase the entangling rate by up to 3 orders of magnitude.

REFERENCES

[1] S. Wehner, D. Elkouss, and R. Hanson, *Quantum internet: A vision for the road ahead,* Science **362** (2018).

[2] M. Ben-Or, C. Crépeau, D. Gottesman, A. Hassidim, and A. Smith, *Secure multiparty quantum computation with (only) a strict honest majority,* Proceedings - Annual IEEE Symposium on Foundations of Computer Science, FOCS , 249 (2006).

[3] A. Broadbent, J. Fitzsimons, and E. Kashefi, *Universal blind quantum computation,* Proceedings - Annual IEEE Symposium on Foundations of Computer Science, FOCS , 517 (2009).

[4] L. Jiang, J. M. Taylor, K. Nemoto, W. J. Munro, R. Van Meter, and M. D. Lukin, *Quantum repeater with encoding,* Physical Review A **79**, 1 (2009).

[5] A. Ekert and R. Renner, *The ultimate physical limits of privacy,* Nature **507**, 443 (2014).

[6] J. I. Cirac, A. K. Ekert, S. F. Huelga, and C. Macchiavello, *Distributed quantum computation over noisy channels,* Physical Review A **59**, 4249 (1999).

[7] D. Gottesman, T. Jennewein, and S. Croke, *Longer-baseline telescopes using quantum repeaters,* Physical Review Letters **109**, 1 (2012).

[8] N. H. Nickerson, J. F. Fitzsimons, and S. C. Benjamin, *Freely scalable quantum technologies using cells of 5-to-50 qubits with very lossy and noisy photonic links,* Physical Review X **4**, 1 (2014).

[9] P. Kómár, E. M. Kessler, M. Bishof, L. Jiang, A. S. Sørensen, J. Ye, and M. D. Lukin, *A quantum network of clocks,* Nature Physics **10**, 582 (2014).

[10] J. D. Bancal, S. Pironio, A. Acín, Y. C. Liang, V. Scarani, and N. Gisin, *Quantum nonlocality based on finite-speed causal influences leads to superluminal signalling,* Nature Physics **8**, 867 (2012).

[11] Y. O. Dudin, A. G. Radnaev, R. Zhao, J. Z. Blumoff, T. A. Kennedy, and A. Kuzmich, *Entanglement of light-shift compensated atomic spin waves with telecom light,* Physical Review Letters **105**, 1 (2010).

[12] K. De Greve, L. Yu, P. L. McMahon, J. S. Pelc, C. M. Natarajan, N. Y. Kim, E. Abe, S. Maier, C. Schneider, M. Kamp, S. Höfling, R. H. Hadfield, A. Forchel, M. M. Fejer, and Y. Yamamoto, *Quantum-dot spin-photon entanglement via frequency downconversion to telecom wavelength,* Nature **491**, 421 (2012).

[13] M. Bock, P. Eich, S. Kucera, M. Kreis, A. Lenhard, C. Becher, and J. Eschner, *High-fidelity entanglement between a trapped ion and a telecom photon via quantum frequency conversion,* Nature Communications **9**, 1 (2018).

[14] P. Farrera, G. Heinze, and H. De Riedmatten, *Entanglement between a Photonic Time-Bin Qubit and a Collective Atomic Spin Excitation,* Physical Review Letters **120**, 100501 (2018).

[15] T. Walker, K. Miyanishi, R. Ikuta, H. Takahashi, S. Vartabi Kashanian, Y. Tsujimoto, K. Hayasaka, T. Yamamoto, N. Imoto, and M. Keller, *Long-Distance Single Photon Transmission from a Trapped Ion via Quantum Frequency Conversion,* Physical Review Letters **120**, 203601 (2018).

[16] V. Krutyanskiy, M. Meraner, J. Schupp, V. Krcmarsky, H. Hainzer, and B. P. Lanyon, *Light-matter entanglement over 50 km of optical fibre,* npj Quantum Information **5** (2019).

[17] D. D. Awschalom, R. Hanson, J. Wrachtrup, and B. B. Zhou, *Quantum technologies with optically interfaced solid-state spins,* Nature Photonics **12**, 516 (2018).

[18] J. Cramer, *Quantum error correction with spins in diamond*, Ph.D. thesis, Delft University of Technology (2016).

[19] G. Waldherr, Y. Wang, S. Zaiser, M. Jamali, T. Schulte-Herbrüggen, H. Abe, T. Ohshima, J. Isoya, J. F. Du, P. Neumann, and J. Wrachtrup, *Quantum error correction in a solid-state hybrid spin register,* Nature **506**, 204 (2014).

[20] T. H. Taminiau, J. Cramer, T. Van Der Sar, V. V. Dobrovitski, and R. Hanson, *Universal control and error correction in multi-qubit spin registers in diamond,* Nature Nanotechnology **9**, 171 (2014).

[21] N. Kalb, A. A. Reiserer, P. C. Humphreys, J. J. Bakermans, S. J. Kamerling, N. H. Nickerson, S. C. Benjamin, D. J. Twitchen, M. Markham, and R. Hanson, *Entanglement distillation between solid-state quantum network nodes,* Science **356**, 928 (2017).

[22] H. Bernien, B. Hensen, W. Pfaff, G. Koolstra, M. S. Blok, L. Robledo, T. H. Taminiau, M. Markham, D. J. Twitchen, L. Childress, and R. Hanson, *Heralded entanglement between solid-state qubits separated by three metres,* Nature **497**, 86 (2013).

[23] T. Miya, Y. Terunuma, T. Hosaka, and T. Miyashita, *Ultimate low-loss single-mode fibre at 1.55 μm,* Electronics letters **15** (1979).

[24] K. Nagayama, M. Kakul, M. Matsul, T. Saitoh, and Y. Chigusa, *Ultra-low-loss (0.1484dB/km) pure silica core fibre and extension of transmission distance,* Electronics letters **38**, 1 (2002).

[25] R. Ikuta, T. Kobayashi, T. Kawakami, S. Miki, M. Yabuno, T. Yamashita, H. Terai, M. Koashi, T. Mukai, T. Yamamoto, and N. Imoto, *Polarization insensitive frequency conversion for an atom-photon entanglement distribution via a telecom network,* Nature Communications **9**, 1 (2018).

[26] Y. Yu, F. Ma, X. Y. Luo, B. Jing, P. F. Sun, R. Z. Fang, C. W. Yang, H. Liu, M. Y. Zheng, X. P. Xie, W. J. Zhang, L. X. You, Z. Wang, T. Y. Chen, Q. Zhang, X. H. Bao, and J. W. Pan, *Entanglement of two quantum memories via fibres over dozens of kilometres,* Nature **578**, 240 (2020).

[27] A. Dréau, A. Tcheborateva, A. E. Mahdaoui, C. Bonato, and R. Hanson, *Quantum Frequency Conversion of Single Photons from a Nitrogen-Vacancy Center in Diamond to Telecommunication Wavelengths,* Physical Review Applied **9**, 2 (2018).

[28] J. D. Franson, *Bell inequality for position and time,* Physical Review Letters **62**, 2205 (1989).

[29] L. Robledo, L. Childress, H. Bernien, B. Hensen, P. F. A. Alkemade, and R. Hanson, *High-fidelity projective read-out of a solid-state spin quantum register,* Nature , 5 (2011).

[30] J. S. Pelc, C. Langrock, Q. Zhang, and M. M. Fejer, *Influence of domain disorder on parametric noise in quasi-phase-matched quantum frequency converters,* Optics Letters **35**, 2804 (2010).

[31] E. Togan, Y. Chu, A. S. Trifonov, L. Jiang, J. Maze, L. Childress, M. V. Dutt, A. S. Sørensen, P. R. Hemmer, A. S. Zibrov, and M. D. Lukin, *Quantum entanglement between an optical photon and a solid-state spin qubit,* Nature **466**, 730 (2010).

[32] R. Vasconcelos, S. Reisenbauer, C. Salter, G. Wachter, D. Wirtitsch, J. Schmiedmayer, P. Walther, and M. Trupke, *Scalable spin–photon entanglement by time-to-polarization conversion,* npj Quantum Information **6**, 1 (2020).

[33] B. Hensen, H. Bernien, A. E. Dreaú, A. Reiserer, N. Kalb, M. S. Blok, J. Ruitenberg, R. F. Vermeulen, R. N. Schouten, C. Abellán, W. Amaya, V. Pruneri, M. W. Mitchell, M. Markham, D. J. Twitchen, D. Elkouss, S. Wehner, T. H. Taminiau, and R. Hanson, *Loophole-free Bell inequality violation using electron spins separated by 1.3 kilometres,* Nature **526**, 682 (2015).

[34] P. C. Humphreys, N. Kalb, J. P. Morits, R. N. Schouten, R. F. Vermeulen, D. J. Twitchen, M. Markham, and R. Hanson, *Deterministic delivery of remote entanglement on a quantum network,* Nature **558**, 268 (2018).

[35] A. Faraon, C. Santori, Z. Huang, V. M. Acosta, and R. G. Beausoleil, *Coupling of nitrogen-vacancy centers to photonic crystal cavities in monocrystalline diamond,* Physical Review Letters **109**, 2 (2012).

[36] S. Johnson, P. R. Dolan, T. Grange, A. A. Trichet, G. Hornecker, Y. C. Chen, L. Weng, G. M. Hughes, A. A. Watt, A. Auffèves, and J. M. Smith, *Tunable cavity coupling of the zero phonon line of a nitrogen-vacancy defect in diamond,* New Journal of Physics **17**, 122003 (2015).

[37] H. Kaupp, T. Hümmer, M. Mader, B. Schlederer, J. Benedikter, P. Haeusser, H. C. Chang, H. Fedder, T. W. Hänsch, and D. Hunger, *Purcell-Enhanced Single-Photon Emission from Nitrogen-Vacancy Centers Coupled to a Tunable Microcavity,* Physical Review Applied **6**, 1 (2016).

[38] D. Riedel, I. Söllner, B. J. Shields, S. Starosielec, P. Appel, E. Neu, P. Maletinsky, and R. J. Warburton, *Deterministic enhancement of coherent photon generation from a nitrogen-vacancy center in ultrapure diamond,* Physical Review X **7**, 1 (2017).

[39] S. Bogdanović, S. B. Van Dam, C. Bonato, L. C. Coenen, A. M. J. Zwerver, B. Hensen, M. S. Liddy, T. Fink, A. Reiserer, M. Lončar, and R. Hanson, *Design and low-temperature characterization of a tunable microcavity for diamond-based quantum networks,* Applied Physics Letters **110** (2017).

[40] N. H. Wan, B. J. Shields, D. Kim, S. Mouradian, B. Lienhard, M. Walsh, H. Bakhru, T. Schröder, and D. Englund, *Efficient Extraction of Light from a Nitrogen-Vacancy Center in a Diamond Parabolic Reflector,* Nano Letters **18**, 2787 (2018).

4

A MULTINODE QUANTUM NETWORK OF REMOTE SOLID-STATE QUBITS

M. Pompili*, S. L. N. Hermans*, S. Baier*, H. K. C. Beukers, P. C. Humphreys, R. N. Schouten, R. F. L. Vermeulen, M. J. Tiggelman, L. dos Santos Martins, B. Dirkse, S. Wehner & R. Hanson

The distribution of entangled states across the nodes of a future quantum internet will unlock fundamentally new technologies. Here, we report on the realization of a three-node entanglement-based quantum network. We combine remote quantum nodes based on diamond communication qubits into a scalable phase-stabilized architecture, supplemented with a robust memory qubit and local quantum logic. In addition, we achieve real-time communication and feed-forward gate operations across the network. We demonstrate two quantum network protocols without postselection: the distribution of genuine multipartite entangled states across the three nodes and entanglement swapping through an intermediary node. Our work establishes a key platform for exploring, testing, and developing multinode quantum network protocols and a quantum network control stack.

The results of this chapter have been published in Science, **372**, 259-264 (2021).

* Equally contributing authors

4.1. INTRODUCTION

Future quantum networks sharing entanglement across multiple nodes [1, 2] will enable a range of applications such as secure communication, distributed quantum computing, enhanced sensing, and fundamental tests of quantum mechanics [3–8]. Efforts in the past decade have focused on realizing the building blocks of such a network: quantum nodes capable of establishing remote entangled links as well as locally storing, processing, and reading out quantum information.

Entanglement generation through optical channels between a pair of individually controlled qubits has been demonstrated with trapped ions and atoms [9–12], diamond nitrogen-vacancy (NV) centers [13, 14], and quantum dots [15, 16]. In addition, a number of quantum network primitives have been explored on these elementary two-node links, including nonlocal quantum gates [17, 18] and entanglement distillation [19]. Moving these qubit platforms beyond two-node experiments has so far remained an outstanding challenge owing to the combination of several demanding requirements. Multiple high-performance quantum nodes are needed that include a communication qubit with an optical interface as well as an efficient memory qubit for storage and processing. Additionally, the individual entanglement links need to be embedded into a multinode quantum network, requiring a scalable architecture and multinode control protocols.

Here, we report on the realization and integration of all elements of a multinode quantum network: optically mediated entanglement links connected through an extensible architecture, local memory qubit and quantum logic, and real-time heralding and feed-forward operations. We demonstrate the full operation of the multinode network by running two key quantum network protocols. First, we establish Greenberger-Horne-Zeilinger (GHZ) entangled states across the three nodes. Such distributed genuine multipartite entangled states are a key ingredient for many network applications [2] such as anonymous transmission [20], secret sharing [21], leader election [22], and clock stabilization [8]. Second, we perform entanglement swapping through an intermediary node, which is the central protocol for entanglement routing on a quantum network enabling any-to-any connectivity [23, 24]. Owing to efficient coherence protection on all qubits, combined with real-time feed-forward operations, these protocols are realized in a heralded fashion, delivering the final states ready for further use. This capability of heralding successful completion of quantum protocols is critical for scalability; its demonstration here presents a key advance from earlier experiments using photons [25] and quantum memories [26].

Our network is composed of three spatially separated quantum nodes (Figure 4.1, A and B), labeled Alice, Bob, and Charlie. Each node consists of an NV center electronic spin as a communication qubit. In addition, the middle node Bob uses a carbon-13 nuclear spin as a memory qubit. Initialization and single-shot readout of the communication qubits are performed through resonant optical excitation and measurement of state-dependent fluorescence [14]. Universal quantum logic on the electronic-nuclear register is achieved through tailored microwave pulses delivered on chip (Section 4.6). The nodes are connected through an optical fiber network for the quantum signals, as well as classical communication channels for synchronizing the control operations and relaying heralding signals (see below).

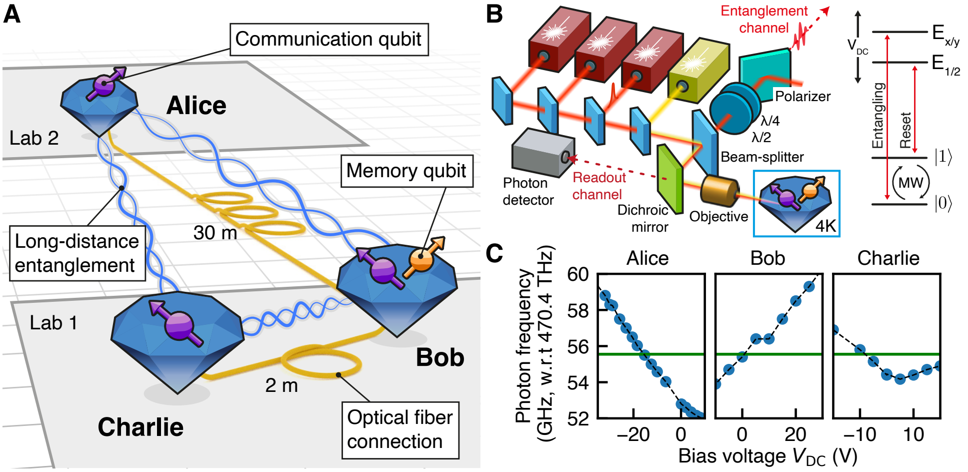

Figure 4.1: **The three-node quantum network.** **(A)** Layout of the network. Three nodes, labeled Alice, Bob, and Charlie, are located in two separate labs. Each node contains an NV center communication qubit (purple). At Bob, an additional nuclear spin qubit (orange) is used in the presented experiments. Fiber connections between the nodes (lengths indicated) enable remote entanglement generation on the links Alice-Bob and Bob-Charlie, which, combined with local quantum logic, allow for entanglement to be shared between all nodes (wiggly lines). **(B)** On the left is a simplified schematic of the optical setup at each node (see Figure 4.6, Table 4.1, and Section 4.6 for additional details). On the right is a diagram of the relevant levels of the electronic spin qubit, showing optical transitions for remote entanglement generation and readout ("entangling"), qubit reset ("reset"), and resonant microwaves ("MW") for qubit control (see Figures 4.7 and 4.14 for additional details). The memory qubit at Bob is initialized, controlled, and read out via the electronic qubit (Figure 4.8). Optical transition frequencies are tuned via the dc bias voltages (V_{DC}). $\lambda/2$ ($\lambda/4$) is a half-waveplate (quarter-waveplate); $E_{x/y}$ and $E_{1/2}$ are electronic excited states. **(C)** Tuning of the optical "entangling" transition at each of the three nodes. The solid line is the working point, 470.45555 THz; the dashed line is a guide to the eye. w. r. t. , with respect to.

Remote entanglement generation hinges on indistinguishability between emitted photons. For NV centers in high-purity low-strain diamond devices, the optical transition frequencies show relatively minor variations (few GHz). We remove the remaining offsets by using dc Stark tuning at each node with bias fields generated on chip (Figure 4.1C). We are thus able to bring the relevant optical transitions of all three nodes to the same frequency, which we choose to be the zero-bias frequency of Bob.

4.2. ESTABLISHING REMOTE ENTANGLEMENT IN A NETWORK ARCHITECTURE

To generate remote entanglement between a pair of nodes (i.e., one elementary link), a single-photon protocol is used [27, 28] (Figure 4.2A). The communication qubits of the nodes are each prepared in a superposition state $|\alpha\rangle = \sqrt{\alpha}|0\rangle + \sqrt{1-\alpha}|1\rangle$. At each node, pulsed optical excitation, which is resonant only for the $|0\rangle$ state, and subsequent photon emission deterministically create an entangled state between the communication qubit and the presence-absence of a photon (the flying qubit). The photonic modes from the two nodes are then interfered on a beam splitter, removing the which-path information. The beam splitter closes an effective interferometer formed by the optical excitation and collection paths. Detection of a single photon after the beam splitter heralds the state $\left|\psi^{\pm}\right\rangle \approx (|01\rangle \pm e^{i\Delta\theta}|10\rangle)/\sqrt{2}$ between the two communication qubits, where the ± sign depends on which of the two detectors clicked and $\Delta\theta$ is the optical phase difference between the two arms of the effective interferometer (Section 4.6). Experimentally, this phase difference is set to a known value by stabilizing the full optical path using a feedback loop [14, 16]. This scheme yields states at maximum fidelity $1-\alpha$ at a rate $\approx 2\alpha p_{\mathrm{det}} r_{\mathrm{attempt}}$, with p_{det} the probability that an emitted photon is detected and r_{attempt} the entanglement attempt rate.

Scaling this entangling scheme to multiple nodes requires each elementary link to be phase-stabilized independently (Figure 4.2B), posing a number of new challenges. The different links, and even different segments of the same link, will generally be subject to diverse noise levels and spectra. Additionally, the optical power levels used are vastly different, from microwatts for the excitation path to attowatts for the single-photon heralding station, requiring different detector technologies for optimal signal detection. We solve these challenges with a hybrid phase-stabilization scheme that is scalable to an arbitrary number of nodes. We decompose the effective interferometer for each link into three independently addressable interferometers and stabilize each separately (see Figure 4.2C for the Alice-Bob link; the link Bob-Charlie is phase-stabilized in an analogous and symmetric way; see Figures 4.9 and 4.12).

First, each node has its own local stabilization that uses unbalanced heterodyne phase detection (Figure 4.2C, left). In comparison to the previous homodyne stabilization method [14], this enables us to obtain a higher bandwidth phase signal from the small part of the excitation light that is reflected from the diamond surface (≈ 1%) by boosting it with a strong reference-light beam at a known frequency offset. Moreover, this scheme allows for optimal rejection of the reflected excitation light by polarization selection, thus preventing excitation light from entering the single-photon path toward the heralding detectors and creating false entanglement heralding events. The measured phase signals are fed back on piezoelectric-mounted mirrors to stabilize the local interferometers.

Second, the global part of the effective interferometer (Figure 4.2C, right) is stabilized by single-photon-level homodyne phase detection with feedback on a fiber stretcher: A small fraction of the strong reference-light beam is directed into the single-photon path, and the interference is measured using the same detectors used for entanglement generation.

This architecture provides scalability in the number of nodes and a higher feedback bandwidth compared with our previous implementation on a single link (Figure 4.13; see Section 4.6 for details). In our current implementation, the central node – Bob – has combining optics to merge the signals coming from Alice and Charlie, so that the single-photon detectors can be shared by the two links.

Crucially, this architecture enables the successive generation of entanglement on the two elementary links as required for network protocols exploiting multinode entanglement. We benchmark its performance by running entanglement generation on both elementary links within a single experimental sequence (Figure 4.2D).

We achieve fidelities of the entangled Bell states exceeding 0.8 for both links (Figure 4.2E), on par with the highest fidelity reported for this protocol for a single link [14]. For the same fidelity, the entangling rates are slightly higher than in Ref. [14] (9 and 7 Hz for links Alice-Bob and Bob-Charlie, respectively), despite the additional channel loss from connecting the two links. The main sources of infidelity are the probability α that both nodes emit a photon, remaining optical phase uncertainty, and double excitation during the optical pulse (see Table 4.2 and Section 4.6). A detailed physical model that includes known error sources is used here and below for comparison to the experimental data (Section 4.6); predictions by the model are indicated by the gray bars in the correlation and fidelity plots.

4.3. MEMORY QUBIT PERFORMANCE AND REAL-TIME FEED-FORWARD OPERATIONS

To distribute entangled states across multiple nodes, generated entangled states must be stored in additional qubits while new entanglement links are created. Carbon-13 nuclear spins are excellent candidates for such memory qubits, thanks to their long coherence times, controllability, and isolation from the control drives on the electronic qubit [29]. Recent work [30] indicated that their storage fidelity under network activity is mainly limited by dephasing errors resulting from the coupling to the electronic spin that is randomized on failed entanglement generation. It was suggested that the memory robustness to such errors may be further improved by operating under an increased applied magnetic field. Here, we use a magnetic field of 189 mT for our central node, as opposed to ≈ 40 mT used in past experiments [19, 30].

This higher field puts much stricter demands on the relative field stability in order to not affect the qubit frequencies; we achieve an order of magnitude reduction in field fluctuations by actively stabilizing the temperature of the sample holder, which in turn stabilizes the permanent magnet inside the cryostat (Section 4.6). Additionally, the higher magnetic field splits the two optical transitions used for electronic spin initialization, hindering fast qubit resets; the addition of a second initialization laser, frequency locked to the first one with an offset of 480 MHz, enables us to maintain high-fidelity (> 0.99) and fast (few microsecond) resets (Section 4.6).

We measure the fidelity of stored states on Bob's memory qubit for a varying number of entanglement generation attempts (Figure 4.3). The two eigenstates ($\pm Z$) do not show appreciable decay as we increase the number of entanglement generation attempts, as expected from the pure dephasing nature of the process [30]. The superposition states

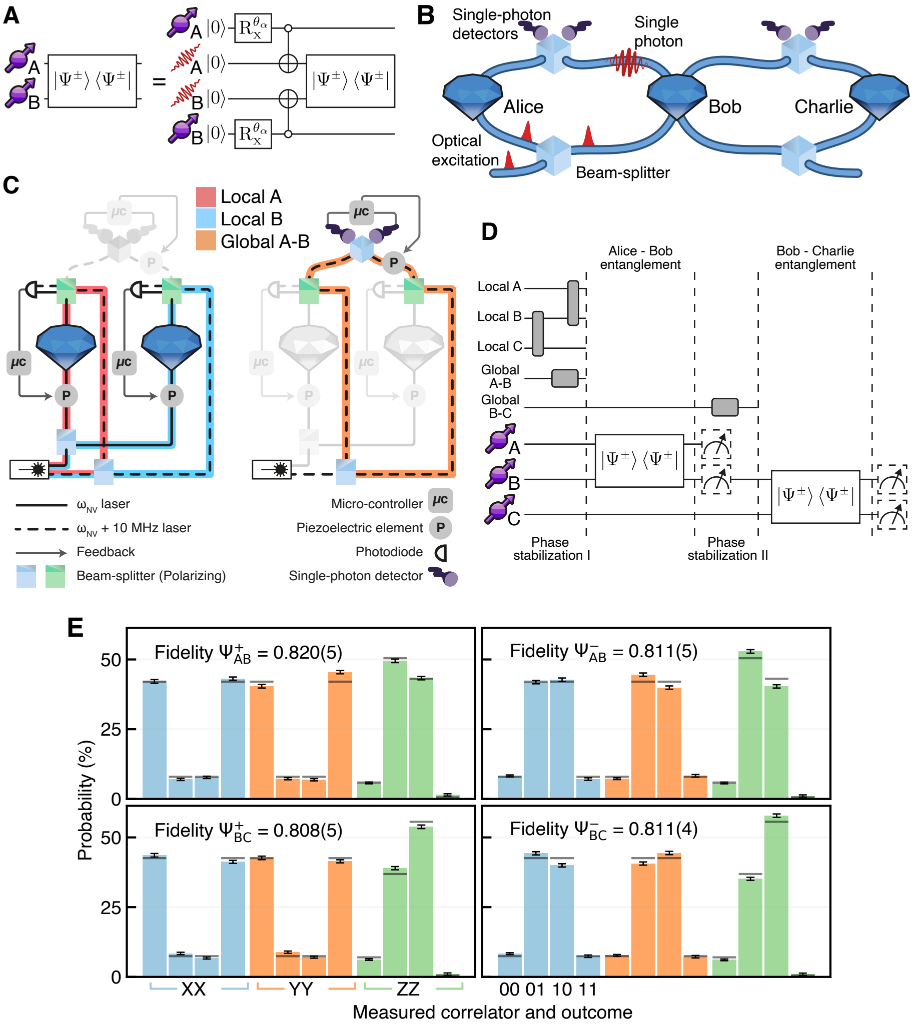

Figure 4.2: **Establishing remote entanglement in a network architecture.** **(A)** Circuit diagram of the single-photon entanglement protocol, where $R_X^{\theta_\alpha}$ is a rotation around the x axis with angle θ_α, $\theta_\alpha = 2\cos^{-1}(\sqrt{\alpha})$. **(B)** Sketch of three quantum network nodes in line configuration, showing the two effective interferometers. **(C)** Phase stabilization diagram of the Alice-Bob link, highlighting the local interferometers (left) and the global interferometer (right). See Section 4.6 for further details. **(D)** Experimental sequence to generate Bell pairs on both Alice-Bob (A-B) and Bob-Charlie (B-C) links. Dashed boxes display measurements used in (E). **(E)** Correlation measurements on entangled states on A-B (top) and B-C (bottom) links. The left plots correspond to $|\Psi^-\rangle$ states; the right plots correspond to $|\Psi^+\rangle$ states. Shown are observed probabilities for outcomes (from left to right) 00, 01, 10, and 11 for correlation measurements in the bases XX (blue), YY (orange), and ZZ (green). Gray bars depict values from the theoretical model. Error bars indicate one standard deviation.

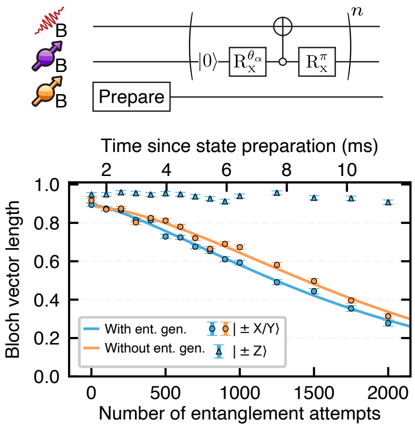

Figure 4.3: **Memory qubit coherence under network activity.** **(Top)** Circuit diagram displaying the experimental sequence, where n is the number of entanglement attempts. **(Bottom)** Blue represents the measured Bloch vector length of memory qubit eigenstates (triangles) and superposition states (circles) versus entanglement attempts, for $\alpha = 0.05$. Orange represents measured superposition decay versus time in the absence of entanglement attempts. Solid lines are fits, yielding decay constants of $N_{1/e} = 1843 \pm 32$ (2042 ± 36) with (without) entanglement generation attempts (see Table 4.5 and Section 4.6 for additional details).

degrade with an average decay constant of $N_{1/e} \approx 1800$ attempts. To gain insight into the contribution of network activity to this decay, we repeat these measurements in the absence of entanglement attempts, in which case dephasing of the memory qubit is mainly due to uncontrolled interactions with nearby nuclear spins. We find this intrinsic dephasing time to be $T_2^\star$ =11.6(2) ms, equivalent to the duration of ≈ 2000 entanglement generation attempts. We conclude that the intrinsic dephasing accounts for most of the decay observed under network activity, indicating the desired robustness. For the experiments discussed below, we use a timeout of 450 attempts before the sequence is restarted, as a balance between optimizing entanglement generation rate and fidelity of the stored state.

Executing protocols over quantum networks requires real-time feed-forward operations among the various nodes: measurement outcomes at the heralding station or at nodes need to be translated into quantum gates on other nodes. We implement an asynchronous bidirectional serial communication scheme between microcontrollers at the nodes, enabling both the required timing synchronization of the nodes and the exchange of feed-forward information for the quantum network protocols (Section 4.6). Furthermore, we integrate the feed-forward operations with local dynamical decoupling protocols that actively protect the communication qubits from decoherence. The resulting methods enable us to run multinode protocols in a heralded fashion: *Flag* signals indicate in real time the successful execution of (sub)protocols and generation of desired states that are then available for further use, thus critically enhancing the efficiency and removing the need for any postselection.

4.4. DEMONSTRATION OF MULTINODE NETWORK PROTOCOLS

We now turn to the full operation of the three-node network that combines the different elements discussed above. We perform two canonical network protocols: the distribution of genuine multipartite entanglement and entanglement swapping to two non–nearest-neighbor nodes.

In both protocols, the sequence depicted in Figure 4.4A is used to establish a remote entangled state on each of the two links. This sequence starts with a preparation step (depicted only in Figure 4.15) that synchronizes the microcontrollers of the nodes and makes sure that the NV centers in each node are in the desired charge state and in resonance with all the relevant lasers. After initialization of the memory qubit, the first entangled state is prepared on the link Alice-Bob. We interleave blocks of entanglement generation attempts with phase-stabilization cycles. Once Alice-Bob entanglement is heralded, Alice's entangled qubit is subject to a dynamical decoupling sequence while awaiting further communication from the other nodes. At Bob, deterministic quantum logic is used to swap the other half of the entangled state to the memory qubit.

The second part of the phase stabilization is then executed, followed by the generation of remote entanglement between the communication qubits of Bob and Charlie. In case of a timeout (no success within the preset number of attempts), the full protocol is restarted. In case of success, a dynamical decoupling sequence is started on Charlie's communication qubit analogous to the protocol on Alice. At Bob, a Z-rotation is applied to the memory qubit to compensate for the acquired phase that depends linearly on the (a priori unknown) number of entanglement attempts. This gate is implemented through an XY4 decoupling sequence on the communication qubit, with a length set in real time by the microcontroller based on which entanglement attempt was successful (Section 4.6). After this step, the two links each share an entangled state ready for further processing: one between the communication qubit at Alice and the memory qubit at Bob and one between the communication qubits of Bob and Charlie.

The first protocol we perform is the generation of a multipartite entangled GHZ state across the three nodes. The circuit diagram describing our protocol is depicted in Figure 4.4B. We first entangle the two qubits at Bob, followed by measurement of the communication qubit in a suitably chosen basis. The remaining three qubits are thereby projected into one of four possible GHZ-like states, which are all equivalent up to a basis rotation. The specific basis rotation depends both on the measurement outcome at Bob and on which Bell states ($\left|\Psi^+\right\rangle$ or $|\Psi^-\rangle$) were generated in the first part of the sequence, which in turn depends on which two photon detectors heralded the remote entangled states. These outcomes are communicated and processed in real time and the corresponding feed-forward operations are applied at Charlie. As a result, the protocol is able to achieve delivery of the same GHZ state $|\mathrm{GHZ}\rangle_{\mathrm{ABC}} = (|000\rangle + |111\rangle)/\sqrt{2}$, irrespective of the intermediate outcomes. Here, we choose to herald only on Bob reporting the $|0\rangle$ readout outcome, because the asymmetry in the communication qubit readout fidelities renders this outcome more faithful (Section 4.6). Additionally, this choice automatically filters out events in which the NV center of Bob was in the incorrect charge state or off resonance (occurrence ≈ 10% in this experiment; see Section 4.6). With this heralding choice, the protocol delivers GHZ states at a rate of about 1/(90s).

We extract the fidelity to the ideal GHZ state from correlation measurements by using

$$F = (1 + \langle IZZ\rangle + \langle ZIZ\rangle + \langle ZZI\rangle + \langle XXX\rangle - \langle XYY\rangle - \rangle YXY\rangle - \langle YYX\rangle)/8 \tag{4.1}$$

and find $F = 0.538(18)$ (Figure 4.4C). The state fidelity above 0.5 certifies the presence of genuine multipartite entanglement distributed across the three nodes [31].
In this experiment, the fidelities of the entangled states on the elementary links bound the fidelity of the heralded GHZ state to about 0.66. Other relevant error sources are the dephasing of the memory qubit and accumulation of small quantum gate errors (see Table 4.3). We emphasize that, contrary to earlier demonstrations of distributed GHZ states with photonic qubits [25] and ensemble-based memories [26] that relied on postselection, we achieve heralded GHZ state generation: a real-time heralding signal indicates the reliable delivery of the states.

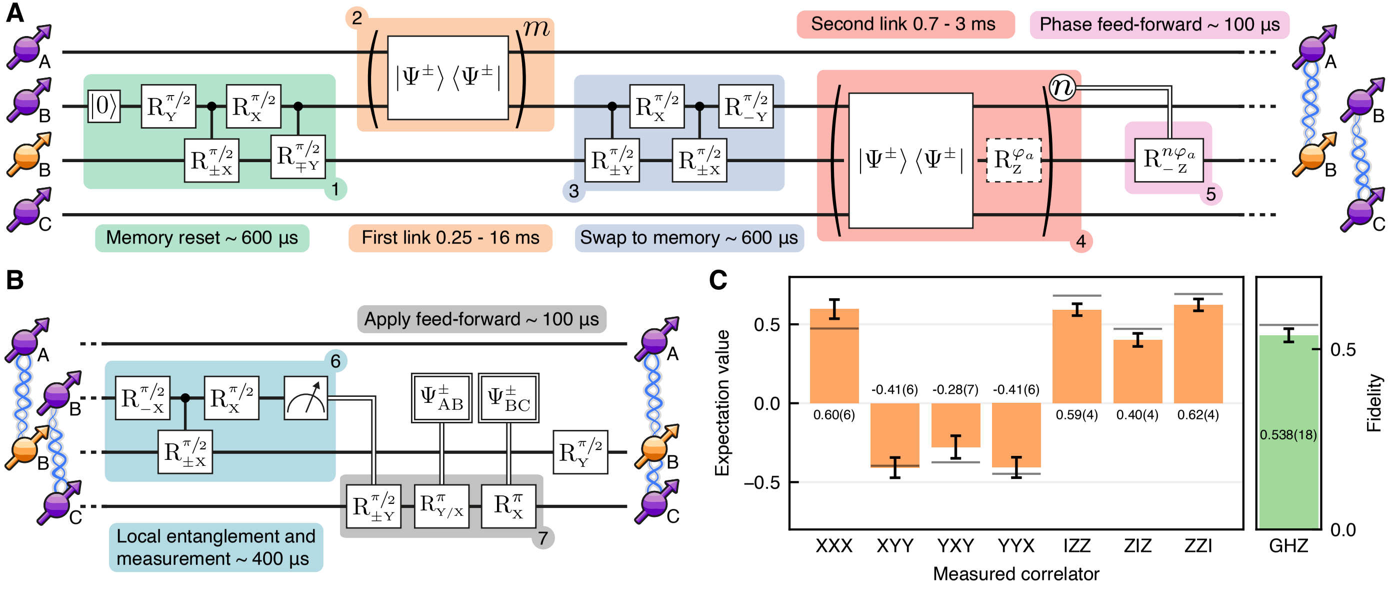

Figure 4.4: **Distribution of genuine multipartite entanglement across the quantum network.** **(A)** Circuit diagram displaying the experimental sequence used to establish entanglement on both elementary links. **(B)** Circuit diagram displaying the experimental sequence for distributing a three-partite GHZ state across the three nodes. **(C)** Outcomes of correlation measurements and the resulting fidelity of the heralded GHZ state, demonstrating genuine multipartite entanglement. Gray bars depict values from the theoretical model. Error bars indicate one standard deviation.

The second protocol, illustrated in Figure 4.5A, demonstrates entanglement swapping of the two direct links into an entangled state of the outer two nodes. Once entanglement is established on the two links as described above, the central part of the entanglement swapping is executed: Bob, the central node, performs a Bell state measurement (BSM) on its two qubits. One way to read this protocol is that the BSM induces teleportation of the state stored on Bob's memory qubit to Charlie, by consuming the entangled state shared by Bob's communication qubit and Charlie. Because the state teleported to Charlie was Bob's share of an entangled state with Alice, the teleportation establishes direct entanglement between Alice and Charlie.

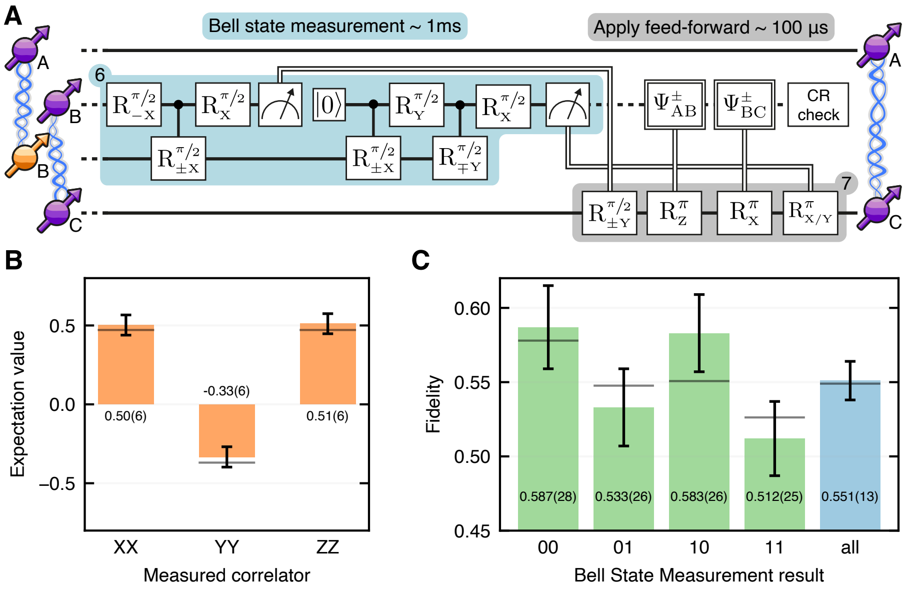

Figure 4.5: **Entanglement swapping on a multinode quantum network.** **(A)** Circuit diagram displaying the experimental sequence for entanglement swapping, yielding an entangled state shared between the two non-connected nodes. **(B)** Outcomes of correlation measurements on the heralded entangled state shared between Alice and Charlie for the selected Bell-state measurement outcome (see main text). **(C)** State fidelities for different outcomes of Bob's Bell-state measurement (green) and the state fidelity averaged over all outcomes (blue). In (B) and (C), gray bars depict values from the theoretical model, and error bars indicate one standard deviation.

After the BSM is completed, we perform a charge and resonance (CR) check on Bob to prevent heralding on events in which the NV center of Bob was in the incorrect charge state or off resonance. We note that this CR check was not used in the heralding procedure of the GHZ generation protocol because its current implementation induces decoherence on Bob's memory qubit, which is part of the final GHZ state to be delivered. To complete the entanglement swapping, feed-forward operations are performed at Charlie to account in real time for the different measurement outcomes, analogous to the previous protocol, resulting in the delivery of the Bell state $|\Phi^+\rangle_{AC} = (|00\rangle + |11\rangle)/\sqrt{2}$.

We assess the performance of the entanglement swapping by measuring three two-node correlators on the generated Bell state shared by Alice and Charlie. Because the BSM is performed with local quantum logic and single-shot readout, it is (except for the CR check step) a deterministic operation. However, given the asymmetry in the readout errors as discussed above, the fidelity of the final state will depend on the readout outcomes. Figure 4.5B shows the results of the correlation measurements on the delivered state for heralding on Bob obtaining twice the outcome $|0\rangle$, yielding a state fidelity of $F = 0.587(28)$. Figure 4.5C compares the state fidelities across the different BSM outcomes, displaying the expected lower fidelities for outcomes of $|1\rangle$ and an average fidelity over all outcomes of $F = 0.551(13)$. The combined heralding rate is $1/(40\text{s})$. The sources of infidelity are similar to the ones discussed above (see Table 4.4). This experiment constitutes the first demonstration of entanglement swapping from previously stored remote entangled states, enabled by the network's ability to asynchronously establish heralded elementary entanglement links, to store these entangled states, and then to efficiently consume them to teleport entanglement to distant nodes.

4.5. CONCLUSION AND OUTLOOK

We have demonstrated the realization of a multinode quantum network. We achieved multipartite entanglement distribution across the three nodes and any-to-any connectivity through entanglement swapping. It is noteworthy that the data acquisition for the network protocols has been performed fully remotely because of the COVID-19 pandemic, highlighting the versatility and stability of our architecture. Near-term advances in the capabilities and performance of the network will be driven by further reducing the infidelities of the elementary links (Section 4.6), by adding new subprotocols such as control methods [29], decoupling sequences [30], and repetitive readout [32] for the nuclear spin qubits; by improved photonic interfaces to enhance the entangling rates [33–35]; and by improved control over the charge state of the NV center [36].

Our results open the door to exploring advanced multinode protocols and larger entangled states, for instance, by extending the local registers at the nodes. We note that a fully controlled 10-qubit register has recently been demonstrated on a similar device [29]. Furthermore, the network provides a powerful platform for developing and testing higher-level quantum network control layers [37–39], such as the recently proposed link layer protocol for quantum networks [40]. Quantum frequency conversion of the NV photons [41] can be used to interface the network nodes with deployed telecom fiber, paving the way to near-term quantum network tests over metropolitan distances. Finally, we expect the methods developed here to provide guidance for similar platforms reaching the same level of maturity in the future [42–45].

4.6. SUPPLEMENTARY INFORMATION

4.6.1. EXPERIMENTAL SETUP

Our experiments are performed on three quantum network nodes. Each node houses a Nitrogen-Vacancy (NV) center in a high-purity type-IIa chemical-vapor-deposition diamond cut along the ⟨111⟩ crystal orientation (Element Six). All three samples have a natural abundance of carbon isotopes. Fabrication of solid immersion lenses and an anti-reflection coating on the diamond samples enhances the photon-collection efficiencies from the NV centers. The samples are housed in home-built cryogenic confocal microscope setups at 4 K. Experimental equipment used for each node is summarized in Table 4.1. In the following we use the letters A, B and C to identify nodes Alice, Bob and Charlie. The numbers 0, 1 refer to the computational basis $|0\rangle, |1\rangle$. Node A is in a different laboratory than nodes B and C, 7 m away. Nodes B and C are on the same optical table, approximately 2 m apart, see also Figure 4.1A of the main text. The optical fiber that connects A with B is 30 m long, while the one that connect B to C is 2 m long.

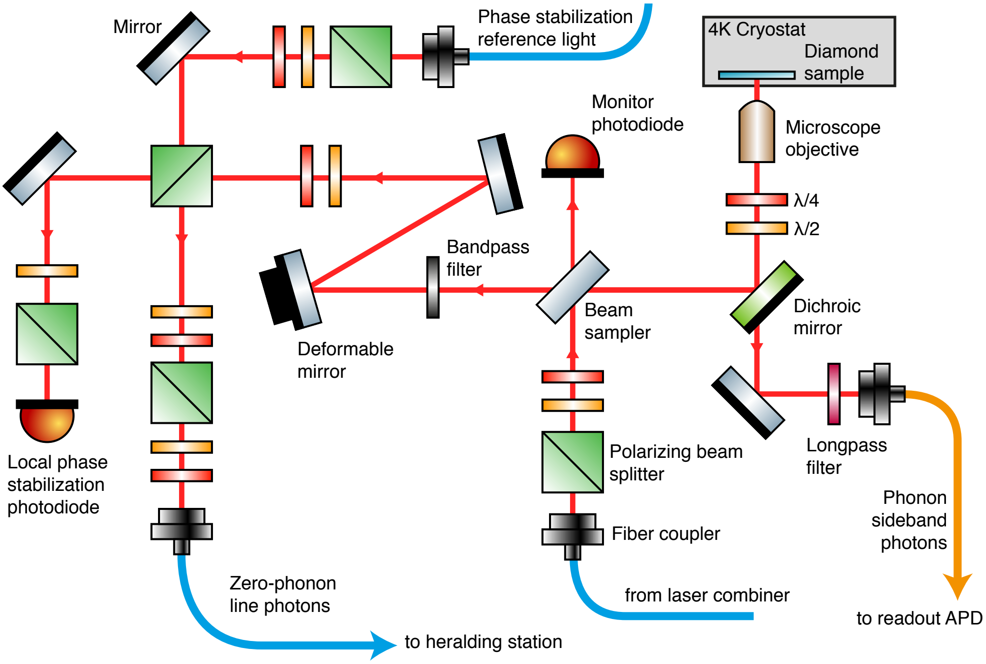

Figure 4.6: **Schematic of the optics used for each node.** The red lines indicate the optical path used both by the laser beams and the single photons. Blue fibers are single-mode polarization maintaining fiber. The orange fiber is a multi-mode fiber. The laser combiner (not depicted) combines, via beam-splitters and dichroic mirrors, the various laser beams and couples them into the single-mode fiber shown in the diagram. The laser combiner also includes a piezoelectric-mounted mirror that is used for the local phase stabilization feedback. The monitor photodiode records the 90% of excitation light that goes through the beam-sampler (and that would otherwise be discarded). We monitor this signal on a digital oscilloscope connected to the measurement computers for debugging purposes.

Table 4.1: **Experimental equipment used in the three nodes.** Non-listed equipment is unchanged from previous experiments and identical for the three setups.

	Alice	Bob	Charlie
Cryostat	attocube attoDRY800	Montana Instruments Cryostation S50	Montana Instruments Cryostation S50
Positioner	Sample on attocube xyz stack	Microscope objective on PI P-615	Microscope objective on PI P-615
Micro-controller	Jäger ADwin-Pro II T12	Jäger ADwin-Pro II T12	Jäger ADwin-Pro II T12
Arbitrary Waveform Generator (AWG)	Tektronix AWG5014	Tektronix AWG5014C	Tektronix AWG5014C
MW source	R&S SGS100A SGMA - up to 6 GHz	R&S SGS100A SGMA - up to 12.75 GHz	R&S SGS100A SGMA - up to 6 GHz
MW amplifier	AR 40S1G4	AR 25S1G4A	AR 40S1G4
Entangling and qubit readout laser	Toptica TA-SHG pro 637 nm	Toptica DL pro 637 nm	Toptica TA-SHG pro 637 nm
Qubit reset laser	Toptica DL pro 637 nm	1 - Toptica TA-SHG pro 637 nm 2 - New Focus Velocity 637 nm	New Focus Velocity 637 nm
Charge reset laser	Toptica DL-SHG pro 575 nm	Cobolt 515 nm	Toptica DL-SHG pro 575 nm
EOM	Jenoptik AM635		Jenoptik AM635
Deformable mirror	Boston Micromachines 12x12	Boston Micromachines 12x12	Boston Micromachines 12x12

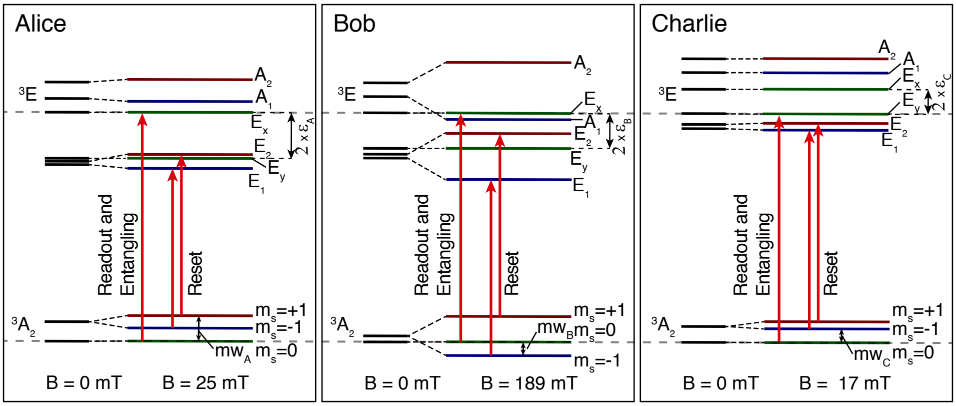

Figure 4.7: **Level structure for the three NV centers.** The optical transitions used within this work are indicated by red solid arrows. DC stark tuning brings all readout transitions to the same frequency, ensuring that the photons generated via the optical excitation pulse are indistinguishable. The spin state $m_S = 0/+1/-1$ of each level is indicated by color (green/red/blue). The communication qubits of nodes A, B and C are encoded in the NV center electronic spin states $|0/1\rangle_A \equiv |m_S = 0/+1\rangle$, $|0/1\rangle_B \equiv |m_S = 0/-1\rangle$ and $|0/1\rangle_C \equiv |m_S = 0/-1\rangle$. The memory qubit of node B is encoded in the nuclear spin state of the addressed ^{13}C atom, $|0/1\rangle \equiv \left|m_I = \pm\frac{1}{2}\right\rangle$.

Figure 4.6 depicts the optics used to deliver and collect light to each sample. For phonon-sideband (PSB) detection, a dichroic mirror (Semrock) and an additional long-pass filter (Semrock) are used to block reflections of the excitation lasers. Photon emission is detected via an avalanche photo-diode (APD, Laser components, quantum efficiency approximately 80 %), with a total collection efficiency of approximately 10 %. For zero-phonon line (ZPL) detection, we isolate the single photons first with a narrow bandpass filter (5 nm, Semrock), then by blocking the reflected excitation light via two polarising beam-splitters (Thorlabs and Semrock). Spatial mode shaping via a deformable mirror (Boston Micromachines) enhances coupling to a polarization-maintaining single-mode fiber. The optical signals from each node are combined on in-fiber polarization-maintaining beam-splitters (Evanescent Optics). The final beam-splitter (where the single photons interfere) has an integrated fiber stretcher used for optical phase stabilization. Finally, the single photons are detected on superconducting nanowire single photons detectors (Photon Spot). They are optimized for 637 nm, have a detection efficiency >95 % and a dark count rate < 1 Hz.

The level structures of the three nodes are depicted in Figure 4.7. Each structure depends on local strain, electric fields and the applied magnetic field B. For nodes A and B the magnetic field is created with a permanent neodymium magnet inside the cryostat, which is located close to the sample and attached to the sample holder. The magnetic field is fine-tuned to be along the symmetry axis of the NV center using permanent neodymium magnets outside the cryostat. Node C has only a single permanent magnet outside the cryostat.

For optical excitation we set the laser frequencies (red arrows in Fig. 4.7) to the corre-

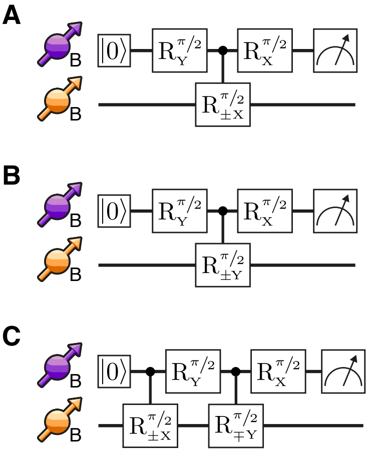

Figure 4.8: **Memory qubit readout sequences.** **(A-C)** Readout sequences of the nuclear spin memory qubit expectation values for $\hat{X}, \hat{Y}, \hat{Z}$ via the communication qubit. The controlled rotations are to be read as follows: $\mathrm{R}^{\pi/2}_{\pm\mathrm{X}}$ is a rotation of the memory qubit around the X axis with an angle of $\pi/2$ if the communication qubit is in $|0\rangle$, and with an angle of $-\pi/2$ if the communication qubit is in $|1\rangle$.

sponding ${}^3A_2$ to ${}^3E$ transition. Spin-selective excitation of ZPL transitions ($\lambda = 637.25$ nm, $\omega = 2\pi \times 470.45$ THz) enables qubit readout ("Entangling" in Fig. 1B of the main text, $m_s = 0 \longleftrightarrow E_{x/y}$) and qubit reset via optical spin-pumping ("Reset" in Fig. 1B of the main text, $m_s = \pm 1 \longleftrightarrow E_{1,2}$). While at low field a single laser is sufficient to address both qubit reset transitions, in case of node B, which operates at 189 mT, we find a reset transitions splitting of 480 MHz. An additional laser is implemented in order to drive both reset transitions efficiently.

In order to tune the readout transitions of each NV center into resonance we employ the DC Stark effect via DC-biasing the strip-line that is used to deliver microwave (MW) signals. The feedback sequence is analogous to the one used in Ref. [46]. Node B operates at 0 V tuning (it is grounded), and it uses non resonant charge reset with a green laser (515 nm). We observe small day to day drift in the readout frequency of node B that we attribute to slow ice build-up on the sample as the transition frequency can be brought back to its original value by a warm-up cool-down cycle. Nodes A and C, which use resonant charge reset with a yellow laser (575 nm), are brought into resonance with node B before starting a measurement.

The memory qubit of node B is the nuclear spin of a ^{13}C atom in the proximity of the NV center. Its electronic-spin-dependent precession frequencies are $\omega_0 = 2\pi\times 2025$ kHz and $\omega_{-1} = 2\pi\times 2056$ kHz, resulting in parallel hyperfine coupling of $A_{\parallel} \approx 2\pi\times$ 30 kHz. The nuclear spin is controlled using dynamical decoupling sequences [19, 29]. The conditional $\pi/2$-rotations on the nuclear spin are performed with 56 decoupling pulses with an inter-pulse delay of $2\tau = 2\times$ 2.818 μs. Gate sequences to readout the memory qubit via the communication qubit are summarized in Fig. 4.8.

For synchronization purposes, the micro-controllers at each node (Jäger ADwin-Pro II T12) share a common 1 MHz clock. To increase the on-off ratio of the AOM RF drivers, and therefore reduce unwanted light leakage, we use home-built fast (150 ns rise-time) RF switches, based on the HMC8038 (Analog Devices), to disconnect the RF drivers from the AOMs when no power should be delivered. We terminate the MW delivery line on each cryostat with a home-built MW envelope detector, that allows us to see on an oscilloscope the microwave pulses being delivered to each sample. We use this for debugging purposes. Parts that are not mentioned in the description above are the same as in Refs. [14, 19, 46].

4.6.2. MODEL OF THE GENERATED STATES

MODEL AND SOURCES OF ERROR

The Python code to model all the generated states and to produce the figures in the main text can be found at [47]. The Jupyter notebooks that generate the figures make direct use of that code to plot the simulated states. The communication qubits of nodes A, B and C are encoded in the NV center electronic spin states $|0/1\rangle_A \equiv |m_S = 0/+1\rangle$, $|0/1\rangle_B \equiv |m_S = 0/-1\rangle$ and $|0/1\rangle_C \equiv |m_S = 0/-1\rangle$. The memory qubit of node B is encoded in the nuclear spin state of the addressed ^{13}C atom, $|0/1\rangle \equiv \left|m_I = \pm\frac{1}{2}\right\rangle$.

Regarding the generation of Bell states on the Alice-Bob and Bob-Charlie links, we extend the model presented in Ref. [14] to allow for different values of the parameters α in the two nodes. We find that to obtain maximum state fidelity the condition $\alpha_A p_A^{\mathrm{det}} \approx \alpha_B p_B^{\mathrm{det}}$ must hold, where $\alpha_{A,B}$ are the populations of the $|0\rangle$ state of each node and $p_{A,B}^{\mathrm{det}}$ is the probability of detecting a photon emitted by the respective node in the detection window. The state that is heralded by the protocol is the following (assuming $p^{\mathrm{det}} \ll 1$):

$$\rho_{AB}^{\pm} = \frac{1}{p_{\mathrm{tot}}} \begin{pmatrix} p_{00} & 0 & 0 & 0 \\ 0 & p_{01} & \pm\sqrt{V p_{01} p_{10}} & 0 \\ 0 & \pm\sqrt{V p_{01} p_{10}} & p_{10} & 0 \\ 0 & 0 & 0 & p_{11} \end{pmatrix}, \tag{4.2}$$

$$p_{00} = \alpha_A \alpha_B (p_A^{\mathrm{det}} + p_B^{\mathrm{det}} + 2p_{\mathrm{dc}}), \tag{4.3}$$

$$p_{01} = \alpha_A (1-\alpha_B)(p_A^{\mathrm{det}} + 2p_{\mathrm{dc}}), \tag{4.4}$$

$$p_{10} = \alpha_B (1-\alpha_A)(p_B^{\mathrm{det}} + 2p_{\mathrm{dc}}), \tag{4.5}$$

$$p_{11} = 2(1-\alpha_A)(1-\alpha_B) p_{\mathrm{dc}}, \tag{4.6}$$

$$p_{\mathrm{tot}} = p_{00} + p_{01} + p_{10} + p_{11} \tag{4.7}$$

where V is the visibility of the two-photon quantum interference, $p_{\mathrm{dc}} \ll 1$ is the probability of detecting a dark count (or in general a non-NV photon) in the detection window, the ± sign depends on which detector clicked. The off-diagonal terms neglect the contribution due to the dark counts with respect to the contribution due to $p_{A,B}^{\mathrm{det}}$, i.e. we assume $p_{\mathrm{dc}} \ll p_{A,B}^{\mathrm{det}}$.

Table 4.2: **Error budget of the generated Bell states and experimental parameters.** The error due to the probability that both nodes emit a photon is related to the values of α (see section 4.6.2) and is therefore intrinsic to the protocol. The infidelity contribution for each of the other errors is estimated as if that error were the only other error present, this way one can easily compare the relative effect of the different infidelity sources. When combined we take into account all the errors at the same time.

Source of infidelity	Expected state infidelity	
	Alice - Bob	Bob - Charlie
Probability that both nodes emit a photon	6.1e-2	8.0e-2
Phase uncertainty	6.0e-2	1.5e-2
Double excitation	5.5e-2	7.0e-2
Photon distinguishability	2.4e-2	2.3e-2
Non-NV and dark counts	5e-3	5e-3
Combined	0.191	0.186
Measured Ψ^+ infidelity	0.180(5)	0.192(5)
Measured Ψ^- infidelity	0.189(5)	0.189(4)
Experimental parameters	Alice - Bob	Bob - Charlie
p_{det}	$p_A^{\text{det}} = 3.6e-4$ $p_B^{\text{det}} = 4.4e-4$	$p_B^{\text{det}} = 4.2e-4$ $p_C^{\text{det}} = 3.0e-4$
α	$\alpha_A = 0.07$ $\alpha_B = 0.05$	$\alpha_B = 0.05$ $\alpha_C = 0.10$
p_{dc}	1.5e-7	1.5e-7
Visibility V	0.90	0.90
Phase uncertainty	30^o	15^o
Entanglement attempt duration	3.8 μs	5.0 μs
Probability of double excitation	0.06	0.08

If one assumes $p_{\text{det}} = p_A^{\text{det}} = p_B^{\text{det}}$, $p_{\text{dc}} = 0$, $\alpha = \alpha_A = \alpha_B$ and $V = 1$, then the fidelity of ρ_{AB} with the closest Bell state is $F = 1 - \alpha$, and the generation rate is $r_{AB} = 2\ \alpha\ p_{\text{det}}\ r_{\text{attempt}}$, with r_{attempt} the attempt rate.

Additional sources of infidelity are uncertainty in the phase of the entangled state and double excitation. See Ref. [14] for details on how they are modeled. We summarize in Table 4.2 the infidelity arising from the aforementioned sources, which is reasonably in agreement with the measured state fidelities. The Bell states between Alice and Bob were generated with $\alpha_A, \alpha_B = 0.07, 0.05$, while the ones between Bob and Charlie with $\alpha_B, \alpha_C = 0.05, 0.10$. These values have been chosen as a trade-off between protocol success rate and fidelity.

To model the states generated in the two demonstrated protocols (GHZ state between Alice Bob and Charlie, and Bell state between Alice and Charlie) we take into account:

- the Bell states generated between Alice and Bob and between Bob and Charlie,

Table 4.3: **Error budget of the generated GHZ states.** For each source of infidelity considered we estimate two quantities: the infidelity induced on the state as if it were the only source of error present; the improvement in fidelity if that error were to be removed while all other errors remain present. When combined we take into account all the errors at the same time.

Source of infidelity	Expected infidelity if only source present	Expected improvement once removed
Ψ_{AB} state infidelity	0.191	0.120
Ψ_{BC} state infidelity	0.186	0.122
Memory qubit depolarising noise	8.3e-2	4.4e-2
Memory qubit dephasing noise	2.8e-2	1.5e-2
Dynamical decoupling of A and C	3.7e-2	1.9e-2
At least one node is in NV^0	1.6e-2	8e-3
Feed-forward errors	6e-3	3e-3
Ψ_{AB} and Ψ_{BC} combined	0.337	0.275
Combined	0.433	
Measured GHZ infidelity	0.462(18)	

- the dephasing of the nuclear spin during the entanglement generation between Bob and Charlie,

- depolarising noise on the nuclear spin that combines initialisation, swap and readout error,

- communication qubit readout errors at Bob that would generate a wrong feed-forward operation at Charlie,

- the depolarising noise on the communication qubits of Alice and Charlie during their dynamical decoupling sequences,

- the possibility that Alice and/or Charlie are in the wrong charge state (NV^0) at the end of the sequence.

Table 4.3 and Table 4.4 summarize the error budget of the generated states. In the case of the entanglement swapping we also report the expected infidelity when accepting any Bell state measurement (BSM) result.

In the protocol demonstrating GHZ distribution across the three nodes we chose to herald on readout outcome “0" only, as explained in the main text. Our model predicts that GHZ states heralded on measurement outcome “1" would have had an additional 3% infidelity (due to the asymmetry in the electron readout infidelities).

FUTURE IMPROVEMENTS TO THE REMOTE ENTANGLEMENT LINKS

The remote entanglement fidelity can be increased in the near term by improving phase stabilization at Alice to a similar level as Bob and Charlie, by lowering the double-excitation

Table 4.4: **Error budget of the generated Alice-Charlie states.** For each source of error considered we estimate two quantities: the infidelity induced on the state as if it were the only source of error present; the improvement in fidelity if that error were to be removed while all other errors remain present. When combined we take into account all the errors at the same time. Errors reported for different Bell state measurement (BSM) results.

Source of infidelity	Expected infidelity if only source present	Expected improvement once removed
Ψ_{AB} state infidelity	0.191	0.115
Ψ_{BC} state infidelity	0.186	0.109
Memory qubit depolarising noise	8.2e-2	4.0e-2
Memory qubit dephasing noise	2.8e-2	1.2e-2
Dynamical decoupling of A and C	3.7e-2	1.7e-2
At least one node is in NV^0	1.6e-2	6e-3
Feed-forward errors (00 BSM result)	1.3e-2	6e-3
Feed-forward errors (any BSM result)	7.5e-2	3.4e-2
Combined (00 BSM result)	0.422	
Combined (any BSM result)	0.451	
Measured Φ_{AC} infidelity (00 BSM result)	0.413(28)	
Measured Φ_{AC} infidelity (any BSM result)	0.449(13)	

probability through a reduction of the optical excitation pulse width, and by using similar devices with higher collection efficiency [46] allowing for operation at smaller α. Additionally, an improvement in fidelity of approximately $\eta_{\mathrm{PSB}}(\alpha + p_{2\mathrm{e}})$ (where η_{PSB} is the probability to collect a photon in the phonon sideband emission and $p_{2\mathrm{e}}$ is the probability of double excitation during the optical pulse) can be obtained by rejecting heralding events for which simultaneously a photon was detected in the phonon sideband emission channel on one of the nodes. In the same way, this filtering will reduce the errors due to double excitation during the optical pulse as well as errors due to heralding on dark counts. This rejection could be implemented in real-time using an additional FPGA on each node. The combination of these improvements would bring the entanglement fidelity above 0.90.

Going beyond the current hardware, the entanglement generation rates may be increased by up to two orders of magnitude by enhancing the collection of coherent NV photons through the use of optical cavities [33, 35]. Alternatively, the development of other color centers in optical waveguides and/or cavities may bring a similar improvement in rates [42–45].

4.6.3. PHASE STABILIZATION

Inherent to an implementation where active phase stabilization is interleaved with free evolution time, there is a trade-off between phase stability (or fidelity of the entangled state) and the free evolution time (which is the time used for entanglement generation). The more often the system is stabilized, the higher the bandwidth of the stabilization and the lower the final uncertainty in $\Delta\theta$ will be.

Our previous implementation used a single homodyne phase detection scheme [14]. While that method allows for the stabilization of the phase of the entangled state, there are several aspects that can be improved; The small fraction of excitation light that is reflected from the diamond surface is partially coupled in the single-photon detection path. By measuring the interference signal after the beam-splitter at the heralding station it is possible to obtain the phase of the interferometer. But leaking some of the reflected excitation light into the single-photon path for phase stabilization purposes increases the chance that, during entanglement generation, some of the reflected excitation light will be detected and mistakenly herald an entangled state. To counteract this effect, the amount of leaked light was somewhat minimized by polarization selection (but never completely, since some light is needed to detect a phase signal) and long integration times (24 ms) were used during phase detection, reducing the phase stabilization bandwidth. Furthermore, exposing the NV center to a relatively long and strong laser pulse makes it more susceptible to spectral jumps and ionization.

To solve these challenges we devised and implemented a new phase stabilization scheme that combines higher bandwith and optimal rejection of the excitation light from the single-photon paths, while maintaining robustness against power level fluctuations and scalability to a higher number of nodes.

PHASE DETECTION METHODS

In a homodyne phase detection scheme the light has the same frequency in both arms of the interferometer. Depending on the optical phase difference $\Delta\theta$, light will constructively or destructively interfere on the output ports of the beam-splitter. Assuming common polarization and perfectly overlapping spatial modes, the intensity $I_{3,4}$ in the output ports is

$$I_{3,4} = I_1 + I_2 \pm 2\sqrt{I_1 I_2}\cos\Delta\theta. \tag{4.8}$$

For known input levels $I_{1,2}$, $\Delta\theta$ can be calculated from the difference in intensity in the output ports of the beams-splitter. Fluctuations in the intensity of the input signals will lead to an error in the phase measurement, except for the case $\cos\Delta\theta = 0$ which gives $I_3 = I_4$ independent of the input intensity.

In a heterodyne phase detection scheme the light has different frequencies in the two arms of the interferometer. Again, assuming common polarization and perfectly overlapping modes, the light will interfere in the output ports resulting in a signal with amplitude

$$I_{3,4} = I_1 + I_2 \pm \sqrt{I_1 I_2}\big(\cos((\omega_1 - \omega_2)t - \Delta\theta) + \cos((\omega_1 + \omega_2)t + \Delta\theta)\big) \tag{4.9}$$

where $\omega_{1,2}$ are the angular frequencies of the light. When we pick a relatively small frequency difference, $(\omega_1 - \omega_2)/2\pi \approx 10$ MHz, we can ignore the last term in Eq. 4.9 and the resulting 10 MHz beat signal can be measured with a photodiode and efficiently filtered from the DC background signal (the last term of Eq. 4.9 will have a frequency in the optical domain and will not be picked up by the photodiode due to the limited bandwidth). The phase of this beat signal corresponds to the optical phase difference in the two paths. Since the phase information is not translated to the amplitude of the beat signal, fluctuations in the input intensity will not cause an error in the measurement. Moreover, this method is very suitable to measure small signals: if the signal is very small in one of the arms, the amplitude of the beat signal can be increased by increasing the intensity in the other arm.

SPLITTING THE INTERFEROMETER IN PARTS

In the experiments with three quantum nodes we have two effective interferometers that share part of their optical paths. We split the interferometers into six parts, see Figures 4.9, 4.10. In total there are four local interferometers and two global interferometers, where the local interferometer comprises the excitation path and free space optical path close to the cryostat of each node and the global interferometer includes the fibers connecting the nodes to the central beam-splitter. With the measured phase, an error signal is computed and feedback is applied to the optical path, either with a mirror on a piezoelectric element or a fiber stretcher.

The two global interferometers, using homodyne phase detection, stabilize the optical path to the beam-splitter and single photon detectors used for entanglement heralding. Since the detectors are shared for the two entanglement links, the optical phase measurement for the two global interferometers has to be multiplexed in time. The local interferometers are stabilized using heterodyne phase detection. The excitation light (the same we use for the optical excitation pulse that generates spin-photon entanglement)

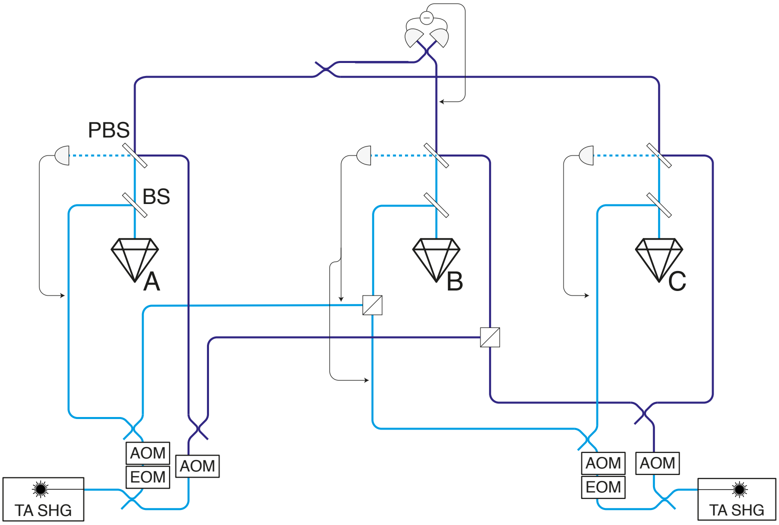

Figure 4.9: **Diagram of the entire layout.** Shown are the paths used by the excitation laser (solid light-blue lines) and the phase light (solid dark-blue lines), which has a frequency offset of $\approx 10MHz$ with respect to the excitation laser. The frequency offset is generated using different frequency modulation set-points for the acousto-optic modulators (AOM) in the excitation and phase path respectively.

is reflected off the diamond surface and since it has (close to) orthogonal polarization with the NV centers emitted photons it can be separated from the single photons using a polarizing beam-splitter (PBS). Afterwards, the weak reflected excitation pulse interferes with a strong laser pulse from the other arm with the frequency offset. The beat signal is measured with a photodiode and the optical phase difference is extracted using an electronic reference signal. The middle node has two local interferometers, one for each link. When all separate interferometers are stabilized, the paths of the excitation light and the single photons used for entanglement heralding will be phase stable.

TECHNICAL DESCRIPTION OF THE LOCAL INTERFEROMETER

For all the local interferometers we use a heterodyne phase detection scheme. A diagram of the optics and electronics is plotted in Figure 4.11. For each entanglement link (Alice-Bob and Bob-Charlie) the phase and excitation light are provided by the outer nodes (Alice and Charlie). To generate the known 10 MHz frequency offset between the light paths, we take advantage of the acousto-optic modulators (AOMs) we use to generate light pulses. By driving two AOMs at respectively 200 MHz and 210 MHz, we establish the required frequency difference between the light paths. Part of the RF signals used to drive the AOMs are tapped off and combined in a mixer to obtain an electronic reference signal. The light from the AOMs is launched in a free space path with several optical elements. The first polarizing beam-splitter (PBS) ensures the phase light to be linearly polarized. The second PBS separates the reflected excitation light from the single photons. At this point the phase-reference light and the reflected excitation light have

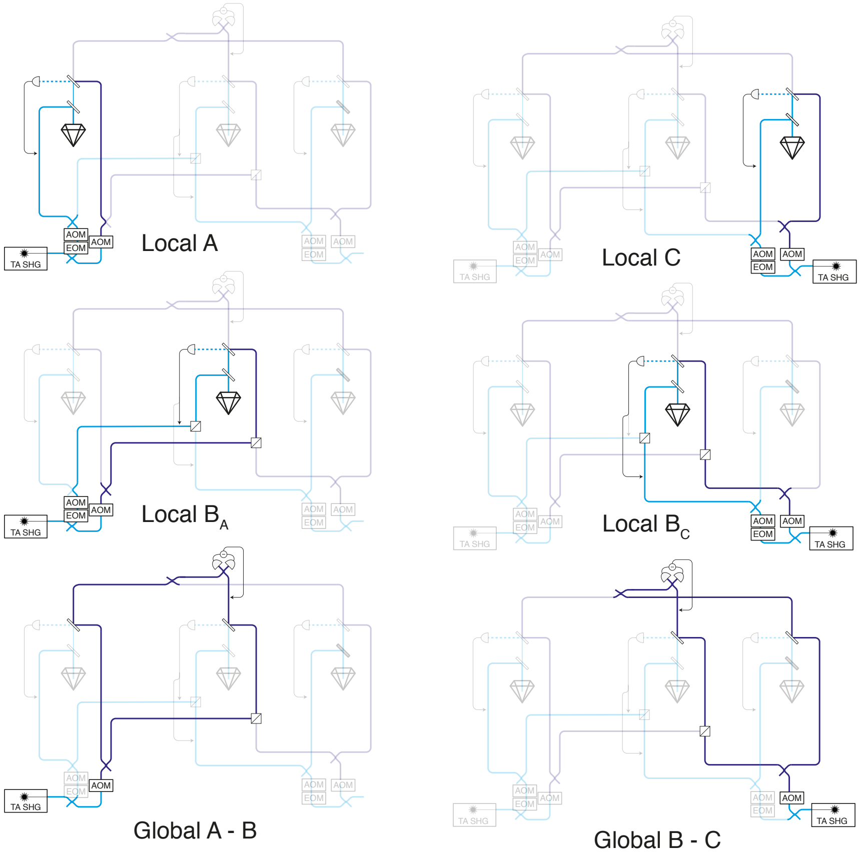

Figure 4.10: **Diagrams of the six interferometers in which the optical set-up is divided.** For the local interferometers, the heterodyne beat signal (dashed light-blue lines) is measured, compared to an electronic reference signal and feedback is applied to the optical path via piezo-electric mounted mirrors. For the global interferometers, the interference is measured by the single photon detectors. The detectors are shared for the two entanglement links using a beam-splitter that combines the photons from Alice with photons from Charlie. A feedback signal is applied to a fiber stretcher which is also shared by the two global interferometers.

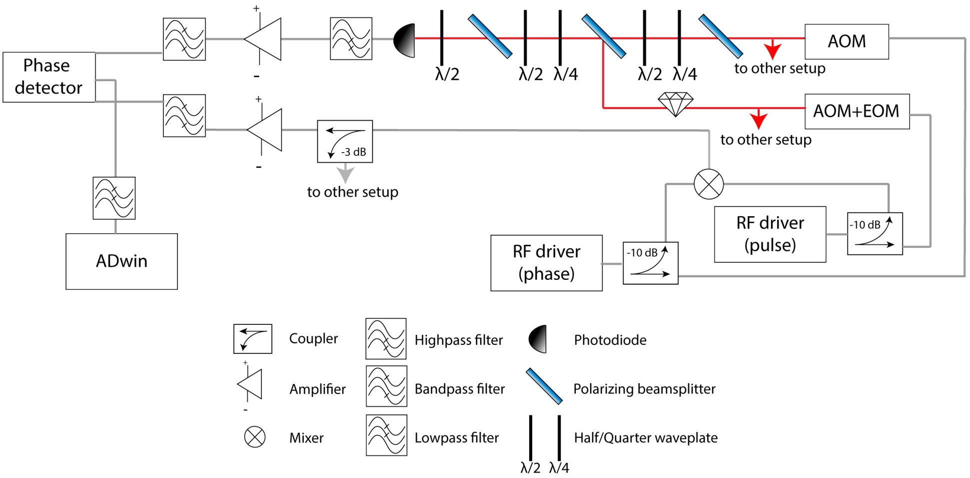

Figure 4.11: **Diagram of the electronics and optics for a local interferometer using a heterodyne phase detection scheme.** Both the electronic reference signal and the excitation light are shared with another setup.

orthogonal polarization. The waveplates in front of the third beam-splitter rotate their polarization such that they can be interfered on the third PBS. This interference leads to a beating signal that can be detected with the photodiode. Consequently, the beating signal is filtered, amplified and, together with the electronic reference signal, used as inputs for the phase detector (Mini-Circuits ZRDP-1+). The output of the phase detector is filtered and impedance matched to an analog to digital converter (ADC) input of the micro-controller, the ADwin.

TIMINGS

The phase stabilization requires synchronization between the different nodes. Nodes A and C provide the phase and excitation light, but all nodes measure the phase of at least one local interferometer. Some of the detectors used for the phase measurements are shared among different interferometers, so not all measurements can be done at the same time. Figure 4.12 shows how the various phase stabilization cycles are interleaved

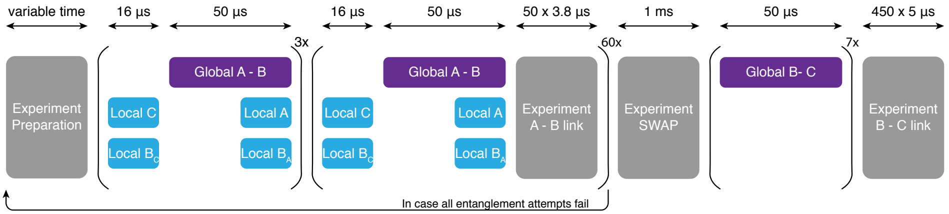

Figure 4.12: **Overview of the timings related to the phase stabilization.** Experimental time (gray blocks) is interleaved with phase stabilization cycles, which include a phase measurement and a feedback. The subscript to B indicates which light is used, either from setup A or C. The local phase stabilization of A and B_A and the global phase stabilization A–B can be performed at the same time since they use the same light sources.

with entanglement generation time.

The choice of free evolution time is governed by the noise sources in the different parts of the system. The local interferometer of node A experiences noise with high frequency components (compared to the other intereferometers) hence the free running time must be short enough to achieve the necessary feedback bandwith. The duration of the preparation part of the experiment, which includes charge and resonance checks, as well as synchronization steps between nodes, can vary from approximately 50 μs to a few seconds. When the phase is completely scrambled due to a too long free running time, it is not possible to reach the set-point in a single feedback round. For this reason we start with multiple rounds of phase stabilization without any free evolution time in between.

PHASE STABILITY

To characterize the performance of the phase stabilization we look at three different aspects: the free evolution of the phase without any stabilization, the frequency spectrum of the noise and the distribution of the phase while actively stabilizing. All the results for the six interferometers are plotted in Figure 4.13 (see Fig. 4.10 for the labeling). The differences in performance can be explained by the noise sources present in our experimental lay-out. We identify two main sources of noise: the relatively noisy fiber connection between nodes A and B and the positioning stages of each node. The three nodes are built in two separates rooms and we use optical fibers (30 m) to connect node A to node B. All nodes have a microscope objective for optically accessing the diamond samples. On node B and C this microscope objective is mounted on a piezo-electric stage. For node A the design is different: here the sample is mounted on a piezo-stack and the microscope objective is fixed. All these piezo-electric stages are susceptible to the vibrations generated by the operation of the cryostats.

The sample stage of node A cause relatively-strong high-frequency (> 500 Hz) noise; the microscope objective stage of nodes B and C cause lower-frequency noise and the optical fiber connection between nodes A and B causes relatively-strong low-frequency components. In the experimental sequence we interleave experimental time with rounds of phase stabilization. With the used timings (see Fig. 4.12) we are able to stabilize frequencies ≤ 500 Hz. Due to its relatively high-frequency components, the noise of the local interferometer of node A is the limiting factor in terms of phase stability of the overall apparatus. We expect that fixing the sample to the cold-finger of the cryostat, and only moving the microscope objective (like we do on nodes B and C) will allow us to lower the phase noise on node A in the future.

ENTANGLED-STATE PHASE DRIFTS

While the phase stabilization scheme allows us to access the entangled state generated by the single photon protocol by fixing the phase $\Delta\theta$, we observe that the phase of the generated entangled state undergoes small drifts on a timescale of hours. That is, even though all the interferometers are stabilized to the same value, the phase of the entangled state will slowly drift by $\approx 10^o$/hour. We hypothesize that these drifts are due to the relative position of the microscope objective and the NV center: while the light used for phase stabilization is reflected off the diamond surface, the NV-emitted photons are

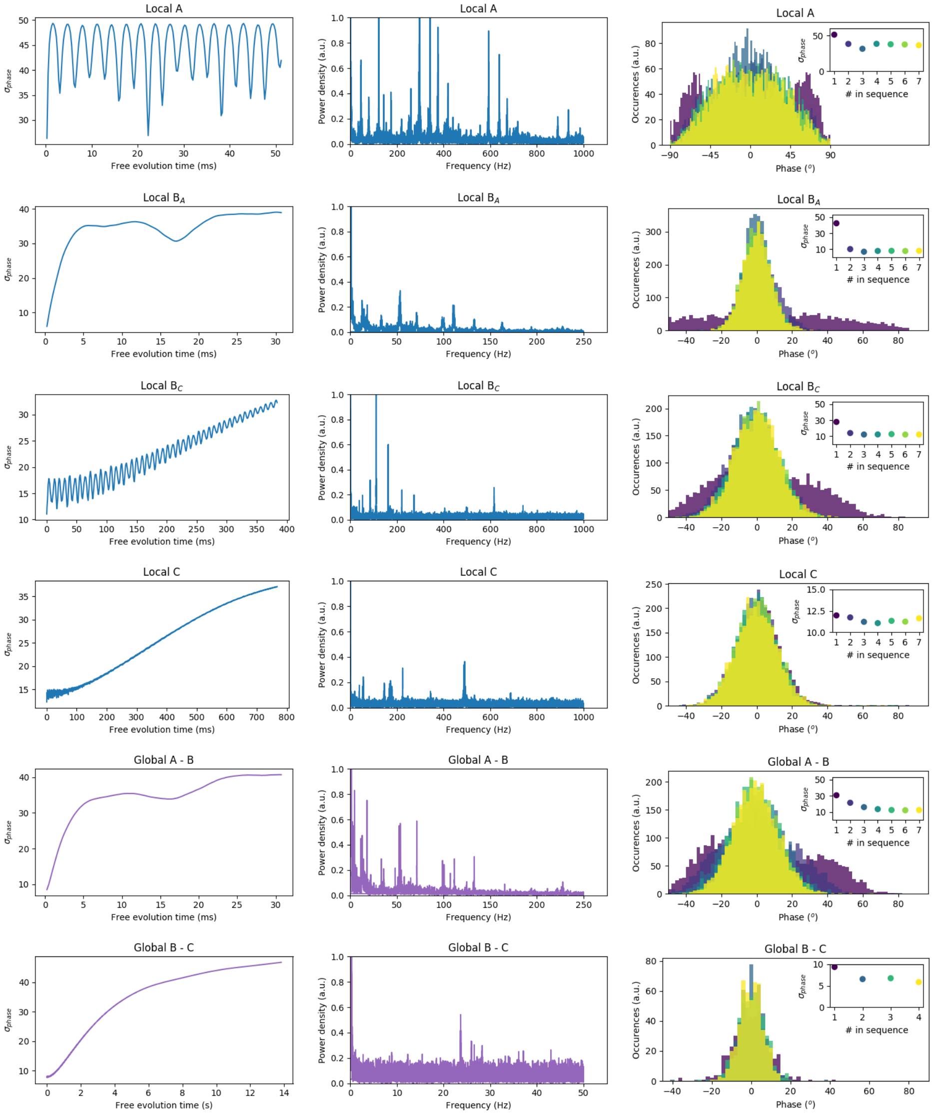

Figure 4.13: **Characterization of the phase stabilization of all six interferometers. (Left)** Standard deviation of the measured phase while changing the free evolution time. **(Center)** Frequency spectrum of the measured noise. **(Right)** Phase distribution for the different rounds of phase stabilization. **(Insets)** Standard deviation of the phase per stabilization round.

generated inside the diamond. Small changes in distance and angle of the microscope objective would not lead to observable differences in the fluorescence measurement we use for position optimization, but may slightly alter the path the photons have to travel. To solve this challenge, after every position optimization (≈ once every hour), we re-calibrate the phase of the generated entangled state (≈ 5 minute measurement per link). More robust positioning systems (both for the sample and the microscope objective) may reduce the phase drifts and alleviate the need for entangled-phase re-calibration.

4.6.4. SINGLE-SHOT READOUT CORRECTION

We correct tomography-related single-shot readouts (SSROs) for known error in order to obtain a reliable estimate of the actual generated states.

SINGLE QUBIT CASE

For a single qubit:

$$\vec{m} = \hat{R}\,\vec{p}, \tag{4.10}$$

where $\vec{p} = (p_0, p_1)^T$ is the (column) vector of expected populations, $\vec{m} = (m_0, m_1)^T$ is the (column) vector of measured populations, and

$$\hat{R} = \begin{pmatrix} r_{00} & r_{01} \\ r_{10} & r_{11} \end{pmatrix} = \begin{pmatrix} F_0 & 1-F_1 \\ 1-F_0 & F_1 \end{pmatrix}$$

is the SSRO operator that connects the two. For example:

$$m_0 = F_0 p_0 + (1-F_1) p_1,$$

i.e. the measured population in $|0\rangle$ is given by the correctly assigned population in $|0\rangle$ plus the incorrectly assigned population in $|1\rangle$. From Eq. 4.10 it follows that:

$$\vec{p} = \hat{R}^{-1}\vec{m}, \tag{4.11}$$

which is what we use in practice to apply the readout correction. This allow us to obtain the vector of expected populations given the measured populations and the SSRO error operator. Experimentally we cannot directly measure $\vec{m}$. We measure events in which the communication qubit is either in $|0\rangle$ or in $|1\rangle$. We repeat this process N times, obtaining N_0 times the outcome $|0\rangle$ and N_1 times the outcome $|1\rangle$. From this we estimate the measured populations $\vec{m}$:

$$m_0 = N_0/N, m_1 = N_1/N \tag{4.12}$$

The probability distribution of the number of events N_0 is a Binomial distribution with expected value Nm_0 and variance $Nm_0(1-m_0)$. From this it is possible to calculate the experimental value and uncertainty for m_0 (and m_1):

$$m_0 = N_0/N \tag{4.13}$$

$$m_1 = 1 - m_0 \tag{4.14}$$

$$\sigma_{m_0} = \sigma_{m_1} = \sqrt{\frac{m_0}{N}(1-m_0)} \tag{4.15}$$

The covariance between m_0 and m_1 is:

$$\mathrm{Cov}(m_0, m_1) = -\frac{m_0(1-m_0)}{N} \tag{4.16}$$

Once Eq. 4.11 has been calculated it is possible to evaluate the expectation value of $\vec{p}$ and its uncertainty. In the one qubit scenario it is easy to invert the expression analytically:

$$p_0 = \frac{F_1\ m_0 + (F_1-1)\ m_1}{F_0+F_1-1} = \frac{F_1+m_0-1}{F_0+F_1-1} \tag{4.17}$$

$$p_1 = \frac{(F_0-1)\ m_0 + F_0\ m_1}{F_0+F_1-1} = \frac{F_0-m_0}{F_0+F_1-1} = 1-p_0 \tag{4.18}$$

$$\sigma_{p_0} = \sigma_{p_1} = \frac{\sigma_{m_0}}{F_0+F_1-1} \tag{4.19}$$

and it is straightforward to propagate uncertainties in $F_{0/1}$ to p_0 and p_1.

TWO AND THREE QUBIT CASE

For two (and more) qubits, the measurement outcomes will be distributed according to a Multinomial distribution (as opposed to a Binomial). While the expectation values of $p_0, \ldots, p_i$ can still be computed analytically relatively straightforwardly, their uncertainties need to take into account the non-trivial covariances in the m_i. Additionally, taking into account uncertainties in the $F_{0/1}$ makes the error propagation even more tedious. We therefore use a Monte Carlo simulation that takes into account the Multinomial distribution as well as the $F_{0/1}$ of each setup to estimate uncertainties on the correlation measurements and the state fidelities, without having to assume normality of the data. The code to run the Monte Carlo simulation is included in the Jupyter notebooks that produce the figures of the main text [47].

4.6.5. PHASE FEED-FORWARD ON THE MEMORY QUBIT

The nuclear spin memory qubit of Bob precesses at a frequency that depends on the spin state of the electronic spin (the communication qubit). Throughout the experimental sequence we keep track of the phase acquired by the nuclear spin to be able to readout and apply gates in the correct bases. While most operations are deterministic in time (nuclear spin initialisation, gates on the electronic spin, etc.) and the phase evolution of the nuclear spin can be calculated in advance, entanglement generation is a probabilistic process. This means that it is not known in advance how long the entanglement operation (number of entanglement attempts) is going to take, and therefore how much phase the nuclear spin is going to acquire. To solve this challenge, we implement a phase feed-forward mechanism that applies a Z-rotation to the nuclear spin that cancels this acquired phase. Since the used Arbitrary Waveform Generator (AWG) only has limited real-time programming capability, we implement this mechanism via a real-time interaction between our node micro-controller (ADwin) and the AWG. Once entanglement is heralded between Bob and Charlie, the AWG of Bob jumps out of the entanglement generation subroutine and starts an XY4 decoupling sequence on the communication qubit. During this XY4, the AWG interacts with the ADwin of Bob (which has recorded how much phase the nuclear spin has acquired during the entanglement operation) to select, via a binary decision tree, the time in between microwave pulses. The binary decision tree allows us to vary the (additional) duration of the XY4 element in steps of 2 ns up to 512 ns, which is more than a 2π precession for the nuclear spin (τ_L =490 ns, feed-forward resolution $\approx 1.5^o$). Regardless of the inter-pulse time selected, the communication qubit will be decoupled. Consequently, the needed additional phase to re-phase the nuclear spin can be conveniently set via the length of the XY4 sequence. We pre-compile the timings that the ADwin will communicate to the AWG to reduce the computational load on the ADwin. We anticipate that an AWG with an integrated programmable FPGA will be able to completely take over the task of phase tracking without need for interaction with the node micro-controller, reducing experimental overhead.

4.6.6. MEMORY QUBIT LIFETIME AND INCREASED MAGNETIC FIELD

An important resource in our experiments is the ability to store entanglement in the nuclear spin memory qubit of Bob while performing further operations on the node. While we have implemented methods to keep track and actively compensate for the phase acquired during entanglement generation (see previous section), additional dephasing may occur. The major source of nuclear spin dephasing during entanglement generation was found to be [30] failed electronic spin control (initialization errors or MW pulse errors).

An entanglement attempt can be broken into the following pieces: communication qubit reset (via optical pumping), MW pulse that creates the communication qubit superposition (named in the following the α pulse), optical excitation pulse that creates the spin-photon entanglement, and a decoupling MW π pulse. The time τ between the α and the de-coupling pulse is chosen such that it equals the time between the decoupling pulse and the average reset time in the subsequent entanglement attempt (see Ref. [30] for details). This ensures that regardless of its initial state, the communication qubit spends an equal amount of time in the $|0\rangle$ and $|1\rangle$ states. However, an error in the MW π pulse will result in an unknown acquired phase on the nuclear spin and lead to dephasing. Previous work [30] suggested that such dephasing can be mitigated when working at a higher magnetic field, which allows for a shorter spacing between subsequent MW pulses.

In order to work at higher fields we have installed a stronger permanent magnet inside the cryostat of Bob reaching a field of 189 mT at the location of the NV center. At such fields, temperature fluctuations of the magnet, mainly due to the MW pulses applied to the sample, can result in a significant change of the magnetic field amplitude. Hence, we stabilize the sample holder via an active feedback loop, ensuring a stable temperature of the permanent magnet. We reach a stability of 1 μT, which results in a maximum variation of the nuclear spin precession frequency of $\approx$ 10 Hz, one order of magnitude below the dephasing rate due to interactions with other spins in its environment.

These improvements allow us to shorten the interpulse spacing to 942 ns, limited by the waiting time after the optical excitation pulse that we need to include in order to allow the AWG to respond in real time to a successful entanglement attempt and jump out of the entangling sequence. As Figure 4.3 of the main text shows, a similar nuclear memory lifetime is observed when applying entanglement attempts or when idling. This shows that the lifetime of the memory qubit, in our magnetic field regime, is mainly limited by natural dephasing and not by electronic spin control errors. We fit the two decays with the following function:

$$f(N) = A\exp\left(-\left(\frac{N}{N_{1/e}}\right)^{n}\right), \tag{4.20}$$

with N the number of entanglement generation attempts, $N_{1/e}$ the N at which the Bloch vector length has decayed to $1/e$ of its initial value A, and n the exponent of the decay. The results of the fit are reported in Table 4.5. For the results *Without ent. gen.* the entanglement generation attempt is replaced by the equivalent free evolution time.

Table 4.5: **Fit results of memory qubit lifetime curves.** Fit results for the curves displayed in Figure 4.3 with and without entanglement generation (Ent. Gen.). See section 4.6.6 for details on the fitting function.

	With Ent. Gen.	Without Ent. Gen.
$N_{1/e}$	1843(32)	2042(36)
n	1.37(5)	1.61(6)
A	0.895(6)	0.885(6)

4.6.7. MICROWAVE PULSE FIDELITY

Errors in the MW pulses can limit the control of the communication qubit as well as induce decoherence on the nuclear spin memory qubit [30]. We use Hermite MW pulse envelopes [29] to perform rotations of the communication qubit spin:

$$h(t) = \left(1 - p\left(\frac{t}{T}\right)^{2}\right)e^{-\left(\frac{t}{T}\right)^{2}}, \tag{4.21}$$

where p affects the shape of the pulse and T changes the length of the pulse. The pulses get distorted by the transmission line before they get to the sample. We apply a linear pre-distortion in frequency domain to compensate part of the error via the following IQ signals:

$$I = a\cdot h(t) \tag{4.22}$$

$$Q = ab\frac{t}{\pi T^{2}}\left(p + 1 - p\left(\frac{t}{T}\right)^{2}\right)e^{-\left(\frac{t}{T}\right)^{2}}, \tag{4.23}$$

where a is the amplitude of the pulse and b is the skewness (slope) of the pre-distortion in frequency domain.

The MW π-pulses are calibrated by initializing the qubit in the $|0\rangle$ state, applying an odd number of consecutive pulses and reading out the final state. If the pulses were perfect one would measure $|1\rangle$ as outcome. The effect of the skewness on the pulse fidelity is investigated with a two dimensional scan; evaluating the fidelity for pulses with different amplitudes (a) and skewness (b). Figure 4.14 shows an example of such a scan, where it

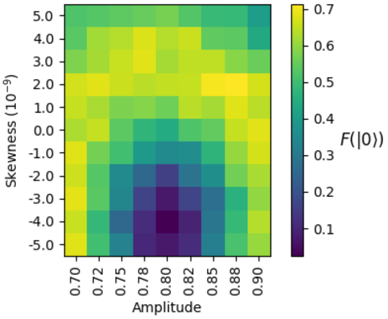

Figure 4.14: **Calibrating the pre-distorted microwave (MW) Hermite pulses**. The π pulses are calibrated by applying 11 sequential pulses: the probability of being in $|0\rangle$ at the end of the sequence is measured for different amplitudes (a) and skewness (b) of the Hermite pulse. The linear frequency pre-distortion allows us to achieve lower errors for the MW pulses.

is clear one can calibrate a and b almost independently. We find that different set-ups require different levels of pre-distortion b, ranging from e-11 to e-8. We estimate that the current errors of our MW pulses are between 0.1 % and 1 % for all the three nodes.

4.6.8. CLASSICAL COMMUNICATION

The three nodes can share information in several ways. The slowest method is based on Python socket interfaces between the measurement computers that allow us to share necessary values and information at a rate of approximately 10 Hz; this method is used for example to frequency lock the lasers, to coordinate calibrations on all nodes from a single computer and to share and record environmental data such as the temperature in the different laboratories. The second, and fastest, method is a direct connection between the micro-controller and the AWGs. This enables the triggering of all the AWGs from a single node, reducing jitter on the output waveforms. The third method is implemented on the micro-controllers and is used for the feed-forward operations across the nodes. Each micro-controller has one input and one output communication port (physically it is a normal digital input-output coaxial port). Bob, which receives signals from both Alice and Charlie, has a digital summing box (OR gate) at its input port, that combines the signals coming from the other two nodes. We designed the experimental sequence such that it is clear who sent a specific message depending on when it arrives. Messages are sent over an off-the-shelf coaxial cable, using a serial communication scheme, with an average bit interval of 60 ns(the shortest the micro-controller can achieve). At the input port of each micro-controller, a fast edge detection (100 MHz) stores changes in the signal level (and the time at which they occur). It is therefore possible to reconstruct what pattern (i.e. message) was sent from one node to the other, directly on the micro-controller. Sending a message takes up to 300 ns (we send up to 5 bits at a time). Receiving and decoding take up to 2 μs combined. A flowchart of the communication steps between the micro-controllers used in the networks protocols demonstrated in the main text is shown in Figure 4.15.

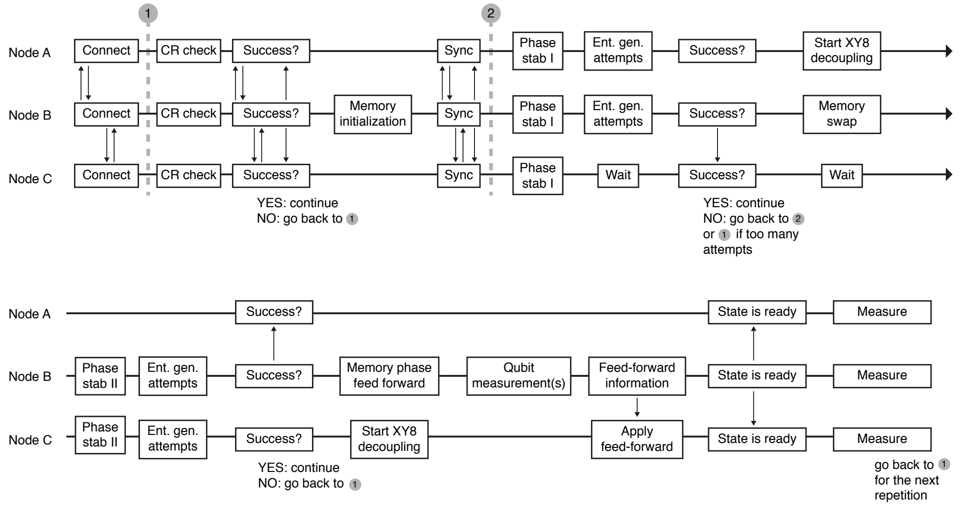

Figure 4.15: **Flowchart of the network protocols demonstrations.** The micro-controllers of the three nodes exchange information to synchronize the experimental sequence and apply feed-forward operations. Vertical lines between the nodes represent communication steps.

4.6.9. FEED-FORWARD OPERATIONS BETWEEN NODES

We implement the feed-forward operations needed for our experimental protocols by combining the classical communication just discussed with a real-time pulse selection sequence by the micro-controller on the AWG. For both network protocols demonstrated we need to apply gates on the communication qubit of Charlie conditional on measurement outcomes at Bob. Once Bob has performed the required readout operations (on the communication qubit for the GHZ state generation or on both qubits for the entanglement swapping) it combines the readout results with the Bell states generation outcomes (i.e. which detectors clicked in the A-B and B-C entanglement generation) to obtain one of four possible feed-forward messages. Combining this information on Bob is an optimization of our communication resources; we could, alternatively, send the bits of information one by one to Charlie and combine the information there should that be a requirement of the protocol (for example in a blind quantum computation scenario). At this point a *FAIL* message could also be sent from Bob to all the nodes in order to abort the whole sequence, for example if the Bell State Measurement result is not the one that gives high-fidelity (see main text). We choose to not send *FAIL* messages and instead continue with the protocol to be able to assess the protocol performance for the less faithful Bell State Measurement outcomes (see Fig. 5C of the main text). In the meantime, Charlie has been applying an XY8 decoupling sequence to the communication qubit to protect its coherence while Bob performed the readout operations. Once Charlie receives the feed-forward information, its micro-controller starts a decision-tree sequence with its AWG to select the required microwave pulse-sequence. This decision tree is incorporated into an XY8 block of the AWG, such that the slow response time of the AWG (1 μs per bit of information) does not affect the coherence of the communication qubit. The microwave pulse sequence selected via the decision tree is appended to the aforementioned XY8 block. After the feed-forward operations are performed, the delivery of the states by the network protocol is completed. Finally, the delivered states are analyzed using a readout sequence (composed of an optional basis rotation and state readout).

4.6.10. DATA ACQUISITION AND CALIBRATIONS

The data supporting the protocol demonstrations in the main text (Figures 4C, 5B, 5C) was gathered in the month of October 2020. Due to the restrictions imposed by the COVID19 pandemic, we operated the setups remotely (from home) and went to the laboratories only when something needed in-situ intervention (like a broken power-supply).

The data has been collected in blocks of approximately 1 hour, interleaved by calibration routines of approximately 20 minutes. For the GHZ state generation protocol we set the target number of data points at 2000. For the entanglement swapping we set the target number of data points at 4000. We stopped the experiment once the measurement block was completed in which the target number of data points was surpassed.

For the GHZ state generation we acquired 55 blocks over 10 days (effective measurement time ≈ 50 hours), obtaining 2028 events, equivalent to a rate of $r_{\mathrm{GHZ}} \approx (90\mathrm{s})^{-1}$.

For the entanglement swapping demonstration we acquired 53 blocks over 7 days (effective measurement time ≈ 45 hours), obtaining 853 events with BSM result “00", equivalent to a rate of $r_{\mathrm{swapping}} \approx (3\mathrm{min})^{-1}$. The other BSM results were: “01”: 1030 events, “10”: 1004 events, “11”: 1168 events. The ratio of events between the BSM results matches the readout characteristics of node B: measured (expected) share of the events, 0.21 : 0.25 : 0.25 : 0.29 (0.23 : 0.25 : 0.25 : 0.27). Combining all the BSM results we obtained a total of 4055 events, equivalent to a rate $r'_{\mathrm{swapping}} \approx (40\mathrm{s})^{-1}$.

Every three measurement blocks we performed a fidelity check on the entangled states between Alice-Bob and Bob-Charlie at the target α (total duration 20 minutes). These fidelity checks, combined over the GHZ and Entanglement Swapping datasets, are used for Figure 4.2E of the main text. We performed a total of 58 fidelity checks, that combined generated: 24197 Ψ^+_{AB} events, 25057 Ψ^-_{AB} events, 26383 Ψ^+_{BC} events and 27459 Ψ^-_{BC} events. The asymmetry in the number of events between the Ψ^+ and the Ψ^- states is due in part to the beam-splitter having a non ideal splitting ratio (0.493 : 0.507), to a slight difference in detector efficiencies (≈ 1%) and to the brightnesses ($\alpha\ p_{\mathrm{det}}$) of the two setups involved not being completely balanced. The asymmetry between the number of events for the Ψ_{AB} and the Ψ_{BC} states is due to the different probability for node B to be in the wrong charge state (NV^0) at the end of the sequence for the two links. To obtain a reliable estimate of the fidelities of the Bell states, we discard events in which a CR (charge and resonance) check performed after readout gives a negative result. We remark that, as mentioned in the main text, we do not perform such an operation for the network protocols demonstrations, which are free from any post-selection. For the GHZ state generation, by heralding only on the $|0\rangle$ readout outcome of the communication qubit of Bob, we automatically reject events in which the NV center of Bob was either in the wrong charge state or off resonant. For the Entanglement Swapping demonstration, we perform a CR check after the Bell state measurement is performed on node B, and we herald success of the whole protocol only if this final CR check gives a positive result. We find that the test gives a positive result in approximately 90% of the cases.

4.6.11. EXPERIMENTAL MONITORING

Analogous to what reported in section J of the SI of Ref. [46], we implement checks while the experiment is running to ensure that the nodes are performing as expected. If one of the checks does not pass, we mark all future data to be disregarded (until the check is passed) and / or pause the experiment to perform further calibrations. Following is a list of all the checks that we use to mark future data to be disregarded (if they don't pass):

- Check that the measured phase of each interferometer is below 50^o before the last piezo feedback is performed.
- Check that the number of photons collected during the qubit reset by optical pumping part of the entanglement generation sequence, averaged over the preceding second, is above a pre-set threshold. If the check does not pass within a matter of seconds, we pause the experiment and scan the laser frequency to find back the qubit reset transition frequency.
- Check that the number of photons collected during the spin-photon entanglement part of the entanglement generation sequence, averaged over the preceding second, is above a pre-set threshold. If the check does not pass within a matter of seconds, we pause the experiment and scan the bias voltage of the setup.

REFERENCES

[1] H. J. Kimble, *The quantum internet,* Nature **453**, 1023 (2008).

[2] S. Wehner, D. Elkouss, and R. Hanson, *Quantum internet: A vision for the road ahead,* Science **362** (2018).

[3] L. Jiang, J. M. Taylor, A. S. Sørensen, and M. D. Lukin, *Distributed quantum computation based on small quantum registers,* Physical Review A **76**, 1 (2007).

[4] A. Broadbent, J. Fitzsimons, and E. Kashefi, *Universal blind quantum computation,* Proceedings - Annual IEEE Symposium on Foundations of Computer Science, FOCS , 517 (2009).

[5] D. Gottesman, T. Jennewein, and S. Croke, *Longer-baseline telescopes using quantum repeaters,* Physical Review Letters **109**, 1 (2012).

[6] A. Ekert and R. Renner, *The ultimate physical limits of privacy,* Nature **507**, 443 (2014).

[7] N. H. Nickerson, J. F. Fitzsimons, and S. C. Benjamin, *Freely scalable quantum technologies using cells of 5-to-50 qubits with very lossy and noisy photonic links,* Physical Review X **4**, 1 (2014).

[8] P. Kómár, E. M. Kessler, M. Bishof, L. Jiang, A. S. Sørensen, J. Ye, and M. D. Lukin, *A quantum network of clocks,* Nature Physics **10**, 582 (2014).

[9] D. L. Moehring, P. Maunz, S. Olmschenk, K. C. Younge, D. N. Matsukevich, L. M. Duan, and C. Monroe, *Entanglement of single-atom quantum bits at a distance,* Nature **449**, 68 (2007).

[10] S. Ritter, C. Nölleke, C. Hahn, A. Reiserer, A. Neuzner, M. Uphoff, M. Mücke, E. Figueroa, J. Bochmann, and G. Rempe, *An elementary quantum network of single atoms in optical cavities,* Nature **484**, 195 (2012).

[11] J. Hofmann, M. Krug, N. Ortegel, L. Gérard, and M. Weber, *Heralded Entanglement Between Widely Separated Atoms,* Science **337**, 72 (2012).

[12] L. J. Stephenson, D. P. Nadlinger, B. C. Nichol, S. An, P. Drmota, T. G. Ballance, K. Thirumalai, J. F. Goodwin, D. M. Lucas, and C. J. Ballance, *High-Rate, High-Fidelity Entanglement of Qubits Across an Elementary Quantum Network,* Physical Review Letters **124**, 1 (2020).

[13] H. Bernien, B. Hensen, W. Pfaff, G. Koolstra, M. S. Blok, L. Robledo, T. H. Taminiau, M. Markham, D. J. Twitchen, L. Childress, and R. Hanson, *Heralded entanglement between solid-state qubits separated by three metres,* Nature **497**, 86 (2013).

[14] P. C. Humphreys, N. Kalb, J. P. Morits, R. N. Schouten, R. F. Vermeulen, D. J. Twitchen, M. Markham, and R. Hanson, *Deterministic delivery of remote entanglement on a quantum network,* Nature **558**, 268 (2018).

[15] A. Delteil, Z. Sun, W. B. Gao, E. Togan, S. Faelt, and A. Imamoglu, *Generation of heralded entanglement between distant hole spins,* Nature Physics **12**, 218 (2016).

[16] R. Stockill, M. J. Stanley, L. Huthmacher, E. Clarke, M. Hugues, A. J. Miller, C. Matthiesen, C. Le Gall, and M. Atatüre, *Phase-Tuned Entangled State Generation between Distant Spin Qubits,* Physical Review Letters **119**, 1 (2017).

[17] P. Maunz, S. Olmschenk, D. Hayes, D. N. Matsukevich, L. M. Duan, and C. Monroe, *Heralded quantum gate between remote quantum memories,* Physical Review Letters **102**, 2 (2009).

[18] S. Daiß, S. Langenfeld, S. Welte, E. Distante, P. Thomas, L. Hartung, O. Morin, and G. Rempe, *A quantum-logic gate between distant quantum-network modules,* Science **371**, 614 (2021).

[19] N. Kalb, A. A. Reiserer, P. C. Humphreys, J. J. Bakermans, S. J. Kamerling, N. H. Nickerson, S. C. Benjamin, D. J. Twitchen, M. Markham, and R. Hanson, *Entanglement distillation between solid-state quantum network nodes,* Science **356**, 928 (2017).

[20] M. Christandl and S. Wehner, *Quantum Anonymous Transmissions,* in *Advances in Cryptology - ASIACRYPT 2005* (2005) pp. 217–235.

[21] M. Hillery, V. Bužek, and A. Berthiaume, *Quantum secret sharing,* Physical Review A **59**, 1829 (1999).

[22] A. Ambainis, H. Buhrman, Y. Dodis, and H. Röhrig, *Multiparty quantum coin flipping,* Proceedings of the Annual IEEE Conference on Computational Complexity **19**, 250 (2004).

[23] H. Briegel, W. Dür, J. I. Cirac, and P. Zoller, *Quantum Repeaters The Role of Imperfect Local Operations in Quantum Communication,* Physical Review Letters **81**, 5932 (1998).

[24] M. Pant, H. Krovi, D. Towsley, L. Tassiulas, L. Jiang, P. Basu, D. Englund, and S. Guha, *Routing entanglement in the quantum internet,* npj Quantum Information **5**, 1 (2019).

[25] D. Bouwmeester, J.-w. Pan, M. Daniell, H. Weinfurter, and A. Zeilinger, *Observation of Three-Photon Greenberger-Horne-Zeilinger Entanglement,* Physical Review Letters **82**, 1 (1999).

[26] B. Jing, X. J. Wang, Y. Yu, P. F. Sun, Y. Jiang, S. J. Yang, W. H. Jiang, X. Y. Luo, J. Zhang, X. Jiang, X. H. Bao, and J. W. Pan, *Entanglement of three quantum memories via interference of three single photons,* Nature Photonics **13**, 210 (2019).

[27] C. Cabrillo, J. I. Cirac, P. Garcia-Fernandez, and P. Zoller, *Creation of entangled states of distant atoms by interference,* Physical Review A **59**, 1025 (1999).

[28] S. Bose, P. L. Knight, M. B. Plenio, and V. Vedral, *Proposal for teleportation of an atomic state via cavity decay,* Physical Review Letters **83**, 5158 (1999).

[29] C. E. Bradley, J. Randall, M. H. Abobeih, R. C. Berrevoets, M. J. Degen, M. A. Bakker, M. Markham, D. J. Twitchen, and T. H. Taminiau, *A Ten-Qubit Solid-State Spin Register with Quantum Memory up to One Minute,* Physical Review X **9**, 31045 (2019).

[30] N. Kalb, P. C. Humphreys, J. J. Slim, and R. Hanson, *Dephasing mechanisms of diamond-based nuclear-spin memories for quantum networks,* Physical Review A **97**, 1 (2018).

[31] O. Gühne and G. Tóth, *Entanglement detection,* Physics Reports **474**, 1 (2009).

[32] L. Jiang, J. S. Hodges, J. R. Maze, P. Maurer, J. M. Taylor, D. G. Cory, P. R. Hemmer, R. L. Walsworth, A. Yacoby, A. S. Zibrov, and M. D. Lukin, *Repetitive readout of a single electronic spin via quantum logic with nuclear spin ancillae,* Science **326**, 267 (2009).

[33] D. Riedel, I. Söllner, B. J. Shields, S. Starosielec, P. Appel, E. Neu, P. Maletinsky, and R. J. Warburton, *Deterministic enhancement of coherent photon generation from a nitrogen-vacancy center in ultrapure diamond,* Physical Review X **7**, 1 (2017).

[34] E. Janitz, M. K. Bhaskar, and L. Childress, *Cavity quantum electrodynamics with color centers in diamond,* Optica **7**, 1232 (2020).

[35] M. Ruf, M. J. Weaver, S. B. Van Dam, and R. Hanson, *Resonant Excitation and Purcell Enhancement of Coherent Nitrogen-Vacancy Centers Coupled to a Fabry-Perot Microcavity,* Physical Review Applied **15**, 1 (2021).

[36] S. Baier, C. E. Bradley, T. Middelburg, V. V. Dobrovitski, T. H. Taminiau, and R. Hanson, *Orbital and Spin Dynamics of Single Neutrally-Charged Nitrogen-Vacancy Centers in Diamond,* Physical Review Letters **125**, 1 (2020).

[37] R. Van Meter, *Quantum Networking* (John Wiley & Sons, Inc., 2014).

[38] A. Pirker and W. Dür, *A quantum network stack and protocols for reliable entanglement-based networks,* New Journal of Physics **21** (2019).

[39] W. Kozlowski and S. Wehner, *Towards Large-Scale Quantum Networks,* in *NANOCOM* (2019).

[40] A. Dahlberg, M. Skrzypczyk, T. Coopmans, L. Wubben, F. Rozpdek, M. Pompili, A. Stolk, P. Pawelczak, R. Knegjens, J. De Oliveira Filho, R. Hanson, and S. Wehner, *A link layer protocol for quantum networks,* SIGCOMM 2019 - Proceedings of the 2019 Conference of the ACM Special Interest Group on Data Communication , 159 (2019).

[41] A. Tchebotareva, S. L. Hermans, P. C. Humphreys, D. Voigt, P. J. Harmsma, L. K. Cheng, A. L. Verlaan, N. Dijkhuizen, W. De Jong, A. Dréau, and R. Hanson, *Entanglement between a Diamond Spin Qubit and a Photonic Time-Bin Qubit at Telecom Wavelength,* Physical Review Letters **123**, 1 (2019).

[42] B. C. Rose, D. Huang, Z. H. Zhang, P. Stevenson, A. M. Tyryshkin, S. Sangtawesin, S. Srinivasan, L. Loudin, M. L. Markham, A. M. Edmonds, D. J. Twitchen, S. A. Lyon, and N. P. De Leon, *Observation of an environmentally insensitive solid-state spin defect in diamond,* Science **361**, 60 (2018).

[43] C. T. Nguyen, D. D. Sukachev, M. K. Bhaskar, B. MacHielse, D. S. Levonian, E. N. Knall, P. Stroganov, R. Riedinger, H. Park, M. Lončar, and M. D. Lukin, *Quantum Network Nodes Based on Diamond Qubits with an Efficient Nanophotonic Interface,* Physical Review Letters **123**, 1 (2019).

[44] M. E. Trusheim, B. Pingault, N. H. Wan, M. Gündoğan, L. De Santis, R. Debroux, D. Gangloff, C. Purser, K. C. Chen, M. Walsh, J. J. Rose, J. N. Becker, B. Lienhard, E. Bersin, I. Paradeisanos, G. Wang, D. Lyzwa, A. R. Montblanch, G. Malladi, H. Bakhru, A. C. Ferrari, I. A. Walmsley, M. Atatüre, and D. Englund, *Transform-Limited Photons from a Coherent Tin-Vacancy Spin in Diamond,* Physical Review Letters **124**, 1 (2020).

[45] N. T. Son, C. P. Anderson, A. Bourassa, K. C. Miao, C. Babin, M. Widmann, M. Niethammer, J. Ul Hassan, N. Morioka, I. G. Ivanov, F. Kaiser, J. Wrachtrup, and D. D. Awschalom, *Developing silicon carbide for quantum spintronics,* Applied Physics Letters **116**, 190501 (2020).

[46] B. Hensen, H. Bernien, A. E. Dreaú, A. Reiserer, N. Kalb, M. S. Blok, J. Ruitenberg, R. F. Vermeulen, R. N. Schouten, C. Abellán, W. Amaya, V. Pruneri, M. W. Mitchell, M. Markham, D. J. Twitchen, D. Elkouss, S. Wehner, T. H. Taminiau, and R. Hanson, *Loophole-free Bell inequality violation using electron spins separated by 1.3 kilometres,* Nature **526**, 682 (2015).

[47] R. H. M. Pompili, S. Hermans, S. Baier, H. Beukers, P. Humphreys, R. Schouten, R. Ver- meulen, M. Tiggelman, L. d. S. Martins, B. Dirkse, S. Wehner, *Data and software supporting "Realization of a multi-node quantum network ofremote solid-state qubits",* (2021).

5

QUBIT TELEPORTATION BETWEEN NON-NEIGHBORING NODES IN A QUANTUM NETWORK

S. L. N. Hermans*, M. Pompili*, H. K. C. Beukers, S. Baier, J. Borregaard & R. Hanson

Future quantum internet applications will derive their power from the ability to share quantum information across the network. Quantum teleportation allows for the reliable transfer of quantum information between distant nodes, even in the presence of highly lossy network connections. While many experimental demonstrations have been performed on different quantum network platforms, moving beyond directly connected nodes has so far been hindered by the demanding requirements on the pre-shared remote entanglement, joint qubit readout and coherence times. Here we realize quantum teleportation between remote, non-neighboring nodes in a quantum network. The network employs three optically connected nodes based on solid-state spin qubits. The teleporter is prepared by establishing remote entanglement on the two links, followed by entanglement swapping on the middle node and storage in a memory qubit. We demonstrate that once successful preparation of the teleporter is heralded, arbitrary qubit states can be teleported with fidelity above the classical bound, even with unit efficiency. These results are enabled by key innovations in the qubit readout procedure, active memory qubit protection during entanglement generation and tailored heralding that reduces remote entanglement infidelities. Our work demonstrates a prime building block for future quantum networks and opens the door to exploring teleportation-based multi-node protocols and applications.

The results of this chapter have been accepted for publication in *Nature*.

* Equally contributing authors

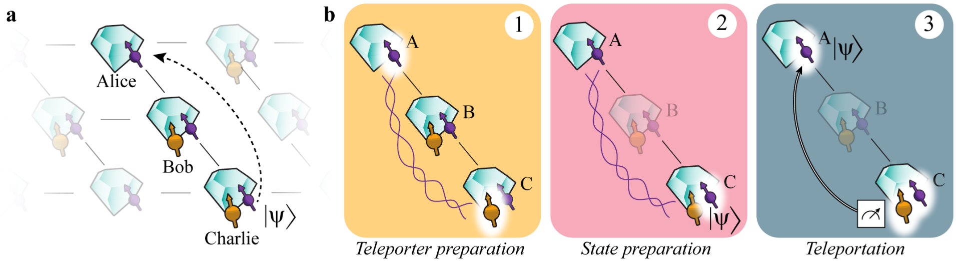

Figure 5.1: **Teleporting a qubit between non-neighboring nodes of a quantum network.** **(a)** Three network nodes, Alice (A), Bob (B) and Charlie (C) are connected via optical fiber links (lines) in a line configuration. Each setup has a communication qubit (purple) that enables entanglement generation with its neighboring node. Additionally, Bob and Charlie contain a memory qubit (yellow). **(b)** The steps of the teleportation protocol: (1) We prepare the teleporter by establishing entanglement between Alice and Charlie using an entanglement swapping protocol on Bob, followed by swapping the state at Charlie to the memory qubit. (2) The qubit state to be teleported is prepared on the communication qubit on Charlie. (3) A Bell-state measurement is performed on Charlie's qubits and the outcome is communicated to Alice over a classical channel. Dependent on this outcome, Alice applies a quantum gate to obtain the teleported qubit state.

5.1. INTRODUCTION

Quantum teleportation is the central routine for reliably sending qubits across lossy network links [1] as well as a key primitive of quantum network protocols and applications [2–4]. Using a teleporter in the form of a pre-shared entangled state, the quantum information is transferred by performing a joint Bell-state measurement on the sender's part of the entangled state and the qubit state to be teleported. The state is recovered on the receiving node by a gate operation conditioned on the Bell-state measurement outcome [1]. Since the quantum information is not transmitted by a physical carrier, the protocol is insensitive to loss in the connecting photonic channels and on intermediate nodes. A deterministic Bell-state measurement combined with real-time feed-forward enables unconditional teleportation, in which state transfer is achieved each time a qubit state is inserted into the teleporter.

Pioneering explorations of quantum teleportation protocols were performed using photonic states [5–7]. Following the development of quantum network nodes with stationary qubits, remote qubit teleportation was realized between trapped ions [8], trapped atoms [9, 10], diamond NV centers [11] and memory nodes based on atomic ensembles [12].

While future quantum network applications will widely employ teleportation between non-connected nodes in the network, the demanding set of requirements on the pre-shared entanglement, the Bell-state measurement and the coherence times for enabling real-time feed-forward has so far prevented the realization of teleportation beyond directly connected stationary network nodes.

Here, we overcome these challenges by a set of key innovations and achieve qubit teleportation between non-neighboring network nodes (see Figure 5.1a). Our quantum network consists of three nodes in a line configuration, Alice, Bob and Charlie. Each node contains a nitrogen-vacancy (NV) center in diamond. Using the NV electronic spin as the communication qubit we are able to generate remote entanglement between each pair of neighboring nodes. In addition, Bob and Charlie each employ a nearby ^{13}C nuclear spin as a memory qubit. The steps of the teleportation protocol are shown in Figure 5.1b. To prepare the teleporter we use an entanglement swapping protocol mediated by Bob, similar to a quantum repeater protocol [13], to establish entanglement between Alice and Charlie. Once successful preparation of teleporter is heralded, the input qubit state is prepared on Charlie and finally teleported to Alice.

5.2. ENTANGLEMENT FIDELITY OF THE NETWORK LINKS

A key parameter for quantum teleportation is the fidelity of the pre-shared entangled state between Alice and Charlie. As we generate this state by entanglement swapping, its fidelity is upper bounded by the errors on the individual links. Therefore, mitigating error sources on the individual links is critical. Our network generates entanglement between neighboring nodes using a single-photon protocol [14, 15] in an optical-phase-stabilized architecture [16]. The building block of this protocol is a qubit-photon entangled state created at each node. To generate this entangled state we initialize the communication qubit in a superposition state $\left|\psi\right\rangle = \sqrt{\alpha}\left|0\right\rangle + \sqrt{1-\alpha}\left|1\right\rangle$ and apply a state-selective optical pulse that transfers the population from $\left|0\right\rangle$ to an optically excited state. Following spontaneous emission, the qubit state is entangled with photon number (0 or 1 photon). We perform this protocol on both nodes and interfere the resonant photonic states on a beam splitter (Figure 5.2a). Detection of a single photon in one of the beam splitter output ports ideally heralds the generation of an entangled state $\left|\psi\right\rangle = (\left|01\right\rangle \pm \left|10\right\rangle)/\sqrt{2}$, where the ± phase is set by which detector clicked. Figure 5.2b displays the joint outcomes of qubit measurements in the computational basis after entanglement is heralded, showing the expected correlations.

The infidelity of the generated state has three main contributions: double $\left|0\right\rangle$ state occupancy, double optical excitation and finite distinguishability of the photons [16, 17] (see Section 5.7.9). In the case of double $\left|0\right\rangle$ state occupancy (which occurs with probability α), both communication qubits are in the $\left|0\right\rangle$ state and have emitted a photon. Detection of one of these photons leads to false heralding of an entangled state. The second effect, double excitation, is due to the finite length of the optical pulse compared to the emitter's optical lifetime. There is a finite chance that the communication qubit emits a photon during this pulse, is subsequently re-excited during the remainder of the pulse and then emits another photon resulting in the qubit state being entangled with two photons. Detection or loss of the first photon destroys the coherence of the qubit-photon entangled state and detection of the second photon can then falsely herald the generation of an entangled state.

Crucially, false heralding events due to double $\left|0\right\rangle$ state occupancy and double excitation are both accompanied by an extra emitted photon. Therefore, detection of this additional photon allows for unambiguous identification of such events and thus for real-time rejection of the corresponding false heralding signals. We implement this rejection

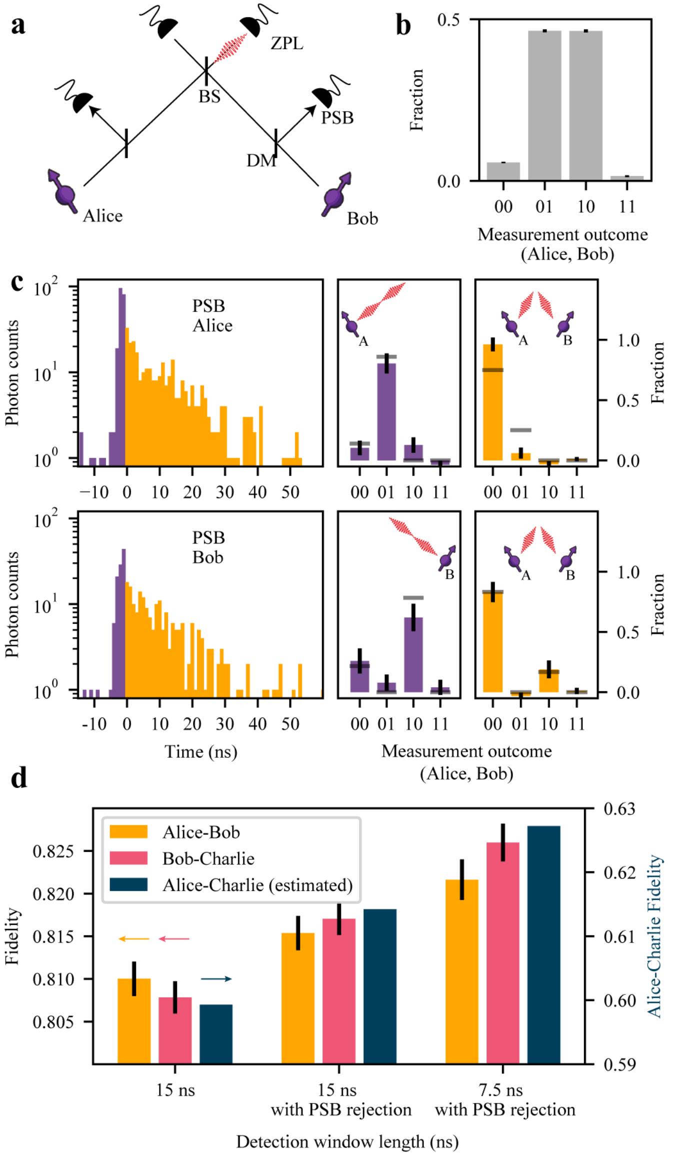

Figure 5.2: **High-fidelity entangled network links.** **(a)** Simplified schematic of the optical link used for generating entanglement between neighboring nodes. Photons emitted by the communication qubits are filtered by a dichroic mirror (DM) to separate the resonant (zero-phonon line, ZPL) photons (3% of emission) from the off-resonant (phonon-side band, PSB) photons (97% of emission). The resonant photons are sent to the beam splitter (BS); detection of a single photon at one of the ZPL detectors heralds successful generation of an entangled state between the two nodes. **(b)** Measured correlations of the communication qubits in the computational basis, conditioned on a heralding event on the ZPL detectors. **(c)** (left) Histograms of the PSB photon detection times on Alice (top) or Bob (bottom), conditioned on a simultaneous ZPL detection in the same entanglement generation attempt. Gray lines show expected correlations based on a quantum-optical model (see Section 5.7.3). **(d)** Measured fidelity of the network links, without PSB rejection (left), with PSB rejection (middle) and with PSB rejection plus shortened detection window (right). The dark blue bars indicate the corresponding expected fidelity on Alice-Charlie after entanglement swapping for each case (Section 5.7.9)). All error bars represent one standard deviation.

scheme by monitoring the off-resonant phonon-side band (PSB) detection path on both setups during and after the optical excitation (see Figure 5.2a).

To investigate the effect of this scheme, we generate entanglement on the individual links and extract the entanglement heralding events for which the PSB monitoring flagged the presence of an additional photon. For these events, we again analyze the corresponding qubit measurements in the computational basis (Figure 5.2c).

We identify two separate regimes: one during the optical pulse (purple) and one after the optical pulse (yellow). When a photon is detected on Alice's (Bob's) PSB detector during the optical pulse we see that the outcome 01 (10) is most probable (purple data in Figure 5.2c) showing that only one setup was in the $|0\rangle$ state and thus that both detected photons originated from Alice (Bob). The detection of PSB photons during the optical pulse thus primarily flags double excitation errors. In contrast, when a photon is detected after the optical pulse in either Alice's or Bob's PSB detector, the outcome 00 is most probable (yellow data in Figure 5.2c), indicating that both setups were in the $|0\rangle$ state and both emitted one photon. PSB photon detection after the optical pulse thus flags the double $|0\rangle$ state occupancy error. We find similar results to Figure 5.2c for the entangled states generated on the Bob-Charlie link, see Section 5.7.3. The improvement in fidelity from rejecting these false heralding events in our experiment is set by the combined probability of occurrence ($\approx 9\%$, see Section 5.7.9) multiplied by the probability to flag them (given here by the total PSB photon detection efficiency of $\approx 10\%$).

The third main source of infidelity, the finite distinguishability, can arise from frequency detunings between the emitted photons [18]. While most of these detunings are eliminated upfront by the charge-resonance (CR) check before the start of the protocol (Section 5.7.1), the communication qubits may still be subject to a small amount of spectral diffusion. In our single-photon protocol, this leads to dephasing that is stronger for photons that are detected later relative to the optical pulse. By shortening our detection window, we can increase the fidelity of the entangled state at the expense of a lower entangling rate. For the experiments below (unless mentioned differently) we use a detection window length of 15ns. Figure 5.2d summarizes the measured improvements on the individual links. For the teleporter, we estimate that their combined effect is an increase in Alice-Charlie entangled state fidelity by $\approx 3\%$. This increase is instrumental in pushing the teleportation fidelity above the classical bound.

5.3. MEMORY QUBIT COHERENCE

In the preparation of the teleporter it is crucial that the first entangled state between Alice and Bob is reliably preserved on the memory qubit while the second link between Bob and Charlie is being generated. For this reason we abort the sequence and start over when the second entangled state is not heralded within a fixed number of attempts, the timeout.

The ^{13}C memory qubits can be controlled with high fidelity via the communication qubit while they can be efficiently decoupled when no interaction is desired. Recent

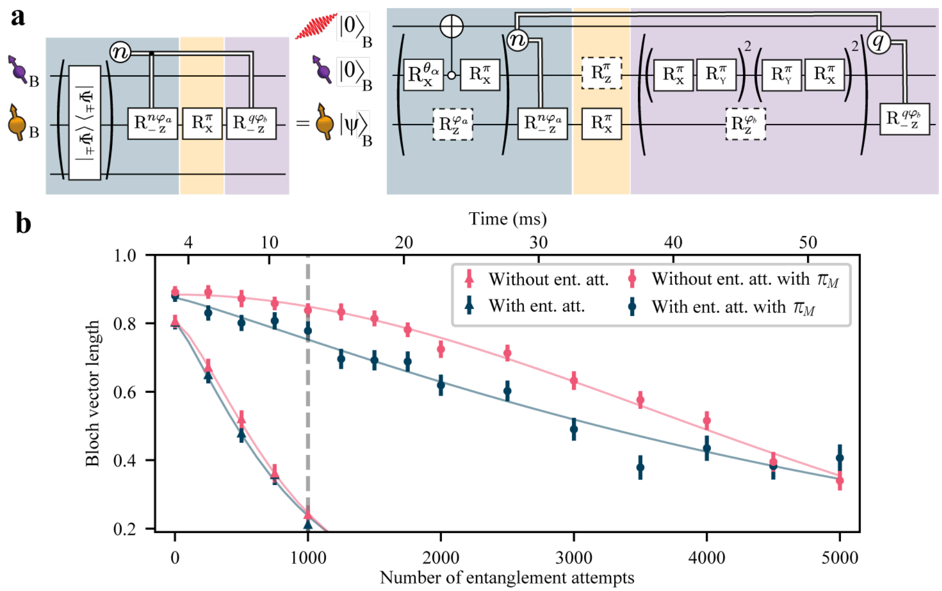

Figure 5.3: **Memory qubit coherence.** **(a)** Gate sequence on Bob for entanglement generation with the communication qubit while preserving states stored on the memory qubit. Entanglement generation attempts are repeated until success or a predetermined timeout. Upon success in the n^{th} attempt, a phase feed-forward is applied to maintain the correct reference frame of the memory qubit [16], followed by a decoupling pulse on the memory qubit. The decoupling π_{M} pulse causes a Z-rotation on the communication qubit. Afterwards, we rephase the memory qubit for the same amount of time as it took to herald entanglement (by applying q blocks of XY8 decoupling sequences on the communication qubit, where q depends on the number of entanglement attempts needed n) and we end with another phase feed-forward on the memory qubit, to compensate for any phase picked up during this decoupling. **(b)** Bloch vector length of a superposition state stored on the memory qubit for different number of entanglement attempts or a time-equivalent wait element. In the case of no decoupling (no π_{M}) on the memory qubit, the gates in the yellow shaded box in (a) are left out. The gray dashed line indicates the chosen timeout of 1000 entanglement attempts. All error bars represent one standard deviation.

work showed that in a magnetic field of 189 mT entanglement generation attempts with the communication qubit do not limit the memory dephasing time $T_2^\star$ [16], opening the door to significantly extending the memory preservation time with active coherence protection from the spin bath [19]. We realize this protection by integrating a decoupling π-pulse on the memory qubit into the experimental sequence that follows a heralding event, while ensuring that all phases that are picked up due to the probabilistic nature of the remote entangling process are compensated in real time (Figure 5.3a).

In Figure 5.3b we check the performance of this sequence by storing a superposition state on the memory qubit and measuring the Bloch vector length. We compare the results for the sequence with and without the decoupling π-pulse, and with and without entanglement attempts. We observe that without the decoupling pulse the decay of the Bloch vector length is not altered by the entanglement attempts, in line with previous findings [16]. In contrast, when we apply the decoupling pulse the decay is slowed down by more than a factor of 6, yielding a $N_{1/e}$ decay constant of ≈ 5300 entanglement attempts, the highest number reported to date for diamond devices. In addition, we observe a difference in the shape of the decay between the cases with and without entangling attempts, indicating that intrinsic decoherence is no longer the only limiting error source. The improved memory coherence enables us to use a timeout of 1000 entangling attempts, more than double that of Ref. [16], which doubles the entanglement swapping rate.

5.4. MEMORY QUBIT READOUT

High-fidelity memory qubit readout is required both in the preparation of the teleporter (at Bob) and during the teleportation protocol itself (at Charlie). The memory qubit is read out by mapping its state onto the communication qubit using quantum logic followed by single-shot readout of the communication qubit using state-dependent optical excitation and detection [20]. Due to limited photon collection efficiency (≈ 10%) and finite cyclicity of the optical transition (≈ 99%), the communication qubit readout fidelity is different for $|0\rangle$ and $|1\rangle$. As a result, for random initial states the probability that the correct state was assigned is significantly larger if one or more photons were detected (assigned outcome 0) than if no photons were detected (assigned outcome 1) [21]. In previous work we circumvented this issue by conditioning on obtaining the outcome 0 [16]. However, this approach scales unfavorably, as it forces the protocol to prematurely abort with probability >50% at each memory qubit readout. Therefore, to access more complex protocols with multiple memory qubit readouts, near-deterministic readout schemes are required.

We resolve this challenge by introducing a basis-alternating repetitive readout for the memory qubit (see Figure 5.3c). The key point of this readout strategy is, in contrast to earlier work [22], to alternatingly map the computational basis states of the memory qubit to the communication qubit state $|0\rangle$. Figure 5.3d shows the readout fidelities of the n-th readout repetition for the two initial states for the memory qubit on Bob (for Charlie, see Section 5.7.6). We clearly observe the expected alternating pattern due to the asymmetry of the communication qubit readout fidelities. Importantly, the readout fidelity decays only by ≈ 1% per readout, showing that the readout is mostly non-demolition and multiple readouts are possible without losing the state. We model the readout procedure using measured parameters (see Section 5.7.6) and plot the model's predictions as dashed lines in Figure 5.3d-f.

Next, we assign the state using the first readout and continue the sequence only when the consecutive readouts are consistent with the first readout. The subsequent readouts therefore add confidence to the assignment in the case of consistent outcomes, while cases of inconsistent outcomes (which have a higher chance of indicating an incorrect assignment) are filtered out. In Figure 5.3e we plot the readout fidelity resulting from this strategy for up to five readouts, with the corresponding rejected fraction due to inconsistent outcomes plotted in Figure 5.3f. We observe that using two readouts already

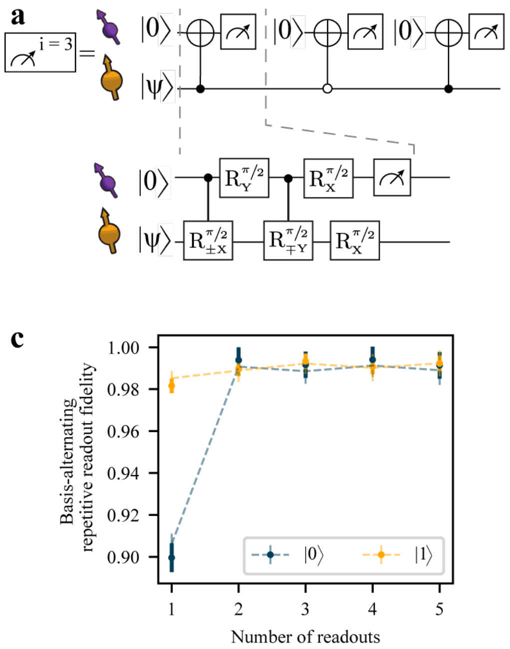

Figure 5.4: **Memory qubit readout. (a)** Gate sequence for the basis-alternating repetitive readout of the memory qubit. **(b)** Readout fidelity for each readout repetition, for state |0⟩ and |1⟩. **(c)** Readout fidelity of the basis-alternating repetitive readout scheme for different number of readout repetitions. s **(d)** Fraction of inconsistent readout patterns for different number of readout repetitions. In (d-f) the dashed lines show a numerical model using measured parameters. All error bars represent one standard deviation.

eliminates most of the asymmetry, reducing the average infidelity from ≈ 6% to below 1%. At this point, the remaining observed infidelity mainly results from cases where the memory qubit was flipped during the first readout block due to imperfect memory qubit gates. While adding further readout blocks does not lead to significant improvements in fidelity, each two additional readouts cut the amount of consistent outcomes by ≈ 10%, due to the communication qubit readout infidelities and gate errors. For the experiments reported below (unless mentioned differently) we use two readout repetitions to benefit from a high average readout fidelity (Bob: 99.2(4)%, Charlie: 98.1(4)%) and a high probability to continue the sequence (Bob and Charlie: ≈ 88%).

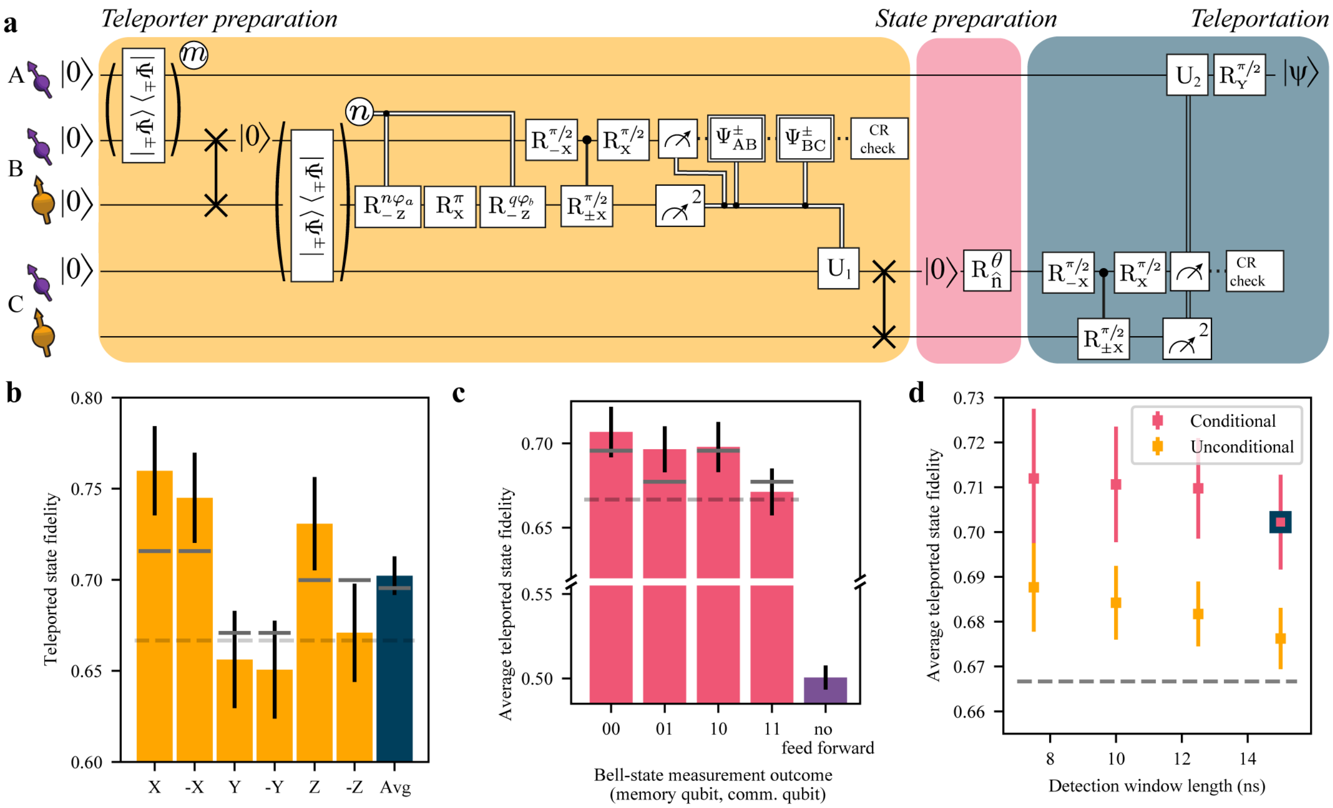

Figure 5.5: **Qubit teleportation between non-neighboring network nodes.** **(a)** Circuit diagram of the teleportation protocol using notation defined in Figure 5.3. m (n) is the number of attempts needed to herald entanglement for the AB (BC) entangled link. See Section 5.7.1for the full circuit diagram. **(b)** Teleported state fidelities for the six cardinal states and their average. The gray lines show the expected fidelities from simulations. The dashed lines in (b-d) represents the classical bound of 2/3. **(c)** Average teleported state fidelity for the different outcomes of the Bell-state measurement on Charlie. The right-most bar shows the resulting fidelity when no feed forward operation on Alice would be applied. **(d)** Average state fidelity for a conditional and unconditional teleportation, for different detection window lengths of the two-node entanglement generation processes. The blue bordered data point is the same point as shown in (b). All error bars represent one standard deviation.

5.5. TELEPORTING QUBIT STATES FROM CHARLIE TO ALICE

With all innovations described above implemented, we perform the protocol as shown in Figure 5.5a. First we generate entanglement between Alice and Bob and store Bob's part of the entangled state on the memory qubit using a compiled SWAP operation. Second, we generate entanglement between Bob and Charlie, while preserving the first entangled state on the memory qubit with the pulse sequence as described in Figure 5.3a. Next, we perform a Bell-state measurement on Bob followed by a CR check. We continue the sequence if the communication qubit readout yields outcome 0, the memory qubit readout gives a consistent outcome pattern and the CR check is passed. At Charlie, we perform a quantum gate that depends on the outcome of the Bell-state measurement and on which detectors clicked during the two-node entanglement generation. Next, we swap the entangled state to the memory qubit. At this point the teleporter is ready and Alice and Charlie share an entangled state with an estimated fidelity of 0.61.

Subsequently, we generate the qubit state to be teleported, $|\psi\rangle$, on Charlie's communication qubit and run the teleportation protocol. First, a Bell-state measurement is performed on the communication and memory qubits at Charlie. With the exception of unconditional teleportation (discussed below), we only continue the sequence when we obtain a 0 outcome on the communication qubit, when we have a consistent readout pattern on the memory qubit and when Charlie passes the CR check. The outcomes of the Bell-state measurement are sent to Alice and by applying the corresponding gate operation we obtain $|\psi\rangle$ on Alice's side.

We teleport the six cardinal states ($\pm$X, $\pm$Y, $\pm$Z), which form an unbiased set [23], and measure the fidelity of the teleported states to the ideally prepared state (Figure 5.5b). We find an average teleported state fidelity of F =0.702(11) at an experimental rate of 1/(117 s). This value exceeds the classical bound of 2/3 by more than three standard deviations, thereby proving the quantum nature of the protocol. We note that this value provides a lower bound to the true teleportation fidelity, as the measured fidelity is lowered by errors in the preparation of the qubit states at Charlie (estimated to be 0.5%, see Section 5.7.11).

The differences in fidelity between the teleported states arise from an interplay of errors in different parts of the protocol that either affect all three axes (depolarizing errors) or only two axes (dephasing errors). These differences are qualitatively reproduced by our model (gray bars in Figure 5.5b). In Figure 5.5c we plot the teleportation fidelity for each possible outcome of the Bell-state measurement. Due to the basis-alternating repetitive readout, the dependence on the second bit (from the memory qubit readout) is small, whereas for the first bit (communication qubit readout) the best teleported state fidelity is achieved for outcome 0 due to the asymmetric readout fidelities. We also analyze the case in which no feed-forward is applied at Alice (Section 5.7.12); as expected, the average state fidelity reduces to a value consistent with a fully mixed state (fidelity F =0.501(7)), emphasizing the critical role of the feed-forward in the teleportation protocol.

Finally, we demonstrate that the network can achieve unconditional teleportation between Alice and Charlie. Unconditional teleportation requires that, following preparation of the teleporter by establishing the remote entangled state, the protocol runs deterministically (each qubit state prepared at Charlie ends up at Alice) while surpassing the classical fidelity bound. We thus require that the Bell-state measurement at Charlie and the subsequent feed-forward operations are performed deterministically. To this end, we revise the protocol at Charlie to accept both communication qubit outcomes, use all memory qubit readout patterns including the inconsistent ones and disregard the outcome of the CR check after the Bell-state measurement. Using this fully deterministic Bell-state measurement lowers the average teleportation fidelity by a few percents (Figure 5.5d). At the same time, shortening the detection windows of the two-node entanglement generation is expected to yield an improvement in the fidelity, as discussed above. We find indeed that the average unconditional teleportation fidelity increases with shorter window lengths, reaching F =0.688(10) for a length of 7.5 ns and a rate of 1/(100 s). The current quantum network is thus able to perform teleportation beyond the classical bound, even under the strict condition that every state inserted into the teleporter be transferred.

5.6. OUTLOOK

In this work we have realized unconditional qubit teleportation between non-neighboring nodes in a quantum network. The innovations introduced here on memory qubit readout and protection during entanglement generation, as well as the real-time rejection of false heralding signals, will be instrumental in exploring more complex protocols [2–4, 24, 25]. Also, these methods can be readily transferred to other platforms such as the group-IV color centers in diamond, the vacancy-related qubits in SiC and single rare-earth ions in solids [26–32].

The development of an improved optical interface for the communication qubit [33] will increase both the teleportation protocol rate and fidelity. Because of the improved memory qubit performance reported here, the network already operates close to the threshold where nodes can reliably deliver a remote entangled state while preserving previously stored quantum states in their memory qubits. With further improvements, for instance by integrating multi-pulse memory decoupling sequences [19] into the entanglement generation, demonstration of deterministic qubit teleportation may come within reach. In that case, the network is able to teleport a qubit state with unit efficiency at any given time, removing the need for heralding successful preparation of the teleporter and opening the door to exploring applications that call the teleportation routine multiple times. In addition, future work will focus on further improving the phase stabilization and extending the current schemes for use in deployed fiber [34].

Finally, by implementing a recently proposed link layer protocol [35], qubit teleportation and applications making use of the teleportation primitive may be executed and tested on the network through platform-independent control software, an important prerequisite for a large-scale future network.

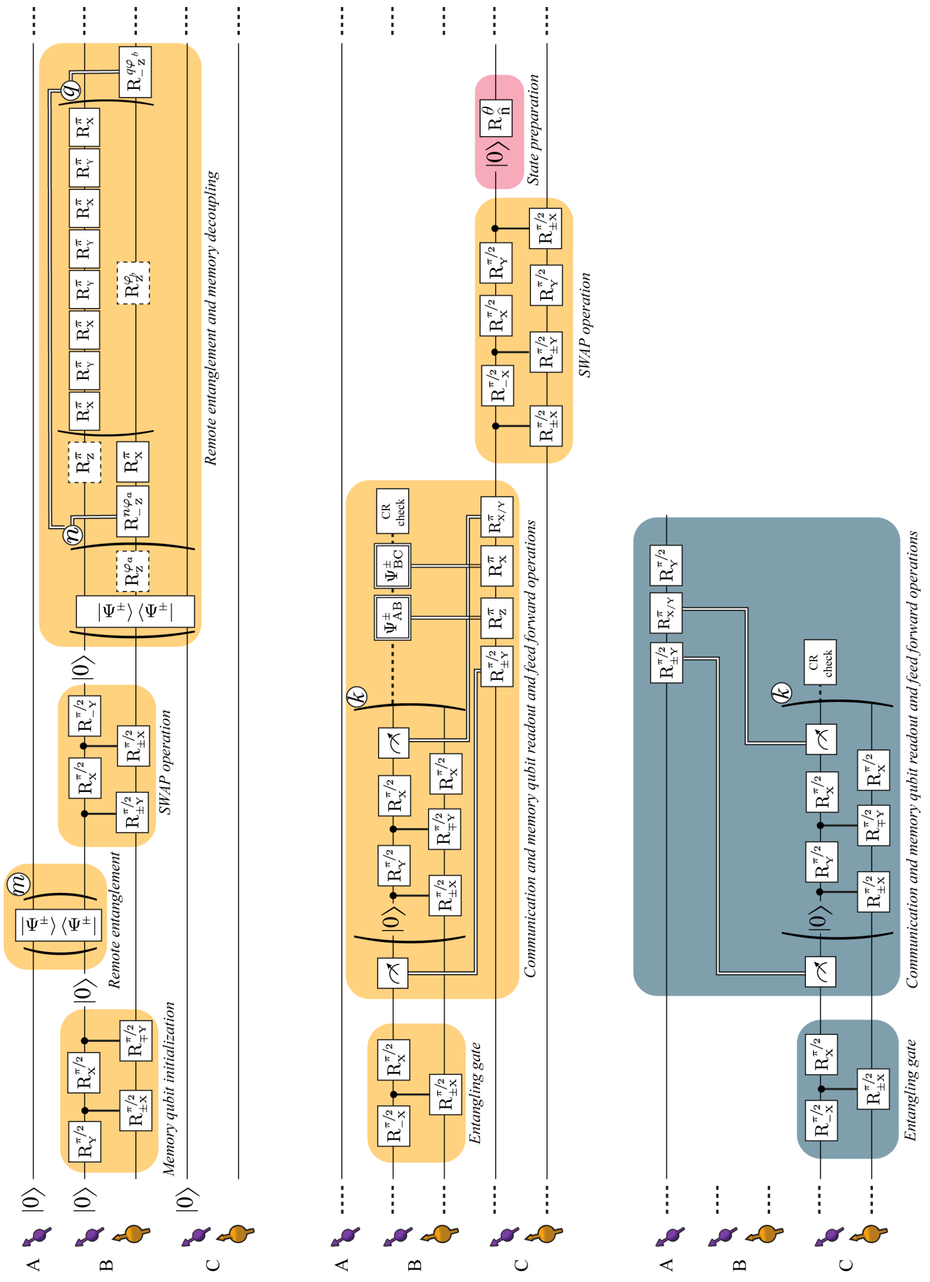

Figure 5.6: Full gate circuit for the teleportation protocol, see text for the description of each element.

5.7. SUPPLEMENTARY INFORMATION

5.7.1. FULL GATE CIRCUIT

Our quantum network consists of three nodes, Alice, Bob and Charlie. In the experiment, we will teleport a qubit from Charlie to Alice, two non-neighboring nodes. The full gate circuit is shown in Figure 5.6. Prior to the sequence, we do a Charge-Resonance (CR) check on each node to ensure that the communication qubits are in the correct charge state (NV^-) and on resonance with the control lasers. Once all the nodes have passed this check, we do a first round of optical phase stabilization of the interferometers, which enables the entanglement generation using the single click protocol [14–17]. After these preparation steps, the sequence is triggered on all setups.

On Bob, we initialize the memory qubit into $|0\rangle$ using the communication qubit [20]. Next, we generate entanglement between the communication qubits of Alice and Bob. When entanglement is heralded, we perform a SWAP operation to store Bob's part of the entangled state on the memory qubit.

We continue with a second round of phase stabilization (not shown in the circuit) and generate entanglement between the communication qubits of Bob and Charlie. Each entanglement attempt slightly decoheres the memory qubit, therefore we limit the number of attempts by a timeout. If we do not succeed within the timeout, we abort the sequence and start over.

During entanglement generation, the memory qubit of Bob picks up an average phase $n\varphi_a$ dependent on the number of entanglement attempts n. Due to the probabilistic nature of the entanglement generation process, we do not know which attempt will be successful, therefore this phase is unknown at the start of the sequence. To maintain the correct reference frame of the memory qubit this phase needs to be corrected in real-time before any other gate can be applied to the memory qubit. We perform this real-time correction by changing the time between pulses on the communication qubit [16]. After the phase correction, the decoupling pulse is applied to the memory qubit via the communication qubit. The back-action of this gate causes a Z-rotation on the communication qubit. To rephase the memory qubit, we wait for the same amount of time as it took to herald the second entangled state while decoupling the communication qubit. This imprints a phase $q\varphi_b$ on the memory qubit, which we compensate in an analogous way.

Bob now shares two entangled states; his memory qubit is entangled with Alice and his communication qubit with Charlie. To establish an entangled state between Alice and Charlie we perform a Bell-state measurement on the two qubits of Bob. To do so, we entangle the communication and memory qubits and do a measurement on the communication qubit. We map its state onto the communication qubit and measure the communication qubit. In the basis-alternating repetitive readout, we repeat the measurement sequence twice. During the first readout we map the $|0\rangle$ state to the $|0\rangle$ state of the communication qubit, and in the second readout we map $|1\rangle$ to $|0\rangle$. The first outcome is used to assign the state and the second outcomes serves as a check. By continuing

Table 5.1: Memory qubit characteristics. In each setup we use a magnetic field with strength B_z aligned to the NV axis. The nuclear spin precession frequencies ($\omega_{m_s=0}$ and $\omega_{m_s=-1}$) depends on the electron spin state. From the frequency difference, the parallel component $A_\parallel$ of the hyperfine interaction can be estimated. Conditional (unconditional) pulses are applied by doing N_{con} (N_{unc}) pulses on the electron spin with an inter-pulse delay of τ_{con} (τ_{unc}).

Setup	B_z	$\omega_{m_s=0}$	$\omega_{m_s=-1}$	$A_\parallel$
Bob	1890 Gauss	$2\pi \times 2025$ kHz	$2\pi \times 2056$ kHz	$2\pi \times 30$ kHz
Charlie	165 Gauss	$2\pi \times 177$ kHz	$2\pi \times 240$ kHz	$2\pi \times 63$ kHz

Setup	τ_{con}	N_{con}	τ_{unc}	N_{unc}
Bob	2.818 μs	54	4.165 μs	144
Charlie	6.003 μs	56	11.996 μs	30

the sequence only when we measure consistent patterns (for instance $(m1, m2) = (1,0)$) we increase our average readout fidelity. After the readout procedure, we perform a CR check on Bob to filter out any event where Bob was in the wrong charge state.

Bob communicates to Charlie which gate operation should be done to obtain the correct entangled state. Which operation is required is determined by the outcomes of the Bell-state measurement on Bob and by which detector heralded the individual links. Charlie performs the feed-forward gate operation and subsequently stores its part of the entangled state on the memory qubit using a SWAP gate. At this point in the sequence the teleporter is ready.

To prepare the state that is to be teleported, we initialize the communication qubit at Charlie and perform the desired qubit rotation. To teleport the qubit, we perform a Bell-state measurement on the qubits of Charlie. Locally, we entangle the communication qubit with the memory qubit. We readout the communication qubit and use the basis-alternating repetitive readout for the memory qubit. Additionally, we do a CR check on Charlie. Charlie communicates the results of the Bell-state measurement to Alice, and Alice performs a feed-forward operation to obtain the teleported state. To verify the teleported state, we measure the state of Alice in the corresponding basis. To prevent any bias in the tomography we measure in both directions, e.g. when we teleport $|+Z\rangle$ we measure both along +Z and -Z axes.

5.7.2. EXPERIMENTAL SETUP

The basics of the experimental setup are described in [16]. In the current experiment, Charlie has access to a carbon-13 nuclear spin that acts as a memory qubit. The parameters used for the memory qubits of Bob and Charlie can be found in Table 5.1. Additionally, we have set up a classical communication channel between Charlie and Alice such that Charlie can directly send the results of the Bell-state measurement to Alice.

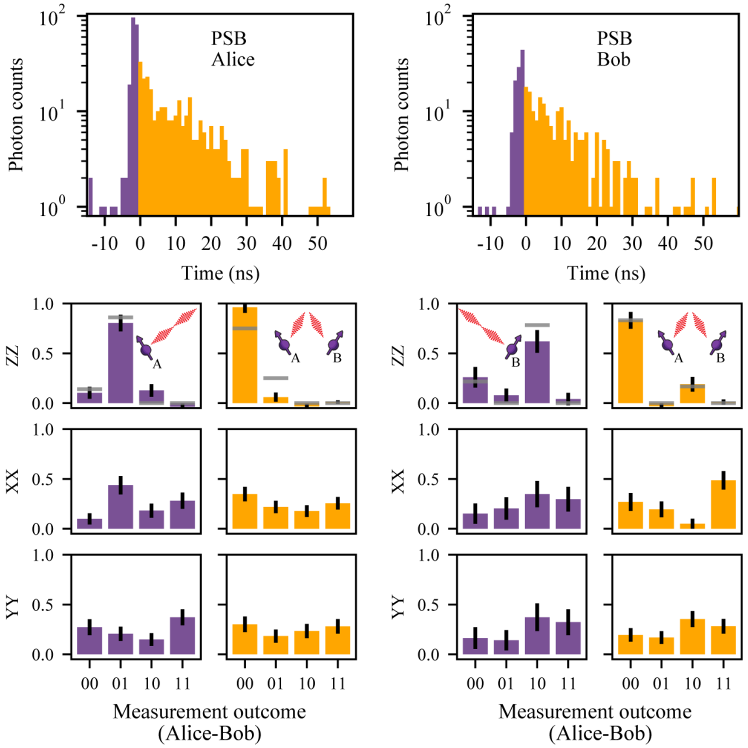

Figure 5.7: (Top) Histograms of the detected PSB photons conditioned on a simultaneous ZPL detection in the entanglement generation attempt, for Alice (left) and Bob (right). (Bottom) Corresponding measured correlations in all bases. The gray bars in the Z basis represent the simulated values. For the X and Y bases, one would expect a probability of 0.25 for all outcomes. All error bars represent one standard deviation.

TEMPORAL SELECTION OF HERALDING PHOTONS

To eliminate any reflected excitation light in the heralding detectors, we make use of a cross-polarization scheme and perform temporal selection of the detected photons as described in Reference [36]. We start the detection windows 4 ns (5 ns) after the highest intensity point of the excitation pulse, for the AB (BC) entangled link, to ensure sufficient suppression of excitation laser light in the detection window.

5.7.3. TAILORED HERALDING OF THE REMOTE ENTANGLED STATES

In the main text we describe several noise mechanisms that reduce the remote two-node entangled state fidelity. Two of these noise mechanisms, double $|0\rangle$ occupancy and double optical excitation, are accompanied by the emission of an extra photon. This extra photon can be detected using the local phonon-side band (PSB) detectors. By monitoring the PSB detectors, we can real-time reject false heralding events.

In Figures 5.7 and 5.8, we plot the histograms of the detection times of the PSB photons

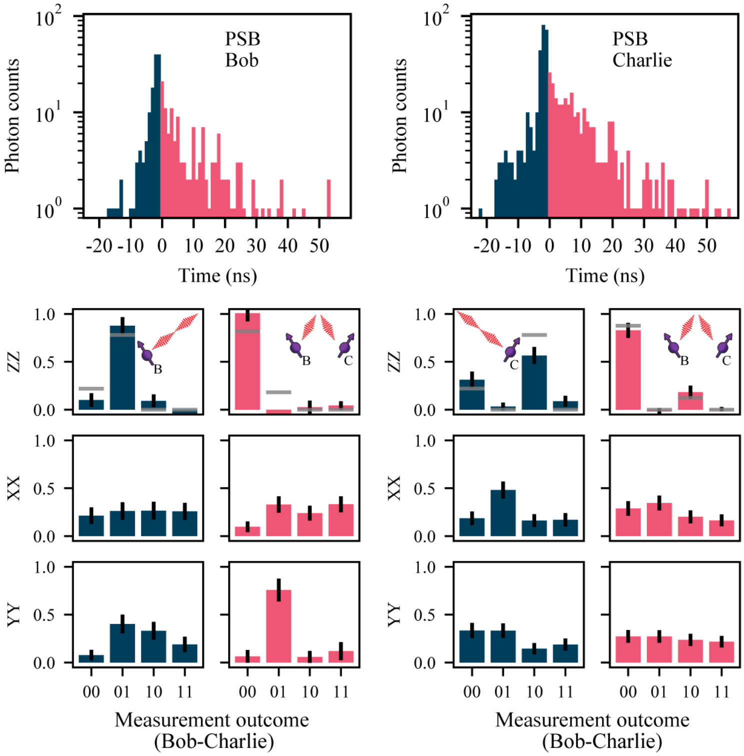

Figure 5.8: (Top) Histograms of the detected PSB photons conditioned on a simultaneous ZPL detection in the entanglement generation attempt, for Bob (left) and Charlie (right). (Bottom) Corresponding measured correlations in all bases. The gray bars in the Z basis represent the simulated values. For the X and Y basis, one would expect a probability of 0.25 for all outcomes. All error bars represent one standard deviation.

Table 5.2: Estimated probabilities for the double optical excitation error and the double $|0\rangle$ occupancy error per node (values in percent). All error bars represent one standard deviation.

Node	Double optical excitation probability	Double $|0\rangle$ occupancy probability
Alice	4.1 ± 0.5	7.6 ± 0.4
Bob (with Alice)	2.6 ± 0.3	4.9 ± 0.3
Bob (with Charlie)	6.9 ± 0.8	4.7 ± 0.8
Charlie	5.7 ± 0.4	9.4 ± 0.4

conditioned on a simultaneous heralding (zero-phonon line, ZPL) photon detection in the same entanglement generation attempt, for the Alice-Bob and Bob-Charlie entangled link respectively. The correlations are measured in the computational (or Z) basis, and in the X and Y basis. In the computational basis we see the behavior dependent on the detection time of the PSB photon as described in the main text together with the simulations (gray bars). In the X and Y basis, all outcomes are equally probable, and the quantum correlations are washed out.

From the data collected, we can extract the probability to detect these additionally emitted PSB photons. We assume the dark counts of the detectors to be negligible, the PSB detections during the pulse to be fully dominated by the double optical excitation error, and the PSB detections after the pulse to be only caused by double $|0\rangle$ occupancy. By correcting for the PSB detection efficiency, we can estimate the probability for double $|0\rangle$ occupancy and double optical excitation errors. The results are given in Table 5.2. The double $|0\rangle$ state error is expected to occur with probability α. The extracted numbers correspond well to the parameter values we use during remote entanglement generation ($\alpha_{\text{Alice}} = 0.07, \alpha_{\text{Bob}} = 0.05, \alpha_{\text{Charlie}} = 0.10$ [16]). The probability for the double optical excitation to occur depends on the shape and the amplitude of the optical excitation pulse, and differs per node.

NUMERICAL MODEL

We compare our PSB detection data (previous section) to a numerical model. We model the NV center as a three level system with two stable ground states $|0\rangle, |1\rangle$ and one excited state $|e\rangle$. The optical $|0\rangle \leftrightarrow |e\rangle$ transition is driven by a resonant laser pulse and is assumed to be a closed transition. The Hamiltonian describing the dynamics of the system in a suitable rotating frame is

$$\hat{H} = \Omega(t)\,|e\rangle\langle 0| + \Omega^*(t)\,|0\rangle\langle e|, \tag{5.1}$$

where $\Omega(t)$ describes the (time-dependent) driving of the optical transition. From the excited state, the NV can spontaneously emit a photon and decay to $|0\rangle$. Without specifying the particular mode this photon is emitted in, we simply model such an emission with a Lindblad jump operator of the form $\hat{L}_1 = \sqrt{\gamma}\,|0, 1_p\rangle\langle e|$. Here γ is the rate of spontaneous emission, $|0, 1_p\rangle$ denotes the state where the NV is in state $|0\rangle$ and one photon was emitted, and we use the convention that when not explicitly stated, there is no emitted photon i.e. $|e\rangle$ denotes the NV in state $|e\rangle$ with zero emitted photons.

Parameter	Description
γ	Spontaneous emission rate of the excited state.
$\Omega(t)$	Optical driving strength.
α	Initial population of the $\|0\rangle$ state.
P_0	Probability of emitting 0 photons (ZPL or PSB).
P_1	Probability of emitting 1 photons (ZPL or PSB).
P_2	Probability of emitting 2 photons (ZPL or PSB or both).
P_z	Probability that an emitted photon is a ZPL photon.
$P_{dz,1}$	Probability that a ZPL photon is within the ZPL detection window, conditioned on a single ZPL photon being emitted.
$P_{db,1}$	Probability that a PSB photon is within the PSB detection window, conditioned on a single PSB photon being emitted.
$P_{dz,2}$	Probability that 2 ZPL photons are within the ZPL detection window, conditioned on two ZPL photons being emitted.
$P_{dz,3}$	Probability that one ZPL photons is within the ZPL detection window and one is not, conditioned on two ZPL photons being emitted.
$P_{db,2}$	Probability that 2 PSB photons are within the PSB detection window, conditioned on two PSB photon being emitted.
$P_{dz,3}$	Probability that one PSB photons is within the PSB detection window and one is not, conditioned on two PSB photons being emitted.
$P_{dzb,1}$	Probability that a ZPL photon is within the ZPL detection window and a PSB photon is within the PSB detection window, conditioned on one ZPL and one PSB photon being emitted.
$P_{dzb,2}$	Probability that a ZPL photon is not within the ZPL detection window and a PSB photon is within the PSB detection window, conditioned on one ZPL and one PSB photon being emitted.
$P_{dzb,3}$	Probability that a ZPL photon is within the ZPL detection window and a PSB photon is not within the PSB detection window, conditioned on one ZPL and one PSB photon being emitte.
η_z	Total transmission and detection efficiency of ZPL photons.
η_p	Total transmission and detection efficiency of PSB photons.

Table 5.3: Explanation of the parameters used in the numerical simulation of the entanglement generation protocol.

To account for double emission errors in the entanglement scheme, we expand the model by letting states $\left|0,1_p\right\rangle, \left|e,1_p\right\rangle$ be coupled by a similar Hamiltonian as in Eq. (5.1) with the same coupling $\Omega(t)$. Double emission is then captured by a Lindblad jump operator $\hat{L}_2 = \sqrt{\gamma}\left|0,2_p\right\rangle\left\langle 1_p,e\right|$. For the specific excitation pulses used in the experiment, we can then numerically solve the Master equation of the system in a basis of $(|0\rangle, |e\rangle, \left|0,1_p\right\rangle, \left|e,1_p\right\rangle, \left|0,2_p\right\rangle)$ to obtain the probability of zero (P_0), one (P_1), or two (P_2) photons being emitted from the system ($P_0 + P_1 + P_2 = 1$). Note that in this model, we neglect the probability of emitting more than two photons from the NV.

Assuming an initial state $\sqrt{\alpha}\,|0\rangle + \sqrt{1-\alpha}\,|1\rangle$ of the NV center, the state after the optical excitation is then modeled as

$$\left|\psi\right\rangle = \sqrt{\alpha}\left(\sqrt{P_0}\,|0\rangle + \sqrt{P_1}\left|0,1_p\right\rangle + \sqrt{P_2}\left|0,2_p\right\rangle\right) + \sqrt{1-\alpha}\,|1\rangle. \tag{5.2}$$

The emitted photons are either PSB (= 97%) or ZPL (= 3%) photons. We model this by performing a standard beam splitter transformation on the photonic modes. Letting $\hat{a}^\dagger$ be the creation operator of a photon ($\left|1_p\right\rangle = \hat{a}^\dagger\left|0_p\right\rangle$), we make the transformation $\hat{a}^\dagger \to \sqrt{P_z}\hat{a}^\dagger_z + \sqrt{1-P_z}\hat{a}^\dagger_b$, where $\hat{a}^\dagger_z$ ($\hat{a}^\dagger_b$) is the creation operator of a ZPL (PSB) photon and $P_z = 3\%$. Consequently, $\left|1_p\right\rangle \to \sqrt{P_z}\,|1_z\rangle + \sqrt{1-P_z}\,|1_b\rangle$, where $|1_z\rangle$ ($|1_b\rangle$) is an emitted ZPL (PSB) photon.

The photons can be emitted either inside or outside the detection time window, i.e. the time interval in which detected photons are accepted. This time interval is in general different for the PSB and ZPL photons. This results in the following transformations:

$$\begin{aligned}
|1_z\rangle \quad &\to \quad \sqrt{P_{dz,1}}\left|1_{d,z}\right\rangle + \sqrt{1-P_{dz,1}}\left|1_{nd,z}\right\rangle && (5.3)\\
|1_b\rangle \quad &\to \quad \sqrt{P_{db,1}}\left|1_{d,b}\right\rangle + \sqrt{1-P_{db,1}}\left|1_{nd,b}\right\rangle && (5.4)\\
|2_z\rangle \quad &\to \quad \sqrt{P_{dz,2}}\left|2_{d,z}\right\rangle + \sqrt{P_{dz,3}}\left|1_{d,z}\right\rangle\left|1_{nd,z}\right\rangle + \sqrt{1-P_{dz,2}-P_{dz,3}}\left|2_{nd,z}\right\rangle && (5.5)\\
|2_b\rangle \quad &\to \quad \sqrt{P_{db,2}}\left|2_{d,b}\right\rangle + \sqrt{P_{db,3}}\left|1_{d,b}\right\rangle\left|1_{nd,b}\right\rangle + \sqrt{1-P_{db,2}-P_{db,3}}\left|2_{nd,b}\right\rangle && (5.6)\\
|1_z\rangle|1_b\rangle \quad &\to \quad \sqrt{P_{dzb,1}}\left|1_{d,z}\right\rangle\left|1_{d,b}\right\rangle + \sqrt{P_{dzb,2}}\left|1_{nd,z}\right\rangle\left|1_{d,b}\right\rangle && (5.7)\\
&\quad + \sqrt{P_{dzb,3}}\left|1_{d,z}\right\rangle\left|1_{nd,b}\right\rangle + \sqrt{1-P_{dz,2}-P_{dz,2}-P_{dz,3}}\left|1_{nd,z}\right\rangle\left|1_{nd,b}\right\rangle.
\end{aligned}$$

The probabilities $P_{dz,1}, P_{db,1}, \ldots$ are defined in table 5.3 and are found through the numerical simulation described above.

Finally, we model transmission loss with standard beam splitter transformations acting on the photon modes emitted in the detection window. Letting $\hat{a}^\dagger_{d,z}$ ($\hat{a}^\dagger_{d,b}$) be the creation operator of a ZPL (PSB) photon emitted in the detection time window, we make the transformations

$$\hat{a}^\dagger_{\mathrm{d,z}} \to \sqrt{\eta_z}\hat{a}^\dagger_{\mathrm{d,z}} + \sqrt{1-\eta_z}\hat{a}^\dagger_{\mathrm{nd,z}} \tag{5.8}$$

$$\hat{a}^\dagger_{\mathrm{d,z}} \to \sqrt{\eta_b}\hat{a}^\dagger_{\mathrm{d,b}} + \sqrt{1-\eta_z}\hat{a}^\dagger_{\mathrm{nd,b}}. \tag{5.9}$$

where η_z is the total transmission efficiency from the NV to the central beam splitter while η_b is the total transmission and detection efficiency of the PSB photons. The operators $\hat{a}^\dagger_{\mathrm{nd,z}}$ and $\hat{a}^\dagger_{\mathrm{nd,b}}$ describe the lost/undetected modes. Tracing over the undetected modes, the output state of a single NV can be written as

$$\rho_\psi = \rho_0 \otimes |0\rangle \langle 0|_{\mathrm{d,b}} + \rho_1 \otimes |1\rangle \langle 1|_{\mathrm{d,b}} + \rho_2 \otimes |2\rangle \langle 2|_{\mathrm{d,b}}, \tag{5.10}$$

where we have neglected any coherence between the photonic PSB modes since these are accompanied by undetected non-radiative decay (phonon emission). The unnormalized density matrices ρ_0, ρ_1, and ρ_2 describe the state of the NV center communication qubit and the ZPL photons emitted in the time window of the ZPL detectors and transmitted to the central beam splitter. In the limit $\eta_z \ll 1$, we can neglect terms of $|2_{\mathrm{d,z}}\rangle$ and these density matrices will all be of the form

$$\rho_j = \sum_{i=1}^{4} |\phi_{i,j}\rangle \langle \phi_{i,j}|, \tag{5.11}$$

where $|\phi_{i,j}\rangle = (a_{i,j}|1\rangle + b_{i,j}|0\rangle)|0_z\rangle + c_{i,j}|0\rangle|1_{\mathrm{d,z}}\rangle$ and $j = 0,1,2$. In Eq. (5.11) i refers to the different number of lost undetected photons

$i = 1$, zero photons being lost
$i = 2$, one ZPL photon being lost
$i = 3$, one PSB photon being lost
$i = 4$, two photons being lost, either two ZPL, two PSB or one ZPL and one PSB

and j to the number of detected PSB photons. We note that all $a_{i,1}$ and $a_{i,2}$ will be zero since ρ_1 and ρ_2 are accompanied by PSB photons (see Eq. (5.10)) meaning that the NV was in state $|0\rangle$. Furthermore, the only non-zero term in ρ_2 will be $b_{i,2}$ since two PSB photons were emitted, meaning that no ZPL photon was emitted since we neglect higher order emissions.

The only term in Eq. (5.10) from which remote spin-spin entanglement between two NVs can be created is $\rho_0 \otimes |0\rangle \langle 0|_{\mathrm{d,b}}$ since this does not have any detected PSB photons. However, PSB and ZPL photons that were emitted but not detected will still decrease the entangled state fidelity. Such events are responsible for the contributions of $|\phi_{2,0}\rangle, |\phi_{3,0}\rangle$ and $|\phi_{4,0}\rangle$ in ρ_0. The only term where no PSB photons were emitted and no ZPL photons were undetected is $|\phi_{1,0}\rangle = \sqrt{1-\alpha}|1\rangle|0_{\mathrm{zpl}}\rangle + \sqrt{\alpha}|0\rangle(\sqrt{P_0}|0_{\mathrm{zpl}}\rangle + \sqrt{P_1 P_{\mathrm{zpl}} P_{\mathrm{d,zpl}}}|1_{\mathrm{d,zpl}}\rangle)$.

The combined state from the two NV centers before the central beam splitter is $\rho_\psi \otimes \tilde{\rho}_\psi$, where $\tilde{\rho}_\psi$ (the state of the second NV) is of the same form as in Eq.5.10 but including that parameters such as initial rotation (α), driving strength (Ω) and transmission efficiencies (η_z, η_b) can be different for the two centers. Furthermore, we include a phase difference between the two paths to the central beam splitter. The central beam splitter is modeled as a perfect 50:50 beam splitter and the finite detection efficiency of the output detectors is assumed to be equal and can be directly included in the transmission efficiencies (η_z)

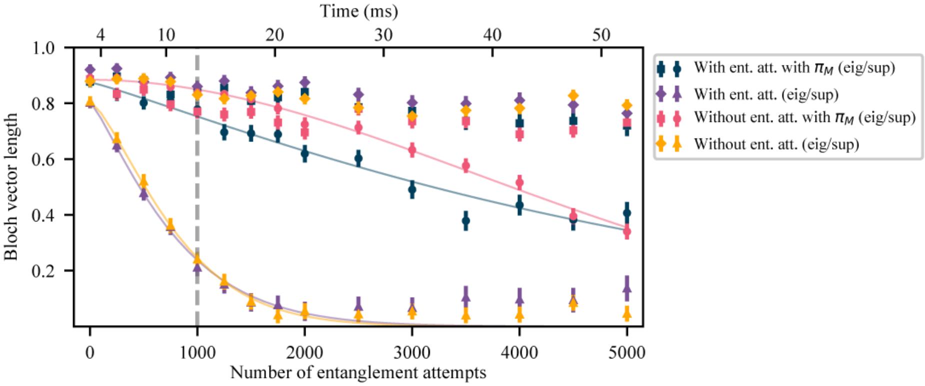

Figure 5.9: Coherence of Bob's memory qubit for superposition states (triangles and circles) and eigenstates (squares and diamonds). We perform the sequence as described in the main text with and without the decoupling pulse π_M on the memory qubit, the dark blue and purple points respectively. Additionally, we perform the sequence with a wait time instead of entanglement attempts with (pink points) and without the decoupling pulse (yellow points). The gray dashed line indicates the timeout of the entanglement generation process used in the teleportation protocol. All error bars represent one standard deviation.

while dark counts are negligible in the experiment and not included. Finally, we include non-perfect visibility between the ZPL photons by reducing the coherence between the output modes of the beam splitter by a factor v. This visibility is estimated from experimental data and can e.g. originate from slightly off-resonant driving of the NV centers.

5.7.4. MEMORY QUBIT COHERENCE BOB

We use the sequence described in Figure 3a of the main text to preserve the state of the memory qubit during entanglement attempts. To characterize the decoupling sequence, we compare it to the sequence where we do not apply the decoupling pulse on the memory qubit and/or the sequence where we idle instead of performing entanglement attempts. We characterize the coherence of the memory qubit by storing the six cardinal states. We average the results for the eigenstates ($|0\rangle, |1\rangle$) and superposition states ($|\pm X\rangle$ and $|\pm Y\rangle$). In Figure 5.9 we plot the Bloch vector length $b = \sqrt{b_x^2 + b_y^2 + b_z^2}$ with b_i the Bloch vector component in direction i.

Table 5.4: Fitted parameters for the memory coherence decay of the superposition states. All error bars represent one standard deviation.

	A	$N_{1/e}$	n
With ent. att. with π_M	0.875 ± 0.015	5327 ± 319	1.13 ± 0.11
With ent. att. without π_M	0.806 ± 0.019	848 ± 39	1.21 ± 0.09
Without ent. att. with π_m	0.884 ± 0.011	5239 ± 163	1.94 ± 0.16
Without ent. att. without π_M	0.807 ± 0.019	880 ± 34	1.37 ± 0.10

Over the measured range, the eigenstates show little decay. The decay of the superposition states is fitted with the function $f(x) = Ae^{-(x/N_{1/e})^n}$. The fitted parameters can be found in Table 5.4.

The use of the decoupling pulse π_M on the memory qubit increases the $N_{1/e}$ by more than a factor 6. Moreover, the initial Bloch vector length A is higher with the π_M pulse. This is mainly explained by the second round of phase stabilization [16] in between swapping the state onto the memory qubit and starting the entanglement generation process. The phase stabilization takes $\approx 350\mu$s and during this time the memory qubit is subject to intrinsic T_2^* dephasing, which can be efficiently decoupled using the π_M pulse.

5.7.5. COMMUNICATION QUBIT COHERENCE

In various parts of the protocol we decouple the communication qubits from the spin bath environment to extend their coherence time. On Alice, we start the decoupling when the first entangled link is established and stop when the results of the Bell-state measurement to teleport the state are sent by Charlie. On Bob, we decouple the communication qubit when the memory qubit is being re-phased. On Charlie, the communication qubit is decoupled from the point that entanglement with Bob is heralded up to the point where Bob has finished the Bell-state measurement, performed the CR check and has communicated the results. All these decoupling times are dependent on how many entanglement attempts are needed to generate the entangled link between Bob and Charlie.

Table 5.5: Fitted parameters for average state fidelity state during communication qubit decoupling. All error bars represent one standard deviation.

		A	$\tau_{coh}(s)$	n
Alice	Eigenstate	0.4930 ± 0.0013	0.459 ± 0.012	1.04 ± 0.03
	Superposition	0.4889 ± 0.0018	0.54 ± 0.02	1.07 ± 0.05
Bob	Eigenstate	0.4738 ± 0.0011	0.130 ± 0.003	1.41 ± 0.04
	Superposition	0.4634 ± 0.0015	0.177 ± 0.006	1.47 ± 0.06
Charlie	Eigenstate	0.4897 ± 0.0009	0.357 ± 0.007	1.67 ± 0.06
	Superposition	0.4936 ± 0.0019	0.56 ± 0.02	0.92 ± 0.04

We characterize the average state fidelities for different decoupling times, see Figure 5.10. We investigate eigenstates and superposition states separately. We fit the fidelity with the function $f(t) = Ae^{-(t/\tau_{coh})^n} + 0.5$. The fitted parameters are summarized in Table 5.5. For each setup, the minimum and maximum used decoupling times are indicated by the shaded regions in Figure 5.10. The left-most border is the decoupling time when the first entanglement attempt on Bob and Charlie would be successful, the right-most border when the last attempt before the timeout of 1000 attempts would herald the entangled state.

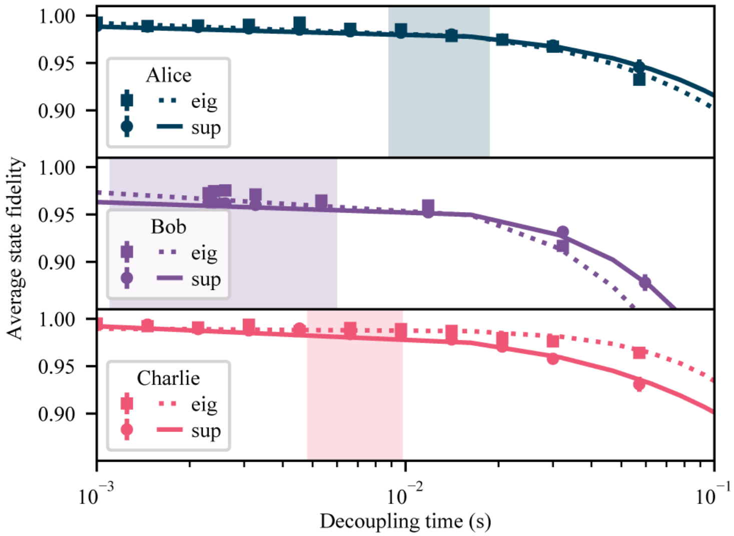

Figure 5.10: Decoupling of the communication qubits. The average state fidelity is plotted for different decoupling times for each setup. The shaded area represent the decoupling times used in the teleportation protocol. All error bars represent one standard deviation.

5.7.6. BASIS-ALTERNATING REPETITIVE READOUT

In the main text we discuss the basis-alternating repetitive readout and the results on Bob's memory qubit are shown in Figure 3. Here we show the results for Charlie's memory qubit. We assign the state using the first readout and only accept the result when the consecutive readouts give a consistent pattern. The results for two different initial states of the memory qubit are plotted in Figure 5.11. We model the expected performance with a Monte Carlo simulation which takes into account the electron readout fidelities, the initial state populations and gate errors, see [37]. In the case of unconditional teleportation, the state is assigned using the first readout and is accepted regardless of the second readout result.

5.7.7. TELEPORTATION RESULTS

The numerical values of the data displayed in Figures 4b and 4c in the main text can be found in Tables 5.6 and 5.7, respectively.

5.7.8. DATA ACQUISITION AND EXPERIMENTAL RATES

At multiple points during the experimental sequence we make a decision on whether to continue the protocol or not. For example, after successful heralding of a two-node entangled state, we can decide to abort the protocol based on whether the flag was raised by any detection of a PSB photon. As all these signals come in real-time, these decisions can be made in real-time, and the sequence can be aborted whenever appropriate. How-

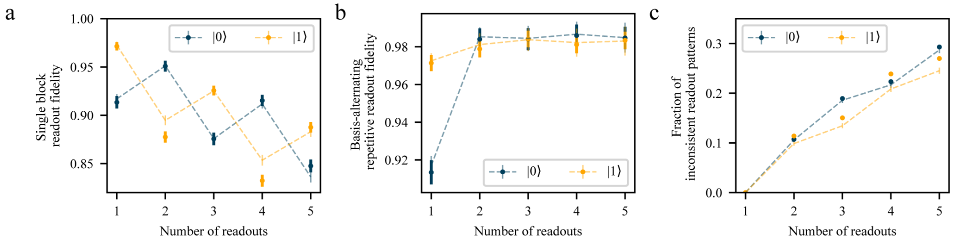

Figure 5.11: Basis-alternating repetitive (BAR) readout results for Charlie's memory qubit. **a** Measured fraction of memory qubit states that were assigned 0 per readout block, for initialization in |0⟩ and in |1⟩. **b** Readout fidelity of the basis-alternating repetitive readout scheme for different number of readout repetitions. **c** Fraction of inconsistent readout patterns for different number of readout repetitions. The dashed lines represent a numerical model using measured parameters. All error bars represent one standard deviation.

Table 5.6: Numerical values of the data displayed in Figure 4b of the main text. All error bars represent one standard deviation.

	Teleported state fidelity
X	0.760 ± 0.024
-X	0.745 ± 0.025
Y	0.656 ± 0.027
-Y	0.651 ± 0.027
Z	0.731 ± 0.026
-Z	0.671 ± 0.027
Average	0.702 ± 0.011

Table 5.7: Numerical values of the data displayed in Figure 4c of the main text. All error bars represent one standard deviation.

Bell-state measurement outcome (memory qubit, communication qubit)	Average teleported state fidelity
00	0.707 ± 0.015
01	0.696 ± 0.014
10	0.698 ± 0.015
11	0.671 ± 0.014
No feed forward	0.501 ± 0.007

ever, we choose to postpone these decisions to the processing after the data acquisition and continue the sequence in any case. In this way, we gain more insight in the performance of the experiment, at the expense of just a marginal increase in experimental time. Processing steps taken after the data acquisition:

- More precise temporal selection than 15 ns.
- PSB rejection.
- Selection of readout outcomes during the Bell-state measurements, including selection on consistent readout patterns for the memory qubit readout.
- Selection on successful Charge-Resonance checks during the sequence.
- Ensure that the last optical phase measurement (before feedback) prior to the heralding event is below $< 50^o$.
- High enough photon count rates on Alice during qubit initialization and optical pulsing, averaged over the second before the heralding signal comes in. (On Alice we perform gate tuning to keep the qubit on resonance with the control lasers. The gate tuning, in combination with the high repetition rate of entanglement attempts, makes the qubit spectrally jumpy. The control loops during the charge-resonance checks should ensure the resonance condition [36], but we use this live-tracking of the photon statistics as an extra check.)

To emphasize, all these processing steps can also be done real-time during the experiment. For the data acquisition, we interleave blocks of measurements with calibrations. The calibrations also serve as an independent measure of the performance of the setups.

We collect the data in blocks of 200 “raw” data points (taking roughly an hour), which result on average in about 30 data points per block after applying the processing steps. We analyzed the data only after completing all data acquisition. Prior to the measurement, we decided on the target total number of data points, the experimental settings, and the processing steps afterwards. The plan was to run a sufficient number of blocks (estimated at 80) such that after processing we would remain with >2,800 data points, and at least 450 per cardinal axis. These target numbers were a trade-off between measurement time and expected violation of the classical bound for the conditional teleportation. Unfortunately, after 80% of the data points were acquired, the setups consistently failed two of the calibrations steps due to the formation of ice on Charlie’s diamond sample (the origin of this, either a leak or an outgassing element, is under investigation at time of writing). Therefore, we decided to end the data acquisition, include all data taken up to that point and analyze. In total, we have acquired 79 blocks of data, and we measured 2272 events ($|+X\rangle$ 382, $|-X\rangle$ 385, $|+Y\rangle$ 385, $|-Y\rangle$ 378, $|+Z\rangle$ 375, $|-Z\rangle$ 367) for the conditional teleportation over a time span of 21 days.

We can determine the experimental rate including all overhead (such as CR checks, communication time and phase stabilization) by dividing the number of measured data points by the total measurement time. In Figure 5.12 we plot the experimental rate for both the conditional and unconditional teleportation sequence. In the case of the unconditional teleportation, we accept all Bell-state measurement outcomes on Charlie and therefore the experimental rate is higher. For shorter detection windows during the two-node en-

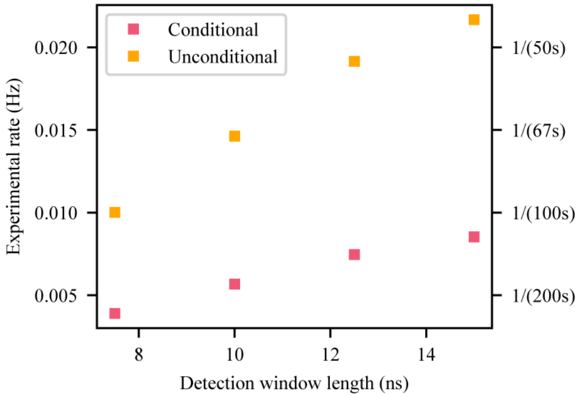

Figure 5.12: Experimental rates of the conditional and unconditional teleportation protocol for different detection window lengths in the two-node entanglement generation.

tanglement, the success probability per attempt is smaller and thus the experimental rate is lower.

5.7.9. MODEL OF THE TELEPORTED STATE

A detailed model of the teleported state can be found at [37]. The model comprises elements from [16] and is further extended for the teleportation protocol. We take the following noise sources into account

- imperfect Bell states between Alice and Bob, and between Bob and Charlie,
- dephasing of the memory qubit of Bob during entanglement generation between Bob and Charlie,
- depolarizing noise on the memory qubits of Bob and Charlie, due to imperfect initialization and swap gates,
- readout errors on the communication qubits of Bob and Charlie and readouts errors on the memory qubits of Bob and Charlie when using the basis-alternating readout scheme which result in incorrect feed-forward gate operations after the Bell-state measurements,
- depolarizing noise on Alice during the decoupling sequence,
- ionization probability on Alice.

An overview of the input parameters and the effect of the different error sources is given in Tables 5.8 and 5.9.

5.7.10. EFFECT OF THE 3 KEY INNOVATIONS ON THE TELEPORTED STATE FIDELITY AND EXPERIMENTAL RATE

We assess the effect of each innovation on the teleportation protocol. First, we estimate the average state fidelity and experimental rate with a set of baseline parameters based

Table 5.8: Overview of parameters used in the simulations for the two-node entangled states. The error due to the $|0\rangle$ state populations is a result of the single click protocol. For the other error sources we compute the estimated infidelity as if it was the only error source present apart from the protocol error. This allows easy comparison between the different error sources.

	Parameter AB	Parameter BC	Infidelity Ψ_{AB}	Infidelity Ψ_{BC}
Detection window length	15 ns	15 ns		
Detection probability setup 1	3.4×10^{-4}	4.3×10^{-4}		
Detection probability setup 2	5.1×10^{-4}	2.4×10^{-4}		
Average detection probability PSB	0.10	0.12		
$|0\rangle$ state populations (α_1, α_2)	(0.07, 0.05)	(0.05, 0.1)	5.5×10^{-2}	6.7×10^{-2}
Dark count rate	10 Hz	10 Hz	5.1×10^{-3}	5.3×10^{-3}
Visibility	0.90	0.90	2.4×10^{-2}	2.4×10^{-2}
Average double excitation probability	0.06	0.08	5.5×10^{-2}	7.1×10^{-2}
Optical phase uncertainty	21^o	12^o	3.1×10^{-2}	1.0×10^{-2}
All error sources combined			0.16	0.17

on the performance in [16]. We use a timeout of 1000 entanglement attempts for the second link (between Bob and Charlie) before aborting the protocol and starting over. In both Bell-state measurements, we continue the sequence for the outcomes "00" and "01" (communication qubit, memory qubit), or abort and start over (in the case of conditional teleportation). Then we incrementally add (1) the basis-alternating repetitive readout scheme for the memory qubits,(2) the improved memory qubit coherence and (3) the tailored heralding scheme of the remote entanglement generation. The results are summarized in 5.10.

5.7.11. ESTIMATED FIDELITY OF STATE TO BE TELEPORTED

The state to be teleported is prepared on the communication qubit of Charlie. Errors in the preparation originate from imperfect initialization and imperfect MW pulses, which are estimated to be $p_{init} = 1.2\times10^{-3}$ and $p_{MW} = 8\times10^{-3}$ [38]. Averaged over the six cardinal states, we estimate the state preparation fidelity to be ≈ 0.995.

5.7.12. CALCULATION OF TELEPORTED STATE FIDELITY WITHOUT FEED-FORWARD OPERATION

Calculation of teleported state fidelity without feed - forward operation In figure 4c in the main text we show the fidelity of the teleported state in case no feed-forward operations would have been applied on Alice. To extract this data we follow the same method as in [11]. We perform classical bit flips on the measurement outcomes to counteract the effect of the feed-forward gate operations (as if the gate was not applied) for each Bell-state measurement outcome. We do this for all six cardinal states and compute the average fidelity. We assume the errors of the gate in the feed-forward operations to be small.

Table 5.9: Overview of parameters used in the simulations for the average teleported state fidelity in case of a conditional Bell-state measurement on Charlie. For each error sources we compute the estimated infidelity as if it was the only error source present apart from the single click protocol errors of the two-node entangled states. This allows easy comparison between the different error sources.

	Parameter	Infidelity
Ionization probability Alice	0.7%	0.6×10^{-2}
Depolarizing noise Alice	0.04	1.7×10^{-2}
Depolarizing noise memory qubit Bob	0.12	5.0×10^{-2}
Dephasing noise memory qubit Bob ($N_{1/e}, n$)	(5300, 1.1)	2.1×10^{-2}
Depolarizing noise memory qubit Charlie	0.14	5.9×10^{-2}
Readout fidelities memory qubit Bob ($\left\|0\right\rangle, \left\|1\right\rangle$)	(0.99, 0.99)	0.6×10^{-2}
Readout fidelities communication qubit Bob ($\left\|0\right\rangle, \left\|1\right\rangle$)	(0.93, 0.995)	0.3×10^{-2}
Readout fidelities memory qubit Charlie ($\left\|0\right\rangle, \left\|1\right\rangle$)	(0.98, 0.98)	1.1×10^{-2}
Readout fidelities communication qubit Charlie ($\left\|0\right\rangle, \left\|1\right\rangle$)	(0.92, 0.99)	0.6×10^{-2}
Two-node entangled states combined		0.192
All error sources combined		0.305

Table 5.10: Simulated effect of the innovations on the teleported state fidelity and experimental rate.

	Fidelity	Rate (Hz)
Baseline parameters using timeout = 1000, BSM outcomes (communication qubit, memory qubit) = "00" or "01"	0.666	1/(53s)
With basis-alternating repetitive readout	0.679	1/(73s)
With improved memory coherence	0.687	1/(73s)
With tailored heralding scheme	0.695	1/(74s)

REFERENCES

[1] C. H. Bennett, G. Brassard, C. Crépeau, R. Jozsa, A. Peres, and W. K. Wootters, *Teleporting an unknown quantum state via dual classical and Einstein-Podolsky-Rosen channels,* Physical Review Letters **70**, 1895 (1993).

[2] S. Wehner, D. Elkouss, and R. Hanson, *Quantum internet: A vision for the road ahead,* Science **362** (2018).

[3] M. Ben-Or, C. Crépeau, D. Gottesman, A. Hassidim, and A. Smith, *Secure multiparty quantum computation with (only) a strict honest majority,* Proceedings - Annual IEEE Symposium on Foundations of Computer Science, FOCS , 249 (2006).

[4] A. S. Arora, J. Roland, and S. Weis, *Quantum weak coin flipping,* Proceedings of the Annual ACM Symposium on Theory of Computing , 205 (2019).

[5] D. Bouwmeester, J. W. Pan, K. Mattle, M. Eibl, H. Weinfurter, and A. Zeilinger, *Experimental quantum teleportation,* Philosophical Transactions of the Royal Society A: Mathematical, Physical and Engineering Sciences **356**, 1733 (1997).

[6] D. Boschi, S. Branca, F. D. Martini, L. Hardy, and S. Popescu, *Experimental Realization of Teleporting an Unknown Pure Quantum State via Dual Classical and Einstein-Podolsky-Rosen Channels,* Physical Review Letters **80**, 1121(5) (1998).

[7] A. Furusawa, J. L. Sørensen, S. L. Braunstein, C. A. Fuchs, H. J. Kimble, and E. S. Polzik, *Unconditional quantum teleportation,* Science **282**, 706 (1998).

[8] S. Olmschenk, D. N. Matsukevich, P. Maunz, D. Hayes, and C. Monroe, *Quantum Teleportation between Distant Matter Qubits,* Science **323**, 486 (2009).

[9] C. Nölleke, A. Neuzner, A. Reiserer, C. Hahn, G. Rempe, and S. Ritter, *Efficient teleportation between remote single-atom quantum memories,* Physical Review Letters **110**, 1 (2013).

[10] S. Langenfeld, S. Welte, L. Hartung, S. Daiss, P. Thomas, O. Morin, E. Distante, and G. Rempe, *Quantum Teleportation between Remote Qubit Memories with only a Single Photon as a Resource,* Physical Review Letters **126**, 130502 (2021).

[11] W. Pfaff, B. J. Hensen, H. Bernien, S. B. Van Dam, M. S. Blok, T. H. Taminiau, M. J. Tiggelman, R. N. Schouten, M. Markham, D. J. Twitchen, and R. Hanson, *Unconditional quantum teleportation between distant solid-state quantum bits,* Science **345**, 532 (2014).

[12] X. H. Bao, X. F. Xu, C. M. Li, Z. S. Yuan, C. Y. Lu, and J. W. Pan, *Quantum teleportation between remote atomic-ensemble quantum memories,* Proceedings of the National Academy of Sciences of the United States of America **109**, 20347 (2012).

[13] H. Briegel, W. Dür, J. I. Cirac, and P. Zoller, *Quantum Repeaters The Role of Imperfect Local Operations in Quantum Communication,* Physical Review Letters **81**, 5932 (1998).

[14] C. Cabrillo, J. I. Cirac, P. Garcia-Fernandez, and P. Zoller, *Creation of entangled states of distant atoms by interference,* Physical Review A **59**, 1025 (1999).

[15] S. Bose, P. L. Knight, M. B. Plenio, and V. Vedral, *Proposal for teleportation of an atomic state via cavity decay,* Physical Review Letters **83**, 5158 (1999).

[16] M. Pompili, S. L. Hermans, S. Baier, H. K. Beukers, P. C. Humphreys, R. N. Schouten, R. F. Vermeulen, M. J. Tiggelman, L. dos Santos Martins, B. Dirkse, S. Wehner, and R. Hanson, *Realization of a multinode quantum network of remote solid-state qubits,* Science **372**, 259 (2021).

[17] P. C. Humphreys, N. Kalb, J. P. Morits, R. N. Schouten, R. F. Vermeulen, D. J. Twitchen, M. Markham, and R. Hanson, *Deterministic delivery of remote entanglement on a quantum network,* Nature **558**, 268 (2018).

[18] T. Legero, T. Wilk, A. Kuhn, and G. Rempe, *Time-resolved two-photon quantum interference,* Applied Physics B: Lasers and Optics **77**, 797 (2003).

[19] C. E. Bradley, J. Randall, M. H. Abobeih, R. C. Berrevoets, M. J. Degen, M. A. Bakker, M. Markham, D. J. Twitchen, and T. H. Taminiau, *A Ten-Qubit Solid-State Spin Register with Quantum Memory up to One Minute,* Physical Review X **9**, 31045 (2019).

[20] J. Cramer, N. Kalb, M. S. Blok, M. A. Rol, T. H. Taminiau, M. Markham, B. Hensen, R. Hanson, and D. J. Twitchen, *Repeated quantum error correction on a continuously encoded qubit by real-time feedback,* Nature Communications **7**, 1 (2016).

[21] L. Robledo, L. Childress, H. Bernien, B. Hensen, P. F. A. Alkemade, and R. Hanson, *High-fidelity projective read-out of a solid-state spin quantum register,* Nature , 5 (2011).

[22] L. Jiang, J. M. Taylor, K. Nemoto, W. J. Munro, R. Van Meter, and M. D. Lukin, *Quantum repeater with encoding,* Physical Review A **79**, 1 (2009).

[23] S. J. Van Enk, N. Lütkenhaus, and H. J. Kimble, *Experimental procedures for entanglement verification,* Physical Review A **75**, 1 (2007).

[24] R. Van Meter, *Quantum Networking* (John Wiley & Sons, Inc., 2014).

[25] A. Broadbent, J. Fitzsimons, and E. Kashefi, *Universal blind quantum computation,* Proceedings - Annual IEEE Symposium on Foundations of Computer Science, FOCS , 517 (2009).

[26] B. C. Rose, D. Huang, Z. H. Zhang, P. Stevenson, A. M. Tyryshkin, S. Sangtawesin, S. Srinivasan, L. Loudin, M. L. Markham, A. M. Edmonds, D. J. Twitchen, S. A. Lyon, and N. P. De Leon, *Observation of an environmentally insensitive solid-state spin defect in diamond,* Science **361**, 60 (2018).

[27] C. T. Nguyen, D. D. Sukachev, M. K. Bhaskar, B. MacHielse, D. S. Levonian, E. N. Knall, P. Stroganov, R. Riedinger, H. Park, M. Lončar, and M. D. Lukin, *Quantum Network Nodes Based on Diamond Qubits with an Efficient Nanophotonic Interface,* Physical Review Letters **123**, 1 (2019).

[28] M. E. Trusheim, B. Pingault, N. H. Wan, M. Gündoğan, L. De Santis, R. Debroux, D. Gangloff, C. Purser, K. C. Chen, M. Walsh, J. J. Rose, J. N. Becker, B. Lienhard, E. Bersin, I. Paradeisanos, G. Wang, D. Lyzwa, A. R. Montblanch, G. Malladi, H. Bakhru, A. C. Ferrari, I. A. Walmsley, M. Atatüre, and D. Englund, *Transform-Limited Photons from a Coherent Tin-Vacancy Spin in Diamond,* Physical Review Letters **124**, 1 (2020).

[29] N. T. Son, C. P. Anderson, A. Bourassa, K. C. Miao, C. Babin, M. Widmann, M. Niethammer, J. Ul Hassan, N. Morioka, I. G. Ivanov, F. Kaiser, J. Wrachtrup, and D. D. Awschalom, *Developing silicon carbide for quantum spintronics,* Applied Physics Letters **116**, 190501 (2020).

[30] D. M. Lukin, M. A. Guidry, and J. Vučković, *Integrated Quantum Photonics with Silicon Carbide: Challenges and Prospects,* PRX Quantum **1**, 1 (2020).

[31] J. M. Kindem, A. Ruskuc, J. G. Bartholomew, J. Rochman, Y. Q. Huan, and A. Faraon, *Control and single-shot readout of an ion embedded in a nanophotonic cavity,* Nature **580** (2020).

[32] S. Chen, M. Raha, C. M. Phenicie, S. Ourari, and J. D. Thompson, *Parallel single-shot measurement and coherent control of solid-state spins below the diffraction limit,* Science **370**, 592 (2020).

[33] M. Ruf, N. H. Wan, H. Choi, D. Englund, and R. Hanson, *Quantum networks based on color centers in diamond,* Journal of Applied Physics **130**, 070901 (2021).

[34] M. E. Grein, M. L. Stevens, N. D. Hardy, and P. Benjamin Dixon, *Stabilization of long, deployed optical fiber links for quantum networks,* 2017 Conference on Lasers and Electro-Optics, CLEO 2017 - Proceedings , 1 (2017).

[35] A. Dahlberg, M. Skrzypczyk, T. Coopmans, L. Wubben, F. Rozpdek, M. Pompili, A. Stolk, P. Pawelczak, R. Knegjens, J. De Oliveira Filho, R. Hanson, and S. Wehner, *A link layer protocol for quantum networks,* SIGCOMM 2019 - Proceedings of the 2019 Conference of the ACM Special Interest Group on Data Communication , 159 (2019).

[36] B. Hensen, H. Bernien, A. E. Dreaú, A. Reiserer, N. Kalb, M. S. Blok, J. Ruitenberg, R. F. Vermeulen, R. N. Schouten, C. Abellán, W. Amaya, V. Pruneri, M. W. Mitchell, M. Markham, D. J. Twitchen, D. Elkouss, S. Wehner, T. H. Taminiau, and R. Hanson, *Loophole-free Bell inequality violation using electron spins separated by 1.3 kilometres,* Nature **526**, 682 (2015).

[37] S. Hermans, M. Pompili, H. Beukers, S. Baier, J. Borregaard, and R. Hanson, *Data and software supporting "qubit teleportation between non-neighboring nodes in a quantum network",* (2021).

[38] N. Kalb, P. C. Humphreys, J. J. Slim, and R. Hanson, *Dephasing mechanisms of diamond-based nuclear-spin memories for quantum networks,* Physical Review A **97**, 1 (2018).

6

ENTANGLING REMOTE QUBITS USING THE SINGLE-PHOTON PROTOCOL: AN IN-DEPTH THEORETICAL AND EXPERIMENTAL STUDY

S. L. N. Hermans, M. Pompili, L. Dos Santos Martins, A. Rodriguez-Pardo Montblanch, H. K. C. Beukers, S. Baier, J. Borregaard & R. Hanson

The ability to generate entanglement between remote matter qubits has developed into a key capability for fundamental investigations as well as for emerging quantum technologies. In the single-photon protocol, initially proposed by Cabrillo et. al., entanglement is heralded by generation of qubit-photon entangled states and subsequent detection of a single photon behind a beam splitter. In this work we perform a detailed theoretical and experimental investigation of this protocol and the various sources of infidelity. We develop an extensive theoretical model and subsequently tailor it to our experimental setting, using nitrogen-vacancy centers in diamond. Experimentally, we verify the model by generating remote states for varying phase and amplitudes of the initial qubit superposition states and varying optical phase difference of the photons arriving at the beam splitter. We show that a static frequency offset between the optical transitions of the qubits leads to an entangled state phase that depends on the photon detection time. We find that the implementation of a Charge-Resonance check on the NV center yields transform-limited linewidths. Moreover, we measure the probability of double optical excitation as a function of the power of the excitation pulse. Finally, we find that non-perfect optical excitation can lead to a detection-arm dependent entangled state fidelity and rate. Even though the experiments were carried using nitrogen-vacancy centers in diamond, the conclusions presented here are readily applicable to other qubit platforms.

6.1. INTRODUCTION

Entanglement between different nodes will be an essential element of future quantum networks. Entangled states will serve as a key ingredient for many applications, such as secure communication, distributed quantum computations and advanced quantum network protocols [1–7]. Remote entanglement between distant nodes can be generated using different protocols. One of these protocols, the single-photon protocol based on emitted photons encoded in number states [8, 9], is especially suited to establish entanglement between distant stationary qubits with high generation rates in the presence of significant photon loss. Since a single photon only has to travel half of the distance between the emitters, photon loss scales with the square root of the distance, as opposed to the linear loss scaling of direct photon transmission and of two-photon entangling protocols [10]. The single-photon protocol has been implemented on various qubit platforms, such as electron and hole spins in quantum dots, nitrogen-vacancy centers in diamond and atomic ensembles in rare-earth-ion doped crystals [11–14].

The single-photon protocol works as follows. Two remote qubits are both prepared in a superposition state $\sqrt{\alpha}\,|0\rangle + \sqrt{1-\alpha}\,|1\rangle$. State-selective excitation of $|0\rangle$, the bright state, creates a qubit-photon entangled state. Interference of both photon states on a beam splitter erases the which-path information. Detection of a single photon projects the two remote qubits into an entangled state $|\Psi\rangle = \frac{1}{\sqrt{2}}(|01\rangle + |10\rangle)$. However, in the presence of photon loss we cannot discriminate between the emission of a single photon and the case that both qubits were in the bright state $|00\rangle$ and emitted a photon but one photon was lost. The latter events will falsely herald entanglement and reduce the average fidelity. In the high photon-loss regime, given the detection of one photon, the probability both qubits are in the bright state is given by the initial population in $|0\rangle$, α. Hence the average heralded density matrix will be $\rho = (1-\alpha)\,|\Psi\rangle\langle\Psi| + \alpha\,|00\rangle\langle 00|$, with a fidelity of $F = 1-\alpha$ with respect to the maximally entangled state.

Apart from the infidelity caused by the protocol, other sources of error can degrade the heralded state. In this paper we provide a detailed theoretical and experimental study of error sources and characteristics associated with the single-photon protocol.

The paper is structured in the following way. In Section 6.2 we describe the single-photon entanglement protocol step-by-step for a general experimental setting and we develop a model describing the effect of experimental imperfections. We introduce our experimental system, nitrogen-vacancy (NV) centers in diamond, in Section 6.3 and we tailor the model to our system in Section 6.4. Afterwards, we discuss the effect of various parameters on the heralded state; the bright state population (Section 6.5), the phase of the entangled state (Section 6.6), photon indistinguishability (Section 6.7), double optical excitation (Section 6.8) and non-excited ground state population (Section 6.9). We conclude in Section 6.10.

Even though we discuss an implementation using NV centers, this work contributes to a better understanding of the effect of general experimental imperfections and its platform-independent insights can be used to improve entanglement generation on var-

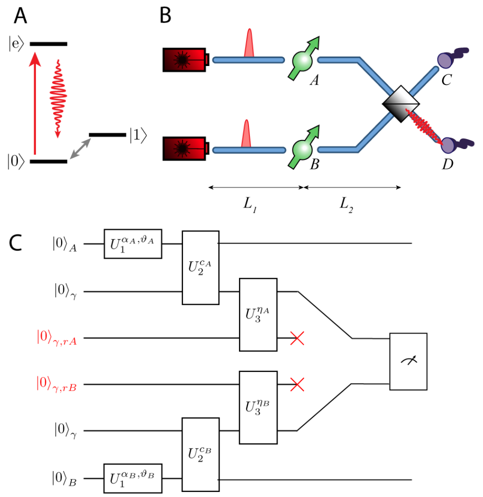

Figure 6.1: **Simplified level structure, generalized experimental layout and overview of unitary operations.** **(A)** L-scheme level structure for the single-photon entanglement protocol. Two ground states are defined as the qubit subspace $|0\rangle$ and $|1\rangle$, and we can drive the transition between them. Furthermore, $|0\rangle$ is optically connected to an excited state $|e\rangle$. **(B)** In a generalized experimental layout, excitation pulses are sent to the two qubits and emitted photons are led to a beam splitter. The output ports C and D of the beam splitter are connected to two single photon detectors. $L_{1,i}$ and $L_{2,i}$ are the distances between the point of creation of the laser pulse and the qubit, and between the qubit and the beam splitter respectively. **(C)** Gate circuit with an overview of the unitary operations described in the text.

ious platforms.

6.2. THE SINGLE-PHOTON ENTANGLEMENT PROTOCOL

In this section we provide a step-by-step derivation of an average heralded state using the single-photon protocol. Figure 6.1A shows an example of the energy levels used by the protocol, in this work we employ a L-scheme for the optical excitation. We would like to emphasize that the single-photon entanglement protocol can also be executed with a Lambda (or Raman) excitation scheme. In that case the optical excitation induces the qubit to flip [8]. In this research we develop our model for the implementation of the L-scheme, as indicated in Figure 6.1A. We label two levels $|0\rangle$ and $|1\rangle$ as our qubit subspace, and can coherently drive the transition between them to create any superposition. Furthermore, one of the ground states is connected to an optically excited state, allowing for state-selective excitation and qubit-photon entanglement. We give a general experimental layout in Figure 6.1B. In this section we describe the various unitaries acting on the single qubit and the photon detection which heralds the entangled state, see Figure 6.1C.

We work in the rotating frame of the emitters and we start with both qubits initialized in the $|0\rangle$ ground state

$$|\Psi_0\rangle_A \otimes |\Psi_0\rangle_B = |0\rangle_A \otimes |0\rangle_B \,. \tag{6.1}$$

Next we create a superposition state on each of the qubits using the unitary

$$U_1^{\alpha_i,\vartheta_i}: |0\rangle \rightarrow \sqrt{\alpha_i}\,|0\rangle + \sqrt{1-\alpha_i}\,e^{-i\vartheta_i}\,|1\rangle\,. \tag{6.2}$$

In unitary U_1^{α,ϑ_i} α_i denotes the population in $|0\rangle$, i.e. the bright state, and ϑ_i represents the phase of the superposition state. At time $t_{e1,i}$, the qubit will be state-selectively excited by exposure to the excitation laser. Subsequent decay to the ground state will result in the emission of a photon at time $t_{s,i}$. At a later point in the protocol, we will describe the detection of a photon at time t, therefore we can already write the photon state as being emitted in that specific mode

$$\begin{aligned}\zeta_i(t_{e1,i}) =& c_{e,i}\vec{\epsilon}_i\mathscr{E}_i(t)e^{-i(\omega_i(t-t_s)-k_i(x-L_1)+\phi_{l,i}+\omega_i(t_s-t_e)+\pi/2)}\\ =& c_{e,i}\vec{\epsilon}_i\mathscr{E}_i(t)e^{-i(\omega_i(t-t_e)-k_i(x-L_1)+\phi_{l,i}+\pi/2)}\end{aligned} \tag{6.3}$$

In Eq. (6.3), $|c_{e,i}|^2$ is the probability to transfer the population to the excited state $|e\rangle$, $\vec{\epsilon}_i$ denotes the polarization of the emitted photon, ω_i is the transition frequency $|0\rangle \rightarrow |e\rangle$ with the corresponding wavenumber k_i, $\phi_{l,i}$ is the phase of laser imprinted on the photon and $\mathscr{E}_i(t)$ is the temporal envelope. For spontaneous decay, this envelope can be modelled as

$$\mathscr{E}_i(t) = \frac{H(t-t_{e1,i})e^{-(t_{e1,i}-t_{s1,i})/2\tau}}{\sqrt{\tau}}, \tag{6.4}$$

with τ the excited state lifetime and $H(t)$ the heaviside function. In practice, the excitation laser pulse has a finite duration and therefore re-excitation of the qubit is possible in case the first decay happens during the optical pulse (we ignore any higher-order emissions). We write the joint photonic mode as $\zeta_{ii}(t_{e1,i}, t_{e2,i})$ and define the double excitation probability as $|c_{ee,i}|^2$ [15, 16]. Again we assume the detection times of both photons to be known (In the presence of photon loss a more correct way to describe the joint photon mode would $\int_{t_{e,1}}^{t_{s,1}} \zeta_1(\tilde{t})d\tilde{t}\zeta_2(t)$, where $t_{e,2} > t_{s,1}$ and $t_{e,2}$ is lies within the duration of the optical pulse. However if a heralding detection window is set to start after the optical pulse any effect of this will be small). Together with the probability to remain in the ground state $|0\rangle$, $c_{0,i}$, the unitary describing the state-selective excitation and emission can be written as

$$U_2^{c_i}: \begin{cases} |0\rangle\,|0\rangle_\gamma \rightarrow |0\rangle \otimes (c_0\,|0\rangle_\gamma + \zeta_i\hat{a}_{1,i}^\dagger\,|0\rangle_\gamma + \zeta_{ii}\hat{a}_{2,i}^\dagger\hat{a}_{1,i}^\dagger\,|0\rangle_\gamma), \\ |1\rangle\,|0\rangle_\gamma \rightarrow |1\rangle\,|0\rangle_\gamma\,, \end{cases} \tag{6.5}$$

where $\hat{a}^\dagger$ is the photon creation operator. The emitted photons are subject to losses, we assume that the losses are equal for all the photons associated with one of the nodes. We use a beam splitter transformation U_3^η to model photon loss

$$U_3^\eta: \hat{a}_i^\dagger\,|0\rangle_\gamma \rightarrow \sqrt{\eta}\hat{a}_{out,i}^\dagger\,|0\rangle_\gamma + \sqrt{1-\eta}\hat{a}_{r,i}^\dagger\,|0\rangle_\gamma\,. \tag{6.6}$$

$\hat{a}_{r,i}^\dagger$ creates a photon in the loss mode $|0\rangle_{\gamma,r}$. We omit the *out* subscript for brevity. The (separable) state in front of the beam splitter will then be given by

$$|\Psi_3\rangle_{AB} = U_3^{\eta_A}U_2^{c_A}U_1^{\alpha_A,\vartheta_A}\,|0\rangle_A \otimes U_3^{\eta_B}U_2^{c_B}U_1^{\alpha_B,\vartheta_B}\,|0\rangle_B\,. \tag{6.7}$$

Let us now turn to the detection. Due to photon loss, double excitation and the presence of noise counts, different detection patterns are possible. We use non-number resolving single photon detectors and we can reject any repetition in which two photons are detected in different detectors, as these events suggest either double excitation or both qubits being in the bright states. Furthermore in the presence of modest losses, we assume maximally two photons arriving at the beam splitter. We treat all the detection patterns separately and later on combine the result to obtain the average heralded density matrix.

Single photon - The first detection pattern we consider is the case where one photon is emitted and one photon is detected. For a detection at time t in port C of the beam splitter, we model the detection by projecting the state onto $\langle 0|_\gamma \hat{a}_{1,C}$. Due to the beam splitter this leads to a linear combination of detecting a photon originating from node A or B

$$\langle 0|_\gamma \hat{a}_{1,C} = \frac{1}{\sqrt{2}} \langle 0|_\gamma \left(\hat{a}_{1,A} + \hat{a}_{1,B}\right). \tag{6.8}$$

Similarly we can define the projector for detecting a photon in port D as

$$\langle 0|_\gamma \hat{a}_{1,D} = \frac{1}{\sqrt{2}} \langle 0|_\gamma \left(\hat{a}_{1,A} - \hat{a}_{1,B}\right). \tag{6.9}$$

For detecting a photon in port C, the corresponding (unnormalized) density matrix is given by

$$\rho_1 = \langle 0|_\gamma \hat{a}_{1,C} |\Psi_3\rangle \langle \Psi_3|_{AB} \hat{a}^\dagger_{1,C} |0\rangle_\gamma \tag{6.10}$$

Two photons - Secondly, we deal with the case where two photons are emitted and both photons arrive at the beam splitter. The first photon will be detected in port C at time t and the second photon at time $t + t0$, also in port C. The projector is then given by

$$\langle 0|_\gamma \hat{a}_{1,C}\hat{a}_{2,C} = \frac{1}{2} \langle 0|_\gamma \left(\hat{a}_{1,A} + \hat{a}_{1,B}\right)\left(\hat{a}_{2,A} + \hat{a}_{2,B}\right), \tag{6.11}$$

and we obtain

$$\rho_2 = \langle 0|_\gamma \hat{a}_{1,C}\hat{a}_{2,C} |\Psi_3\rangle \langle \Psi_3|_{AB} \hat{a}^\dagger_{2,C}\hat{a}^\dagger_{1,C} |0\rangle_\gamma, \tag{6.12}$$

again a unnormalized density matrix.

At least one lost photon - When at least one photon is lost, detection of any remaining photon will falsely herald entanglement. This cannot lead to coherence between the qubit states and therefore we can project on each detection pattern separately and sum over the resulting density matrices

$$\rho_{\text{incoherent}} = \sum_{i,j} \rho_{r,i,j}. \tag{6.13}$$

Since the detection time of the lost photon is unknown we can integrate over all possible times, for example $|\int \zeta_i(t_r)dt_r| = |c_{e,i}|^2$.

Noise photon - A detector dark count or stray light will additionally lead to falsely heralded entangled states. We assume the contribution of such noise counts small compared to actual signal photons and we assume that a noise count can solely cause a detection event in the absence of a signal photon. We distinguish two scenarios; no photon is emitted, or none of the emitted photons arrived at the beam splitter. The first scenario leads to a separable state, but the single qubit coherence is not lost, while the latter projects the corresponding qubit state and its coherence is lost. We can deal with these two scenarios separately. By projecting on the vacuum state $|0\rangle_\gamma$, we get the density matrix

$$\rho_0 = |\Psi_0\rangle\langle\Psi_0|_A \otimes |\Psi_0\rangle\langle\Psi_0|_B, \tag{6.14}$$

with

$$|\Psi_0\rangle_i = (\sqrt{\alpha_i}c_{0,i}|0\rangle + e^{-i\vartheta_i}\sqrt{1-\alpha_i}|1\rangle). \tag{6.15}$$

On the contrary, when none of the emitted photons arrive at the beam splitter, we can trace over all the lost photons to obtain

$$\rho_r = \sum_{i,j}\rho_{i,j}. \tag{6.16}$$

We add the two noise contributions and multiply by the probability for a noise count being detected, p_d and construct

$$\rho_{\text{noise}} = p_d(\rho_0 + \rho_r). \tag{6.17}$$

Having discussed all the detection patterns we can finally combine all the contributions to extract the probability to get a detection event in port C

$$p_{\text{click,C}} = \text{Tr}(\rho_1) + \text{Tr}(\rho_2) + \text{Tr}(\rho_{\text{incoherent}}) + \text{Tr}(\rho_{\text{noise}}). \tag{6.18}$$

We add all the density matrices and normalize using the detection probability $p_{\text{click,C}}$ and we obtain an expression for the average density matrix ρ_C heralded by a detection in port C

$$\rho_C = \frac{1}{p_{\text{click,C}}}(\rho_1 + \rho_2 + \rho_{\text{incoherent}} + \rho_{\text{noise}}). \tag{6.19}$$

In Appendix 6.11.1, we provide the full description of the density matrix.

In the introduction we discussed the expected fidelity in the high loss regime and here we check that our model matches the intuitive result. In the limit of high photon loss ($\eta \ll 1$), equal experimental settings ($\eta_A = \eta_B \equiv \eta$ and $\alpha_A = \alpha_B \equiv \alpha$), perfect optical excitation pulses $|c_{e,i}|^2$, perfectly indistinguishable photons with equal optical phase upon arrival at the beam splitter $\zeta_A = \zeta_B$ and absence of noise counts p_d, we can simplify the results to

$$\begin{aligned} p_{\text{click},\eta\ll 1,C} =& \operatorname{Tr}\big(\rho_1\big) + \operatorname{Tr}\big(\rho_{\text{incoherent}}\big) \\ =& \alpha(1-\alpha)\eta|\zeta(t)|^2 + \alpha^2\eta|\zeta(t)|^2 \\ =& \alpha\eta|\zeta(t)|^2 \end{aligned} \tag{6.20}$$

and $\eta|\zeta(t)|^2$ can be interpreted as the probability to detect a photon in the detection window. The density matrix can be written as

$$\begin{aligned} \rho_{\eta\ll 1,C} =& \frac{1}{p_{\text{click},\eta\ll 1,C}}\left(\rho_1 + \rho_{\text{incoherent}}\right), \\ =& \frac{\alpha(1-\alpha)\eta|\zeta(t)|^2}{p_{\text{click},\eta\ll 1,C}} \left|\Psi\right\rangle\left\langle\Psi\right| + \frac{\alpha^2\eta|\zeta(t)|^2}{p_{\text{click},\eta\ll 1,C}} \left|00\right\rangle\left\langle 00\right|, \\ =& (1-\alpha)\left|\Psi\right\rangle\left\langle\Psi\right| + \alpha\left|00\right\rangle\left\langle 00\right|, \end{aligned} \tag{6.21}$$

where $|\Psi\rangle = \frac{1}{\sqrt{2}}(|01\rangle + |10\rangle)$, the maximally entangled Bell state, matching exactly our intuitive prediction presented in Section 6.1.

6.3. EXPERIMENTAL SETUP: NV CENTERS

In this work we use nitrogen-vacancy centers (NV$^-$) in bulk diamond. This defect consists of a substitutional nitrogen-atom with the adjacent lattice site left vacant. In the negative charge state an additional electron from the environment is trapped and a spin-1 system is formed. We use two ground states, $|0\rangle = |m_s = 0\rangle$ and $|1\rangle = |m_s = -1\rangle$ (or $|m_s = +1\rangle$), as our qubit subspace. The $|m_s = 0\rangle$ state is connected to an optically excited state $|e\rangle = |E_x\rangle$ (or $\left|E_y\right\rangle$, for node C), and the transition can be selectively addressed at cryogenic temperatures [17, 18]. Spontaneous decay from the excited state $|e\rangle$ to $|0\rangle$ happens resonantly ≈ 3% of the time, into the so-called zero-phononline (ZPL) [19]. In the remaining ≈ 97%, the decay happens off-resonantly into the phonon-side band (PSB); the emitted photon is accompanied with the emission of a phonon. Inherent loss of the phonon will project the qubit into $|0\rangle$, prohibiting PSB photons to be used for entanglement generation. In the optical setup we separate the ZPL from the PSB photons using a dichroic mirror [20].

In this work, we use the same experimental setups as used in the quantum network of References [20] and [21]. We label the nodes A, B and C, and they are connected such that we can generate entanglement on two links; AB and BC. The exact connections are given in [20]. By applying a DC voltage via on-chip electrodes, we tune the optical transitions of nodes A and C to match the frequency of node B using the DC Stark effect [22]. For each link the nodes share the excitation laser and the short excitation pulses are generated using an electro-optic modulator (EOM, Jenoptik) driven by an arbitrary waveform generator (AWG, Zürich Instruments). To provide additional extinction of the pulse, we make use of an acousto-optic modulator (AOM, Gooch&Housego). We use microwave

(MW) pulses to drive the transition between the qubit states, with I- and Q-modulation we can generate any superposition. We actively stabilize the optical phases acquired by the excitation pulses and photons using a combination of heterodyne and homodyne phase detection methods and feedback [20].

The optical transition frequencies of the NV center are sensitive to (laser-induced) changes in the charge-environment, to mitigate this effect we perform a Charge-Resonance (CR) check prior to every experimental run [23, 24]. During a CR check, we turn on the control lasers to ensure the emitter is on resonance with the control lasers and in the correct charge state. Only when a number of photons above a pre-set threshold are detected, an experimental repetition is started.

6.4. TAILORING THE MODEL FOR NV CENTERS

In Section 6.2 we have considered the single-photon protocol in a general way. Considering our experimental implementation using NV centers in bulk diamond, we can make several approximations to simplify the results. Due to the small fraction of resonantly emitted photons and limited detection efficiency (≈ 2%), we can assume $\eta \ll 1$. By using high-power laser pulses we can assume all population to be transferred to the excited state, $c_{0,i} = 0$. We set a detection window which starts after the arrival time of the optical pulse to mitigate noise counts due to leaking excitation light. As a consequence, during a double excitation event the first photon will never result into the a photon detection, $\eta_i(1-\eta_i)|\zeta_{ii}(t,t_r)|^2 = 0$. In this way, we can define the parameter p_{de} as the probability that a second photon is emitted given a photon detection; $|\zeta_{ii}(t_r,t)|^2 = p_{de}$.

With these assumptions we can simplify Eq. (6.18) and (6.19), and we obtain for the probability to detect a photon in port C

$$p_{\text{click,NV,C}} = \text{Tr}\big(\rho_1\big) + \text{Tr}\big(\rho_{\text{incoherent}}\big) + \text{Tr}\big(\rho_{\text{noise}}\big), \tag{6.22}$$

The average heralded density matrix is given by

$$\begin{aligned}\rho_{\text{NV,C}} &= \frac{1}{p_{\text{click,NV,C}}}\left(\rho_1 + \rho_{\text{incoherent}} + \rho_{\text{noise}}\right)\\ &= \frac{1}{p_{\text{click,NV,C}}}\begin{pmatrix} a_{00} & 0 & 0 & 0\\ 0 & a_{11} & a_{12} & 0\\ 0 & a_{12}^{*} & a_{22} & 0\\ 0 & 0 & 0 & a_{33}\end{pmatrix}\end{aligned} \tag{6.23}$$

with the elements

$$\begin{aligned}
a_{00} =& \alpha_A\alpha_B\left(\frac{1}{2}\eta_A|\zeta_A(t)|^2 + \frac{1}{2}\eta_B|\zeta_B(t)|^2 + \frac{1}{2}\eta_A p_{de} + \frac{1}{2}\eta_B p_{de} + p_d\right), && (6.24)\\
a_{11} =& \alpha_A(1-\alpha_B)\left(\frac{1}{2}\eta_A|\zeta_A(t)|^2 + \frac{1}{2}\eta_A p_{de} + p_d\right), && (6.25)\\
a_{22} =& (1-\alpha_A)\alpha_B\left(\frac{1}{2}\eta_B|\zeta_B(t)|^2 + \frac{1}{2}\eta_B p_{de} + p_d\right), && (6.26)\\
a_{12} =& \frac{1}{2}Ae^{-i\phi}, && (6.27)\\
a_{33} =& p_d(1-\alpha_A)(1-\alpha_B). && (6.28)
\end{aligned}$$

In the expression of a_{12}, A is the magnitude of the coherence term

$$A = \sqrt{\alpha_A(1-\alpha_A)\alpha_B(1-\alpha_B)\eta_A\eta_B} \times (\vec{\epsilon}_A \cdot \vec{\epsilon}_B)c_{e,A}c_{e,B}\mathcal{E}_A(t)\mathcal{E}_B(t), \tag{6.29}$$

and ϕ represents the phase of the entangled state

$$\phi = \vartheta_B - \vartheta_A - \omega_A t_{d,A} + \omega_B t_{d,B} - \phi_{l,A} + \phi_{l,B}. \tag{6.30}$$

In Eq. (6.30) we express the detection time of the photon as the time with respect to the arrival of the excitation pulse, $t_{d,i} = t - \frac{L_{1,i}+L_{2,i}}{c}$. In other words, $t_{d,i}$ can be viewed as the time the emitter has spent in the excited state.

In our experimental implementation, the emitters share the excitation laser and we can rewrite Eq. (6.30). Naturally, the phase and the frequency of the laser will be $\phi_{l,A} = \phi_{l,B} \equiv \phi_l$ and the frequency of the laser $\omega_{l,A} = \omega_{l,B} \equiv \omega_l$. We introduce a detuning Δ_i between the laser and the emitters optical transition, $\omega_l - \omega_i = \Delta_i$. Using these definitions we can write ϕ as

$$\phi = -\omega_l(t_{d,A} - t_{d,B}) + \Delta_A t_{d,A} - \Delta_B t_{d,B} - \vartheta_A + \vartheta_B \tag{6.31}$$

Even though the emitters share the same excitation pulse, the arrival times of the optical pulses do not have to be the same (see Figure 6.2) and their difference in arrival time dt is given by the path length difference $L_{1,A} + L_{2,A} - L_{1,B} - L_{2,B} = dL$. As $t_{d,i}$ is defined as the detection time of the photon with respect to the arrival time of the excitation pulse at the detector, $t_{d,B}$ can be expressed as $t_{d,B} = t_{d,A} + dt = t_{d,A} + \frac{dL}{c}$ and the expression of the phase becomes

$$\phi = \omega_l\frac{dL}{c} + \Delta_A t_{d,A} - \Delta_B t_{d,B} - \vartheta_A + \vartheta_B \tag{6.32}$$

in which $\omega_l\frac{dL}{c}$ is the optical path we stabilize to set point $\delta\varphi$. Assuming that the arrival time difference is small compared to the photon detection time, we can write the entangled state phase as

$$\begin{aligned}
\phi =& \delta\varphi + \Delta_A t_{d,A} - \Delta_B(t_{d,A} + dt) - \vartheta_A + \vartheta_B\\
=& \delta\varphi + \Delta_A t_d - \Delta_B t_d - \vartheta_A + \vartheta_B
\end{aligned} \tag{6.33}$$

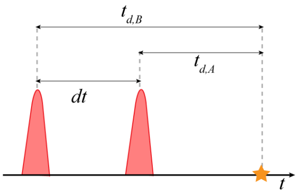

Figure 6.2: **Photon arrival time.** Photon detection times $t_{d,i}$ are defined as the detection time with respect to the arrival times of the optical pulses and correspond to the time the emitter has spent in the excited state.

where t_d is the photon detection time with respect to the (nearly equal) arrival time of the optical pulses.

In the remainder of the paper, we use this model to simulate the fidelity with respect to the maximally entangled state and the success probability.

6.5. BRIGHT STATE POPULATION

In this section we study the effect of the bright state population α. First, we will vary α and discuss the effect on the fidelity of the heralded state in the presence of noise. Secondly, we will discuss optimal settings for the individual α_i when the detection efficiencies of the nodes are not the same.

In a practical experimental setting, entanglement might be falsely heralded by noise photons. The noise counts can originate from different sources, such as dark counts of the detector, excitation light leaking into the detectors or stray light. The effect on the fidelity of the average heralded state depends on the ratio between noise and signal photons. In Figure 6.3A we plot the measured and simulated fidelity with the maximally entangled state for various settings of α. For high values of α we observe the linear scaling of the fidelity with α as suggested by the model for the high-photon loss regime $\eta \ll 1$. For low values of α, the fidelity deviates from the linear behavior and for sufficiently low α's we observe a sharp drop-off, indicating a significant contribution of falsely heralding noise counts. We would like to add that off-resonant excitation of undesired transitions or errors in the preparation of the superposition state (unitary $U_1^{\alpha,\vartheta}$) can also lead to a sharp drop-off in fidelity for low values of α. In Figure 6.3B we plot the success probability p_{click} as a function of α, which shows an expected linear behavior.

We now turn to the individual detection efficiency η. Generally, the detection efficiency or loss parameter, η, is not the same for the two qubits due to differences in the individual experimental setups or unequal fiber loss in the paths from the nodes to the beam splitter. For this reason we would like to find optimal settings for α_A and α_B to establish remote entanglement with the highest fidelity for a fixed success probability p_{click}. In other words, we want to optimize $F(\alpha_A, \alpha_B)$ subject to $\eta_A\alpha_A + \eta_B\alpha_B = p_{click}$ in the high-loss regime. For simplicity, we assume no other errors than the protocol error (i.e.

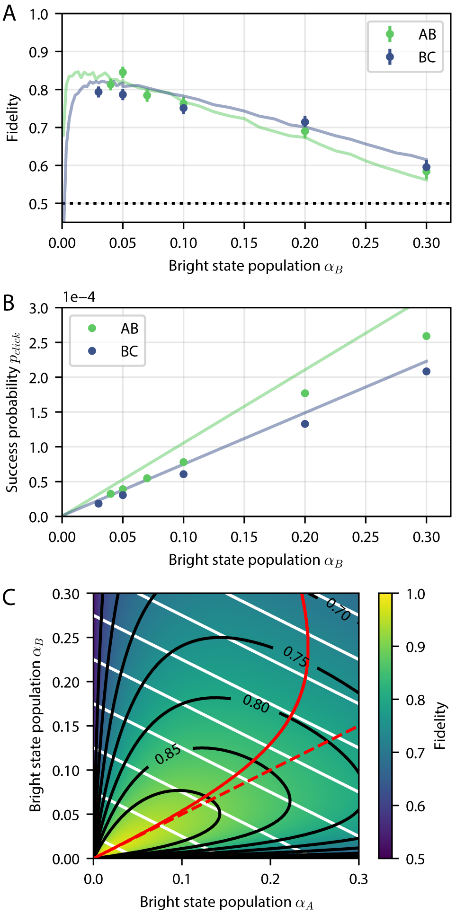

Figure 6.3: **Effect of bright state population.** Fidelity with respect to the maximally entangled state **(A)** and probability to herald a state **(B)** as a function of the bright state populations α. The data (circles) is measured on two links of the network of Reference [20], AB and BC. The x-axis represents the bright state population of setup B in both cases. The bright state population of node A is scaled to be $\alpha_A \approx \frac{\eta_B}{\eta_A}\alpha_B$, while $\alpha_C = \alpha_B$. The solid lines are given by our model, see Table 6.1 for the parameters. **(C)** In absence of errors other than the protocol error, we calculate the entangled state fidelity for various settings of (α_A, α_B) for the case $\eta_B = 2\eta_A$. The black and white solid lines are isolines for the entangled state fidelity and success probability respectively. The red solid line indicates the optical settings to obtain the highest fidelity with respect to the maximally entangled state for a fixed success probability. The red dashed line represents the $\eta_A\alpha_A = \eta_B\alpha_B$ scenario.

no noise counts, no double excitation, perfectly indistinguishable photons), set an entangled state phase of $\phi = 0$ and integrate over all possible detection times such that $|\zeta_i(t)|^2 = 1$. To compute the fidelity we calculate the overlap with the maximally entangled state

$$\begin{aligned} F &= \langle\Psi|\rho_C|\Psi\rangle, \\ &= \frac{1}{4p_{click,C}}(a_{11} + a_{22} + 2|a_{12}|), \\ &= \frac{1}{4p_{click,C}}(\alpha_A\eta_A(1-\alpha_B) + \alpha_B\eta_B(1-\alpha_A) + 2\sqrt{\alpha_A\alpha_B(1-\alpha_A)(1-\alpha_B)}), \end{aligned} \tag{6.34}$$

and the success probability per attempt

$$\begin{aligned} p_{click} &= a_{00} + a_{11} + a_{22}, \\ &= \frac{1}{2}(\eta_A\alpha_A + \eta_B\alpha_B). \end{aligned} \tag{6.35}$$

We use a Langrangian formalism and write the condition for optimal settings as

$$\begin{aligned} (\nabla p_{click})_\perp \cdot \nabla F = 0 \\ -\eta_B\frac{\partial F}{\partial\alpha_A} + \eta_A\frac{\partial F}{\partial\alpha_B} = 0 \end{aligned} \tag{6.36}$$

We solve Eq. (6.36) numerically for the case $\eta_B = 2\eta_A$. In Figure 6.3C we plot the entangled state fidelity for different values of α_A and α_B. The optimal settings are represented by the red solid line. For high-fidelity states, the optimal settings are close to $\alpha_A\eta_A = \alpha_B\eta_B$ (red dashed line). We can interpret this result as balancing the probability of the photon to originate from either setup. For low-fidelity states, the optimal settings differ from balancing the detection probabilities. This can be explained with a simple example; by setting $\alpha_A = 0$ and $\alpha_B \neq 0$ the detected photon will always originate from setup B and thus we will measure perfect classical anti-correlations. However any quantum correlations are completely washed out and we obtain a fidelity $F = 0.5$, irrespective of the value of α_B. On the contrary, if we set both $\alpha_A, \alpha_B \neq 0$ we do get quantum correlations but the protocol error can now push the fidelity to below 0.5. Hence, for low-fidelity states the optimal settings for α_A and α_B optimize classical anti-correlation at the expense of quantum correlations.

6.6. PHASE OF THE ENTANGLED STATE

In Section 6.4 we discussed the phase of the entangled state ϕ and derived the expression for the phase in case the excitation laser is shared between the emitters, Eq. (6.33). Here we experimentally verify the effect of the different parameters on the entangled state phase, using nodes B and C.

We measure the phase of the entangled state by sweeping the readout basis of node C over the XY-plane of the Bloch sphere (black arrows in Figure 6.4A) while we fix the readout basis of node B to be along the +X axis (red arrow). In Figure 6.4B we plot the correlations of the measured readout outcomes as a function of the readout basis of node B for

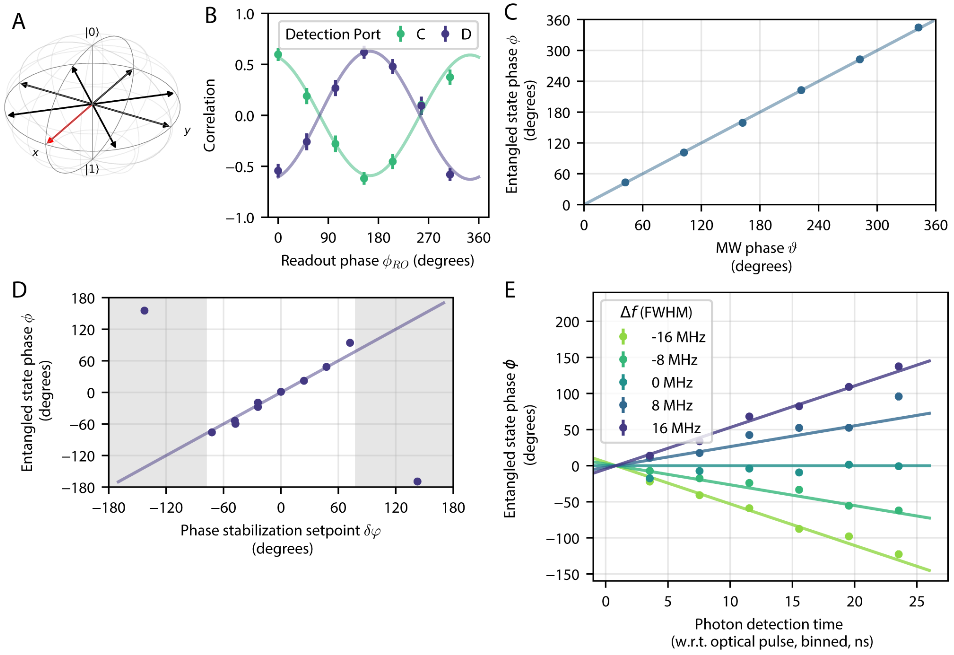

Figure 6.4: **Entangled state phase.** **(A)** We determine the entangled state phase by measuring along the $+X$ axis on setup B (red arrow), while sweeping the measurement axis of setup C over the equator plane of the Bloch sphere (black arrows). In this way we obtain oscillating correlations between the measurement outcomes, as shown in **(B)**, for states heralded by detector C (turquoise circles) and D (purple circles). We jointly fit the data for the two detectors to extract ϕ, the phase offset with respect to a cosine. **(C)** The entangled state phase ϕ as a function of the phase of the microwave (MW) pulse we use to create the initial superposition state (see Eq. (6.2)). Here we fix $\vartheta_C = 0$ and sweep ϑ_B. Due to a small difference of the stabilized path compared to the path of the excitation pulses and the single photons, there is a nonzero phase offset [20]. We fit the measured phase values with a line with slope 1 and subtract the fitted offset. The solid line represents the expected behavior. **(D)** The entangled state phase as a function of the optical phase stabilization set point. Again we account for the phase offset due to path difference and shows the expected response (solid line). **(E)** The entangled state phase as function of the detection time of the photon for different frequency offsets between the setups. The photon detection times are binned in bins of 4 ns, and the x value represents the middle of the bin. The time scale is with respect to the highest intensity point of the optical pulse. The solid lines are a joint fit the data with the zero point crossing x_0 as the only free parameter. The fit gives $x0 = (0.8 \pm 0.3)$ ns. The error bars of the data plotted in (C), (D) and (E) are smaller than the symbol size.

states heralded by detecting a photon in port C (turqoise circles) or port D of the beam splitter (purple circles). To extract the phase we jointly fit the two curves and extract ϕ, the phase offset with respect to a cosine.

First we vary the phase of the microwave pulse that creates the superposition state on setup B, i.e. we change ϑ_B, the phase of the initial superposition state. The outcomes are plotted in Figure 6.4C and again we observe the expected linear dependence, indicated by the straight line.

The next parameter we vary is the set point for the optical phase stabilization to change $\delta\varphi$. In Figure 6.4C we plot the measured entangled state phase ϕ for different set points of the stabilization (blue circles) together with the expected behavior (solid green line). We use the phase stabilization architecture as explained in Reference [20]. Due to the use of three independent interferometers we can stabilize to set points further away from 0, but ultimately the non-linear sinusoidal phase signals limit effective stabilization. In Figure 6.4D we have shaded the regime where the slope of the phase signals of the three individual interferometers is below $\cos\left(\delta\varphi/3\right) < 0.9$.

The third parameter we modify is the frequency difference between the emitters on both setups. We change the frequency of the excitation laser and shift the resonance condition of one of the emitters to the new frequency using the DC Stark effect (we apply a DC voltage via on-chip electrodes), while leaving the other emitter at its original emission frequency (thus introducing a detuning to the excitation laser). As derived in Eq. (6.33) a frequency difference results in a shift of the entangled state phase depending on the detection time of the photon. In Figure 6.4E we plot the measured entangled state phase as a function of the detection time of the photon (in bins of 4 ns) for various frequency offsets between the emitters. The time axis is with respect to the highest intensity point of the excitation pulse. We perform a combined fit of the data with fixed slopes given by our model. The fitted crossing of the lines can be viewed as the average starting point of the time spent in the excited state. For large frequency detunings (comparable to the inverse of the pulse width), the effective averaging over different excitation times could also lead to decrease of the average fidelity, however we expect this contribution to be small for our pulse width (2 ns). All in all, the dependence of the entangled state phase on the photon detection time can be clearly explained by our model.

6.7. PHOTON DISTINGUISHABILITY

The next aspect we study is the photon distinguishability. Ideally, the which-path information is completely erased by the beam splitter, any distinguishability of the photons will therefore affect the average heralded density matrix, see Section 6.2. A difference in arrival time or temporal shape will result in different probability to detect a photon originating from either node at a certain point in time and we discussed this property in Section 6.5. We would like to mention that different spatial modes of the photons will have a similar effect, but since we work with fiber-coupled photons we neglect this effect here.

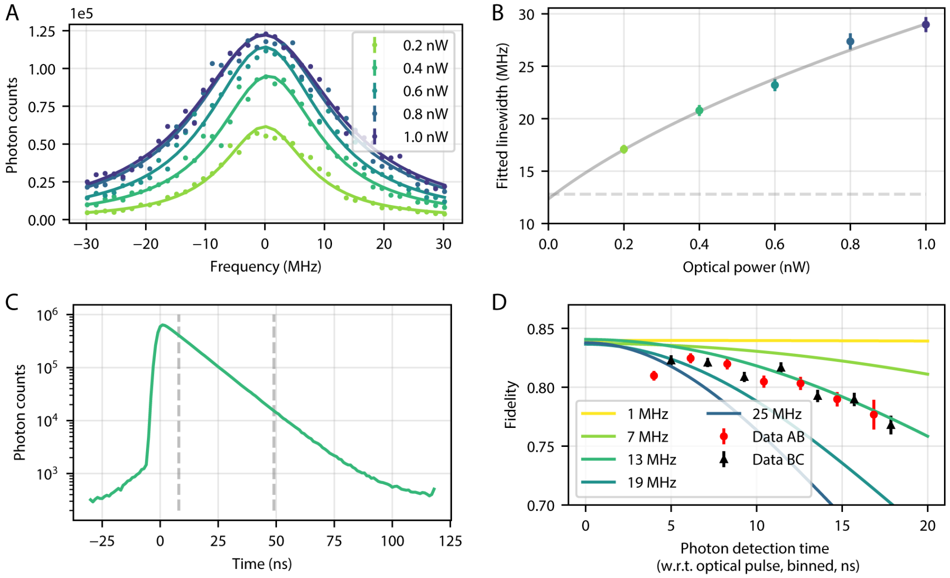

Figure 6.5: **Transform limited spectral linewidth.** **(A)** After passing a Charge-Resonance (CR) check, see Section 6.3, we expose the emitter to a laser pulse with a variable frequency and count the emitted photons. We fit the result with a Lorentzian pulse shape (solid lines) and repeat the measurements for different powers of the applied laser pulse. **(B)** Extracted linewidths (colored circles) from panel (A) as function of optical power. We fit the curve given by Eq. (6.37) to extract the natural linewidth (solid gray line). The dashed gray line shows the expected transform-limited linewidth. **(C)** Histogram of PSB photon counts. We use the region between the dashed lines to extract the excited state lifetime and compute the expected linewidth in panel (B). **(D)** Fidelity with respect to the maximally entangled state as a function of the detection time of the heralding photon. We measure the entangled state fidelity for both the AB (red circles) and the BC (black triangles) links of Reference [20]. The detection time is binned is bins of 1 ns and the x value represents the start of the bin. The x axis is the detection time with respect to the highest intensity point of the optical pulse. Using a Monte-Carlo simulation, we model the entangled state fidelity for a frequency difference between the emitted photon given by a Gaussian distribution, for different values of the full-width half-maximum of the distribution.

Distinguishability in polarization or frequency will act on the off-diagonal terms of the density matrix. A difference in polarization decreases the magnitude of the off-diagonal term, see Eq. (6.29). We work with a fiber-based beam splitter consisting of polarization maintaining (PM) fibers. Alignment to the slow or fast axis of the PM fibers can easily be done with a polarization extinction ratio of >20dB and therefore we assume the polarization mismatch to be small. As discussed in the previous section, a fixed frequency offset causes the entangled state phase to be dependent on the detection time of the photon. In Figure 6.4E, we introduced a fixed frequency difference throughout the entire duration of the experiment. However, if the frequency difference varies each experimental run, an entangled state with a different phase will be heralded each repetition. Averaging over many repetitions will give a constant phase, but the fidelity with respect to the target state will decrease for later detection times of the photon.

In Section 6.3 we discussed the Charge-Resonance (CR) check as way to ensure the NV centers to be on resonance with the excitation laser and to eliminate any frequency difference between the emitters. Here we assess the performance of the CR check by measuring the spectral linewidth of the NV after passing the CR check. We turn on an additional laser with a variable frequency and count the emitted photons. We perform this procedure many times before moving to a different frequency set point of the additional laser. This way we scan over a range of ± 30 MHz around the frequency of the excitation laser, see Figure 6.5A. We fit the measured counts with a Lorentzian shape and extract γ, the full-width at half-maximum (FWHM). Non-zero laser power induces broadening of the linewidth [25], therefore we repeat this measurement for different powers of the scanning laser. In Figure 6.5B we plot the extracted linewidth for the different optical powers and fit the measured linewidths as a function of optical power P

$$\gamma = \sqrt{\gamma_0^2 + b \cdot P}, \tag{6.37}$$

to find the natural linewidth γ_0. In Eq. (6.37), b is a scaling factor relating the externally calibrated applied power to the optical Rabi-frequency. We find $\gamma_0 = (12.4 \pm 0.8)$ MHz and $b = (690 \pm 40)$ MHz^2/nW.

We compare the observed natural linewidth with an expected linewidth extracted from an excited state lifetime measurement on the same NV center. We apply an optical π-pulse to the NV center and record the detection times of the photons, see Figure 6.5C. We fit the regime between the dashed lines, for which the influence of the pulse and dark counts is negligible, with an exponential decay and we find a lifetime $\tau = (12.43 \pm 0.02)$ ns. The corresponding life-time limited linewidth is $\gamma_{0,l} = (12.81 \pm 0.02)$ MHz. We thus conclude that implementing a CR check can yield transform-limited linewidths within measurement accuracy and thus allows access to (near-)perfectly coherent photons.

Having addressed the spectral properties of a single NV center, we now move to the photon distinguishability of two emitters and its effect on the entangled state fidelity. We measure the fidelity of generated entangled states between setup A and B as well as between setup B and C. In Figure 6.5D, we show the measured fidelity versus the detection time of the photon. We observe a drop in fidelity for later detection times of the photon. Since the signal-to-noise ratio is approximately constant over the entire detection window, the observed drop in fidelity may be attributed to a varying frequency mismatch of the emitters.

We use a Monte-Carlo simulation to predict how large the frequency mismatch would have to be to explain the measured data. In this simulation we pick a random frequency difference from a Gaussian distribution, calculate the resulting entangled state phase and compute the fidelity to the target state (with target phase). By averaging over many repetitions and repeating for different widths of the Gaussian distribution, we obtain the entangled state fidelity as a function of detection time and FWHMs of the frequency distribution (solid lines in Figure 6.5D). The measured entanglement data appears to be consistent with a fluctuating frequency mismatch with standard deviation of ≈ 13 MHz between the emitters. Interestingly, we observe a quantitatively similar dependence for the link between Alice and Bob and for the link between Bob and Charlie. Note that this ≈ 13 MHz standard deviation of the frequency mismatch is inconsistent with the observed life-time limited linewidth and the accuracy of the wavemeter to which the lasers are locked (<2 MHz). Future work should focus on the identification of the origin of this frequency mismatch in two-setup experiments.

6.8. DOUBLE OPTICAL EXCITATION

In Sections 6.2 and 6.4 we have briefly discussed double optical excitation. During the finite duration of the excitation pulse, the emitter can get re-excited after emission of a first photon during the pulse. In the high-photon loss regime, the probability that both photons arrive at the beam splitter will be negligible. Loss of one of the two photons will project that state of the qubit and result in a lowered fidelity of the heralded state. In our experiment we start the detection window after the pulse has (approximately) ended and we define double excitation as the probability that one emitter has emitted two photons given a photon detection in the heralding window, $p_{de} = |\zeta(t_r, t)|^2$. Here we extract the double excitation probability for our specific optical excitation pulse and measure its dependence of the power of the optical pulse.

The double excitation probability depends on the pulse duration with respect to the lifetime of the excited shape, but also on the exact pulse shape and power of the pulse. As mentioned in Section 6.3, in our experiment setting we generate the optical pulse using an AWG, EOM and AOM. The combination of the response times and output of these three instruments determine the shape of the excitation pulse. In Figure 6.6A we plot the optical pulse intensity and indicate the heralding detection window.

We measure the double excitation probability for different powers of the optical pulse for nodes B and C. We scale the intensity of the pulse by changing the voltage sent to the AOM to maintain the same pulse shape for different powers. We measure the emitted photons using two different detection paths, namely the detection path of the resonant ZPL photons (one of the detectors after the beam splitter in Figure 6.1A), and an addi-

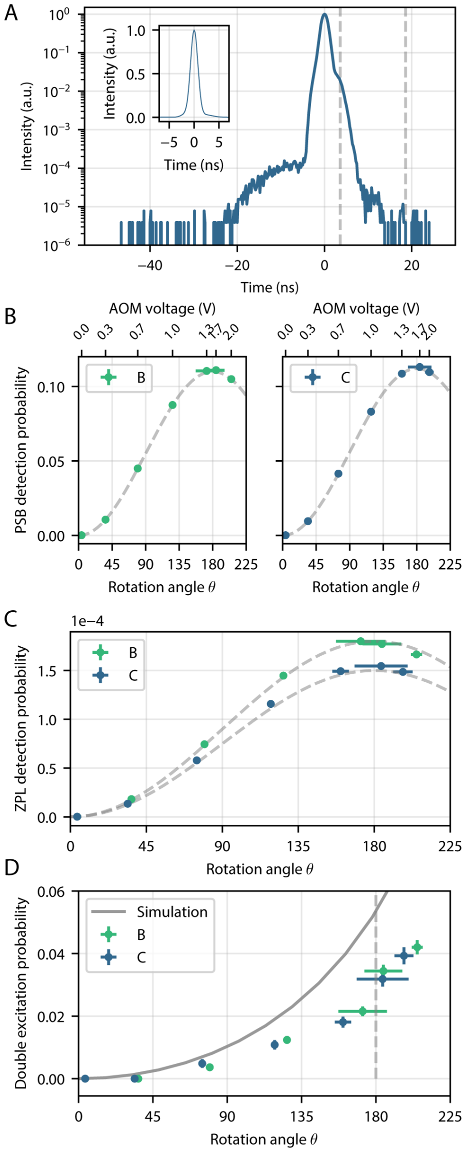

Figure 6.6: **Double excitation probability (A)** Temporal shape of the excitation pulse. The exact shape is determined by the different components we use to generate the pulse. The region between the dashed lines is the detection window in which we accept heralding photons. Photon detection probabilities for off-resonant phonon-sideband (PSB) photons **(B)** and resonant zero-phononline (ZPL) photons. **(C)**. The dashed curves show expected behavior. In (B) we indicate the voltage applied to the AOM in the top axis.**(D)** Extracted double excitation probability using Eq. (6.41) and result from our model (gray line).

tional detection path for the off-resonant PSB photons [21]. We extract the rotation angles from the photon detection probability in the PSB detector (Figure 6.6B), assuming that double excitation is small. For each power, or rotation angle, we measure coincidence events where both detectors (ZPL and PSB) detected a photon, N_{coin}. The ZPL detection window is indicated in Figure 6.6A and we set the detection window of the PSB photons to start and end well before and after the pulse.

Since we start the heralding detection window of the ZPL after the optical pulse has (approximately) ended and therefore re-excitation is not possible during this window, we can assume that all measured coincidence events consist of a PSB photon during the optical pulse and a ZPL photon in the detection window. To compute the double excitation probability p_{de} from the measured coincidence events N_{coin}, we can thus reformulate p_{de} as

$$p_{de} = \frac{P_2}{P_1 + P_2}, \tag{6.38}$$

where P_1 (P_2) is the probability of a single (two) photon emission, given a photon detected in the window. However, P_1 and P_2 have different probabilities to be detected, and we can define the corresponding detection probabilities as

$$\begin{aligned} P'_2 &= \eta_P \eta_Z P_2, && (6.39)\\ P'_1 &= \eta_Z P_1. && (6.40) \end{aligned}$$

Here η_Z and η_P are the detection efficiencies of the ZPL and PSB detection path respectively. Filling in the definitions of P_1 and P_2 in Eq. (6.38) gives

$$\begin{aligned} p_{de} &= \frac{P'_2}{\eta_P P'_1 + P'_2},\\ &= \frac{N_{\text{coin}}}{\eta_P N_{\text{all}} - (\eta_P - 1) N_{\text{coin}}}, \end{aligned} \tag{6.41}$$

in which we have used $N_{\text{coin}} = nP'_2$ and $N_{\text{all}} = n(P'_1 + P'_2)$ for n repetitions.

Figure 6.6D shows the extracted double excitation probability for different rotation angles θ for the two emitters (turquoise and blue circles), together with the simulated double excitation probability for our exact pulse shape. There is a clear qualitative agreement between the data and the simulations. The quantitative difference between the data and simulations could potentially be explained by measurement errors in the pulse shape displayed in Figure 6.6A. We note that the simulations are very sensitive on the exact shape of the pulse, and any measurement artifact such as reflections in the optical path could broaden the measured pulse shape. Importantly, we find from both the measured data and simulations that the double optical excitation probability can be mitigated by choosing a smaller rotation angle θ, albeit at the cost of a lowered entanglement generate rate (which scales with $\cos^2 \frac{\theta}{2}$). On the other hand, it is important to note that over rotation, setting a $\theta > \pi$, results in a lowered entanglement rate and fidelity, and therefore should be avoided.

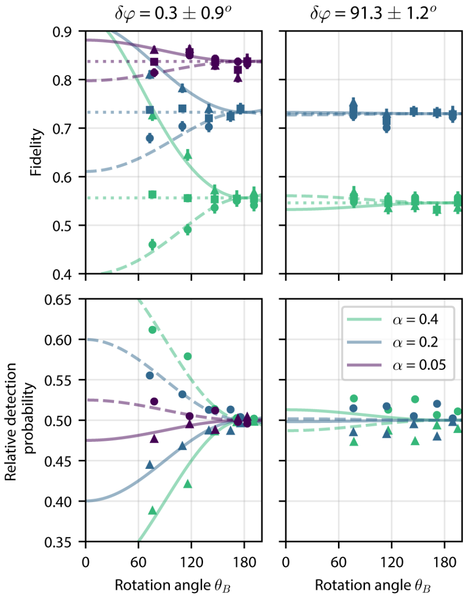

6

Figure 6.7: **Fidelity and relative detection probability in case of non-excited ground state population.** In the top panels, we measure the entangled state fidelities as a function of optical rotation angle θ for states heralded by a photon detection in detectors 1 (circles) and 2 (triangles), and the weighted average (squares) for different values of α ($\alpha = 0.05, 0.2, 0.4$ for the purple, blue and green data points respectively). In the bottom panels we plot the relative probability to detect the heralding photon in each detector. We perform these measurements for two different set points $\delta\varphi$ of the optical phase stabilization (left and right panels). The dashed and lines lines are the results of the model explained in the main text. To include other error sources than the protocol error, we scale the results of the model to the measured average fidelities.

6.9. NON-EXCITED GROUND STATE POPULATION

Up to now we have considered sufficiently good optical π-pulses, such that $c_{0,i} = 0$. In this section, we study the case of $c_{0,i} \neq 0$. To isolate the effect of $c_{0,i} \neq 0$, we make several assumptions. We assume high photon loss ($\eta \ll 1$), no double excitation ($|c_{ee,i}|^2 = 0$), perfectly overlapping polarization of the photons ($\vec{\epsilon_A} \cdot \vec{\epsilon_B} = 1$), no frequency difference between the emitters ($\omega_A = \omega_B$), no noise photons ($p_d = 0$), we consider the two setups to have equal bright state populations and photon losses ($\alpha_A = \alpha_B \equiv \alpha, \eta_A = \eta_B \equiv \eta$) and the phase of the entangled state reduces to the optical phase difference in front of the beam splitter $\phi = -\delta\varphi$. Furthermore, we define

$$c_0 = \cos\frac{\theta}{2} \tag{6.42}$$

$$c_e = \sin\frac{\theta}{2}, \tag{6.43}$$

where θ can be considered as the optical rotation angle between the ground and excitation state.

We rewrite Eq. (6.18) and (6.19) using these assumptions. The probability $p_{\mathrm{click,C/D}}$ to detect a photon in either port C or D of the beam splitter is now given by

$$\begin{aligned} p_{\mathrm{click,C/D}} =& \alpha\eta \sin^2\frac{\theta}{2} \pm \alpha^2\eta\cos\delta\varphi\sin^2\frac{\theta}{2}\cos^2\frac{\theta}{2}, \\ =& \alpha\eta\sin^2\frac{\theta}{2}(1\pm\alpha\cos\delta\varphi\cos^2\frac{\theta}{2}). \end{aligned} \tag{6.44}$$

Using the corresponding density matrices $\rho_{C,D}$, we compute the fidelity with the maximally entangled state with a phase ϕ_T

$$\begin{aligned} F_{C/D} =& \langle\Psi|\,\rho_{C,D}\,|\Psi\rangle \\ =& \frac{1}{4p_{\mathrm{click,C/D}}}(a_{11}+a_{22}+a_{12}e^{-i\phi_T}+a_{12}^{*}e^{i\phi_T}) \\ =& \frac{(1-\alpha)}{2(1\pm\alpha\cos\delta\varphi\cos^2\frac{\theta}{2})}(1+\cos\big(\delta\varphi-\phi_T\big)) \end{aligned} \tag{6.45}$$

From Eq. (6.44) and (6.45) it becomes apparent that the fidelity of the heralded entangled state depends on which detector detects the single photon, the optical phase difference $\delta\varphi$ and the optical excitation rotation angle θ. Surprisingly, for $\delta\varphi = 0$ and $\theta \to 0$ the fidelity of the entangled state heralded by one of the detectors approaches 1, albeit with a small probability to occur. On the contrary, for $\delta\varphi = 90^o$ no difference in entangled state fidelities and their probabilities to be heralded is expected. This result can be interpreted as the interference of the different photonic states associated with the $|00\rangle_{AB}$ qubit states. Dependent on $\delta\varphi$, constructive or destructive interference of the $|00\rangle_{AB}\,\hat{a}_A^\dagger$ state with $|00\rangle_{AB}\,\hat{a}_B^\dagger$ causes different heralding probabilities and consequently different average heralded state fidelities. The fact that the heralded fidelity can approach 1 for particular settings is explained by reduction of the protocol error (the error resulting from both qubits being in the bright state): a low excitation probability makes the probability that two photons were emitted small and destructive interference ensures that if one photon was emitted it is directed towards the other detector.

We compare these theoretical results with experimental data in Figure 6.7. We stabilize the interferometer to different set points to obtain $\delta\varphi = 0.3 \pm 0.9^o$ and $\delta\varphi = 91.3 \pm 1.2^o$ (left and right panels). For different values of α ($\alpha = [0.05, 0.2, 0.4]$, purple, blue and green data points respectively) we generate entanglement while varying optical rotation angle. We record the fidelity (top panels) for heralding signals detected by the two different detectors (triangles and circles) and the mean fidelity (square data points), and the relative probability to detect a photon on each detector (bottom panels). In the same figure we plot the theoretical model scaled to the mean measured fidelity to incorporate additional errors (solid, dashed and dotted lines). Our measured data is in excellent agreement with the theoretical model, we observe the effect of the lowered excitation power on the fidelity heralded by the different detectors for the case $\delta\varphi \approx 0^o$ and the absence of this effect for $\delta\varphi \approx 90^o$. Note that the (mean) fidelity is additionally improved by the reduction of the double excitation errors due to the lowered optical power, however the data displayed here has a too high measurement uncertainty to resolve this effect (we expect an improvement on the fidelity F of ≈ 0.01, see Figure 6.6D).

6.10. CONCLUSIONS AND DISCUSSION

In conclusion, we have performed a detailed theoretical and experimental investigation of the single-photon entanglement protocol. We have developed a general model for states heralded using the single-photon protocol. Subsequently, we have tailored the model to our experimental setting, NV centers in bulk diamond, and experimentally verified the effect of several experimental parameters.

We have studied the effect of the bright state population α on the generated entangled state and the success probability to herald a state. We demonstrated the entangled state phase dependence on MW pulse phases ϑ, the optical phase stabilization set point $\delta\varphi$ and the detection time of the heralding photon detection in combination with an emission frequency difference between the qubits. We have shown the observation of a transform-limited spectral linewidth, by using a Charge-Resonance (CR) check to remove any spectral shift. However, our data on remote entanglement is consistent with a Gaussian distributed frequency difference with a FWHM of 13 MHz between the emitters, this will be a subject for future work. We have observed a decrease of the double excitation probability for lowered optical power of the entangling laser pulses. Additionally, we have shown that reducing the optical laser power can also lead to a different heralded state fidelities dependent on which detector has detected the heralding photon.

Even though the experiments carried out in this work involved the nitrogen-vacancy center as qubit platform, the conclusions presented here are readily applicable to other qubit platforms, such as other solid state defects and quantum dots. The insights gained in this work be crucial in improving the entangled state fidelities using a single-photon entanglement protocol.

6.11. SUPPLEMENTARY INFORMATION

6.11.1. AVERAGE HERALDED DENSITY MATRIX

In this work we derive a general theoretical model for two-qubit states heralded by the single-photon entanglement protocol. The different steps and the corresponding unitaries are given in the main text. In this Appendix we write the expressions for the resulting density matrices for the different detection patterns.

The average heralded density matrix for a photon detection in port C of the beam splitter is given by

$$\rho_C = \frac{1}{p_{\text{click,C}}}(\rho_1 + \rho_2 + \rho_{\text{incoherent}} + \rho_{\text{noise}}). \tag{6.46}$$

with the success probability $p_{\mathrm{click,C}}$

$$p_{\mathrm{click,C}} = \mathrm{Tr}\big(\rho_1\big) + \mathrm{Tr}\big(\rho_2\big) + \mathrm{Tr}\big(\rho_{\mathrm{incoherent}}\big) + \mathrm{Tr}\big(\rho_{\mathrm{noise}}\big). \tag{6.47}$$

Single photon In the case of a single detected photon and no loss, the density matrix is given by

$$\begin{aligned} \rho_1 =& \big|\Psi_{4,1}\big\rangle\big\langle\Psi_{4,1}\big| \\ =& \frac{1}{2}\begin{pmatrix} a_{00} & a_{01} & a_{02} & 0 \\ a_{01}^* & a_{11} & a_{12} & 0 \\ a_{02}^* & a_{12}^* & a_{22} & 0 \\ 0 & 0 & 0 & 0 \end{pmatrix} \end{aligned} \tag{6.48}$$

with elements

$$a_{00} = \alpha_A \alpha_B (c_{0,A}^2 \eta_B |\zeta_B|^2 + c_{0,B}^2 \eta_A |\zeta_A|^2 + c_{0,A} c_{0,B} \sqrt{\eta_A}\sqrt{\eta_B}(\zeta_B \zeta_A^* + \zeta_A \zeta_B^*)) \tag{6.49}$$

$$a_{01} = \alpha_A \sqrt{\alpha_B}\sqrt{1-\alpha_B}\, e^{i\vartheta_B}(c_{0,A}\sqrt{\eta_B}\zeta_A^* \zeta_B + c_{0,B}\sqrt{\eta_A}|\zeta_A|^2) \tag{6.50}$$

$$a_{02} = \sqrt{\alpha_A}\sqrt{1-\alpha_A}\,\alpha_B e^{i\vartheta_A}(c_{0,A}\sqrt{\eta_B}|\zeta_B|^2 + c_{0,B}\sqrt{\eta_A}\zeta_A \zeta_B^*) \tag{6.51}$$

$$a_{11} = \alpha_A(1-\alpha_B)\eta_A|\zeta_A|^2 \tag{6.52}$$

$$a_{12} = \sqrt{\alpha_A}\sqrt{1-\alpha_A}\sqrt{\alpha_B}\sqrt{1-\alpha_B}\sqrt{\eta_A}\sqrt{\eta_B}\, e^{-i(\vartheta_B-\vartheta_A)}\zeta_A \zeta_B^* \tag{6.53}$$

$$a_{22} = (1-\alpha_A)\alpha_B \eta_B |\zeta_B|^2 \tag{6.54}$$

Two photons When two photons arrive at the beam splitter without any lost photon, we accept an heralding event when both photons are being detected in port C of the beam splitter. The first photon is detected at time t and the second photon at time $t + t_0$. For these states we obtain the following density matrix

$$\begin{aligned} \rho_2 =& \big|\Psi_{4,2}\big\rangle\big\langle\Psi_{4,2}\big| \\ =& \frac{1}{4}\begin{pmatrix} a_{00} & a_{01} & a_{02} & 0 \\ a_{01}^* & a_{11} & a_{12} & 0 \\ a_{02}^* & a_{12}^* & a_{22} & 0 \\ 0 & 0 & 0 & 0 \end{pmatrix} \end{aligned} \tag{6.55}$$

with elements

$$\begin{aligned}a_{00} =&\alpha_A\alpha_B(c_{0,B}^2\eta_A^2|\zeta_{AA}|^2 + c_{0,A}^2\eta_B^2|\zeta_{BB}|^2 + c_{0,A}c_{0,B}\eta_A\eta_B(\zeta_{AA}\zeta_{BB}^* + \zeta_{BB}\zeta_{AA}^*)\\ &+\eta_A\eta_B(|\zeta_A(t)\zeta_B(t+t_0)+\zeta_A(t+t_0)\zeta_B(t)|^2)\\ &+c_{0,A}\sqrt{\eta_A}\eta_B\sqrt{\eta_B}(\zeta_{BB}\zeta_A^*(t)\zeta_B^*(t+t_0)+\zeta_{BB}\zeta_A^*(t+t_0)\zeta_B^*(t)\\ &+\zeta_A(t)\zeta_B(t+t_0)\zeta_{BB}^*+\zeta_A(t+t_0)\zeta_B(t)\zeta_{BB}^*)\\ &+c_{0,B}\eta_A\sqrt{\eta_A}\sqrt{\eta_B}(\zeta_{AA}\zeta_A^*(t)\zeta_B^*(t+t_0)+\zeta_{AA}\zeta_A^*(t+t_0)\zeta_B^*(t)\\ &+\zeta_A(t)\zeta_B(t+t_0)\zeta_{AA}^*+\zeta_A(t+t_0)\zeta_B(t)\zeta_{AA}^*))\end{aligned} \tag{6.56}$$

$$\begin{aligned}a_{01} =&\alpha_A\sqrt{\alpha_B}\sqrt{1-\alpha_B}e^{i\vartheta_B}(c_{0,A}\eta_A\eta_B\zeta_{AA}^*\zeta_{BB}\\ &+\eta_A\sqrt{\eta_A}\sqrt{\eta_B}\zeta_{AA}^*(\zeta_A(t)\zeta_B(t+t_0)+\zeta_A(t+t_0)\zeta_B(t))+\eta_A^2|\zeta_{AA}|^2)\end{aligned} \tag{6.57}$$

$$\begin{aligned}a_{02} =&\sqrt{\alpha_A}\sqrt{1-\alpha_A}\alpha_B e^{i\vartheta_A}(c_{0,B}\eta_A\eta_B\zeta_{BB}^*\zeta_{AA}\\ &+\sqrt{\eta_A}\eta_B\sqrt{\eta_B}\zeta_{BB}^*(\zeta_A(t)\zeta_B(t+t_0)+\zeta_A(t+t_0)\zeta_B(t))+\eta_B^2|\zeta_{BB}|^2)\end{aligned} \tag{6.58}$$

$$a_{11} =\alpha_A(1-\alpha_B)\eta_A^2|\zeta_{AA}|^2 \tag{6.59}$$

$$a_{12} =\sqrt{\alpha_A}\sqrt{1-\alpha_A}\sqrt{\alpha_B}\sqrt{1-\alpha_B}\eta_A\eta_B e^{-i(\vartheta_B-\vartheta_A)}\zeta_{AA}\zeta_{BB}^* \tag{6.60}$$

$$a_{22} =(1-\alpha_A)\alpha_B\eta_B^2|\zeta_{BB}|^2 \tag{6.61}$$

Lost photons We consider all the detection patterns for which at least one photon is being detected in port C of the beam splitter and at least one photon is lost. We sum over all the individual detection patterns and arrive at

$$\begin{aligned}\rho_{\text{incoherent}} =&\sum_{i,j}\rho_{r,i,j}\\ =&\frac{1}{2}\begin{pmatrix} a_{00} & 0 & 0 & 0\\ 0 & a_{11} & 0 & 0\\ 0 & 0 & a_{22} & 0\\ 0 & 0 & 0 & 0\end{pmatrix}\end{aligned} \tag{6.62}$$

with elements

$$\begin{aligned}a_{00} =&\alpha_A\alpha_B(\\ &\eta_A|\zeta_A(t)|^2((1-\eta_B)|\zeta_B(t_r)|^2)+c_{ee,B}^2-\eta_B^2|\zeta_{BB}(t',t')|^2)\\ &+\eta_B|\zeta_B(t)|^2((1-\eta_A)|\zeta_A(t_r)|^2)+c_{ee,A}^2-\eta_A^2|\zeta_{AA}(t',t')|^2)\\ &+\eta_A(1-\eta_A)|\zeta_{AA}(t,t_r)|^2(c_{0,B}^2+c_{e,B}^2+c_{ee,B}^2)\\ &+\eta_A(1-\eta_A)|\zeta_{AA}(t_r,t)|^2(c_{0,B}^2+c_{e,B}^2+c_{ee,B}^2)\\ &+\eta_B(1-\eta_B)|\zeta_{BB}(t,t_r)|^2(c_{0,A}^2+c_{e,A}^2+c_{ee,A}^2)\\ &+\eta_B(1-\eta_B)|\zeta_{BB}(t_r,t)|^2(c_{0,A}^2+c_{e,A}^2+c_{ee,A}^2)\\ &+\eta_A^2|\zeta_{AA}(t,t')|^2(|\zeta_B(t_r)|^2+c_{ee,B}^2-\eta_B^2|\zeta_{BB}(t',t')|^2)\\ &+\eta_B^2|\zeta_{BB}(t,t')|^2(|\zeta_A(t_r)|^2+c_{ee,A}^2-\eta_A^2|\zeta_{AA}(t',t')|^2))\end{aligned} \tag{6.63}$$

$$a_{11} =\alpha_A(1-\alpha_B)\eta_A(1-\eta_A)(|\zeta_{AA}(t,t_r)|^2+|\zeta_{AA}(t_r,t)|^2) \tag{6.64}$$

$$a_{22} =(1-\alpha_A)\alpha_B\eta_B(1-\eta_B)(|\zeta_{BB}(t,t_r)|^2+|\zeta_{BB}(t_r,t)|^2) \tag{6.65}$$

Here we have used the relations $\eta_i|\zeta_i(t)|^2 + (1-\eta_i)|\zeta_i(t_r)|^2 = |c_{e,i}|^2$ and $\eta_i^2|\zeta_{ii}(t,t')|^2 + (1-\eta_i)\eta_i|\zeta_{ii}(t,t_r)|^2 + (1-\eta_i)\eta_i|\zeta_{ii}(t_r,t)|^2 + (1-\eta_i)^2|\zeta_{ii}(t_r,t_r)|^2 = |c_{ee,i}|^2$ to simplify the matrix elements.

Noise counts In case of a false heralding event by a noise count the average density matrix consists of two parts

$$\rho_{\text{noise}} = p_d(\rho_0 + \rho_r) \tag{6.66}$$

ρ_0 when no photon is emitted and ρ_r when all emitted photons are lost.

$$\begin{aligned}\rho_0 &= |\Psi_{4,0}\rangle_A\langle\Psi_{4,0}|_A \otimes |\Psi_{4,0}\rangle_B\langle\Psi_{4,0}|_B \\ &= \begin{pmatrix} a_{00} & a_{01} \\ a_{01}^* & a_{11}\end{pmatrix} \otimes \begin{pmatrix} b_{00} & b_{01} \\ b_{01}^* & b_{11}\end{pmatrix}\end{aligned} \tag{6.67}$$

with elements

$$a_{00} = \alpha_A c_{0,A}^2 \tag{6.68}$$

$$a_{01} = \sqrt{\alpha_A}\sqrt{1-\alpha_A}c_{0,A}e^{i\vartheta_A} \tag{6.69}$$

$$a_{11} = (1-\alpha_A) \tag{6.70}$$

and similar elements for b_{ij}. ρ_r represents the density matrix in case all photons are lost

$$\begin{aligned}\rho_r &= \sum_{i,j}\rho_{i,j} \\ &= \begin{pmatrix} a_{00} & 0 & 0 & 0 \\ 0 & a_{11} & 0 & 0 \\ 0 & 0 & a_{22} & 0 \\ 0 & 0 & 0 & 0\end{pmatrix}\end{aligned} \tag{6.71}$$

with elements

$$\begin{aligned}a_{00} =& \alpha_A\alpha_B(c_{0,A}^2((1-\eta_B)|\zeta_B(t_r)|^2 + (1-\eta_B)^2|\zeta_{BB}(t_r,t_r)|^2) \\ &+ c_{0,B}^2((1-\eta_A)|\zeta_A(t_r)|^2 + (1-\eta_A)^2|\zeta_{AA}(t_r,t_r)|^2) \\ &+ (1-\eta_A)(1-\eta_B)|\zeta_A(t_r)|^2|\zeta_B(t_r)|^2)\end{aligned} \tag{6.72}$$

$$a_{11} = \alpha_A(1-\alpha_B)((1-\eta_A)|\zeta_A(t_r)|^2 + (1-\eta_A)^2|\zeta_{AA}(t_r,t_r)|^2) \tag{6.73}$$

$$a_{22} = (1-\alpha_A)\alpha_B((1-\eta_B)|\zeta_B(t_r)|^2 + (1-\eta_B)^2|\zeta_{BB}(t_r,t_r)|^2) \tag{6.74}$$

6.11.2. EXPERIMENTAL PARAMETERS FOR SIMULATIONS

In Figures 6.3 and 6.5 we provide simulations for the average fidelity with respect to the maximally entangled states using the model developed in Section 6.4. The parameters we use for these simulations are listed in Table 6.1, both for the AB link as well as the BC entangled state.

Table 6.1: **Table with experimental parameters.** The start of the detection window is with respect to the maximum intensity of the optical pulse and the detection probability for each setup is integrated over the detection window. Furthermore, these experiments used the same optical pulse used in References [20, 21] and is different from the optical pulse shape indicated in Figure 6.6A.

	AB	BC
Excited state lifetime	12.4 ns	12.4 ns
Detection window start	4 ns	5 ns
Detection window duration	15 ns	15 ns
Bright state population α_A	0.07	-
Bright state population α_B	0.05	0.05
Bright state population α_C	-	0.1
Detection probability $\eta_A \int \mathscr{E}(t)^2 dt$	3.8e-4	-
Detection probability $\eta_B \int \mathscr{E}(t)^2 dt$	5.2e-4	4.6e-4
Detection probability $\eta_C \int \mathscr{E}(t)^2 dt$	-	2.8e-4
Double excitation probability	0.06	0.08
Noise countrate	10 Hz	30 Hz
Phase stability $\sigma_{\delta\varphi}$	30^o	21^o
FWHM frequency difference Δf_{FWHM}	13 MHz	13 MHz
Polarization mismatch	8^o	8^o

REFERENCES

[1] H. J. Kimble, *The quantum internet,* Nature **453**, 1023 (2008).

[2] S. Wehner, D. Elkouss, and R. Hanson, *Quantum internet: A vision for the road ahead,* Science **362** (2018).

[3] A. Ekert and R. Renner, *The ultimate physical limits of privacy,* Nature **507**, 443 (2014).

[4] A. Broadbent, J. Fitzsimons, and E. Kashefi, *Universal blind quantum computation,* Proceedings - Annual IEEE Symposium on Foundations of Computer Science, FOCS , 517 (2009).

[5] M. Ben-Or, C. Crépeau, D. Gottesman, A. Hassidim, and A. Smith, *Secure multiparty quantum computation with (only) a strict honest majority,* Proceedings - Annual IEEE Symposium on Foundations of Computer Science, FOCS , 249 (2006).

[6] M. Christandl and S. Wehner, *Quantum Anonymous Transmissions,* in *Advances in Cryptology - ASIACRYPT 2005* (2005) pp. 217–235.

[7] S. W. de Bone, R. Ouyang, K. Goodenough, and D. Elkouss, *Protocols for Creating and Distilling Multipartite GHZ States With Bell Pairs,* in *IEEE Quantum Engineering* (2020).

[8] C. Cabrillo, J. I. Cirac, P. Garcia-Fernandez, and P. Zoller, *Creation of entangled states of distant atoms by interference,* Physical Review A **59**, 1025 (1999).

[9] S. Bose, P. L. Knight, M. B. Plenio, and V. Vedral, *Proposal for teleportation of an atomic state via cavity decay,* Physical Review Letters **83**, 5158 (1999).

[10] S. D. Barrett and P. Kok, *Efficient high-fidelity quantum computation using matter qubits and linear optics,* Physical Review A **71**, 2 (2005).

[11] A. Delteil, Z. Sun, W. B. Gao, E. Togan, S. Faelt, and A. Imamoglu, *Generation of heralded entanglement between distant hole spins,* Nature Physics **12**, 218 (2016).

[12] R. Stockill, M. J. Stanley, L. Huthmacher, E. Clarke, M. Hugues, A. J. Miller, C. Matthiesen, C. Le Gall, and M. Atatüre, *Phase-Tuned Entangled State Generation between Distant Spin Qubits,* Physical Review Letters **119**, 1 (2017).

[13] P. C. Humphreys, N. Kalb, J. P. Morits, R. N. Schouten, R. F. Vermeulen, D. J. Twitchen, M. Markham, and R. Hanson, *Deterministic delivery of remote entanglement on a quantum network,* Nature **558**, 268 (2018).

[14] D. Lago-rivera, S. Grandi, J. V. Rakonjac, A. Seri, and H. D. Riedmatten, *Telecom-heralded entanglement between multimode solid-state quantum memories,* Nature **594** (2021).

[15] S. Das, L. Zhai, M. Čepulskovskis, A. Javadi, S. Mahmoodian, P. Lodahl, and A. S. Sørensen, *A wave-function ansatz method for calculating field correlations and its application to the study of spectral filtering and quantum dynamics of multi-emitter systems,* arXiv:1912.08303 (2019).

[16] K. Tiurev, P. L. Mirambell, M. B. Lauritzen, M. H. Appel, A. Tiranov, P. Lodahl, and A. S. Sørensen, *Fidelity of time-bin entangled multi-photon states from a quantum emitter,* Physical Review A **052604**, 1 (2020).

[17] L. Robledo, H. Bernien, T. V. D. Sar, and R. Hanson, *Spin dynamics in the optical cycle of single nitrogen-vacancy centres in diamond,* New Journal of Physics **13** (2011), 10.1088/1367-2630/13/2/025013.

[18] L. Robledo, L. Childress, H. Bernien, B. Hensen, P. F. A. Alkemade, and R. Hanson, *High-fidelity projective read-out of a solid-state spin quantum register,* Nature , 5 (2011).

[19] D. Riedel, I. Söllner, B. J. Shields, S. Starosielec, P. Appel, E. Neu, P. Maletinsky, and R. J. Warburton, *Deterministic enhancement of coherent photon generation from a nitrogen-vacancy center in ultrapure diamond,* Physical Review X **7**, 1 (2017).

[20] M. Pompili, S. L. Hermans, S. Baier, H. K. Beukers, P. C. Humphreys, R. N. Schouten, R. F. Vermeulen, M. J. Tiggelman, L. dos Santos Martins, B. Dirkse, S. Wehner, and R. Hanson, *Realization of a multinode quantum network of remote solid-state qubits,* Science **372**, 259 (2021).

[21] S. L. N. Hermans, M. Pompili, H. K. C. Beukers, S. Baier, J. Borregaard, and R. Hanson, *Qubit teleportation between non-neighboring nodes in a quantum network,* arXiv:2110.11373 , 1 (2021).

[22] P. Tamarat, T. Gaebel, J. R. Rabeau, M. Khan, A. D. Greentree, H. Wilson, L. C. Hollenberg, S. Prawer, P. Hemmer, F. Jelezko, and J. Wrachtrup, *Stark shift control of single optical centers in diamond,* Physical Review Letters **97**, 1 (2006).

[23] M. W. Doherty, N. B. Manson, P. Delaney, and L. C. Hollenberg, *The negatively charged nitrogen-vacancy centre in diamond: The electronic solution,* New Journal of Physics **13** (2011).

[24] H. Bernien, B. Hensen, W. Pfaff, G. Koolstra, M. S. Blok, L. Robledo, T. H. Taminiau, M. Markham, D. J. Twitchen, L. Childress, and R. Hanson, *Heralded entanglement between solid-state qubits separated by three metres,* Nature **497**, 86 (2013).

[25] M. L. Citron, H. R. Gray, C. W. Gabel, and C. R. Stroud, *Experimental study of power broadening in a two-level atom,* Physical Review A **16**, 1507 (1977).

7

CONCLUSIONS AND OUTLOOK

This thesis focuses on different aspects of realizing a quantum network. In the previous chapters we discussed separate building blocks as well as demonstrations and protocols executed on the quantum network. In this chapter we summarize the key results and findings. Furthermore, we provide recommendations and considerations for near-term experiments as well as future research directions.

7.1. SUMMARY OF RESULTS

In this thesis, we have developed a multi-node quantum network consisting of three quantum nodes based on nitrogen-vacancy centers in diamond. We have explored new methods and techniques to build and improve various elements of the network. The gained insights have enabled us to perform multiple experiments on the network. Here we provide a short summary of the results obtained in the different chapters:

- In **Chapter 3** we employed a difference frequency generation process to convert photons emitted by the nitrogen-vacancy center from 637 nm to 1588 nm, a wavelength in the telecom-band. Using this conversion process, we generated an entangled state between the electron spin qubit and a telecom-wavelength photon with time-bin encoding. To verify the entangled state, we used an imbalanced fiber interferometer to access the measurement bases other than the computational basis of the photonic qubit.

- In **Chapter 4** we realized a multi-node quantum network. We developed a scalable architecture for stabilizing the optical phase, we implemented a high magnetic field to improve the coherence of the memory qubit during network activity and we achieved real-time communication and feed-forward operations across the network. We have demonstrated two experiments on the quantum network; we established a genuine multi-partite entangled state across all nodes and performed entanglement swapping.

- In **Chapter 5** we extended the capabilities of the network. We implemented a tailored heralding scheme for high-fidelity two-node entanglement generation, we developed a basis-alternating repetitive readout sequence to enhance the average readout fidelity of the memory qubit and improved the memory qubit coherence during network activity by including a decoupling $\pi-$pulse. Using these improvements, we have demonstrated qubit teleportation between the non-neighboring nodes of the quantum network.

- In **Chapter 6** we studied the entangled state heralded by the single-photon protocol in more detail. We have developed a general theoretical model, tailored the result to our experimental implementation and experimentally verified the effect of several parameters. We have provided optimal settings for the bright state populations in case of unequal detection efficiencies. We have found the entangled state phase to depend on the phase of the microwave pulses, the optical phase difference of the photons arriving at the beam splitter and a frequency difference between the emitters. We have shown that the implementation of a Charge-Resonance check can yield transform-limited optical linewidths and verified the double excitation probability as a function of excitation power. Additionally, we have shown that lowered excitation power can lead to a different entangled state fidelity depending on which detector has detected the heralding photon.

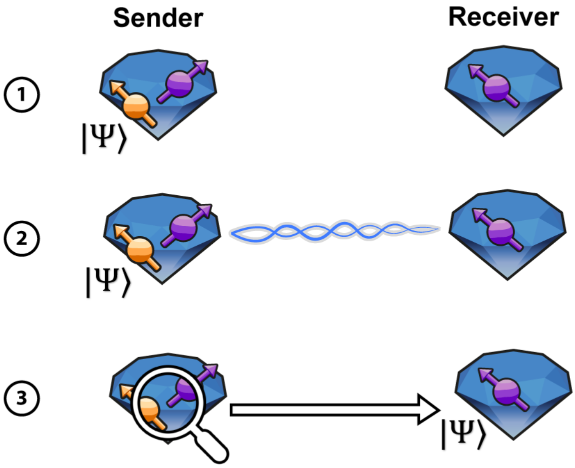

Figure 7.1: **Deterministic teleportation procotol.** Step 1: In the deterministic teleportation protocol, the state to be teleported is created or obtained and stored on the memory qubit (orange spin). Step 2: The entangled state between the communication qubits (purple spins) of the sender and receiver is generated. This state forms the teleporter. Step 3: A Bell-state measurement is performed on the qubits of the sender. Depending on the outcomes of the measurement, the receiver applies a feedforward operation to reconstruct the correct qubit state.

7.2. NEAR-TERM EXPERIMENTS

In this section we will discuss experiments that could be executed with modest improvements to the experimental apparatus and protocols.

7.2.1. DETERMINISTIC TELEPORTATION

Since the introduction of the protocol (see Section 2.6) many teleportation experiments using stationary nodes have been performed [1–5]. Several of these experiments implemented the teleportation protocol in an unconditional fashion (as we did in Chapter 5, see Figure 5.5D). This implementation relies on a pre-shared entangled state, the teleporter, between the sender and receiver. Only when this state is established, the state to be teleported is generated. Subsequently, a Bell-state measurement is performed and a feed-forward operation depending on the outcomes is applied on the receiver's qubit to reconstruct the teleported state. The unconditionality of the protocol refers to all steps after the state to be teleported is created; every generated state at the sender's side will end up at the receiver, unconditional of the measured Bell-state or other in-sequence measurements.

In deterministic teleportation the order of the steps is different, see Figure 7.1. Instead of relying on a pre-shared entanglement state, the state to be teleported is created or obtained first. Next the teleporter between the sender and receiver is established and lastly the Bell-state measurement and feed-forward operation will be done. This different order of the steps allows for a fundamentally different use. The state to be teleported does not necessarily need to be created at the sender's node, it could also be received from another node or be the outcome of a computation. To run the protocol in a deterministic fashion, every repetition must deliver a state at the receiver at the end of the protocol, with a process fidelity beating the classical bound, despite the probabilistic entanglement generation.

The deterministic teleportation protocol puts demanding requirements on the storage of the state to be teleported. To successfully implement deterministic teleportation using NV centers, several challenges need to be addressed. As the state to be teleported will be stored in a memory qubit, the memory qubit must stay coherent while entanglement is being heralded. Near-term research should tackle this challenge from both sides, the memory qubit coherence needs to be improved, as well as the success probability to herald entanglement per attempt. Furthermore, for a large number of entanglement attempts, ionization of the NV center becomes an issue. In the remainder of this section we will give recommendations to approach each of these challenges.

One way to improve the memory coherence during network activity is by shortening the time between the microwave pulses in the entanglement generation element. In this element the first microwave pulse, the α-pulse, determines the bright state population in the single-photon entanglement protocol. The second microwave pulse is a π-pulse, used to ensure the phase that the memory qubit acquires to be independent of the state of the communication qubit. The time between the microwave pulses, defined as τ, and the length of the entire element are chosen with a few considerations in mind: (i) the time between the α-pulse and the π-pulse is equal to the time between the π-pulse and the average qubit initialization time of the next element, (ii) repeating the entanglement element should not lead to undesired rotations on the memory qubit, (iii) τ should be chosen as short as possible to mitigate the effect of communication qubit initialization and microwave errors on the memory qubit and to increase the repetition rate of entanglement attempts. Given these considerations, τ should be set to a multiple of τ_L, the Larmor period, ideally $\tau = \tau_L$ [6].

In Chapter 4 and 5, our choice of τ was limited by the response time of the arbitrary waveform generator (AWG); the *Tektronix 5014* AWG required a 950 ns response time with respect to the detection of the heralding photon to stop attempting entanglement. As a result, we have set τ to 942 ns (see Section 4.6.6), close to $2 \times \tau_L$ for a magnetic field of $B = 1890$ Gauss. New hardware (*Zürich Instruments HDAWG*) with a faster response time will allow future research to set $\tau = \tau_L$ and consequently improve the memory qubit coherence during network activity.

Additionally, multi-pulse decoupling sequences on the memory qubit will improve its coherence. In Chapter 5 we have introduced a single decoupling pulse after a successful entanglement attempt and rephased the memory qubit by an equal amount of time as it took to herald entanglement. An improvement would be to introduce multiple decoupling pulses, for instance an XY4 sequence [7], interleaved by blocks of entanglement attempts. When entanglement is heralded during one of these blocks, the remaining rephasing time can be covered with just idling while protecting the communication qubits coherence.

Another near-term improvement would be to increase the success probability to herald entanglement per attempt. One way to increase the success probability per attempt is to increase the bright state population α used the entanglement protocol. However, this requires careful optimization as the communication qubit initialization error and therefore memory qubit coherence depend on α. A second way is to optimize the starting point and length of the detection window during entanglement generation. In Chapter 6 we observe the fidelity of the heralded state to depend on the time the photon is detected, see Figure 6.5E. A start of the detection window closely after the excitation pulse would result in a higher fraction of detected photons, however imperfect extinction of the excitation pulse could lead to a lowered fidelity. A long duration of the detection window will also result in a higher detection probability, but the fidelity could be decreased due to frequency differences between the emitters. Thus again, careful optimization is required.

The heralding rate, fidelity of the heralded state and the memory qubit coherence are affected by ionization of the NV center. In an ionization event, the NV^-loses its extra electron in a two-photon absorption process and becomes NV^0[8]. The optical transitions of NV^0 are not resonant with the excitation light, therefore any detected photon must originate from the other node and will falsely herald entanglement. Ionization is a probabilistic process and NV^0 is a spin-1/2 system, hence the memory qubit will acquire an unknown phase for an unknown amount of time and consequently dephase.

Ionization is believed to be caused mostly by the communication qubit initialization, which is done using a fast high power laser pulse resonant with $|m_s = \pm 1\rangle \rightarrow |E_{1,2}\rangle$ transition (Section 2.2.2). To mitigate the ionization probability, the initialization pulse can be optimized by finding a trade-off between the power and the duration of the pulse, while keeping the initialization errors small. The initialization errors must be kept small because any remaining population in $|1\rangle$ or in the ground state spin level outside the qubit subspace ($|m_s = +1\rangle$ for the node with the high magnetic field) will contribute to the memory dephasing [9].

Apart from mitigating ionization itself, one could also mitigate the effect of ionization. As proposed by *Baier et al.* [10], fast microwave driving of the ground states of NV^0could cancel out the coupling of NV^0 to the memory qubit. As this procedure effectively creates a $|m_s = 0\rangle$ spin state, it removes the problem of the unknown state. To deal with the unknown time spent in NV^0, continuous exposure to the yellow laser (resonant with NV^0optical transitions) and measurement of fluorescence would allow for tracking of the charge state. Depending on the time spent in NV^0, a phase feedback can be applied to the memory qubit. Although promising, a lot of development is needed before spin-locking and charge-state-tracking can be implemented. Practical matters, such as the delivery of these microwaves, and potential side effects, such as heating or induced spectral diffusion, need to be addressed.

In conclusion, many experimental parameters are interconnected. With thorough optimization, improvements on the memory qubit coherence, heralding rate and mitigation of (the effect of) ionization can be achieved and deterministic teleportation would come within reach.

7.2.2. INTEGRATION WITH A QUANTUM NETWORK STACK

To execute the experiments in this thesis, we have always directly programmed our full experimental sequences on the control hardware. To be able to use the quantum hardware as a resource in future large networks, we require more abstraction of the control layers and the development of a quantum network stack [11, 12]. The different layers of the stack are allocated by function. Such an architecture would allow for platform-independent control and high-level representation of applications.

The fundamentally different way of connecting quantum nodes, using entanglement, necessitates a new design compared to the classical internet stack. Recent efforts have resulted in first design of a quantum network stack [13] and a first experimental demonstration of integration with quantum hardware [14]. In Reference [13], *Dahlberg et al.* outline the different layers, listed by increased abstraction; the physical layer controls the quantum hardware and is responsible for attempting to generate entanglement, the link layer provides robust two-node entanglement generation as service for the higher layers, the network layer is responsible for establishing large-distance entangled states between non-directly connected nodes, the transport layer governs the transmission of qubits by means of qubit teleportation. In Reference [14], *Pompili and Delle Donne et al.* experimentally demonstrate the integration of a two-node physical layer with the link layer, by showing robust generation of entangled states and remote state preparation.

Next steps will be further integration of larger networks and nodes with multiple qubits. To achieve these goals real-time control of memory qubits and scheduling of tasks must be realized. Additionally, expiration of qubits need to be handled; memory qubits have limited coherence times during network activity, see Chapters 4, 5 and Section 7.2.1.

7.3. FUTURE RESEARCH DIRECTIONS

In this section we provide discussions and recommendations for longer-term research directions. First we will discuss the concept of a quantum repeater, and evaluate the performance of the entanglement swapping protocol presented in Chapter 4 in this regard. Next, we will list several research directions on how to extend the quantum network, both in the number of nodes as well as the distance between the nodes.

7.3.1. TOWARDS A QUANTUM REPEATER

With increased distance between the nodes, the photons traveling between nodes will experience high transmission losses. As a consequence, the rate at which entanglement can be heralded will drop exponentially and, in the presence of noise or detector dark counts, even become impossible. To overcome this issue, the concept of a quantum repeater was introduced by *Briegel et al.* in 1998 [15]. Instead of covering the entire distance between the nodes, the link is cut into smaller sections, so-called elementary links. Entangled qubit pairs are generated on the elementary links and, if desired, purified [15, 16]. By subsequent entanglement swapping, an entangled state between the end nodes can be established.

In Chapter 4, we have used the middle node to establish entanglement between the end nodes in the network using the entanglement swapping protocol, but can we consider this experiment a demonstration of a quantum repeater? To assess whether the quantum repeater configuration outperforms direct end-to-end-node entanglement generation, both fidelity and rate must be taken into account. Here, we compare the number of channel uses required to generate an entangled state between the end nodes for a fixed fidelity. We define the number of channel uses as the number of times (part of) the channel between the end nodes is used.

The number of channel uses depend on the loss of the channel. We can distinguish two types of loss: (i) loss associated with the emission of the photon $1/\eta_e$, for instance due to the limited fraction of resonantly emitted photons and limited fraction of photon collected in the optical fibers connecting distant nodes, and (ii) transmission losses due to the photon traveling a distance L, $1/\eta_L$. For different configurations of the network, i.e. number of nodes, the channel uses can be written as a function of η_e and η_L. For direction transmission (DT) one can for example use a time-bin encoding and the corresponding channel uses c_{DT} are given by

$$c_{DT} = \frac{1}{\eta_e \eta_L}. \tag{7.1}$$

For a two-node configuration with the use of the single-photon protocol to establish entanglement between the nodes (see Section 2.5), the number of channel uses $c_{N=2}$ is

$$\begin{aligned} c_{N=2} &= \frac{1}{2\alpha\eta_e\eta_{L/2}}, \\ &= \frac{1}{2\alpha\eta_e\sqrt{\eta_L}}, \end{aligned} \tag{7.2}$$

where α is the bright state population used in the entanglement protocol. Lastly, in the case of a three-node configuration using entanglement swapping to generate the entangled state between the outer nodes, the number of channel uses additionally depends on the performance of the memory. In case of a perfect memory qubit (no decoherence during network activity), the number of channel uses is just the sum of the uses of the two separate links

$$\begin{aligned} c_{N=3,\text{perfect}} &= \frac{1}{2\alpha\eta_e\eta_{L/4}} + \frac{1}{2\alpha\eta_e\eta_{L/4}}, \\ &= \frac{1}{\alpha\eta_e\sqrt[4]{\eta_L}}. \end{aligned} \tag{7.3}$$

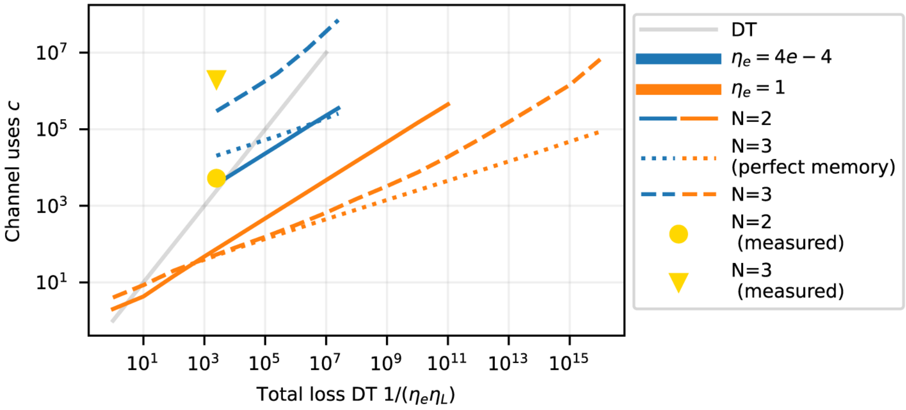

Figure 7.2: **Channel uses as a function of total loss.** We plot the number of channel uses as function of $1/(\eta_e\eta_L)$, the total loss for direction transmission. The number of channel uses is computed using the model developed in Chapter 4. Settings for α and T (see text) are chosen such that an entangled state with a fidelity of $F = 0.58$ is generated between the end nodes with a minimum number of channel uses. We perform the computation for two different values of loss associated with the emission of the photon, $1/\eta_e$, indicated by the blue and orange lines respectively. The yellow circle and triangle display the measured number of channels uses for the experiments presented in Figure 4.5B and 6.3A, for $\eta_e \approx 4e-4$ and $\eta_L = 1$.

In Equations 7.2 and 7.3, the effect of the quantum repeater becomes apparent. For large transmission losses $1/\eta_L$, the channel uses using 3 nodes $c_{N=3,\text{perfect}}$ will be smaller than the configuration using two nodes $c_{N=2}$.

However, decoherence of the memory qubit during network activity (as in Chapter 4) affects the number channel uses. In case of decoherence on the memory qubit, we make use of a timeout T, given in units of channel uses. We abort the sequence and start over when the second entangled state is not heralded within the timeout. The probability to herald the second state within the timeout is given by p_T. For small p_T, the channel uses can be approximated by

$$c_{N=3} \approx \left(\frac{1}{2\alpha\eta_e\sqrt[4]{\eta_L}} + T\right)/p_T. \tag{7.4}$$

In Figure 7.2 we plot the minimal number of channel uses as a function of $1/(\eta_e\eta_L)$, for states with a fidelity of $F = 0.58$. To extract the α and T for these states, we use the model developed in Chapter 4. We show the number of channel uses for two different values of η_e, the emission losses as roughly measured in Chapter 4[1] $\eta_e = 4e-4$ (blue lines) and the case if η_e would be 1 (a lossless spin-photon interface, orange lines). Furthermore, we display the measured number of channel uses as measured in Figure 4.5B and Figure 6.3A (rightmost data point of the AB data set).

---

[1] In Chapter 4 the distance between the nodes is on the order of tens of meters and the transmission losses are considered to be negligible.

We can draw several conclusions from Figure 7.2. With our experimental implementation, using NV centers in bulk diamond, the three-node configuration cannot outperform the two-node configuration, due to the high losses related to the emission of the photons. However with a sufficiently high η_e, our protocol of entanglement swapping in a three-node configuration with the current performance of the memory qubit and Bell-state measurement outperforms a two-node configuration for transmission losses $1/\eta_L > 10^3$.

For our current system to operate as a quantum repeater, the losses associated with the emission of a photon thus need to be reduced. A solution would be to embed the emitter in an optical cavity. When the cavity is tuned on resonance with the optical transition, the fraction of photons emitted in the zero-phonon line will be increased due to the Purcell effect [17, 18]. Moreover, these photons are emitted in the spatial mode supported by the cavity and thus the collection efficiency into an optical fiber will be enhanced.

These optical cavities can be constructed in different ways, for instance by fabricating a structure around the emitter, a photonic crystal cavity. However, this method is not suitable for NV centers, as the NV must be close to the diamond surface ($< 100nm$) to realize high finesse cavities [18, 19]. Consequently, surface charges will affect the optical properties of the NV due to its high sensitivity to electric fields [20]. Another approach is to embed an NV in a thin diamond membrane (with a thickness of $\approx \mu m$) and to place it in an open tunable Fabry-Pérot cavity [21, 22]. This approach has shown promising results, however also presented engineering challenges in the mechanical stability of the experimental system when operated in a closed-cycle cryostat [22].

Alternatively, a different defect in diamond could be used. Recent progress has presented SiV and SnV centers as promising qubit platforms [23–27]. These group-IV defects in diamond are in first order insensitive to electric field and thus surface charges. This allows them to be embedded in photonic crystal cavities and therefore they can provide an efficient spin-photon interface [25, 28–32]. Yet more development is needed for universal control of these qubits as well as coupling to memory qubits [33].

7.3.2. EXTENDING THE NETWORK

Another future research direction is the extension of the network, both in the number of nodes as well as in the distance between the nodes. A quantum network with more nodes will allow for the exploration of more complex protocols, for instance anonymous entanglement or distributed quantum computation with multiple memory qubits per node [34, 35]. Moving away from lab-based experiments, a quantum network with an increased distance between the nodes will build up towards a real-world large-scale quantum network. Expansion of the network in either of these directions will bring along new challenges.

The feasibility of experiments on an extended quantum network will depend on the rate at which entanglement between nodes can be generated (r_{ent}), as well as the storage time of entangled states during network activity ($1/r_{\mathrm{mem}}$). In Reference [36] this metric is defined as the active link efficiency $\eta^*_{\mathrm{link}} = r_{\mathrm{ent}}/r_{\mathrm{mem}}$. η^*_{link} sets the number of available entangled pairs in a sequence and for future large-scale networks $\eta^*_{\mathrm{link}} \gg 1$ is desired to perform any task with high fidelity.

The active link efficiency can be increased by generating entanglement at a higher rate. In the previous section (Section 7.3.1) we have discussed several ways to increase the number of available photons by integrating the emitter in optical cavities and subsequently increase the entanglement rate. Reducing losses in the connections between the nodes can be done by operating in the telecom-regime. Conversion of visible light photons to the telecom wavelength band can be done using quantum frequency conversion processes, as explained in Chapter 3.

On the other hand, improvement of the storage time of qubit states during network activity will also increase the active link efficiency. In Section 7.2.1 we have listed several near-term improvements. But to achieve error rates below the quantum error correction threshold, different approaches are most probably required. The use of more weakly coupled nuclear spins in isotopically purified diamond, coupling to memory qubits via a bus-qubit or encoding qubits in multiple nuclear spins, for instance spin pairs or decoherence protected subspaces could be promising approaches to improve the storage time during network activity significantly [6, 36–38].

Apart from increasing the active link efficiency, several practical matters require reconsideration. The experiments performed in this thesis required a lot of manual calibration of the experimental setups and human supervision during operation. This human involvement becomes unsustainable for large quantum networks with many nodes. The development of robust autonomous operation is a must and should be considered a serious engineering effort due to the complexity of the system.

7.4. CONCLUSION

This thesis has focused on the development of quantum networks using spins in diamond. On the road towards large-scale quantum networks, there are many interesting new challenges ready to be faced. The future is bright.

REFERENCES

[1] S. Olmschenk, D. N. Matsukevich, P. Maunz, D. Hayes, and C. Monroe, *Quantum Teleportation between Distant Matter Qubits,* Science **323**, 486 (2009).

[2] X. H. Bao, X. F. Xu, C. M. Li, Z. S. Yuan, C. Y. Lu, and J. W. Pan, *Quantum teleportation between remote atomic-ensemble quantum memories,* Proceedings of the National Academy of Sciences of the United States of America **109**, 20347 (2012).

[3] C. Nölleke, A. Neuzner, A. Reiserer, C. Hahn, G. Rempe, and S. Ritter, *Efficient teleportation between remote single-atom quantum memories,* Physical Review Letters **110**, 1 (2013).

[4] W. Pfaff, B. J. Hensen, H. Bernien, S. B. Van Dam, M. S. Blok, T. H. Taminiau, M. J. Tiggelman, R. N. Schouten, M. Markham, D. J. Twitchen, and R. Hanson, *Unconditional quantum teleportation between distant solid-state quantum bits,* Science **345**, 532 (2014).

[5] S. Langenfeld, S. Welte, L. Hartung, S. Daiss, P. Thomas, O. Morin, E. Distante, and G. Rempe, *Quantum Teleportation between Remote Qubit Memories with only a Single Photon as a Resource,* Physical Review Letters **126**, 130502 (2021).

[6] A. Reiserer, N. Kalb, M. S. Blok, K. J. van Bemmelen, T. H. Taminiau, R. Hanson, D. J. Twitchen, and M. Markham, *Robust quantum-network memory using decoherence-protected subspaces of nuclear spins,* Physical Review X **6**, 1 (2016).

[7] G. de Lange, Z. H. Wang, D. Ristè, V. V. Dobrovitski, and R. Hanson, *Universal Dynamical Decoupling of a Single Solid-State Spin from a Spin Bath,* Science **330**, 60 (2010).

[8] N. Aslam, G. Waldherr, P. Neumann, F. Jelezko, and J. Wrachtrup, *Photo-induced ionization dynamics of the nitrogen vacancy defect in diamond investigated by single-shot charge state detection,* New Journal of Physics **15** (2013).

[9] N. Kalb, P. C. Humphreys, J. J. Slim, and R. Hanson, *Dephasing mechanisms of diamond-based nuclear-spin memories for quantum networks,* Physical Review A **97**, 1 (2018).

[10] S. Baier, C. E. Bradley, T. Middelburg, V. V. Dobrovitski, T. H. Taminiau, and R. Hanson, *Orbital and Spin Dynamics of Single Neutrally-Charged Nitrogen-Vacancy Centers in Diamond,* Physical Review Letters **125**, 1 (2020).

[11] A. Pirker and W. Dür, *A quantum network stack and protocols for reliable entanglement-based networks,* New Journal of Physics **21** (2019).

[12] W. Kozlowski and S. Wehner, *Towards Large-Scale Quantum Networks,* in *NANOCOM* (2019).

[13] A. Dahlberg, M. Skrzypczyk, T. Coopmans, L. Wubben, F. Rozpdek, M. Pompili, A. Stolk, P. Pawelczak, R. Knegjens, J. De Oliveira Filho, R. Hanson, and S. Wehner,

A link layer protocol for quantum networks, SIGCOMM 2019 - Proceedings of the 2019 Conference of the ACM Special Interest Group on Data Communication , 159 (2019).

[14] M. Pompili, C. Delle Donne, I. te Raa, B. van der Vecht, M. Skrzypczyk, G. Ferreira, L. de Kluijver, A. J. Stolk, S. L. N. Hermans, P. Pawełczak, W. Kozlowski, R. Hanson, and S. Wehner, *Experimental demonstration of entanglement delivery using a quantum network stack,* arXiv:2111.11332 (2021).

[15] H. Briegel, W. Dür, J. I. Cirac, and P. Zoller, *Quantum Repeaters The Role of Imperfect Local Operations in Quantum Communication,* Physical Review Letters **81**, 5932 (1998).

[16] L. Childress, J. M. Taylor, A. S. Sørensen, and M. D. Lukin, *Fault-tolerant quantum repeaters with minimal physical resources and implementations based on single-photon emitters,* Physical Review A **72**, 1 (2005).

[17] E. Purcell, *Spontaneous Emission Probabilities at Radio Frequencies,* Physical Review **69** (1946).

[18] A. Faraon, C. Santori, Z. Huang, V. M. Acosta, and R. G. Beausoleil, *Coupling of nitrogen-vacancy centers to photonic crystal cavities in monocrystalline diamond,* Physical Review Letters **109**, 2 (2012).

[19] M. Ruf, *Cavity-Enhanced Quantum Network Nodes in Diamond*, Ph.D. thesis, Delft University of Technology (2021).

[20] M. W. Doherty, N. B. Manson, P. Delaney, and L. C. Hollenberg, *The negatively charged nitrogen-vacancy centre in diamond: The electronic solution,* New Journal of Physics **13** (2011).

[21] D. Riedel, I. Söllner, B. J. Shields, S. Starosielec, P. Appel, E. Neu, P. Maletinsky, and R. J. Warburton, *Deterministic enhancement of coherent photon generation from a nitrogen-vacancy center in ultrapure diamond,* Physical Review X **7**, 1 (2017).

[22] M. Ruf, M. J. Weaver, S. B. Van Dam, and R. Hanson, *Resonant Excitation and Purcell Enhancement of Coherent Nitrogen-Vacancy Centers Coupled to a Fabry-Perot Microcavity,* Physical Review Applied **15**, 1 (2021).

[23] C. Hepp, T. Müller, V. Waselowski, J. N. Becker, B. Pingault, H. Sternschulte, D. Steinmüller-Nethl, A. Gali, J. R. Maze, M. Atatüre, and C. Becher, *Electronic structure of the silicon vacancy color center in diamond,* Physical Review Letters **112**, 1 (2014).

[24] B. Pingault, D. D. Jarausch, C. Hepp, L. Klintberg, J. N. Becker, M. Markham, C. Becher, and M. Atatüre, *Coherent control of the silicon-vacancy spin in diamond,* Nature Communications **8**, 1 (2017).

[25] C. T. Nguyen, D. D. Sukachev, M. K. Bhaskar, B. MacHielse, D. S. Levonian, E. N. Knall, P. Stroganov, C. Chia, M. J. Burek, R. Riedinger, H. Park, M. Lončar, and M. D. Lukin, *An integrated nanophotonic quantum register based on silicon-vacancy spins in diamond,* Physical Review B **100**, 1 (2019).

[26] T. Iwasaki, Y. Miyamoto, T. Taniguchi, P. Siyushev, M. H. Metsch, F. Jelezko, and M. Hatano, *Tin-Vacancy Quantum Emitters in Diamond,* Physical Review Letters **119**, 1 (2017).

[27] M. E. Trusheim, B. Pingault, N. H. Wan, M. Gündoğan, L. De Santis, R. Debroux, D. Gangloff, C. Purser, K. C. Chen, M. Walsh, J. J. Rose, J. N. Becker, B. Lienhard, E. Bersin, I. Paradeisanos, G. Wang, D. Lyzwa, A. R. Montblanch, G. Malladi, H. Bakhru, A. C. Ferrari, I. A. Walmsley, M. Atatüre, and D. Englund, *Transform-Limited Photons from a Coherent Tin-Vacancy Spin in Diamond,* Physical Review Letters **124**, 1 (2020).

[28] A. Sipahigil, R. E. Evans, D. D. Sukachev, M. J. Burek, J. Borregaard, M. K. Bhaskar, C. T. Nguyen, J. L. Pacheco, H. A. Atikian, C. Meuwly, R. M. Camacho, F. Jelezko, E. Bielejec, H. Park, M. Lončar, and M. D. Lukin, *An integrated diamond nanophotonics platform for quantum-optical networks,* Science **354**, 847 (2016).

[29] R. E. Evans, M. K. Bhaskar, D. D. Sukachev, C. T. Nguyen, A. Sipahigil, M. J. Burek, B. Machielse, G. H. Zhang, A. S. Zibrov, E. Bielejec, H. Park, M. Lončar, and M. D. Lukin, *Photon-mediated interactions between quantum emitters in a diamond nanocavity,* Science **362**, 662 (2018).

[30] C. T. Nguyen, D. D. Sukachev, M. K. Bhaskar, B. MacHielse, D. S. Levonian, E. N. Knall, P. Stroganov, R. Riedinger, H. Park, M. Lončar, and M. D. Lukin, *Quantum Network Nodes Based on Diamond Qubits with an Efficient Nanophotonic Interface,* Physical Review Letters **123**, 1 (2019).

[31] M. K. Bhaskar, R. Riedinger, B. Machielse, D. S. Levonian, C. T. Nguyen, E. N. Knall, H. Park, D. Englund, M. Lončar, D. D. Sukachev, and M. D. Lukin, *Experimental demonstration of memory-enhanced quantum communication,* Nature **580**, 60 (2020).

[32] A. E. Rugar, S. Aghaeimeibodi, D. Riedel, C. Dory, H. Lu, P. J. McQuade, Z. X. Shen, N. A. Melosh, and J. Vučković, *Quantum Photonic Interface for Tin-Vacancy Centers in Diamond,* Physical Review X **11**, 19 (2021).

[33] M. Ruf, N. H. Wan, H. Choi, D. Englund, and R. Hanson, *Quantum networks based on color centers in diamond,* Journal of Applied Physics **130**, 070901 (2021).

[34] M. Christandl and S. Wehner, *Quantum Anonymous Transmissions,* in *Advances in Cryptology - ASIACRYPT 2005* (2005) pp. 217–235.

[35] A. Broadbent, J. Fitzsimons, and E. Kashefi, *Universal Blind Quantum Computation,* (2009) pp. 517–526.

[36] C. E. Bradley, S. W. de Bone, P. F. W. Moller, S. Baier, M. J. Degen, S. J. H. Loenen, H. P. Bartling, M. Markham, D. J. Twitchen, R. Hanson, D. Elkouss, and T. H. Taminiau, *Robust quantum-network memory based on spin qubits in isotopically engineered diamond,* arXiv:2111.09772 (2021).

[37] M. J. Degen, S. J. Loenen, H. P. Bartling, C. E. Bradley, A. L. Meinsma, M. Markham, D. J. Twitchen, and T. H. Taminiau, *Entanglement of dark electron-nuclear spin defects in diamond,* Nature Communications **12** (2021).

[38] H. P. Bartling, M. H. Abobeih, B. Pingault, M. J. Degen, and S. J. H. Loenen, *Coherence and entanglement of inherently long-lived spin pairs in diamond,* arXiv:2103.07961v1 (2021).

ACKNOWLEDGEMENTS

During my PhD I have had help and support of lots of people. Here I will try to acknowledge you all!

First of all, Ronald. Thank you very much for all your help and guidance throughout the years. You have motivated me a lot to work towards clear (and realistic) research goals, while keeping an eye on personal development. I appreciated the 3 months meeting a lot, they encouraged me to reflect, to learn how to improve myself and to become an independent researcher. Our research projects greatly benefited from your knowledge and curiosity. Team Diamond has a great team spirit and is a fantastic work environment, thanks to you.

Stephanie, thank you for being my copromotor and your support during my PhD. I have learned a lot from you and I enjoyed working with you and your group. I am grateful for the many opportunities you have provided me with. And I would like to thank you for your efforts on making QuTech a more inclusive workplace.

Matteo, these four years would not have been the same without you. Your amazing feel for code combined with your extreme dedication and loyalty to the team made our work a great success. You proved that everything can be solved using a Monte Carlo simulation, or turning the device off and on again. I am very happy for you and Grace that you are now finally together in Chicago and I wish you all the best!

Suzanne, you marked the starting point of my steps in science. You have taught me so many things, in the lab but also in other aspects of research. Even when I had already started my PhD you kept coaching me, and together we worked out how to deal with difficult situations. Thank you very much!

Simon, it was so much fun to have you as a colleague! I did notice correlations between you staying at the university until 10 PM and your family being on a trip to Innsbruck, or was it just a guide to eye?! Thank you all the great conversations during our coffee breaks and outside lunches. I wish you, Katrin, Florian and David all the luck!

Hans, you have been a great colleague. I thank you for taking over at 14:00 for 21 days in a row, for not looking at the data, but also for sharing the champagne afterwards! I will always remember how you beat Ronald in a game of koehandel with the ultimate bluff.

Johannes, we have worked together on quite some projects and I would like to thank you for all your work, clear explanations and help (even when my questions came in on very short notice). I wish you and your group the best of luck.

Anna, I learned a lot from you, both during the time we worked on the Telecom project as well as afterwards. Thank you for letting me ask so many questions, your tips and advice are very valuable to me. I hope we can continue with our occasional coffee catch-ups. I wish you and your family all the best.

Romy, you were my first MSc student and I think we both learned a lot during your project. I liked the way you always tried to make something pink in your presentations and I am happy that I could be part of your project. Lars, you were such a motivated BSc student. I'm happy to hear you successfully graduated. Lastly Laura, you came to the Netherlands right before the pandemic hit. It wasn't easy to switch to full remote operation of the setups, but your efforts have led to a really interesting project with an intriguing result. I have had a really nice time working with you, good luck with your PhD in Paris!

To the rest of Team Diamond, thank you for the great team spirit. Norbert and Peter, thank you for all your explanations of the setups, entanglement protocol and measurement procedures. After you left, we still had some laughs on your code comments (PH: We need to fix this, NK: fix what? PH: I forgot). Valeria, even though our time together in Delft was short, I was really happy to meet you again Rome. Stefan, thank you for all your help during my MSc thesis. Wouter, thank you for the casual talks in the lab, those were a real confidence booster. Good luck with starting your group here in Delft! Arian, ik heb vandaag deze tasje aan. Pffff, all these discussions with you, they were intense, but fun! Max, I really admire your need to understand everything to the smallest detail. Your relaxed vibe, barbecues and home-brewed beers contributed a lot to the amazing atmosphere of Team Diamond. Matthew, you were always patient and willing to help with anything. Good luck to you and Vidar! Marie-Christine, I was really happy when you re-joined Team Diamond again as a post-doc. And thank you (and Josh) for these all Austrian and Canadian sweets. Kian, congratulations with your appointment as Face of Science, really well-deserved! Good luck with your new home. Matteo Jr. (or is it already just Matteo?), your uplifting spirit will even make the M^2 laser behave nicely. Nina and Julia, I was really happy when you joined the group, I will miss our lunch breaks. Good luck with the tin-project, but I'm sure that it will work out with your cleanroom skills! Christopher, I enjoyed our short time as officemates, succes met de Nederlandse les! Alejandro and Mariagrazia, it was really nice to work with you and introduce you to the networks experiments. With your enthusiasm I'm convinced that the Networkies team will remain to rock! Yanik and Julius, good luck with the new cavity system! To all MSc students that joined the group over the years, thank you for your contributions to Team Diamond and often organizing the social activities!

Tim, thank you for all the interesting discussions over the years. I really appreciated your always critical but constructive feedback. Mohamed and Conor, I enjoyed our time in F027 and thank you for all the times you have helped us with the nuclear spin control. Good luck in the US, and I hope that all shoulders and elbows stay safe. Maarten, have fun on all your travels and good luck. Joe, how many instruments can you play? Thank you for all the good (music) times. Hans, expert on spin pairs, thank for all the nice times in F027. Sjoerd, thank you for the interesting lunch discussions and the wonderful game of King Fridge, good luck with the SiC project together with Guido. Damian, thank you for all the conversations and fun stories. Nicolas and Benjamin, nuclear spins are now serious business within the Networkies. The struggles with the AWG will pay off (who needs real-time multiplication and more than 16 variables anyways?) and I'm really curious how the surface-7 experiment will work out. Good luck!

I would also really like to thank you, Julia. I have learned a lot about outreach from you (just do it) and I frequently copied your excellent examples for explaining superposition and entanglement to all sorts of audiences. I will always remember us as proud paranymphs of Suzanne. Good luck with your group in Leiden. Aletta, thank you too! It was nice to have a basketball friend around and all the best with your PhD!

Jelmer, we shared an office for quite some time. It was fun to occasionally watch Tour de France with you and I enjoyed all our scientific and non-scientific discussions.

A warm thank you to the communications team of QuTech; Leonie, Rianne, Aldo and others. Thank you for the great outreach opportunities and always thinking along. I would also like to thank Martine and Jeffrey for making the Faces of Science possible and providing a wonderful platform for sharing our research.

I would like to thank all the management assistants for their support and the willingness to answer all sorts of questions. In particular Chantal, thank you and I wish you good luck in Miami!

To Bas, Tim, Victoria, Francisco, Carlo, Wojciech, Bart and all others from Stephanie's group; thank you for all the interesting discussions, help with mathematical problems and optimizations and the collaborations on the link layer experiments. Without the great support of the technicians and engineers QuTech would never be able to achieve all its ambitious goals. Thank you Raymond and Raymond with your help on the phase stabilization electronics. Mariya and Martin, thank you for your work as optical engineers and making everyone familiar with laser safety. Jason and Olaf, thank you for all the help with the cryostats. Siebe, Remco, Roy, Jelle, Mark, thank you for all your help and solutions in the lab! Henri, Ingmar and the others, thank you for all your software support!

During the years, I appreciated a lot the female scientist lunches. Charlotte, thank you for organizing. Anne-Marije, Floor, Victoria, Nandini, Sara, Willemijn, Nora, Delphine, Marta and all others, thank you for all the interesting discussions, honest reflections and the gezelligheid!

And to all others at QuTech, thank you for the great times. QuTech sparks ambition, but there is always time for fun, cake, sports and drinks! The only thing I can say is that I have really enjoyed my time at QuTech!

Het einde van mijn PhD betekent ook het einde van een fantastische tijd in Delft. Lief Bestuur 83, Zeswecan, Vie, Punch ladies, Panini's, Flammies en huisgenoten van Hof van Eden, dank jullie wel voor deze ontzettende leuke 11 jaar.

Constance, Marcel, Hidde en Judith, dank jullie wel voor het warme welkom in de familie. Ik voel me enorm gesteund door jullie en ik waardeer jullie altijd gemeende interesse heel erg!

Ward en Marieke, we zijn alle drie heel anders, maar toch ook weer niet. Ik weet dat ik altijd op jullie kan vertrouwen, dankjulliewel! En ik hoop dat jullie samen met Colas, Paul, Joep en Nr. 2, snel langs kunnen komen in LA.

Papa, ik moet je helaas teleurstellen, ik heb nog geen kat naar de maan geteleporteerd. Pap, dankjewel voor al je vertrouwen, ik weet dat je altijd achter me staat, je hebt me altijd aangemoedigd om vragen te durven stellen en mezelf uit te dagen. Mama, ook al is quantum niet jouw 'cup of tea', je biedt altijd een luisterend oor en staat altijd voor me klaar. Je hebt me geleerd om eerlijk te zijn naar mezelf en voor mezelf op te komen. Papa en Mama, dank jullie voor alle kansen die jullie me hebben geboden. Ik hou van jullie!

Daan, ik kan me geen wereld zonder jou voorstellen. Ik hou van jou, voor nu en voor altijd!

CURRICULUM VITÆ

Sophie Lucia Nathalie HERMANS
December 24th, 1992, Utrecht, The Netherlands

2005-2011	Secondary school College de Heemlanden, Houten, The Netherlands
2011-2014	Bachelor of Science, Applied Physics Delft University of Technology, Delft, The Netherlands Thesis: *"Cloud Base Height Computation with Stereo Whole-Sky Cameras"* Supervisor: Prof. Harm Jonker
Fall 2013	Erasmus Exchange, minor Sustainable Technologies Norwegian University of Science and Technology, Trondheim, Norway
2014-2017	Master of Science, Applied Physics Delft University of Technology, Delft, The Netherlands Thesis: *"Towards Purcell enhancement of the zero-phonon line of nitrogen-vacancy centers in diamond in an open Fabry-Pérot microcavity"* Supervisors: Dr. Suzanne van Dam and Prof. Ronald Hanson
2018-2022	PhD, Physics Delft University of Technology, Delft, The Netherlands Thesis: *"Quantum Networks using Spins in Diamond"* Supervisors: Prof. Ronald Hanson and Prof. Stephanie Wehner

LIST OF PUBLICATIONS

6. **Hermans, S. L. N.**, Pompili, M., Dos Santos Martins, L., Rodriguez-Pardo Montblanch, A., Beukers, H. K. C., Baier, S., Borregaard, J., & Hanson, R. Entangling remote qubits using the single-photon protocol: an in-depth theoretical and experimental study *In preparation.*

5. Pompili, M.*, Delle Donne, C. *, Te Raa, I. , Van der Vecht, B., De Kluijver, L., Stolk, A., **Hermans, S. L. N.**, Kozlowski, W., Pawełczak, P., Wehner, S., & Hanson, R., Entanglement delivery with a quantum network stack, *Submitted for peer review.*

4. **Hermans, S. L. N.***, Pompili, M.*, Beukers, H. K. C., Baier, S., Borregaard, J., & Hanson, R. Qubit teleportation between non-neighboring nodes in a quantum network. *Accepted for publication in Nature.*

3. Hanson, R., **Hermans, S. L. N.**, (2021) Een netwerk van verstrengelde quantumbits, *Nederlands Tijdschrijft voor Natuurkunde*, 87-8, 36–41.

2. Pompili, M.*, **Hermans, S. L. N.***, Baier, S.*, Beukers, H. K. C., Humphreys, P. C., Schouten, R. N., Vermeulen, R. F. L., Tiggelman, M. J., Dos Santos Martins, L., Dirkse, B., Wehner, S., Hanson, R. (2021). Realization of a multinode quantum network of remote solid-state qubits. *Science*, 372(6539), 259–264.

1. Tchebotareva, A.*, **Hermans, S. L. N.***, Humphreys, P. C., Voigt, D., Harmsma, P. J., Cheng, L. K., Verlaan, A. L., Dijkhuizen, N., De Jong, W., Dréau, A., Hanson, R. (2019). Entanglement between a Diamond Spin Qubit and a Photonic Time-Bin Qubit at Telecom Wavelength. *Physical Review Letters*, 123(6)

* These authors contributed equally to this work.

Casimir PhD Series 2022-09
ISBN 978-90-8593-520-9